
DOCTORAL THESIS

PARAMETER IDENTIFICATION AS THE BASIS
FOR PROGNOSSES IN GEOTECHNICAL ENGINEERING

DISSERTATION

PARAMETERIDENTIFIKATION ALS GRUNDLAGE
FÜR PROGNOSEN IM GRUNDBAU

ausgeführt zum Zwecke der Erlangung des akademischen
Grades eines Doktors der technischen Wissenschaften

eingereicht an der Technischen Universität Wien
Fakultät für Bauingenieurwesen

von

Dipl.-Ing. Bernhard Pichler

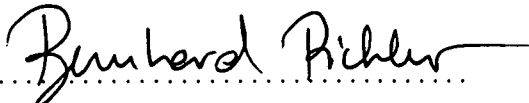
Matrikelnummer: 92 27 000

Leibnifrostgasse 4/5, 1040 Wien, Österreich

Referent: O. Univ. Prof. Dipl.-Ing. Dr. techn. Dr. h.c. mult. Herbert Mang, Ph.D.
Institut für Festigkeitslehre, Technische Universität Wien
Karlsplatz 13/202, 1040 Wien, Österreich

Koreferent: Prof. Dr. inz. habil. Dr. h.c. Zenon Waszczyszyn
Institut für Computer Methoden im Bauingenieurwesen
Technische Universität Krakau, Warszawska 24, 31-155 Krakau, Polen

Wien, im November 2003


.....

Meiner zukünftigen Frau Christina herzlich gewidmet

Danksagung

An dieser Stelle möchte ich mich bei Herrn O. Univ. Prof. Dipl.-Ing. Dr. techn. Dr. h. c. mult. Herbert Mang, Ph.D., Vorstand des Instituts für Festigkeitslehre an der Technischen Universität Wien, aufrichtig bedanken. Sein großes Interesse an der Zielausrichtung und am Fortschritt der vorliegenden Arbeit, die idealen Arbeitsbedingungen am Institut sowie die große Freiheit, die mir bei der Behandlung des Themas "Parameteridentifikation" eingeräumt wurde, habe ich sehr geschätzt. Für die finanzielle und wissenschaftliche Unterstützung in Zusammenhang mit meiner Teilnahme an internationalen Tagungen möchte ich genauso danken wie für sein oftmals geäußertes Credo, Parameteridentifikation dürfe nicht zum Selbstzweck durchgeführt werden, sondern müsse vielmehr die Grundlage für Ingenieurprognosen sein. Dieser Leitspruch hat den Charakter dieser Arbeit stark beeinflusst.

Bedanken möchte ich mich auch beim Koreferenten dieser Arbeit, Herrn Prof. Dr. inz. habil. Dr. h.c. Zenon Waszczyszyn, für die von ihm vermittelte Begeisterung für die Methoden des soft-computing, sein Interesse an meinen Arbeiten auf diesem Gebiet sowie für das Einräumen der Möglichkeit bei zahlreichen internationalen Tagungen über neue Fortschritte berichten zu können. Dank gebührt auch Herrn O. Univ. Prof. Dr. phil. Peter Schuster, mit dem ich zu Beginn meines Doktoratsstudiums ein wichtiges Gespräch geführt habe, das großen Einfluss auf konzeptionelle Aspekte meiner Arbeit gehabt hat.

Vielen Dank möchte ich an Herrn Dipl.-Ing. Dr. techn. Christian Hellmich richten, von dessen Unterstützung ich im Rahmen unserer Zusammenarbeit in hohem Maße profitiert habe. Sein Bekenntnis, sich immer auf den physikalischen Gehalt der Mechanik zu konzentrieren, hat mich stets bestärkt und mir viel Motivation beim Anfertigen der vorliegenden Arbeit gegeben. Besonders dankbar bin ich für die vielen tiefgehenden Diskussionen und seinen bei weitem nicht nur fachlichen Zuspruch in Situationen des Rückschlags.

Für zur Verfügung gestellte Materialroutinen sei Herrn Univ.-Doz. Dipl.-Ing. Dr. techn. Roman Lackner, Herrn Dipl.-Ing. Dr. techn. Christian Kropik und Frau Dipl.-Ing. Yvonne Spira aufrichtig gedankt. Für die sehr wertvolle Anleitung im Zusammenhang mit der Computerprogrammierung sowie die oftmals im Stillen erfolgte Betreuung des Rechnersystems möchte ich mich bei Herrn Univ.-Doz. Dipl.-Ing. Dr. techn. Peter Mackenzie-Helwein, Herrn Dipl.-Ing. Dr. techn. Thomas Huemer und Herrn Dipl.-Ing. Christian Schranz, M.Sc., bedanken. Bei Herrn Univ. Prof. Dipl.-Ing. Dr. techn. Josef Eberhardsteiner möchte ich mich für seine vermittelnde Art und sein stets offenes Ohr bedanken. Er hat maßgeblichen Einfluss auf das überaus gute Arbeitsklima am Institut für Festigkeitslehre gehabt, für das

ich mich auch bei den bereits genannten Kollegen, sowie bei Frau Dipl.-Ing. Karin Hofstetter, Frau Martina Pöll, Herrn Dipl.-Ing. Dr. techn. Herbert Rattensperger, Herrn Dipl.-Ing. Dr. techn. Jürgen Macht, Herrn Dipl.-Ing. Dr. techn. Peter Pivonka, Herrn Dipl.-Ing. Christian Pichler, Herrn Dipl.-Ing. Martin Fleischmann und allen anderen Mitarbeitern des Instituts bedanken möchte.

Herrn Dipl.-Ing. Oswald Steiner, Herrn Manfred Unterluggauer und Herrn Ing. Christian Stöckl, Transalpine Ölleitung in Österreich Ges.m.b.H., Herrn Dipl.-Ing. Dr. techn. Josef Schedelberger und Herrn Mag. Hannes Mayer, Zivilingenieurbüro Schedelberger, sowie Herrn Josef Schmöllnerl, Hottinger Baldwin Messtechnik Ges.m.b.H., sei an dieser Stelle für die Kooperation im Zusammenhang mit der Realisierung von Experimenten gedankt.

Meinen Freunden und Bekannten, die mich während der Entstehungszeit dieser Arbeit begleitet haben, möchte ich ebenfalls aufrichtig danken.

Mein herzlicher Dank gebührt der Familie. Allen voran sei meinen Eltern gedankt, die mich in meinen Bestrebungen stets unterstützt und perfekte private Rahmenbedingungen geschaffen haben, die es mir erlaubten, mich sorglos und ohne behindernde Ablenkungen meinen Studien zu widmen. Meinen Geschwistern, deren Familien, den Großeltern und meinen zukünftigen Schwiegereltern sei ebenfalls in aller Form gedankt. Sie alle waren mir sehr wertvolle Wegbegleiter in den vergangenen Jahren.

Von ganzem Herzen möchte ich mich bei meiner Verlobten bedanken. Sie war mir stets die wichtigste Stütze in allen Belangen.

Kurzfassung

Zuverlässige numerische Simulationen im Ingenieurwesen setzen mathematische Modelle zur wirklichkeitsnahen Beschreibung des Verhaltens der eingesetzten Materialien voraus. Sie beinhalten Materialparameter, die zur quantitativen Festlegung des Materialverhaltens gewählt werden müssen. Für die gängigsten Werkstoffe des Bauingenieurwesens, d. h. für Stahl und Beton, wurden in den vergangenen Jahrzehnten ausgereifte Materialmodelle entwickelt sowie die darin aufscheinenden Materialparameter bestimmt. Sie erlauben eine zuverlässige und wirtschaftliche Dimensionierung von Stahl- und Betonkonstruktionen.

Numerische Simulationen im Grundbau sind hingegen weiterhin umstritten, obwohl in den vergangenen Jahren durchaus wirklichkeitsnahe Materialmodelle zur Beschreibung der unterschiedlichsten Arten von Böden entwickelt wurden. Prognosen des Strukturverhaltens bei grundbaulichen Baumaßnahmen konnten allerdings selbst durch den Einsatz moderner numerischer Methoden, wie z. B. der Finiten Elemente Methode, nicht ausreichend zuverlässig gemacht werden. Hauptursache dafür – und somit Grundlage für die vergleichsweise geringe Akzeptanz numerischer Simulationen im Grundbau – ist die Streuung der Materialeigenschaften von Böden.

In der vorliegenden Arbeit wird die Rolle der Parameteridentifikation im Grundbau umfassend behandelt. Aufgezeigt wird ihre Rolle als Bindeglied zwischen theoretischer Entwicklung von Materialmodellen und deren Anwendung in der Strukturanalyse. Methodischen Aspekten wird mit der Entwicklung eines neuen Parameteridentifikationsalgorithmus Rechnung getragen. Dabei kommen Verfahren des *soft computing* wie z. B. künstliche neuronale Netze und genetische Algorithmen zum Einsatz. Die neue Methode erlaubt eine rasche und zuverlässige sowie simultane Identifikation mehrerer Parameter. Sie wird somit den speziellen Anforderungen von Identifikationsproblemen im Grundbau gerecht. Konzeptionelle Aspekte der Parameteridentifikation im Grundbau werden im Rahmen der Auseinandersetzung mit einer praktischen Problemstellung behandelt. Es wird die Belastung einer mit Schotter eingeschütteten Stahlrohrleitung durch Felssturz untersucht. Die Identifikation der Materialparameter von Schotter wird durch Auswertung von eigens entwickelten und durchgeführten Experimenten sowie durch Analyse von Versuchsdaten aus der einschlägigen Fachliteratur vorgenommen. Die Verifikation eines entwickelten Strukturmodells erfolgt anhand der Ergebnisse eines großmaßstäblichen Felssturzexperimentes auf eine eingeschüttete Rohrleitung. Es wird gezeigt, dass Identifikation von Materialparametern und Verifikation eines Strukturmodells strikt zu trennen sind, wenn ein numerisches Werkzeug entwickelt werden soll, das zuverlässige Prognosen im Grundbau ermöglicht.

Abstract

Reliable numerical simulations in engineering require mathematical models characterizing material behavior in a realistic manner. In order to capture quantitative aspects, respective material parameters must be specified. In the past decades, reliable material models were developed for the standard materials most frequently used in civil engineering, i. e. for steel and concrete, and their material parameters were identified. Accordingly, a reliable and economic mode of design of steel and concrete constructions became possible.

Numerical simulations in geotechnical engineering, however, are still controversial even though realistic material models describing the behavior of the various types of existing soils were developed. Prognoses of the structural behavior considering a geotechnical construction site did not become sufficiently reliable by using modern numerical simulation-methods such as, e. g., the Finite Element Method. The reason for this circumstance – which is responsible for the rather small acceptance of numerical simulations in geotechnical engineering – is the distinctive scatter of the material properties of soils.

In this thesis the role of parameter identification in geotechnical engineering is treated in an integrated manner. Its important role as a link between theoretical material modeling and structural application of such models is pointed out. Methodical aspects are covered by proposing a new parameter-identification method resting on *soft computing* such as artificial neural networks and genetic algorithms. The new algorithm permits fast, reliable, and simultaneous identification of several parameters. Therefore, it is well suited for parameter identification problems in geotechnical engineering. Conceptual aspects of parameter identification in geotechnical engineering are also addressed. As an example, the loading of a gravel-buried steel pipe subjected to rockfall is considered. Identification of the material parameters of gravel is based on the evaluation of designed and performed experiments as well as on test data taken from the open literature. Verification of the developed structural model rests on a real-scale rockfall experiment onto a gravel-buried steel pipe. It is shown that identification of material parameters and verification of a structural model must be separated strictly in order to prove whether or not a numerical simulation tool is capable to provide reliable prognoses in geotechnical engineering.

Contents

1	Introduction and scope of the work	1
2	Parameter identification (PI) in geotechnical engineering	4
2.1	Brief review of established PI methods employed in geotechnical engineering	5
2.1.1	Local and global search techniques	5
2.1.2	Gradient-free and gradient-based search techniques	6
2.2	Motivation for the development of a new PI method resting on soft computing	6
3	Artificial neural networks	8
3.1	Structure and functionality of biologic neurons	8
3.2	History of Artificial Neural Networks	9
3.2.1	The McCulloch-Pitts cell (1943)	10
3.2.2	Rosenblatt's perceptron (1958)	12
3.3	State of the art of Artificial Neural Networks	14
3.3.1	The Multi Layer Perceptron (MLP)	15
3.3.2	Training of MLPs	18
3.3.3	The problem of overfitting and underfitting	19
3.3.4	Protection of MLPs against underfitting and overfitting	20
	Definition of the architecture of MLPs	21
	Criterion for termination of training of MLPs	22
3.3.5	Operational phase of MLPs	22
4	Parameter identification resting on soft computing	24
4.1	Outline of the new PI method	26
4.1.1	Training of the modified MLP	27
4.1.2	Treatment of the underfitting and overfitting problem	29
	Determination of initial network weights employing a genetic algorithm (GA)	30
	The "reduced-training" algorithm	30

Initial choice of number of neurons in the hidden layer	32
4.1.3 Estimate and assessment of an optimal parameter set	32
4.1.4 Graphical interpretation of the proposed PI method	34
4.2 Assessment of the new PI method: back analysis of material properties from experimental data	35
4.2.1 Numerical analysis of direct-shear tests	36
4.2.2 Reduced versus classical training of ANNs	38
4.2.3 Back analysis of unknown material properties	40
4.2.4 Concluding remarks	43
4.3 Application to ground improvement by means of jet grouting	44
4.3.1 Statement of problem and proposed solution	45
4.3.2 Numerical analysis of temperature history in jet-grouted columns .	46
4.3.3 Parameter identification	47
4.4 Application to NATM tunneling	51
4.4.1 Statement of problem and proposed solution concept	51
4.4.2 Numerical analysis of the excavation process	53
4.4.3 "Measurement data" of underground station "Taborstraße"	55
4.4.4 Parameter identification	56
4.4.5 Parameter identification based on inaccurate measurement data . .	60
4.4.6 Predictions of displacements and of the level of loading of the shotcrete tunnel shell	61
4.5 Extension to first-order approximation neural networks	63
4.5.1 Outline of the extended parameter identification method	63
4.5.2 Application to ground improvement by means of jet grouting	65
Results from the first PI iteration steps	67
Results from the second PI iteration steps	68
Results from the last PI iteration steps	70
Comparison of the obtained results	72
4.6 Conclusions	72
5 Loading of a gravel-buried steel pipe subjected to rockfall	74
5.1 Introduction	75
5.2 Theoretical and experimental material characterization	76
5.2.1 Elasto-plastic material behavior of steel	76
5.2.2 Elasto-plastic material behavior of gravel	76
5.2.3 Identification of gravel elasticity	79
5.2.4 Identification of inelastic behavior of gravel	84

Identification of the parameters governing shear failure of gravel . . .	84
Identification of the parameters governing compaction of gravel . . .	86
Initial size and shape of the cap and tensile failure of gravel	86
5.2.5 Discussion and final remarks regarding the identified material parameters of gravel	87
5.3 Estimation of penetration depth and impact force arising from rockfall onto gravel	88
5.3.1 Impact of rocks onto gravel – Dimensional analysis	88
5.3.2 Design of experiments	90
5.3.3 Evaluation of experimental results	95
Estimation of penetration depth	96
Estimation of impact duration and impact force	99
5.3.4 Summary and Conclusions	105
5.4 Development and assessment of a structural model	105
5.4.1 Preliminary investigation of structural behavior – design of experimental setup	107
5.4.2 Real-scale rockfall test: performance and results	110
5.4.3 3D Finite Element structural model	112
5.5 Prognoses of the structural behavior	115
5.6 Summary and conclusions	117
6 Summary and conclusions	119
7 Bibliography	121
Appendices:	128
A Genetic algorithm (GA)	128
B Backpropagation algorithm for first-order approximation ANNs	130
C Experimentally obtained values of C_{1111} and C_{1212} of gravel	134
D Kinematic model of the impact used for the PFEA	135
Curriculum Vitae	137

Chapter 1

Introduction and scope of the work

In the last decades, numerical simulations became a popular tool supporting decision-making processes in geotechnical engineering. Material models were developed which are suitable to describe the rather complex behavior of various types of existing soils and rocks. Development of such models requires the introduction of material parameters. Therefore, reliable numerical simulations require both, adequate material modeling and identification of the involved material parameters. The scattering of material properties in geotechnical engineering renders the parameter identification process a challenging task. It represents the major contrast to material modeling of steel and – to some extent – concrete. For such standard materials adequate material model are established *and* the involved material parameters are nowadays well known for most practical applications. In geotechnical engineering, parameter identification will stay an important aspect of numerical simulations, given the various types of existing soils and rocks that are encountered at construction sites.

Monitoring of the structural behavior at geotechnical construction sites became state-of-the-art in the last decades. Nowadays, displacement measurements are performed routinely at almost every construction site. Trends of measured displacements are key-features on which experienced engineers base their risk assessments. Accordingly, structural monitoring supports decisions whether or not additional safety constructions must be built in order to prevent a structure from hazardous situations. To provide engineers with even more insight into the structural behavior, numerical analyses are carried out parallel to structural monitoring. Such simulations are commonly performed by means of the Finite Element (FE) method. Results of respective FE analyses allow at least for a qualitative assessment of the structural behavior in inaccessible domains. In order to increase the

reliability of such numerical simulations, parameter identification is performed to adjust the model output to the monitored structural behavior. Model parameters, i. e. in most cases material parameters, are back analyzed such that results from numerical simulations meet the performed measurements as well as possible. In this context, parameter identification and respective numerical analyses contribute to the documentation of construction processes. However, they do not aim at estimating future structural behavior.

Within this thesis, parameter identification is treated in a more integrated manner. Its role in the context of quantitative prognoses of the structural behavior in geotechnical engineering is addressed. Such prognoses require a reliable structural model as the basis for numerical simulations. In this context, engineering skill is required in order to choose or develop a model which is as sophisticated as necessary but also as simple as possible. Assuming the proper simplifying hypotheses represents the major challenge of modeling in geotechnical engineering. This mode of model selection or development requires verification of the chosen hypotheses. It is referred to as model verification. Results obtained by means of the selected or developed model must meet experimental measurements satisfactorily. If model verification is completed successfully, prognoses of the structural behavior under investigation become possible.

As a part of this concept, material parameters must be identified prior and independently to model verification. For the purpose of parameter identification experiments must be performed. Preferably, these tests should refer to a single physical phenomenon. Such experiments permit explicit parameter identification. However, some standardized and, hence, routinely performed tests in geomechanics activate a number of physical effects. Such experiments require a parameter identification method searching for optimal parameters in an implicit manner. In all cases parameter identification should take into account the scattering of material parameters. This requires redundant information about the material behavior of soils. Therefore, a situation where several *independent* types of tests are available in order to back analyze material parameters is optimal for parameter identification.

After parameter identification is completed, model verification can be tackled. In this context, measurements referring to the structural behavior under investigation are required. These experimental measurements must be independent from the test results used to back analyze material parameters. Otherwise, it cannot be proved that the model is capable to provide genuine predictions of the structural behavior.

In this thesis, parameter identification is addressed with special emphasis on the predictive capability of the involved models as outlined above. In the first part, methodical aspects of parameter identification are considered. A brief discussion of existing PI meth-

ods is presented in Chapter 2. It represents the motivation for the development of a new parameter identification method. It is resting on soft computing including artificial neural networks (ANNs). Therefore, the theoretical background of ANNs is addressed in Chapter 3. It is dedicated to readers that are not familiar with ANNs. In Chapter 4 the new parameter identification method is described. First, the proposed algorithm is outlined. Secondly, it is shown that new proposals concerning the training of ANNs are reasonable. Finally, it is proved that the new method fulfills the requirements defined in Chapter 2 by solving parameter identification problems related to (i) tunneling according to the New Austrian Tunneling Method and (ii) ground improvement by means of jet-grouting. In the second part of this thesis, the role of parameter identification as an important feature for prognoses in geotechnical engineering is demonstrated. As an example, the loading of a gravel-buried steel pipe subjected to rockfall is considered in Chapter 5. Subchapter 5.1 provides an introduction into the problem under consideration. In Subchapter 5.2, material parameters of gravel are identified based on designed and performed experiments as well as on test data taken from the open literature. In Subchapter 5.3, loading assumptions for rockfall onto gravel are addressed. They include dimensionless estimation formulae for penetration depth and maximum impact force representing functions of the mass of the downfalling rock boulder, its height of fall, and the indentation resistance of gravel. In Subchapter 5.4, the development and the verification of a three-dimensional elasto-plastic Finite Element model for the structural analysis of rockfall onto a gravel-buried steel pipe is presented. In Subchapter 5.5, finally, prognoses of the loading of a gravel-buried steel pipe subjected to rockfall events that were not investigated experimentally are described. It is shown that identification of material parameters and verification of a structural model must be separated strictly in order to develop a numerical tool capable to provide reliable prognoses in geotechnical engineering.

Chapter 2

Parameter identification (PI) in geotechnical engineering

In the last decades, numerical simulations became a popular tool supporting decision-making processes in geotechnical engineering. Material models were developed which are suitable to describe the rather complex behavior of various types of existing soils and rock. Development of such models requires the introduction of material parameters. The material models provide a qualitative description of the behavior of soils and rock, whereas the quantitative aspects are governed by the material parameters. Therefore, reliable numerical simulations require both, adequate material modeling and identification of the involved material parameters. The scattering of material properties in geotechnical engineering renders the parameter identification process a challenging task.

In order to solve a PI problem, an error function must be defined. It represents the difference between measurements from experiments or from the construction site and corresponding quantities obtained from numerical analyses. The error function depends on the unknown parameters. It can be defined as

$$\mathcal{R}^h(\mathbf{p}) = \sqrt{\frac{1}{n_o} \sum_{r=1}^{n_o} \left(\frac{u_r^h(\mathbf{p}) - u_r}{u_r} \right)^2}, \quad (2.1)$$

where u_r and u_r^h , $r = 1, 2, \dots, n_o$, are the selected measurements and the corresponding numerical results, respectively. Obviously, u_r^h depends on the unknown model parameters collected in the vector \mathbf{p} . Based on the error function (2.1), back analysis aims at determination of the absolute minimum of $\mathcal{R}^h(\mathbf{p})$, which reads in mathematical terms

$$\mathcal{R}^h(\mathbf{p}) \rightarrow \text{minimum}. \quad (2.2)$$

This is a challenging task since usually $\mathcal{R}^h(\mathbf{p})$ is a nonlinear function. Therefore, $\mathcal{R}^h(\mathbf{p})$ may have several local minima.

There is a large number of established methods to solve PI problems. They will be addressed in Subchapter 2.1. A comparison of the properties of these methods considering the requirements of PI problems in geotechnical engineering will be presented in Subchapter 2.2. It represents the motivation for the development of a new parameter identification method resting on soft computing.

2.1 Brief review of established PI methods employed in geotechnical engineering

PI as defined in (2.2) leads to an optimization problem. Therefore, established optimization methods are commonly employed to solve PI problems. There exists a great variety of such procedures. In the following two sections, a categorization of optimization methods will be presented. Thereby, two key properties of such methods will be taken into account. In Section 2.1.1, methods representing *local* search techniques will be distinguished from *global* search techniques. Subsequently, *gradient-free* optimization methods and *gradient-based* approaches will be addressed in Section 2.1.2.

2.1.1 Local and global search techniques

A local search technique starts with an arbitrarily chosen parameter vector \mathbf{p} . After computation of $\mathcal{R}^h(\mathbf{p})$, it searches for a new parameter vector in the vicinity of \mathbf{p} that reduces the value of the error function \mathcal{R}^h . Thereby, commonly so-called line-search techniques are employed. If such a parameter vector is found, the search for an even better solution is continued in the vicinity of this new parameter vector. Step by step, parameter vectors will be found associated with values of \mathcal{R}^h that are continuously decreasing. The algorithm will be stopped, if a minimum of the error function is found, i. e., if continuation of the algorithm does not lead to a further reduction of \mathcal{R}^h anymore. At that stage, a local search technique provides insight into the shape of \mathcal{R}^h along a specific decreasing path. However, most parts of the error function will still remain unknown. Therefore, local search techniques suffer from the drawback that they may get trapped in a local minimum of \mathcal{R}^h . To overcome this problem, local search techniques must be started from different points in the parameter space, i. e., from differently chosen initial parameter vectors. If all these independently performed local searches for an optimal parameter vector end up at the same point, the respective minimum of \mathcal{R}^h will be regarded as the global mini-

mum. Most classical optimization methods, such as Powell's method, the gradient-descent method, conjugated-gradient methods, variable-metric methods, and Newton's method are local search techniques (Vanderplaats, 1984).

Global search techniques are parallel solution strategies, i. e., they work with a large number of different parameter vectors. Accordingly, at each iteration step, several values of the error function \mathcal{R}^h are evaluated in the entire parameter space. Therefore, such solution strategies provide global insight in the shape of \mathcal{R}^h . Purely stochastic search techniques, for instance, determine the parameter vectors randomly. Hence, the entire parameter space will be covered rather evenly with candidates for an optimal parameter vector. In contrast to this property, genetic algorithms increase the density of parameter vectors in promising domains of \mathcal{R}^h . Hence, in successive iteration steps, the chosen parameter vectors will be concentrated in regions where \mathcal{R}^h takes on small values. On the other hand, only few parameter vectors will be located in domains characterized by large values of \mathcal{R}^h . A global search for an optimal parameter set will be terminated, if an already found low value of \mathcal{R}^h cannot be outperformed in successive iteration steps.

Local search techniques are more efficient than global search techniques, i. e., local methods require a much smaller number of computations of \mathcal{R}^h than global methods. However, global search techniques are more robust than local search techniques since they do not get trapped in local minimas of \mathcal{R}^h .

2.1.2 Gradient-free and gradient-based search techniques

Gradient-free PI methods do not require derivatives of \mathcal{R}^h with respect to \mathbf{p} . Such methods are, e. g., Powell's method, stochastic search techniques, and genetic algorithms.

Gradient-based PI methods require derivatives of \mathcal{R}^h with respect to \mathbf{p} . The gradient-descent method, for instance, requires computation of the first derivative of \mathcal{R}^h with respect to \mathbf{p} . Newton's method requires first and second derivatives of \mathcal{R}^h with respect to \mathbf{p} . Computation of these derivatives accompanying to a large FE simulation requires major modifications of the FE code (Mahnken and Stein, 1996a; Mahnken and Stein, 1996b). This circumstance renders gradient-based PI in geotechnical engineering a rather challenging task.

2.2 Motivation for the development of a new PI method resting on soft computing

In general, existing PI methods suffer from the following drawbacks:

- They are either robust or efficient.
- Classical PI methods do not take into account information about the shape of \mathcal{R}^h obtained in previous iteration steps. Only local properties of \mathcal{R}^h influence the direction in which the search for an optimal parameter set is continued.
- If an optimal solution was found, existing PI methods do not provide insight into the sensitivity of the solution. Hence, commonly a separate sensitivity analysis is required to assess an obtained solution.

Therefore, a new PI method should satisfy the following requirements:

1. It should be both efficient and robust. Accordingly, a hybrid approach must be chosen. First, the PI method should search globally in order to provide a parameter vector in the vicinity of the global minimum of \mathcal{R}^h . There, starting from this near optimal solution, a local search technique should yield the parameter vector associated with the global minimum of \mathcal{R}^h .
2. Information *from each* FE analysis that has already been performed should influence the prognosis of an optimal parameter set. Only such an approach will allow for finding the solution of a PI problem and keeping the number of required FE simulations as small as possible.
3. The PI method should provide insight into the sensitivity of the obtained solution.

In order to meet these requirements, a new PI method is proposed. It is based on soft computing since application of such methods allowed for promising solutions of similar problems (Huber, 2000; Feng et al., 2000; Waszczyszyn and Ziemiański, 2001). In Chapter 3, an overview over selected historical developments concerning artificial neural networks (ANNs) will be presented. Moreover, the state of the art of Multi Layer Perceptrons (MLPs), which is a specific type of ANN, will be addressed. In Chapter 4, the new PI method resting on soft computing will be presented.

Chapter 3

Artificial neural networks

Development of modern artificial neural networks (ANNs) dates back to the 1940s. ANNs were designed to imitate biologic neural networks. For this purpose, the governing properties of biologic neurons were studied with special emphasis on their data processing. Nervous systems consist of thousands up to millions of interconnected neurons. This distinctive and hierarchical cross-linkage of neurons is nowadays interpreted to be the *conditio sine qua non* for consciousness and complex behavior, (Rojas, 1996).

3.1 Structure and functionality of biologic neurons

Biologic neurons are highly complex cells. For the purpose of designing artificial neurons, four elements of biologic neurons (see Figure 3.1 (a)) are considered in a simplified manner: dendrites, cell body, axon, and synapses. Dendrites receive chemical signals from other cells and convert them into electrical signals (pulses) which are transmitted to the cell body. These electrical signals cause an electrical depolarization of the surface of the cell body. If the amount of depolarization becomes equal to the stimulus threshold of the cell, it will become active. Therefore, a number of pulses must arrive at the same time or within a very short time span at a certain neuron. Otherwise, the neuron will not be activated. If the stimulus of a cell body is larger than its threshold, an activation potential, i. e. an electrical impulse (see Figure 3.1 (b)), will be initiated. The axon carries these impulses from the cell body to the synapses which transmit them in general chemically to the respective innervated cell. Activation potentials have always the same shape and amplitude. Hence, in order to document the extent of its activation, a stimulated neuron fires a series of such impulses. The firing frequency is proportional to the activation of the cell.

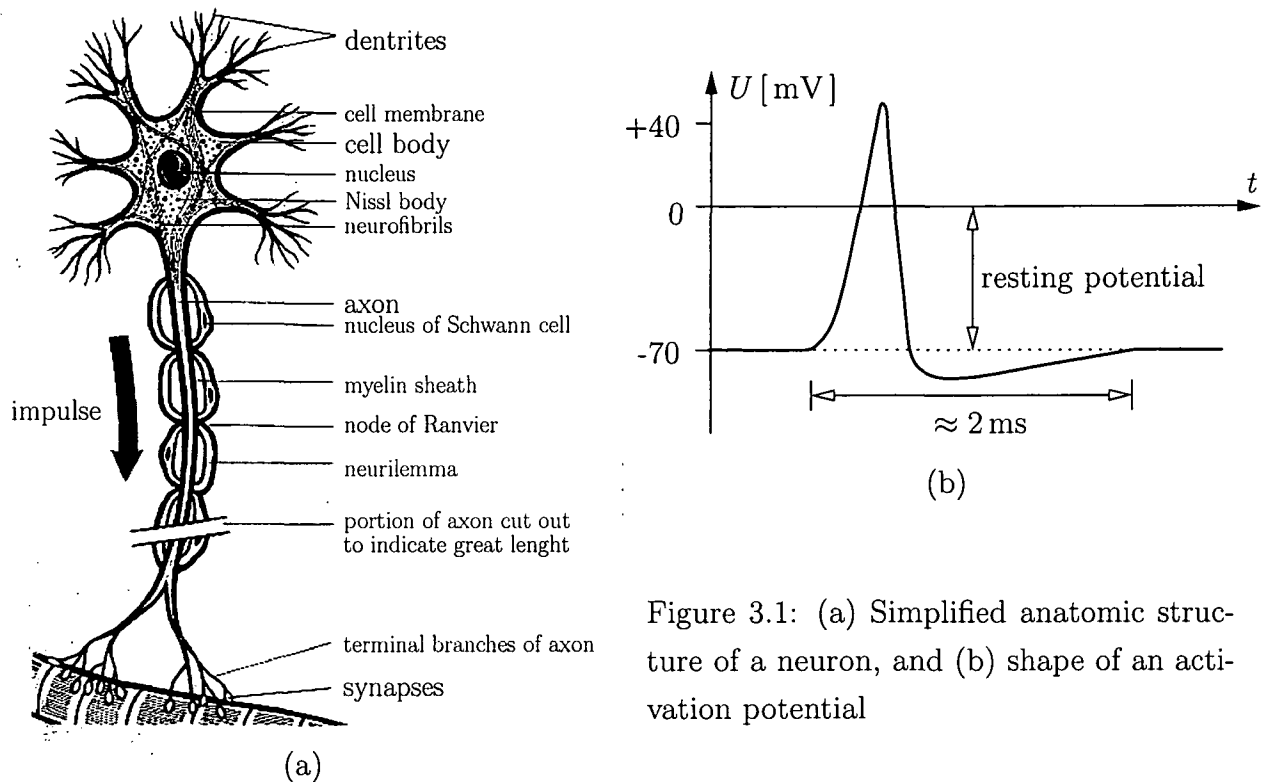


Figure 3.1: (a) Simplified anatomic structure of a neuron, and (b) shape of an activation potential

3.2 History of Artificial Neural Networks

The development of ANNs dates back to the 1940s. Warren S. McCulloch, a psychiatrist and neuroanatomist, and Walter Pitts, a mathematician, tried to assess the capacity and efficiency of human brains. In 1943, they developed the well known McCulloch-Pitts cell which formally models cerebral activity. In the late 1950s, Frank Rosenblatt, a psychologist, developed a neural network model called perceptron. It was proposed to solve problems of recognition and classification of visual patterns. The perceptron is still widely considered as one of the most important and influential neural network models. In the following two sections, an overview over these two specific trend-setting models will be presented.

The historical overview is restricted to these two models, since they were the basis for the development of the so-called Multi Layer Perceptron. This specific type of ANN which is frequently used in civil engineering will be the only type of ANN considered in this thesis. A more general discussion of historical developments and the theoretical background of ANNs may be found in standard textbooks, such as, e.g., (Fausett, 1994; Rojas, 1996; Haykin, 1999).

3.2.1 The McCulloch-Pitts cell (1943)

The first mathematical model of cerebral activity by means of an artificial neuron was the McCulloch-Pitts cell, (McCulloch and Pitts, 1943). Such a cell works with binary information only, i. e., inputs and outputs can be equal either to zero or one. It contains a stimulus threshold θ which can be equal to an arbitrary real number, see Figure 3.2 (a). It is assumed, that all inputs x_1, x_2, \dots, x_n arrive at the cell at the same time. The sum

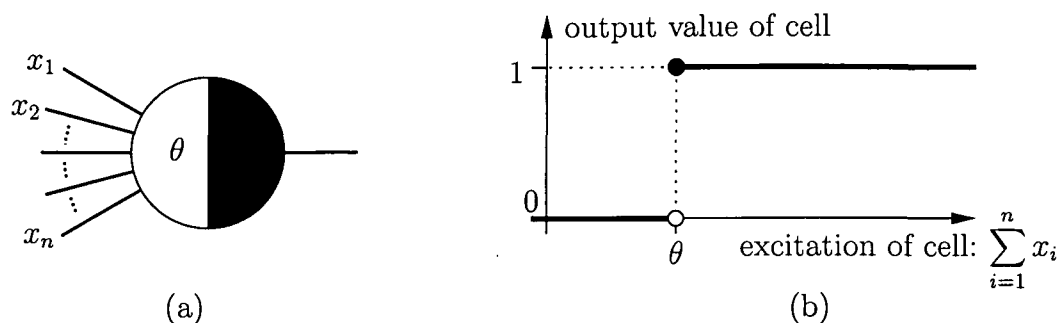


Figure 3.2: McCulloch-Pitts cell with stimulus threshold θ : (a) structure (Minsky, 1967), and (b) output function, i. e., the Heaviside step-function

of all inputs represents the *excitation* of the cell. Hence, if there are no input signals, the excitation of the cell will be equal to zero. In order to calculate the *activation* of the cell, the stimulus threshold θ is subtracted from the excitation. If the activation is greater than or equal to zero, i. e., if the sum of input quantities is greater than or equal to θ , the output of the cell will be one. In all other cases, the output of the cell is equal to zero. Accordingly, the output function of the cell is a Heaviside step-function, see Figure 3.2 (b).

Based on a single McCulloch-Pitts cell, logic functions such as for instance *AND* and *OR* can be modeled: In this context, the numerical values zero and one represent the logical values *false* and *true*. An *AND*-cell with two inputs, for instance, will fire one, only if both inputs are equal to one. I. e., the cell will produce *true* as an output, only if both inputs are *true*, see Figure 3.3 (a). An *OR*-cell with two inputs will fire one, only if at least one of both inputs is equal to one, see Figure 3.3 (b).

McCulloch-Pitts cells considered so far consisted of so-called stimulating input connections. Based on such cells, monotonic logical functions, i. e., a subset of all logical functions, can be modeled (Rojas, 1996). Modeling of non-monotonic logical functions requires so-called inhibitory input connections. If a pulse, i. e., if the numerical value one arrives along an inhibitory input connection at a McCulloch-Pitts cell, the cell will be deactivated. In such a case, the output of the cell is always equal to zero, no matter how much other possible connections contribute to the activation of the cell. If, however, the numerical value zero arrives along an inhibitory input connection at a McCulloch-Pitts cell, this input will

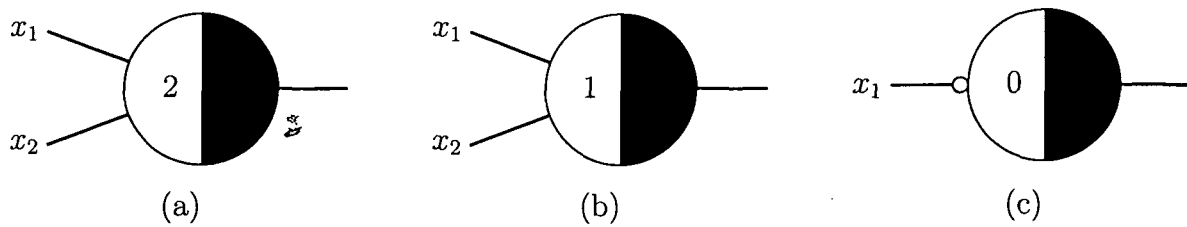


Figure 3.3: McCulloch-Pitts cells modeling logic functions: (a) AND-cell with two inputs, (b) OR-cell with two inputs, and (c) NOT-cell with one inhibitory input connection

contribute regularly to the activation of the cell. Based on an inhibitory input connection, the logical function NOT, i. e., the negation, can be modeled, see Figure 3.3 (c). A NOT-cell with one input will fire one (*true*), only if its input equal to zero (*false*). It will produce zero (*false*) as an output, if the input is equal to one (*true*).

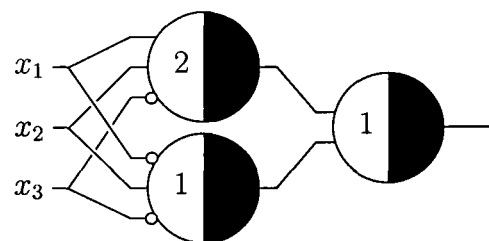
The presented McCulloch-Pitts cells are nowadays still of great importance in electrical engineering. AND, OR, and NOT-gates are the most practical devices for building *any* electrical circuit. In mathematical terms, the importance of McCulloch-Pitts cells is given by the following theorem (Rojas, 1996)

Any logical function of n binary variables can be calculated based on ANNs consisting of McCulloch-Pitts cells modeling the functions AND, OR, and NOT.

An example for such an ANN consisting of McCulloch-Pitts cells is illustrated in Figure 3.4.

input vectors \mathbf{x}	$F(\mathbf{x})$
(1, 1, 0)	1
(0, 1, 0)	1
all others	0

(a)



(b)

Figure 3.4: (a) Definition of a logical function F and (b) example for the realization of F with an ANN consisting of McCulloch-Pitts cells

Learning algorithms for ANNs consisting of McCulloch-Pitts cells are rather complicated. The only possibility to modify such a network in order to improve its performance is to change the topology of the ANN and/or the threshold values of the McCulloch-Pitts cells. Automatization of such learning algorithms is a very challenging task. This drawback was discussed by the American psychologist Frank Rosenblatt. In order to improve

the situation, Rosenblatt proposed another type of ANNs called *perceptron* (Rosenblatt, 1958).

3.2.2 Rosenblatt's perceptron (1958)

A perceptron is a so-called weighted ANN. Accordingly, all input connections of a neuron are associated with a numerical value called the weight of the connection, see Figure 3.5(a). Each input value x_i it will be multiplied by the respective weight, w_i . The sum of all weighted inputs represents the excitation of the respective neuron. If the excitation is equal to or larger than the stimulus threshold of the perceptron, it will produce plus one as its output. In all other cases, the neuron will produce minus one as its output. Accordingly, the output function of a perceptron is the signum function, see Figure 3.5 (b).

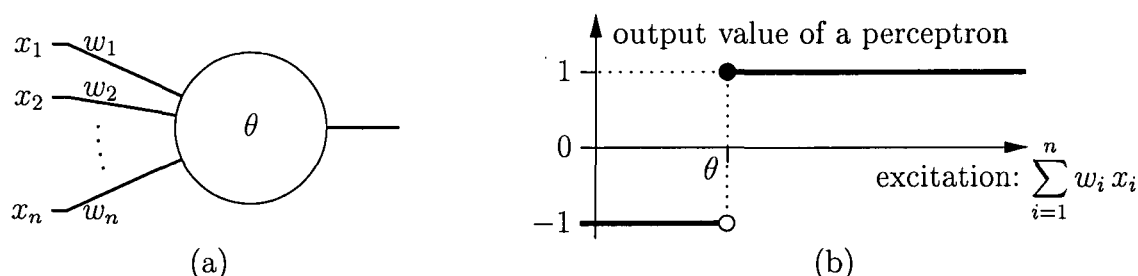


Figure 3.5: Perceptron with stimulus threshold θ : (a) structure with n weighted input connections, and (b) output function (signum function)

This basic property of a perceptron allows for solution of binary classification problems. In this context, it is assumed that every input vector \mathbf{x} belongs to one of two mutually exclusive classes ω_1 and ω_2 . The weights of the input connections and the stimulus threshold of the perceptron must be set such that (i) the output of the perceptron is $+1$ for any input vector $\mathbf{x} \in \omega_1$ and (ii) the output of the perceptron is -1 for any input vector $\mathbf{x} \in \omega_2$. Based on a perceptron linearly separable problems can be solved. This fact can be pointed out by a geometrical interpretation: The equation

$$\sum_{i=1}^n w_i x_i = \mathbf{w}^T \mathbf{x} = \theta \quad (3.1)$$

defines a $(n-1)$ -dimensional hyper-plane embedded in \mathbb{R}^n . \mathbf{w} , representing the weight vector of the perceptron, is equal to the normal vector of the hyper-plane. For $n = 2$, (3.1) represents a line, see Figure 3.6. The hyper-plane $\mathbf{w}^T \mathbf{x} = \theta$ partitions \mathbb{R}^n in two half spaces: $H_1 = \{\mathbf{x} : \mathbf{w}^T \mathbf{x} \geq \theta\}$ and $H_2 = \{\mathbf{x} : \mathbf{w}^T \mathbf{x} < \theta\}$. H_1 and H_2 are called *decision regions*. Therefore, the separating hyper-plane $\mathbf{w}^T \mathbf{x} = \theta$ is also referred to as a *linear decision boundary*.

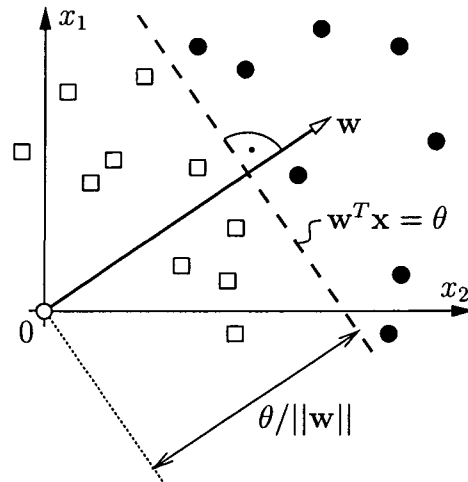


Figure 3.6: Geometrical interpretation of the functionality of a perceptron with two inputs ($n = 2$): The decision boundary $\mathbf{w}^T \mathbf{x} - \theta = 0$ is illustrated as a dashed line; input vectors \mathbf{x} of classes ω_1 and ω_2 are represented by black circles and white squares, respectively

Adjusting the network weights of a perceptron in order to solve a binary classification problem is referred to as the perceptron learning algorithm. It is started from a randomly initialized weight distribution. Sequentially, all input vectors are presented to the perceptron. If a training vector $\mathbf{x}_j \in \omega_1$ (desired output: $+1$) is misclassified, i. e., if $\mathbf{w}^T \mathbf{x}_j < \theta$, $\gamma \mathbf{x}_j$ will be added to \mathbf{w} . $\gamma > 0$ denotes a scalar parameter referred to as the learning rate. The described procedure moves the decision boundary towards the misclassified vector, which can be shown as

$$(\mathbf{w} + \gamma \mathbf{x}_j)^T \mathbf{x}_j = \mathbf{w}^T \mathbf{x}_j + \gamma \|\mathbf{x}_j\|^2 > \mathbf{w}^T \mathbf{x}_j, \quad \forall \gamma > 0. \quad (3.2)$$

Similarly, if a training vector $\mathbf{x}_k \in \omega_2$ (desired output: -1) is misclassified, i. e., if $\mathbf{w}^T \mathbf{x}_k > \theta$, $-\gamma \mathbf{x}_k$ will be added to \mathbf{w} . Again, the described procedure moves the decision boundary towards the misclassified vector:

$$(\mathbf{w} - \gamma \mathbf{x}_k)^T \mathbf{x}_k = \mathbf{w}^T \mathbf{x}_k - \gamma \|\mathbf{x}_k\|^2 < \mathbf{w}^T \mathbf{x}_k, \quad \forall \gamma > 0. \quad (3.3)$$

In both cases, depending on the chosen value of γ , it is possible that other, previously correctly-classified training vectors, will be misclassified by the new hyper-plane. However, assuming a constant learning rate γ and a linearly separable problem, i. e. a problem that can be solved with a perceptron, the described algorithm will converge to the solution (Rojas, 1996).

The equivalence of $\mathbf{w}^T \mathbf{x} = \theta$ and $\mathbf{w}^T \mathbf{x} - \theta = 0$ was the motivation for a practical modification of the structure of a perceptron. The stimulus threshold is *pulled* into the

weight vector by introducing an additional input $x_0 \equiv 1$ and a corresponding weight $w_0 = -\theta$, see Figure 3.7. Input vectors extended by $x_0 \equiv 1$ are called input vectors



Figure 3.7: Perceptrons with stimulus threshold θ (a) classical representation, and (b) equivalent representation with input vector in homogeneous coordinates

in *homogeneous coordinates*. Considering such a representation, the threshold value of a perceptron is treated as the weight of an additional connection. This is a great advantage for the training of a perceptron, where both input weights and the stimulus threshold should be adjusted in order to improve the performance of the perceptron.

3.3 State of the art of Artificial Neural Networks

ANNs are nowadays employed in a number of different scientific fields such as for instance computer science, mathematics, physics, electrical engineering, civil engineering, biology, medicine, psychology, and behavioral science. They are used to solve a great variety of problems such as, e. g., problems of classification, regression, clustering, pattern matching, pattern completion, noise removal, optimization, control, and simulation.

In order to solve such a spectrum of problems, three different learning procedures were developed. They can be summarized as:

Supervised learning is employed, if the given data base comprises couples of both input vectors and corresponding desired outputs. In such situations, ANNs are trained to deal with unknown data, i. e., they are trained to provide interpolations and – to less extent – extrapolations of known relations between vectors. Accordingly, supervised learning is performed for instance for classification problems and regression purposes.

Unsupervised learning is characterized by the fact that only inputs are given. Corresponding outputs are not known *a priori*. ANNs are trained to find a structure in the input data. Similar input vectors should be assigned to similar output vectors. Unsupervised learning is performed, e. g., for cluster analyses and dimensionality reduction problems.

Reinforcement learning is characterized by the fact that desired outputs are not known exactly. The data basis suffices only to decide whether the output of an ANN is *correct or wrong*, or *better or worse*, respectively.

In civil engineering nowadays different kinds of ANNs are established. The most often chosen type of ANN are the Multi Layer Perceptron (MLP) and Radial Basis Function (RBF) networks. So-called recurrent networks such as Elman and Hopfield networks are further types of ANNs capable to solve civil engineering problems. However, as compared with MLPs and RBF networks they are infrequently applied.

Within this thesis, only the first type, MLPs, will be considered. Such networks are characterized by supervised-learning procedures. In the following sections, the state of the art of such ANNs is presented. The principle functionality of MLPs is addressed in Section 3.3.1. Training algorithms for MLPs are discussed in Section 3.3.2. The problem of underfitting and overfitting, also well known as the bias-variance problem, is addressed in Section 3.3.3.

3.3.1 The Multi Layer Perceptron (MLP)

A MLP consists of several layers of neurons and nodes. Without loss of generality, the following considerations are restricted to a three-layer perceptron, see Figure 3.8. Such

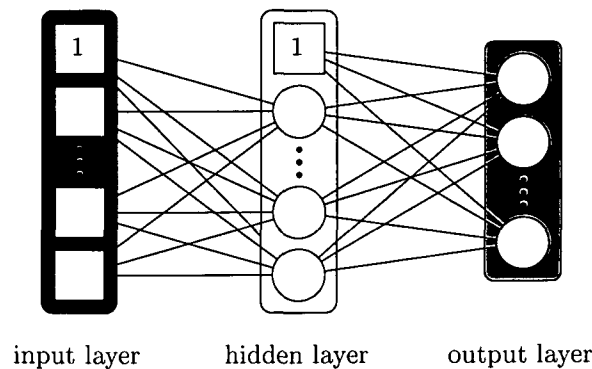


Figure 3.8: Multi-layer perceptron with one hidden layer

a MLP consists of an input layer, a so-called hidden layer, and an output layer. These layers contain neurons and nodes. A MLP provides a map from an n_i -dimensional input vector onto an n_o -dimensional output vector. Therefore, the input layer consists of $n_i + 1$ input nodes. One of these nodes contains the value 1. This node accounts for the stimulus threshold of the neurons of the hidden layer. All nodes of the input layer are connected to the n_h neurons of the hidden layer via weighted connections. For the hidden layer, an additional node containing the value 1 is considered which accounts for the stimulus

threshold of the neurons of the output layer. This node and all neurons of the hidden layer are connected to the n_o neurons of the output layer via weighted connections. The weighted connections are commonly referred to as *edges* of the ANN.

Traversing an input vector from the input layer of an MLP to its output layer is performed according to a codified calculation scheme. This algorithm is called the *feedforward procedure*: The input vector is presented to the MLP at the input layer. If a component of the input vector, x_j , moves from node j of the input layer (index i) along an edge to neuron k of the hidden layer (index h), it will be multiplied by the respective edge weight w_{jk}^{ih} . As weighted values from different edges enter a neuron k of the hidden layer, they are summed up. The sum σ_k^h represents the activation of the respective neuron of the hidden layer:

$$\sigma_k^h = \sum_{j=0}^{n_i} x_j w_{jk}^{ih}. \quad (3.4)$$

Since homogeneous coordinates are used, $x_0 \equiv 1$ accounts for the additional node of the input layer containing the value 1. The weights connecting this input node and the neurons of the hidden layer can be interpreted as the negative stimulus threshold of the neurons of the hidden layer, i. e., $w_{0k}^{ih} = -\theta_k$, $k = 1, 2, \dots, n_h$. A *transfer function*¹ t^h is applied to the activation, yielding $t^h(\sigma_k^h)$ which represents the output of neuron k of the hidden layer. The output of all neurons of the hidden layer are "shot" along the edges to the neurons of the output layer. Analogous to Eq. (3.4), the activation of neuron r of the output layer (index o) is obtained as

$$\sigma_r^o = \sum_{k=0}^{n_h} t^h(\sigma_k^h) w_{kr}^{ho}, \quad (3.5)$$

with $t^h(\sigma_0^h) := 1$ accounting for the additional node of the hidden layer containing the value 1. The weights connecting this node and the neurons of the output layer can be interpreted as the negative stimulus threshold of the neurons of the output layer, i. e., $w_{0r}^{ho} = -\theta_r$, $r = 1, 2, \dots, n_o$. Application of a transfer function t^o to σ_r^o yields the r -th output value of the ANN: $o_r = t^o(\sigma_r^o)$. Consequently, the outputs of a MLP with one hidden layer read

$$o_r = t^o \left(\sum_{k=0}^{n_h} t^h \left(\sum_{j=0}^{n_i} x_j w_{jk}^{ih} \right) w_{kr}^{ho} \right), \quad r = 1, 2, \dots, n_o. \quad (3.6)$$

They are the result of the feedforward procedure. According to Eq. (3.6), a MLP can be interpreted as a vector function. The outputs of a MLP are functions of the inputs and of the edge weights of the ANN. The type of function represented by the MLP strongly depends on the chosen type of transfer functions.

¹The commonly chosen types of transfer functions will be discussed subsequently.

MLPs are commonly applied to provide approximations of vector functions or to solve multi-dimensional regression problems. Therefore, transfer functions characterized by discontinuities, such as the Heaviside step-function or the signum function, are useless. Transfer functions yielding continuous, i. e., smooth outputs are required. The simplest of such transfer functions is the linear transfer function

$$f(a) = a, \quad (3.7)$$

where a denotes the activation of the neuron, see Figure 3.9(a) The output of a neuron characterized by a such a transfer function will be equal to its activation.

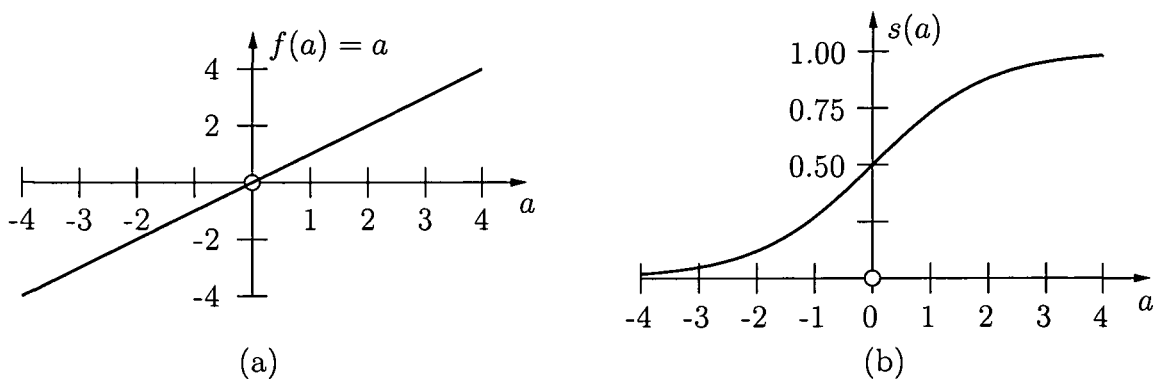


Figure 3.9: Continuous transfer functions (a) linear transfer function $f(a) = a$ and (b) sigmoidal transfer function $s(a) = [1 + \exp(a)]^{-1}$ (a represents the activation of a respective neuron)

A MLP with linear transfer functions only is characterized by $t^h = f$ and $t^o = f$. Therefore, the output vector of such a MLP reads

$$o_r = f \left(\sum_{k=0}^{n_h} f \left(\sum_{j=0}^{n_i} x_j w_{jk}^{ih} \right) w_{kr}^{ho} \right), \quad r = 1, 2, \dots, n_o. \quad (3.8)$$

According to Eq. (3.8), a MLP with linear transfer functions provides a *linear* map of an input vector onto an output vector.

In order to provide a *non-linear* mapping based on a MLP, the neurons of at least one layer have to work with a non-linear transfer function. The non-linear transfer functions most frequently used are sigmoidal functions, see, e. g. Figure 3.9 (b). The mathematical definition of the unipolar sigmoid, s , and of the bipolar sigmoid, \tanh , read

$$s(a) = \frac{1}{1 + e^{-a}}, \quad \tanh(a) = \frac{e^a - e^{-a}}{e^a + e^{-a}}. \quad (3.9)$$

In most applications, a non-linear transfer function is chosen for the neurons of the hidden layer ($t^h = s$), whereas the neurons of the output layer operate with the linear transfer

function ($t^o = f$). The outputs of such a three-layer MLP read

$$o_r = f \left(\sum_{k=0}^{n_h} s \left(\sum_{j=0}^{n_i} x_j w_{jk}^{ih} \right) w_{kr}^{ho} \right) = \sum_{k=0}^{n_h} s \left(\sum_{j=0}^{n_i} x_j w_{jk}^{ih} \right) w_{kr}^{ho}, \quad r = 1, 2, \dots, n_o. \quad (3.10)$$

3.3.2 Training of MLPs

MLPs are ANNs that are trained by supervised learning procedures. Accordingly, learning of MLPs requires a given data base consisting of n_d couples of both input vectors and corresponding desired outputs. The ANN can be trained to approximate the relationships between these multi-dimensional vectors, referred to as training data sets. During training of the ANN, each input vector of the n_d training data sets, \mathbf{x}_d , $d = 1, 2, \dots, n_d$, is fed into the network and a feedforward procedure is performed. The so-obtained output vectors of the ANN, $\mathbf{o}(\mathbf{x}_d)$, are compared with the respective given output vectors $\mathbf{o}^h(\mathbf{x}_d)$ of the training data sets. The ANN approximation-error for the training data sets, \mathcal{R}^{*h} , is evaluated as

$$\mathcal{R}^{*h} = \sqrt{\frac{1}{n_d} \sum_{d=1}^{n_d} \mathcal{R}_d^{*h}}, \quad (3.11)$$

with

$$\mathcal{R}_d^{*h} = \frac{1}{n_o} \sum_{r=1}^{n_o} \left(\frac{o_r(\mathbf{x}_d) - o_r^h(\mathbf{x}_d)}{o_r^h(\mathbf{x}_d)} \right)^2. \quad (3.12)$$

Training of the ANN is equal to minimizing \mathcal{R}^{*h} by adjusting the network weights. There are different methods to solve the nonlinear minimization problem $\mathcal{R}^{*h}(w_{jk}^{ih}, w_{kr}^{ho}) \rightarrow$ minimum. The most popular methods commonly employed are (i) the gradient-descent method, (ii) the so called resilient backpropagation algorithm (RPROP-algorithm), and (iii) the Levenberg-Marquardt method. Throughout this thesis, the gradient-descent method (GDM) is considered, which is well known as the *backpropagation algorithm* (Rojas, 1996). In an iterative manner, the network weights are continuously updated. The increments of network weights related to one GDM iteration step, Δw_{jk}^{ih} and Δw_{kr}^{ho} , are functions of $\partial \mathcal{R}^{*h} / \partial w_{jk}^{ih}$ and $\partial \mathcal{R}^{*h} / \partial w_{kr}^{ho}$, respectively, reading

$$\Delta w_{jk}^{ih} = \Delta w_{jk}^{ih} \left(\frac{\partial \mathcal{R}^{*h}}{\partial w_{jk}^{ih}} \right) \quad \text{and} \quad \Delta w_{kr}^{ho} = \Delta w_{kr}^{ho} \left(\frac{\partial \mathcal{R}^{*h}}{\partial w_{kr}^{ho}} \right) \quad (3.13)$$

(for details, see, e.g., (Rojas, 1996)). The derivatives of \mathcal{R}^{*h} required for determination of the increments of the unknown network weights (see Equations (3.13)) are computed as:

$$\frac{\partial \mathcal{R}^{*h}}{\partial w_{kr}^{ho}} = \sum_{d=1}^{n_d} \frac{\partial \mathcal{R}^{*h}}{\partial \mathcal{R}_d^{*h}} \frac{\partial \mathcal{R}_d^{*h}}{\partial w_{kr}^{ho}} \quad \text{and} \quad \frac{\partial \mathcal{R}^{*h}}{\partial w_{jk}^{ih}} = \sum_{d=1}^{n_d} \frac{\partial \mathcal{R}^{*h}}{\partial \mathcal{R}_d^{*h}} \frac{\partial \mathcal{R}_d^{*h}}{\partial w_{jk}^{ih}}, \quad (3.14)$$

with

$$\frac{\partial \mathcal{R}_d^{*h}}{\partial w_{kr}^{ho}} = \frac{\partial \mathcal{R}_d^{*h}}{\partial o_r} \frac{\partial o_r}{\partial \sigma_r^o} \frac{\partial \sigma_r^o}{\partial w_{kr}^{ho}} = \frac{2}{n_o} \frac{o_r(\mathbf{x}_d) - o_r^h(\mathbf{x}_d)}{[o_r^h(\mathbf{x}_d)]^2} \frac{\partial f(\sigma_r^o)}{\partial \sigma_r^o} s(\sigma_k^h) \quad (3.15)$$

and

$$\begin{aligned} \frac{\partial \mathcal{R}_d^{*h}}{\partial w_{jk}^{ih}} &= \sum_{r=1}^{n_o} \left[\frac{\partial \mathcal{R}_d^{*h}}{\partial o_r} \frac{\partial o_r}{\partial \sigma_r^o} \frac{\partial \sigma_r^o}{\partial s(\sigma_k^h)} \right] \frac{\partial s(\sigma_k^h)}{\partial \sigma_k^h} \frac{\partial \sigma_k^h}{\partial w_{jk}^{ih}} = \\ &= \frac{2}{n_o} \sum_{r=1}^{n_o} \left[\frac{o_r(\mathbf{x}_d) - o_r^h(\mathbf{x}_d)}{[o_r^h(\mathbf{x}_d)]^2} \frac{\partial f(\sigma_r^o)}{\partial \sigma_r^o} w_{kr}^{ho} \right] \frac{\partial s(\sigma_k^h)}{\partial \sigma_k^h} x_{j,d}, \end{aligned} \quad (3.16)$$

where $x_{j,d}$ represents the j -th component of \mathbf{x}_d . The subscript $d = 1, 2, \dots, n_d$ denotes the different data sets and $j = 1, 2, \dots, n_i$, $k = 1, 2, \dots, n_h$, and $r = 1, 2, \dots, n_o$. Eqs. (3.15) and (3.16) contain the partial derivatives of the activation functions with respect to their arguments. Considering Eqs. (3.7) and (3.9), they can be calculated as

$$\frac{\partial f(\sigma_r^o)}{\partial \sigma_r^o} = 1 \quad \text{and} \quad \frac{\partial s(\sigma_k^h)}{\partial \sigma_k^h} = s(\sigma_k^h) \cdot [1 - s(\sigma_k^h)]. \quad (3.17)$$

In the next iteration step, a feedforward procedure of all n_d input vectors is performed on the basis of the updated network weights w_{jk}^{ih} and w_{kr}^{ho} . The so-obtained updated output vectors $\mathbf{o}(\mathbf{x}_d)$ allow to determine the new value of the error function \mathcal{R}^{*h} , which is the basis for a subsequent iteration step in the training process. During the training of the ANN, \mathcal{R}^{*h} will be decreasing continuously, i.e., step by step the performance of the ANN to reproduce the relationships between the multi-dimensional vectors of the training data sets will increase.

Design of MLPs and training of such ANNs has to be treated carefully, since there exists the danger of *overfitting* and *underfitting*. This problem will be addressed in the following section.

3.3.3 The problem of overfitting and underfitting

MLPs are trained on the basis of a given data base comprising couples of both input vectors and corresponding output vectors, referred to as desired output vectors. The trained ANNs are used to deal with unknown data, i.e., they are trained to provide interpolations and – to a smaller extent – extrapolations of known relations between vectors. Therefore, MLP training is characterized by two contending goals:

- The trained MLP should reliably map unknown input vectors onto the respective output vectors, i.e., the trained ANN should provide a good generalization of the information contained in the training data sets.

Very flexible models such as MLPs with a large number of neurons in the hidden layer(s) can minimize \mathcal{R}^{*h} to a very small value. Such networks will almost perfectly reproduce the relations between input vectors and output vectors of the training data sets. The provided mode of interpolation will be highly nonlinear. This situation is known as *overfitting*. The trained MLPs will fail to capture the function governing the relationship between input vectors and output vectors reliably. The performance of such MLPs in dealing with unknown data sets will be rather poor.

- The MLP should be flexible enough to represent the underlying target function, i. e., the function governing the relationship between input vectors and output vectors.

A linear network, e. g., cannot represent quadratic functions. Hence, if a linear model is used to describe a nonlinear problem, it will yield a large training error. Since the model is too simple, the attainable value of the error function \mathcal{R}^{*h} will not be satisfactorily small. This situation is known as *underfitting*.

An illustrative example pointing out this problem will be presented in the following. The task of polynomial regression in the presence of normally distributed noise will be considered. The second-order polynomial

$$o = 2x^2 + 10x - 28 + \epsilon \quad (3.18)$$

serves as the target function. ϵ represents normally distributed noise with mean $\mu = 0$ and standard deviation $\sigma = 20$. A training data set is computed by evaluating Eq. (3.18) for six values of x equally spaced in the interval $[-10, 10]$. Accordingly, $x_1 = -10$, $x_2 = -6$, $x_3 = -2$, $x_4 = 2$, $x_5 = 6$, and $x_6 = 10$. The obtained training data sets (x_i, o_i) , $i = 1, 2, \dots, 6$, are used to adjust the parameters of two models (i) a fifth-order polynomial and (ii) a first-order polynomial.

The fifth-order polynomial fits the training data exactly, see Figure 3.10. However, its overall shape differs significantly from the target function. The fifth-order polynomial is too flexible which causes overfitting.

The first-order polynomial obtained by a least squares optimization is a rather poor approximation of the target function, see Figure 3.10. The linear function is not flexible enough to provide a useful approximation of the training data sets which causes underfitting.

3.3.4 Protection of MLPs against underfitting and overfitting

Theoretically, both underfitting and overfitting could be avoided by choosing an extremely flexible MLP and providing an infinite amount of training data. Practically, for a limited

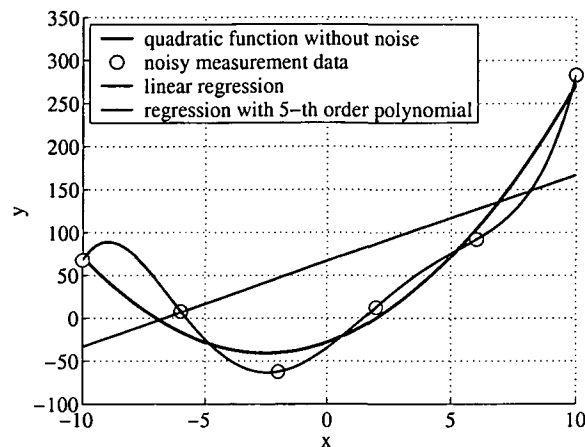


Figure 3.10: Polynomial regression: Approximation of a second-order polynomial (black curve) using a fifth-order polynomial (blue curve) and a first-order polynomial (green curve) for a training data set consisting of six equally spaced data points afflicted with normally distributed noise

number of training data sets, the flexibility of the MLP should be adjusted accordingly. This problem is referred to as model selection. It requires *a priori* knowledge about the problem under consideration. Since MLPs are employed in situations where the governing functional dependencies of inputs and outputs are unknown, this *a priori* knowledge is not available. This fact renders model selection a challenging task.

There exists a large number of strategies to avoid underfitting and overfitting in practical applications. Independent of the problem under consideration, two recommendations can be made. They refer to the choice of the network architecture and to a criterion for termination of MLP training.

Definition of the architecture of MLPs

The number of layers of a MLP and the number of neurons contained in these layers is referred to as the *architecture* of the MLP. The number of network weights, i. e., the number of parameters of a MLP, is closely related to the architecture of the ANN. It must be chosen such that the number of network weights is kept as small as possible in order to avoid overfitting. However, at the same time this number must be as large as necessary in order to avoid underfitting. Accordingly, MLPs with different network architectures must be included in a study focusing on the training success of the ANNs. Results from the respective training procedures provide evidence about the best choice for the architecture of the MLP.

Criterion for termination of training of MLPs

For the purpose of protecting MLPs against underfitting and overfitting, not all of the n_{tot} given data sets are used for training of the ANN. These sets are divided randomly into three groups: (i) n_d training data sets, (ii) n_t test data sets, and (iii) n_v validation data sets, with $n_{tot} = n_d + n_t + n_v$. As outlined in Section 3.3.2 only the n_d training data sets are involved in the learning procedure of the ANN. Accordingly, network weight corrections are computed resting on the training data sets only. Accompanying the training procedure, the quality of interpolations between the training data sets provided by the MLP is assessed by the n_t test data sets: Between two subsequent training iteration steps, a feedforward procedure is performed for each input vector of the test data sets, \mathbf{x}_d , $d = 1, 2, \dots, n_t$. The obtained output vectors of the MLP, $\mathbf{o}(\mathbf{x}_d)$, are compared with the respective given output vectors $\mathbf{o}^h(\mathbf{x}_d)$ of the test data sets. Consequently, the value of the MLP approximation-error corresponding to the test data sets, \mathcal{R}_{test}^{*h} , can be evaluated on the basis of Eq. (3.12) as

$$\mathcal{R}_{test}^{*h} = \sqrt{\frac{1}{n_t} \sum_{d=1}^{n_t} \mathcal{R}_d^{*h}}. \quad (3.19)$$

In general, both \mathcal{R}^{*h} and \mathcal{R}_{test}^{*h} are decreasing at the beginning of the ANN training. Hence, both the approximation of the training data sets provided by the MLP and the ability of the ANN to interpolate between these sets are improved. At a certain stage of the training procedure, \mathcal{R}_{test}^{*h} attains a minimum. Continuation of training results in further improvement of the approximation of the training data sets, i.e., \mathcal{R}^{*h} is decreasing. The value of the testing error \mathcal{R}_{test}^{*h} , however, will be increasing. Hence, the ability of the network to interpolate between the training data sets is reduced. Consequently, ANN training will be terminated when \mathcal{R}_{test}^{*h} attains a minimum. Subsequently, the validation data sets, representing *unknown* data sets, are presented to the trained ANN. The MLP approximation-error corresponding to the validation data sets, \mathcal{R}_{val}^{*h} , is computed as

$$\mathcal{R}_{val}^{*h} = \sqrt{\frac{1}{n_v} \sum_{d=1}^{n_v} \mathcal{R}_d^{*h}}, \quad (3.20)$$

where Eq. (3.12) is considered. The attained three values of the error functions \mathcal{R}^{*h} , \mathcal{R}_{test}^{*h} , and \mathcal{R}_{val}^{*h} represent measures of the success of the training procedure and provide insight whether or not underfitting or overfitting has occurred.

3.3.5 Operational phase of MLPs

At the end of the training procedure outlined in Section 3.3.2 and 3.3.4, the MLP is ready for the operational phase. The trained ANN can be used to deal with unknown

data. Thereby, the network weights will remain unchanged and feedforward procedures are performed only. Any input vector presented to the MLP is mapped onto an output vector representing an interpolation between the training data sets.

Chapter 4

Parameter identification resting on soft computing

In this chapter, a parameter identification (PI) method for determination of unknown model parameters in geotechnical engineering is proposed which satisfies the requirements addressed in Subchapter 2.2. It is based on measurement data provided by experiments or the construction site. Model parameters for finite element (FE) analyses are identified such that the results of these calculations agree with available measurement data as well as possible.

In order to solve a PI problem, an error function must be defined. It represents the difference between available measurements and corresponding quantities obtained from a numerical analysis. The error function depends on the unknown parameters. Herein, it is defined as

$$\mathcal{R}^h(\mathbf{p}) = \sqrt{\frac{1}{n_o} \sum_{r=1}^{n_o} \left(\frac{u_r^h(\mathbf{p}) - u_r}{u_r} \right)^2}, \quad (2.1)$$

where u_r and u_r^h , $r = 1, 2, \dots, n_o$, are the measurements and the corresponding numerical results, respectively. The values u_r^h depend on the unknown model parameters collected in the vector \mathbf{p} . Based on the error function (2.1), back analysis aims at determination of the absolute minimum of \mathcal{R}^h . This minimum provides the best agreement between the available measurements and numerical results.

In general, the solution of a PI problem requires a large number of numerical simulations. This represents the major problem of PI in geotechnical engineering, since the

trained to provide an approximation of results from FE analyses (Figure 4.1). After the

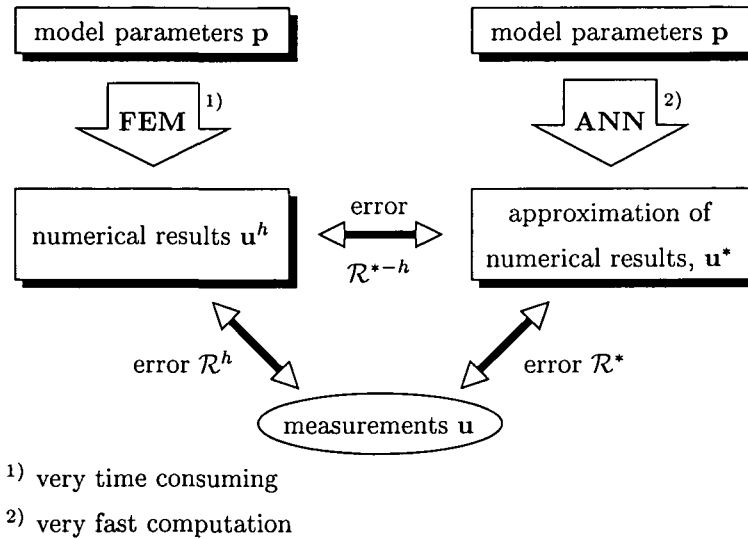


Figure 4.1: Approximation of the time consuming FE analysis by a Multi Layer Perceptron which can be evaluated very quickly (for the mathematical definitions of the error functions \mathcal{R}^h , \mathcal{R}^* , and \mathcal{R}^{*-h} see Eqs. (2.1), (4.1), and (4.5), respectively)

training of such an ANN, it is easy to evaluate, allowing for thousands of evaluations within a few seconds. This renders PI feasible even for problems associated with very time consuming numerical simulations.

The MLP is trained in order to incorporate the knowledge obtained from already performed FE analyses. Hence, MLP training is based on both (i) model parameters which were chosen for already performed FE simulations and (ii) the obtained numerical results. Vectors of model parameters \mathbf{p} serve as input vectors for the MLP. Respective numerical results of FE simulations collected in the vector \mathbf{u}^h represent the desired output vectors during training of the ANN. At the end of the training procedure, the MLP reproduces the correlation between model parameters and results from FE analyses. Moreover, it provides a generalization of this correlation. The ANN maps parameter sets that were not used as input for FE analyses onto interpolated values of numerical results. Accordingly, \mathcal{R}^h can be approximated by the trained MLP as

$$\mathcal{R}^*(\mathbf{p}) = \sqrt{\frac{1}{n_o} \sum_{r=1}^{n_o} \left(\frac{u_r^*(\mathbf{p}) - u_r}{u_r} \right)^2}, \quad (4.1)$$

where u_r^* , $r = 1, 2, \dots, n_o$, are the output quantities of the ANN. The global minimum of the error function \mathcal{R}^* corresponds to an estimate of an optimal parameter set. This estimate is computed by means of a genetic algorithm and a gradient-descent method

(GDM), which requires a large number of evaluations of the MLP. However, since a MLP can be evaluated very quickly, this procedure is not very time consuming. The quality of the estimated optimal parameters is assessed by the value of the error function \mathcal{R}^h , requiring an additional FE analysis.

Subchapter 4.1 deals with the structure of the MLP, training of the ANN, and determination of an optimal parameter set. The advantages of theoretical developments concerning both the structure and the training of the MLP will be illustrated by the identification of material properties from experimental data in Subchapter 4.2. Finally, the performance of the proposed PI method will be demonstrated by two problems taken from geotechnical engineering. First, the PI method will be applied to a PI problem related to ground improvement by means of jet grouting, see Subchapter 4.3. Secondly, the PI method will be applied to back analysis of soil parameters considering tunneling according to the New Austrian Tunneling Method (NATM), see Subchapter 4.4. The impact of back analysis on the actual construction process will be outlined. In Subchapter 4.5 the proposed PI method will be extended to first-order approximation neural networks.

4.1 Outline of the new PI method

In the context of the proposed PI method, a modified MLP with one hidden layer is employed, see Figure 4.2. The input layer consists of n_i input nodes, the hidden layer

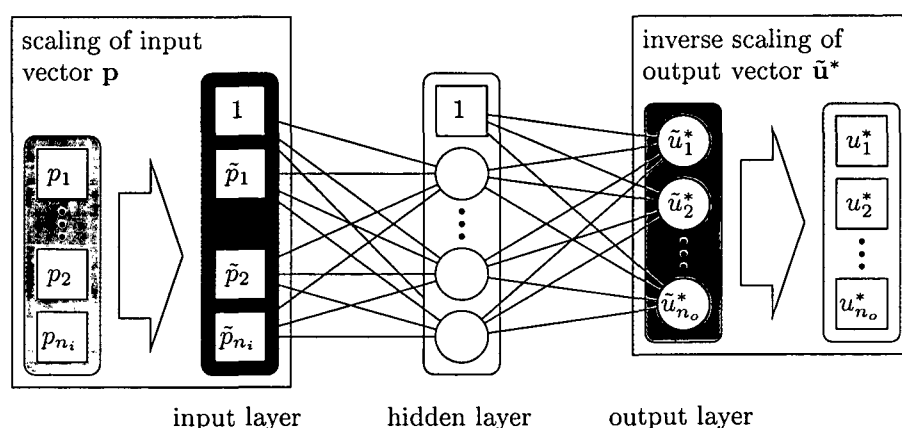


Figure 4.2: Structure of the employed MLP with one hidden layer (circles: neurons; squares: nodes)

of n_h neurons, and the output layer of n_o output neurons. Homogeneous coordinates as defined in Section 3.2.2 are introduced. Accordingly, for the input layer and the hidden layer an additional node containing the value 1 is considered, see Figure 4.2. The ANN maps n_i -dimensional input vectors \mathbf{p} onto n_o -dimensional output vectors \mathbf{u}^* .

Both vectors of a data set may contain values with different physical units and of different orders of magnitude. In order to improve the situation, all components of the input vectors of the different data sets, \mathbf{p} , are scaled to dimensionless values within a certain interval. Frequently, the interval $[0.1, 0.9]$ is chosen (Rojas, 1996), which is also used herein. The vectors containing the scaled and dimensionless input values are denoted as $\tilde{\mathbf{p}}$, see Figure 4.2.

Traversing such a vector $\tilde{\mathbf{p}}$ from the input layer of the ANN to its output layer is performed according to the feedforward procedure, described in Section 3.3.1. Accordingly, the *activation* of the respective neuron of the hidden layer reads

$$\sigma_k^h = \sum_{j=0}^{n_i} \tilde{p}_j w_{jk}^{ih}, \quad (4.2)$$

with $\tilde{p}_0 \equiv 1$ accounting for the additional node of the input layer containing the value 1, see Figure 4.2. A unipolar sigmoid, see Eq. (3.9), is applied to this sum, yielding

$$s(\sigma_k^h) = \left[1 + \exp(-\sigma_k^h) \right]^{-1}, \quad (4.3)$$

where $s(\sigma_k^h)$ represents the output of neuron k of the hidden layer. Analogous to Eq. (4.2), the activation of neuron r of the output layer (index o) is obtained as

$$\sigma_r^o = \sum_{k=0}^{n_h} s(\sigma_k^h) w_{kr}^{ho}, \quad (4.4)$$

with $s(\sigma_0^h) := 1$ accounting for the additional node of the hidden layer containing the value 1, see Figure 4.2. In order to increase the degree of nonlinearity provided by the MLP, again the unipolar sigmoid is used as the activation function for the neurons of the output layer. Accordingly, the r -th dimensionless output value of the ANN is obtained as $\tilde{u}_r^* = s(\sigma_r^o)$. Considering Eq. (3.9), $\tilde{u}_r^* \in (0.0, 1.0)$.

In order to obtain correct physical units and correct orders of magnitude, output vectors $\tilde{\mathbf{u}}^*$ computed by means of the feedforward procedure are scaled. For this purpose, the scaling operation used to scale the desired output vectors \mathbf{u}^h to dimensionless values within the interval $[0.1, 0.9]$ is reversed. Output vectors of the ANN, characterized by the correct physical units and the correct orders of magnitude, are denoted as \mathbf{u}^* , see Figure 4.2. They are functions of the respective input parameters p_j , $j = 1, 2, \dots, n_i$, and of the network weights.

4.1.1 Training of the modified MLP

Training of the modified MLP is performed basically according to the procedure described in Section 3.3.2. Because of the modified structure of the employed MLP, the presented

formulae for quantification of the ANN approximation error and for computation of network weight corrections must be extended. The ANN approximation-error for the training data sets, \mathcal{R}^{*h} , is evaluated in the form

$$\mathcal{R}^{*h} = \sqrt{\frac{1}{n_d} \sum_{d=1}^{n_d} \mathcal{R}_d^{*h}}, \quad (4.5)$$

with

$$\mathcal{R}_d^{*h} = \frac{1}{n_o} \sum_{r=1}^{n_o} \left(\frac{u_r^*(\mathbf{p}_d) - u_r^h(\mathbf{p}_d)}{u_r^h(\mathbf{p}_d)} \right)^2. \quad (4.6)$$

Training of the ANN is equal to minimizing \mathcal{R}^{*h} by adjusting the unknown network weights. The nonlinear minimization problem $\mathcal{R}^{*h}(w_{jk}^{ih}, w_{kr}^{ho}) \rightarrow \text{minimum}$ is solved by means of a gradient-descent method (GDM): the backpropagation algorithm (Rojas, 1996). Iteratively, the network weights are continuously updated. The incremental network weights related to one GDM iteration step, Δw_{jk}^{ih} and Δw_{kr}^{ho} , are functions of $\partial \mathcal{R}^{*h} / \partial w_{jk}^{ih}$ and $\partial \mathcal{R}^{*h} / \partial w_{kr}^{ho}$, reading

$$\Delta w_{jk}^{ih} = \Delta w_{jk}^{ih} \left(\frac{\partial \mathcal{R}^{*h}}{\partial w_{jk}^{ih}} \right) \quad \text{and} \quad \Delta w_{kr}^{ho} = \Delta w_{kr}^{ho} \left(\frac{\partial \mathcal{R}^{*h}}{\partial w_{kr}^{ho}} \right). \quad (4.7)$$

The derivatives of \mathcal{R}^{*h} required for the determination of the increments of the unknown network weights are computed as:

$$\frac{\partial \mathcal{R}^{*h}}{\partial w_{kr}^{ho}} = \sum_{d=1}^{n_d} \frac{\partial \mathcal{R}_d^{*h}}{\partial \mathcal{R}_d^{*h}} \frac{\partial \mathcal{R}_d^{*h}}{\partial w_{kr}^{ho}} \quad \text{and} \quad \frac{\partial \mathcal{R}^{*h}}{\partial w_{jk}^{ih}} = \sum_{d=1}^{n_d} \frac{\partial \mathcal{R}_d^{*h}}{\partial \mathcal{R}_d^{*h}} \frac{\partial \mathcal{R}_d^{*h}}{\partial w_{jk}^{ih}}, \quad (4.8)$$

with

$$\frac{\partial \mathcal{R}_d^{*h}}{\partial w_{kr}^{ho}} = \frac{\partial \mathcal{R}_d^{*h}}{\partial u_r^*} \frac{\partial u_r^*}{\partial \tilde{u}_r^*} \frac{\partial \tilde{u}_r^*}{\partial \sigma_r^o} \frac{\partial \sigma_r^o}{\partial w_{kr}^{ho}} = \frac{2}{n_o} \frac{u_r^*(\mathbf{p}_d) - u_r^h(\mathbf{p}_d)}{[u_r^h(\mathbf{p}_d)]^2} \frac{\partial u_r^*}{\partial \tilde{u}_r^*} \frac{\partial s(\sigma_r^o)}{\partial \sigma_r^o} s(\sigma_k^h) \quad (4.9)$$

and

$$\begin{aligned} \frac{\partial \mathcal{R}_d^{*h}}{\partial w_{jk}^{ih}} &= \sum_{r=1}^{n_o} \left[\frac{\partial \mathcal{R}_d^{*h}}{\partial u_r^*} \frac{\partial u_r^*}{\partial \tilde{u}_r^*} \frac{\partial \tilde{u}_r^*}{\partial \sigma_r^o} \frac{\partial \sigma_r^o}{\partial s(\sigma_k^h)} \right] \frac{\partial s(\sigma_k^h)}{\partial \sigma_k^h} \frac{\partial \sigma_k^h}{\partial w_{jk}^{ih}} = \\ &= \frac{2}{n_o} \sum_{r=1}^{n_o} \left[\frac{u_r^*(\mathbf{p}_d) - u_r^h(\mathbf{p}_d)}{[u_r^h(\mathbf{p}_d)]^2} \frac{\partial u_r^*}{\partial \tilde{u}_r^*} \frac{\partial s(\sigma_r^o)}{\partial \sigma_r^o} w_{kr}^{ho} \right] \frac{\partial s(\sigma_k^h)}{\partial \sigma_k^h} \tilde{p}_{j,d}, \end{aligned} \quad (4.10)$$

where $\tilde{p}_{j,d}$ represents the j -th component of $\tilde{\mathbf{p}}_d$. The index $d = 1, 2, \dots, n_d$ denotes the different data sets and $j = 1, 2, \dots, n_i$, $k = 1, 2, \dots, n_h$, and $r = 1, 2, \dots, n_o$. Eqs. (4.9) and (4.10) contain the partial derivatives of the activation function with respect to its argument. Considering Eq. (3.9), they can be calculated as

$$\frac{\partial s(\sigma_r^o)}{\partial \sigma_r^o} = s(\sigma_r^o) \cdot [1 - s(\sigma_r^o)] \quad \text{and} \quad \frac{\partial s(\sigma_k^h)}{\partial \sigma_k^h} = s(\sigma_k^h) \cdot [1 - s(\sigma_k^h)]. \quad (4.11)$$

In the next iteration step, a feedforward procedure of all n_d input vectors is performed on the basis of the updated network weights w_{jk}^{ih} and w_{kr}^{ho} . The so-obtained updated output vectors $\mathbf{u}^*(\mathbf{p}_d)$ allow to determine the new value of the error function \mathcal{R}^{*h} (see Equation (4.5)).

4.1.2 Treatment of the underfitting and overfitting problem

The commonly used strategy to avoid underfitting and overfitting of a MLP addressed in Section 3.3.4 is not feasible in the case of PI involving MLPs. In the following, the reason for this fact will be given. Moreover, an alternative way to treat the underfitting and overfitting problem will be discussed.

In the context of the proposed PI method, the ANN is trained to approximate results from FE analyses. Considering PI in geotechnical engineering, the required FE analyses are, in general, characterized by comparatively high computational efforts. In order to keep the effort for PI reasonably small, only few analyses are performed for determination of data sets prior to PI. Training and testing of the ANN on the basis of a few data sets only is controversial: \mathcal{R}_{test}^{*h} will attain a minimum at an early stage of the training algorithm and, hence, training of the ANN will be stopped. At this stage, however, the obtained value of the error function \mathcal{R}^{*h} , which is based on the training data sets, is still rather large. Consequently, the approximation of the training data sets by the ANN is poor, rendering interpolations between these data sets by the ANN useless. Classical training of a MLP used for PI in geotechnical engineering yields underfitting ANNs.

In order to avoid such a situation, the precomputed data sets are not divided into training data sets, test data sets, and validation data sets. All given data sets are instead used for training of the ANN. Hence, $n_d = n_{tot}$, whereas $n_t = 0$ and $n_v = 0$. Since no data sets are available for testing of the ANN, the criterion $\mathcal{R}_{test}^{*h} \rightarrow \text{minimum}$ used for termination of network training is replaced by:

$$\mathcal{E}_{r,d}^{*h} \leq \bar{\mathcal{E}}^{*h} \quad \forall \quad \begin{cases} r = 1, 2, \dots, n_o \\ d = 1, 2, \dots, n_d \end{cases} \quad (4.12)$$

with

$$\mathcal{E}_{r,d}^{*h} = \left| \frac{u_r^*(\mathbf{p}_d) - u_r^h(\mathbf{p}_d)}{u_r^h(\mathbf{p}_d)} \right|, \quad (4.13)$$

where $\bar{\mathcal{E}}^{*h}$ denotes a prespecified threshold value. If (4.12) is satisfied, the MLP will be able to reproduce every output value of each available data set with a prespecified accuracy. Hence, there is no risk to obtain an underfitting MLP.

In some cases, however, the training procedure fails to converge because of a small number of values $u_r^*(\mathbf{p}_d)$ violating condition (4.12). The reasons for this situation are as

follows:

1. The GDM used for training of the ANN approaches a local minimum of \mathcal{R}^{*h} in the n_w -dimensional network-weight space.
2. Values $u_r^*(\mathbf{p}_d)$ that already satisfy condition (4.12) result in contributions to the gradient of \mathcal{R}^{*h} (see Equations (4.9) and (4.10)) contradictory to the contributions of values $u_r^*(\mathbf{p}_d)$ violating condition (4.12). Hence, the computed network-weight corrections do not yield a reduction of $\mathcal{E}_{r,d}^{*h}$ for values $u_r^*(\mathbf{p}_d)$ violating condition (4.12).

In order to improve the training procedure, two modifications are proposed:

1. The probability that training of the ANN by means of the GDM approaches a local minimum of \mathcal{R}^{*h} is reduced by employing a genetic algorithm for determination of the initial choice of the network weights.
2. A so-called “reduced-training” algorithm is performed. It is characterized by reducing the contributions to the gradient of \mathcal{R}^{*h} corresponding to values $u_r^*(\mathbf{p}_d)$ satisfying condition (4.12).

Determination of initial network weights employing a genetic algorithm (GA)

At the beginning of the GA, a generation (see Appendix A) of 50 individuals¹, i. e., of 50 different choices of initial weights, is generated randomly. Hence, 50 different networks are obtained. For each ANN, a prespecified number of iteration steps is performed within the framework of the GDM. Based on the so-obtained networks, a feedforward procedure of all available input vectors is carried out. This allows to determine the value of the error function \mathcal{R}^{*h} corresponding to each of the 50 ANNs. The error function \mathcal{R}^{*h} is related to the fitness function \mathcal{F} (see Appendix A) of the GA, with $\mathcal{F} = 1/\mathcal{R}^{*h}$. The “fittest” ANN is characterized by the largest fitness function \mathcal{F} and, hence, the smallest value of \mathcal{R}^{*h} . Based on the obtained values of the fitness function, a new generation of network weights is computed by means of genetic operations as outlined in Appendix A. The fittest ANN after a prespecified number of generations is the output of the GA. The network weights corresponding to this ANN are the starting values for the “reduced-training” algorithm.

The “reduced-training” algorithm

Based on the network weights provided by the GA, the GDM is employed for determination of network weights finally satisfying condition (4.12). In contrast to classical training algorithms, the “reduced-training” algorithm is characterized by the reduction of contributions

¹This is a very small number for a genetic algorithm.

to the gradient of \mathcal{R}^{*h} corresponding to output values that already satisfy condition (4.12). For this purpose, an exponential scaling function $\rho(\mathcal{E}_{r,d}^{*h})$ is introduced:

$$\rho(\mathcal{E}_{r,d}^{*h}) = \begin{cases} 1 & \text{for } \mathcal{E}_{r,d}^{*h} > \bar{\mathcal{E}}^{*h}, \\ \exp \left[\ln(\alpha) \left(\frac{10}{9} \right)^2 \left(\frac{\mathcal{E}_{r,d}^{*h} - \bar{\mathcal{E}}^{*h}}{\bar{\mathcal{E}}^{*h}} \right)^2 \right] & \text{for } \mathcal{E}_{r,d}^{*h} \leq \bar{\mathcal{E}}^{*h}, \end{cases} \quad (4.14)$$

where $\alpha < 1$ is a constant scalar parameter. Figure 4.3 shows the scaling function $\rho(\mathcal{E}_{r,d}^{*h})$ for two different values of α . For the “reduced training” of the ANN, the derivatives given

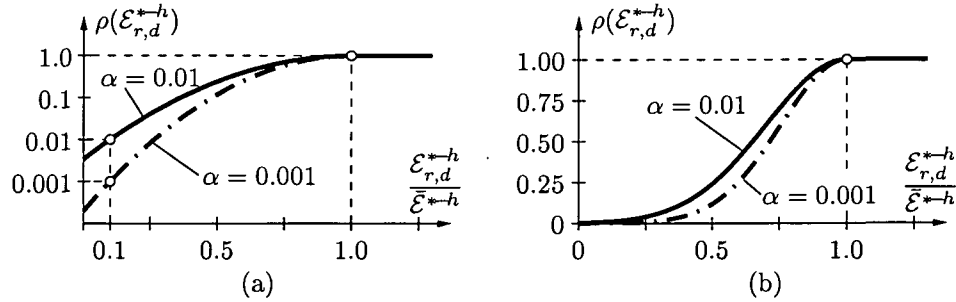


Figure 4.3: Scaling function $\rho(\mathcal{E}_{r,d}^{*h})$ used during “reduced training” of the ANN for two different values of α : (a) logarithmic scale and (b) natural scale

in Equations (4.9) and (4.10), which are used in the context of the GDM, become

$$\frac{\partial \mathcal{R}_d^{*h}}{\partial w_{kr}^{ho}} \rightarrow \rho(\mathcal{E}_{r,d}^{*h}) \frac{\partial \mathcal{R}_d^{*h}}{\partial u_r^*} \frac{\partial u_r^*}{\partial \tilde{u}_r^*} \frac{\partial \tilde{u}_r^*}{\partial \sigma_r^o} \frac{\partial \sigma_r^o}{\partial w_{kr}^{ho}} \quad (4.15)$$

and

$$\frac{\partial \mathcal{R}_d^{*h}}{\partial w_{jk}^{ih}} \rightarrow \sum_{r=1}^{n_o} \left[\rho(\mathcal{E}_{r,d}^{*h}) \frac{\partial \mathcal{R}_d^{*h}}{\partial u_r^*} \frac{\partial u_r^*}{\partial \tilde{u}_r^*} \frac{\partial \tilde{u}_r^*}{\partial \sigma_r^o} \frac{\partial \sigma_r^o}{\partial s(\sigma_k^h)} \right] \frac{\partial s(\sigma_k^h)}{\partial \sigma_k^h} \frac{\partial \sigma_k^h}{\partial w_{jk}^{ih}}. \quad (4.16)$$

A contribution to the gradient of \mathcal{R}^{*h} corresponding to an output value $u_r^*(\mathbf{p}_d)$ which is characterized by a mapping accuracy of, e.g., $\mathcal{E}_{r,d}^{*h} = \bar{\mathcal{E}}^{*h}/10$ is reduced by the factor $\rho(\mathcal{E}_{r,d}^{*h}) = \alpha$. A contribution to the gradient of \mathcal{R}^{*h} corresponding to an output value $u_r^*(\mathbf{p}_d)$ violating condition (4.12) is not affected by $\rho(\mathcal{E}_{r,d}^{*h})$.

If, however, condition (4.12) is violated although a prespecified number of iteration steps within the framework of the GDM was performed, the training of the ANN will be terminated. In order to avoid underfitting, the number of network weights n_w must be increased in order to improve the approximation capability of the MLP. Considering a fixed number of inputs and outputs of the MLP, i.e., $n_i = \text{const}$ and $n_o = \text{const}$, n_w is related to the number of neurons in the hidden layer. Accordingly, the number of neurons in the hidden layer is increased by one. Training of the new MLP is started by the determination of the initial network weights by means of the GA followed by the “reduced-training” algorithm.

Initial choice of number of neurons in the hidden layer

At the beginning of the PI process, the initial number of neurons in the hidden layer, n_h , must be specified. In order to avoid the risk of overfitting, the number of network weights must be kept as small as possible.² Since all available data sets are used for training of the MLP, an upper bound for the initial number of network weights is recommended following from the inequality

$$n_w \leq \sum_{d=1}^{n_d} n_o = n_o \cdot n_d. \quad (4.17)$$

Accordingly, the number of network weights n_w must be smaller than or equal to the number of output values n_o summed up over all data sets n_d . The number of network weights for a MLP with one hidden layer is obtained from

$$n_w = (1 + n_i) \cdot n_h + (1 + n_h) \cdot n_o, \quad (4.18)$$

see Figure 4.2. Substitution of Equation (4.18) in (4.17) gives an upper bound for the initial number of neurons in the hidden layer n_h as

$$n_h \leq \frac{n_o \cdot (n_d - 1)}{1 + n_i + n_o}. \quad (4.19)$$

However, in order to avoid “compression” of ANN input data (Rojas, 1996), the number of neurons in the hidden layer must be greater than the number of input nodes

$$n_h \geq n_i. \quad (4.20)$$

The initial number of neurons in the hidden layer must be chosen such that both conditions (4.19) and (4.20) are satisfied.

4.1.3 Estimate and assessment of an optimal parameter set

The trained ANN provides an approximation of the results of the n_d performed FE analyses. Accordingly, a parameter set belonging to the precomputed n_d data sets is mapped by the ANN onto the corresponding FE results with an accuracy higher than or equal to $\bar{\mathcal{E}}^{*h}$. Parameter sets which do not belong to the n_d data sets are mapped onto interpolated values of FE results.

A parameter set yielding the smallest difference between the corresponding FE results and the respective *in situ* measurements is an optimal parameter set. The ANN, providing an approximation of the FE analysis, can be used to compute an estimate of an optimal

²Therefore, MLPs are considered that are characterized by one hidden layer only.

parameter set. This estimate is obtained by means of minimization of the error function \mathcal{R}^* :

$$\mathcal{R}^*(\mathbf{p}) = \sqrt{\frac{1}{n_o} \sum_{r=1}^{n_o} \left(\frac{u_r^*(\mathbf{p}) - u_r}{u_r} \right)^2} \rightarrow \text{minimum.} \quad (4.21)$$

The minimization problem (4.21) is solved in two steps:

1. A GA is employed to search for a near optimal solution in the entire parameter space. 100 000 different parameter combinations per generation are presented to the network. \mathcal{R}^* is evaluated for each one of them. The parameter combination yielding the highest value of the fitness function \mathcal{F} , with $\mathcal{F} = 1/\mathcal{R}^*$ and, hence, the lowest value of the error \mathcal{R}^* within a prespecified number of generations represents the output of the GA.
2. Starting from the near optimal solution provided by the GA, a GDM is employed to compute the parameters associated with the absolute minimum of \mathcal{R}^* . Iteratively, the input parameters are continuously updated. The incremental parameters related to one GDM iteration step, Δp_j , is a function of $\partial \mathcal{R}^*/\partial p_j$, reading $\Delta p_j = \Delta p_j(\partial \mathcal{R}^*/\partial p_j)$, $j = 1, 2, \dots, n_i$. The required derivative of the error function with respect to the unknown parameters is given by

$$\begin{aligned} \frac{\partial \mathcal{R}^*}{\partial p_j} &= \sum_{r=1}^{n_o} \left[\frac{\partial \mathcal{R}^*}{\partial u_r^*} \frac{\partial u_r^*}{\partial \tilde{u}_r^*} \frac{\partial \tilde{u}_r^*}{\partial \sigma_r^o} \sum_{k=1}^{n_h} \left(\frac{\partial \sigma_r^o}{\partial s(\sigma_k^h)} \frac{\partial s(\sigma_k^h)}{\partial \sigma_k^h} \frac{\partial \sigma_k^h}{\partial \tilde{p}_j} \right) \right] \frac{\partial \tilde{p}_j}{\partial p_j} = \\ &= \frac{1}{\mathcal{R}^* n_o} \sum_{r=1}^{n_o} \left[\frac{u_r^* - u_r}{u_r^2} \frac{\partial u_r^*}{\partial \tilde{u}_r^*} \frac{\partial s(\sigma_r^o)}{\partial \sigma_r^o} \sum_{k=1}^{n_h} \left(w_{kr}^{ho} \frac{\partial s(\sigma_k^h)}{\partial \sigma_k^h} w_{jk}^{ih} \right) \right] \frac{\partial \tilde{p}_j}{\partial p_j}, \quad (4.22) \end{aligned}$$

with $j = 1, 2, \dots, n_i$.

In general, this two-step procedure yields the parameter set associated with the absolute minimum of \mathcal{R}^* .

An additional FE analysis on the basis of the estimated optimal parameter set yields the respective value of the error function \mathcal{R}^h . In general, because of measurement errors and deficiencies of the numerical model, the attainable minimum of \mathcal{R}^h is greater than zero. Traditional gradient-free PI methods are considered as having converged if an obtained minimum of \mathcal{R}^h cannot be outperformed anymore.

In contrast to such methods, the use of an ANN in the context of the proposed PI method yields an estimate of the attainable minimum of \mathcal{R}^h . The output values obtained from traversing the estimated optimal parameter set through the ANN can be interpreted as an estimate of attainable numerical results as close as possible to the measurements. Hence, the computed minimum of \mathcal{R}^* is an estimate of the attainable precision of reproducing the

measurements by an FE simulation. Consequently, the difference between \mathcal{R}^h and \mathcal{R}^* corresponding to the estimated optimal parameter set, $|\mathcal{R}^h - \mathcal{R}^*|$, is used as an indicator of the quality of the obtained parameter set. If $|\mathcal{R}^h - \mathcal{R}^*|$ is smaller than a prespecified tolerance value, i.e., if

$$|\mathcal{R}^h - \mathcal{R}^*| \leq \text{tolerance}, \tag{4.23}$$

the PI is assumed to have converged. If, on the other hand, $|\mathcal{R}^h - \mathcal{R}^*| > \text{tolerance}$, the PI will be restarted from the beginning. This time, however, the optimal parameter set that has just been estimated and the respective FE results are added to the data sets. Hence, “ $n_d = n_d + 1$ ”. Based on the increased number of training data sets, a better approximation quality of the next ANN and, hence, a better estimate of optimal parameters can be expected.

4.1.4 Graphical interpretation of the proposed PI method

Figure 4.4 provides a graphical interpretation of the proposed PI method. In order to reduce the complexity of the illustration, a simplified problem involving a single unknown input parameter p is considered. The circles in Figure 4.4(a) represent known values of

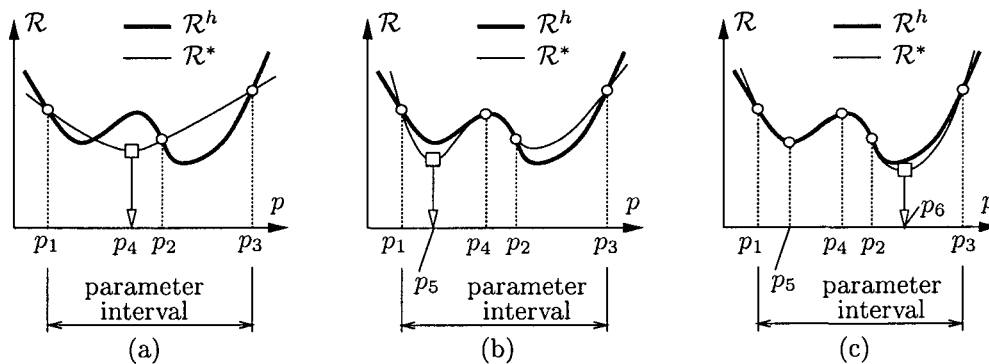


Figure 4.4: 1D graphical interpretation of the PI method: error functions $\mathcal{R}^h(p)$ and $\mathcal{R}^*(p)$ for (a) the first, (b) the second, and (c) the third iteration step of the PI

\mathcal{R}^h . These values are computed from the difference between measurements and numerical results obtained from three FE analyses based on the parameters p_1 , p_2 , and p_3 . The thick curve represents the unknown function of $\mathcal{R}^h(p)$. The PI method should give the parameter value that corresponds to the global minimum of $\mathcal{R}^h(p)$ within the prespecified parameter interval. I.e., it should provide the value of p associated with the smallest possible difference between measurements and corresponding FE results. Hereby, the algorithm should not get trapped in a local minimum of $\mathcal{R}^h(p)$.

The first ANN is trained to reproduce the three known values of \mathcal{R}^h , i.e., $\mathcal{R}^h(p_1)$, $\mathcal{R}^h(p_2)$, and $\mathcal{R}^h(p_3)$. Hence, the approximation of $\mathcal{R}^h(p)$ by the ANN, $\mathcal{R}^*(p)$, is good at $p = p_1, p_2$, and p_3 . For other values of p , \mathcal{R}^* provides an approximation of \mathcal{R}^h (see the thin curve in Figure 4.4(a)). The global minimum of $\mathcal{R}^*(p)$ (the square in Figure 4.4(a)) is determined. An estimate of an optimal parameter is obtained, with $p = p_4$. The quality of the parameter value p_4 is assessed by means of an FE simulation, giving $\mathcal{R}^h(p_4)$. As shown in Figure 4.4(a), the deviation of \mathcal{R}^* from \mathcal{R}^h at p_4 is rather large. Hence, the criterion for terminating the PI given in Eq. (4.23) is violated. Consequently, another PI iteration step is performed.

Training of the next ANN is based on the results from four FE analyses performed on the basis of p_1, p_2, p_3 , and p_4 . Consequently, the second approximation of \mathcal{R}^h by \mathcal{R}^* will give a good approximation of the four known values of \mathcal{R}^h , i.e., $\mathcal{R}^h(p_1)$ to $\mathcal{R}^h(p_4)$ (see the circles in Figure 4.4(b)). In general, the quality of the approximation of \mathcal{R}^h by \mathcal{R}^* will be improved as compared to the previous iteration step (compare the thin curves in Figures 4.4(a) and (b)). Again the global minimum of \mathcal{R}^* is determined. The respective estimate of an optimal parameter is assessed by means of another FE simulation. Again, the difference between the values of the errors \mathcal{R}^h and \mathcal{R}^* is too big, indicating that another PI iteration step must be performed.

Step-by-step, the quality of subsequent approximations of \mathcal{R}^h by \mathcal{R}^* is increasing. Hence, the PI method will yield an optimal choice for the unknown parameter. The presented algorithm can escape local minima of \mathcal{R}^h . This is illustrated in Figures 4.4(b) and 4.4(c). The PI will be completed if \mathcal{R}^* is sufficiently close to \mathcal{R}^h at the global minimum of \mathcal{R}^h .

4.2 Assessment of the new PI method: back analysis of material properties from experimental data

In the following, the performance of the proposed mode of PI will be illustrated. The advantages of determination of initial weights by a GA and the “reduced-training” algorithm will be assessed. Moreover, the influence of the number of neurons in the hidden layer on the success of the ANN training will be investigated.

The mentioned characteristics of PI will be illustrated by means of identification of material properties (“unknown model parameters”) from experimental data (“available measurements”) reported in (Sterpi, 1999). The material considered in (Sterpi, 1999) consists of cylindrical aluminum bars. The results obtained from direct-shear tests of this artificial material are shown in Figure 4.5(a). The illustrated data refer to four tests

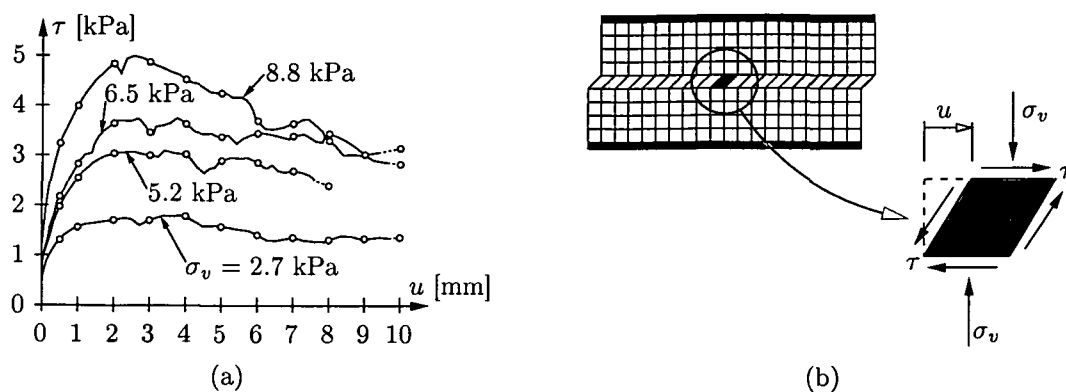


Figure 4.5: Direct-shear tests of aluminum bar assemblies: (a) experimental results and (b) one-element FE model (σ_v : prescribed vertical pressure; u : prescribed displacement; τ : evaluated shear stress)

characterized by different values of the vertical pressure σ_v . The 42 circles in Figure 4.5(a) indicate the data selected for back analysis. Hence, $n_o = 42$.

4.2.1 Numerical analysis of direct-shear tests

The shear tests are simulated by means of the FEM. A one-element model is subjected to the respective vertical pressure (see Figure 4.5(b)). Thereafter, the horizontal displacement at the top of the element is increased from 0 to 10 mm.

The material model employed for the simulation of the mechanical behavior of the aluminum-bar assembly is based on a Drucker-Prager loading surface, given by

$$f_D(\boldsymbol{\sigma}, \kappa_D) = \sqrt{J_2} + \kappa_D(I_1 - k_D) = 0, \quad (4.24)$$

where κ_D and k_D are material parameters. They are related to the cohesion c and the angle of internal friction φ by enforcing the Drucker-Prager meridian to coincide with the tensile meridian of the Mohr-Coulomb criterion (see, e.g., (Regueiro and Borja, 1999)), giving

$$\kappa_D = \frac{2 \sin \varphi}{\sqrt{3}(3 + \sin \varphi)} \quad \text{and} \quad k_D = \frac{6c}{\tan \varphi}. \quad (4.25)$$

Frictional hardening/softening is considered by means of a variable value of κ_D (Spira et al., 2001; Marcher and Vermeer, 2001) (see Figure 4.6(a)). The initial, peak, and residual values of κ_D are computed from the respective angles of internal friction according to Eq. (4.25), reading

$$\kappa_{D,i} = \frac{2 \sin \varphi_i}{\sqrt{3}(3 + \sin \varphi_i)}, \quad \kappa_{D,p} = \frac{2 \sin \varphi_p}{\sqrt{3}(3 + \sin \varphi_p)}, \quad \kappa_{D,r} = \frac{2 \sin \varphi_r}{\sqrt{3}(3 + \sin \varphi_r)}, \quad (4.26)$$

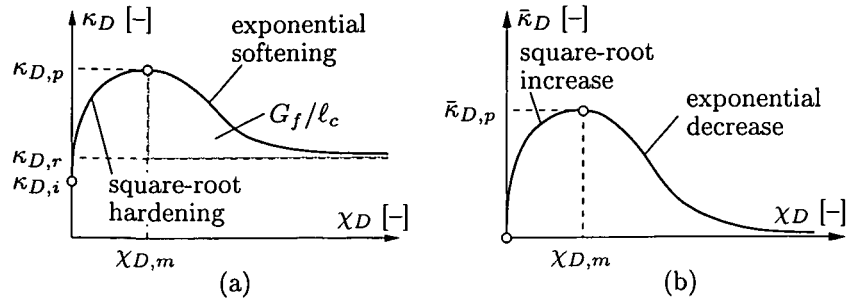


Figure 4.6: Material model employed for PI: (a) hardening/softening law and (b) evolution of $\bar{\kappa}_D$ according to (Spira et al., 2001)

whereas k_D is set equal to $6c/\tan\varphi_p$. Hardening/softening is controlled by the strain-like internal variable χ_D , employing a square-root function in the hardening and an exponential function in the softening regime (see Figure 4.6(a)):

$$\kappa_D = \begin{cases} \kappa_{D,i} + (\kappa_{D,p} - \kappa_{D,i}) \sqrt{\frac{\chi_D(2\chi_{D,m} - \chi_D)}{\chi_{D,m}^2}} & \text{for } \chi_D \leq \chi_{D,m} , \\ (\kappa_{D,p} - \kappa_{D,r}) \exp\left[-\left(\frac{\chi_D - \chi_{D,m}}{\chi_{D,u}}\right)^2\right] + \kappa_{D,r} & \text{for } \chi_D \geq \chi_{D,m} . \end{cases} \quad (4.27)$$

The calibration parameter $\chi_{D,u}$ is obtained from setting the area under the softening branch equal to the softening material parameter G_f divided by the *characteristic length* ℓ_c (see Figure 4.6(a)):

$$\frac{G_f}{\ell_c} = \int_{\chi_{D,m}}^{\infty} (\kappa_D - \kappa_{D,r}) d\chi_D \quad \Rightarrow \quad \chi_{D,u} = \frac{2}{\kappa_{D,p} - \kappa_{D,r}} \frac{G_f}{\ell_c \sqrt{\pi}} . \quad (4.28)$$

ℓ_c is related to the width of the shear band (Spira et al., 2001). In the present analysis, it is set equal to the side length of the undeformed quadratic element.

Friction hardening/softening is connected with deviatoric deformations. Consequently, χ_D is related to the deviatoric part of the plastic strain tensor, \mathbf{e}^p , as follows (see (Regueiro and Borja, 1999; Sterpi, 1999; Vermeer and de Borst, 1984) for similar definitions):

$$\dot{\chi}_D = \sqrt{\frac{2}{3}} \dot{\mathbf{e}}^p : \dot{\mathbf{e}}^p . \quad (4.29)$$

The evolution of the plastic strain tensor is controlled by a non-associative flow rule, reading

$$\dot{\mathbf{e}}^p = \dot{\gamma}_D \frac{\partial g_D}{\partial \boldsymbol{\sigma}} , \quad \text{where} \quad g_D(\boldsymbol{\sigma}, \bar{\kappa}_D) = \sqrt{J_2} + \bar{\kappa}_D I_1 \quad (4.30)$$

is the plastic potential. g_D depends on $\bar{\kappa}_D$ which is a function of the strain-like internal variable χ_D (see Figure 4.6(b)). The peak value of $\bar{\kappa}_D$ is related to the peak value of the angle of dilatancy, ψ_p , giving

$$\bar{\kappa}_{D,p} = \frac{2 \sin \psi_p}{\sqrt{3}(3 + \sin \psi_p)} . \quad (4.31)$$

The parameters of the employed material model can be summarized as follows:

- two material parameters describing the elastic behavior of the material: i.e., Young's modulus E and Poisson's ratio ν ;
- the cohesion c ;
- the initial, peak, and residual value of the angle of internal friction: φ_i , φ_p , and φ_r ;
- the peak value of the angle of dilatancy, ψ_p ;
- the value of the strain-like variable χ_D referring to the peak values of κ_D and $\bar{\kappa}_D$, $\chi_{D,m}$; and
- the softening material parameter used for determination of $\chi_{D,u}$, G_f .

According to (Sterpi, 1999), $E = 3387$ kPa, $\nu = 0.18$, and $\psi_p = 8.7^\circ$. The cohesion of the considered material can be neglected, i.e., $c = 0$. Hence, there are five unknown parameters: φ_i , φ_p , φ_r , $\chi_{D,m}$, and G_f .

4.2.2 Reduced versus classical training of ANNs

For the assessment of the ANN-training procedure, a PI problem involving three unknown parameters is considered. For this purpose, the initial value and the peak value of the angle of internal friction are set equal to 6° and 32.2° , respectively.³ The remaining three unknown parameters φ_r , $\chi_{D,m}$, and G_f ($n_i = 3$) are collected in the vector \mathbf{p} , reading

$$\mathbf{p} = [\varphi_r, \chi_{D,m}, G_f]^T . \quad (4.32)$$

The intervals of these parameters are chosen based on plausibility as

$$\begin{aligned} \varphi_r &\in [20.0^\circ, 25.0^\circ] , \\ \chi_{D,m} &\in [0.025, 0.075] , \\ G_f &\in [0.10 \text{ mm}, 0.15 \text{ mm}] . \end{aligned} \quad (4.33)$$

ANN training is based on eight pairs of parameters and respective FE results. Hence, $n_d = 8$. The eight parameter sets correspond to every possible combination of the limit values of the parameter intervals given in (4.33).

³The reduction of unknowns from five to three allows for computation of validation data sets that cover the entire parameter space with satisfactory density, see Table 4.1. The choices $\varphi_i = 6^\circ$ and $\varphi_p = 32.2^\circ$ correspond to the results obtained from the solution of the PI problem involving all five unknown parameters, see Eqs. (4.39).

Different ANNs are considered. Hereby, the number of neurons in the hidden layer is varied from $n_h = 3$ to $n_h = 6$. These values satisfy condition (4.19) reading:

$$n_h \in \{3, 4, 5, 6\} < 6.39 = \frac{42 \cdot (8 - 1)}{1 + 3 + 42} = \frac{n_o \cdot (n_d - 1)}{1 + n_i + n_o}. \quad (4.34)$$

The input layers of the considered ANNs contain three input nodes corresponding to three unknown parameters. The output layers of the networks consist of 42 neurons corresponding to 42 numerically-obtained values approximating the selected measurements depicted in Figure 4.5(a). The quality of the underlying ANN training procedure is related to the quality of interpolations between the eight training data sets provided by the trained ANN. To assess this property of the ANN, $11^3 = 1331$ different validation data sets are considered. They are computed from 1331 FE analyses. The input parameters for these FE analyses correspond to every possible combination of the parameter values given in Table 4.1. These parameter values follow from subdivision of the parameter intervals

Table 4.1: Parameter values used for determination of $11^3 = 1331$ validation sets

φ_r [°]	20.0	20.5	21.0	21.5	22.0	22.5	23.0	23.5	24.0	24.5	25.0
$\chi_{D,m}$ [-]	0.025	0.030	0.035	0.040	0.045	0.050	0.055	0.060	0.065	0.070	0.075
G_f [mm]	0.100	0.105	0.110	0.115	0.120	0.125	0.130	0.135	0.140	0.145	0.150

(4.33) into ten equidistant parts.

The initial weights for the considered networks are determined by means of a GA. For each one of the four considered ANNs, six different GAs are performed. They differ in the number of generations and of iteration steps in the context of the GDM (see first and second column in Table 4.2). Moreover, starting from the initial weights obtained by the GAs, both the “reduced-training” algorithm, with $\alpha = 0.001$, and a classical training algorithm are employed. The latter is obtained from setting $\rho(\mathcal{E}_{r,d}^{*h}) = 1.0$. For termination of the ANN training, the criterion (4.12) is used. The threshold value $\bar{\mathcal{E}}^{*h}$ is set equal to 1.0%. Training procedures still violating criterion (4.12) after 100 000 iteration steps within the framework of the GDM are viewed as having failed to converge. They are marked with “NC” (No Convergence) in Table 4.2.

The quality of the approximation of FE analyses by successfully trained ANNs is assessed by the 1331 validation sets. The respective values of the error function \mathcal{R}_{val}^{*h} (see Eq. (3.20)) are listed in Table 4.2. The best result is obtained from an ANN characterized by five neurons in the hidden layer and performing classical training: $\mathcal{R}_{val}^{*h} = 10.53\%$. Nevertheless, independent of the chosen properties of the GA, the most reliable results are

Table 4.2: Values of \mathcal{R}_{val}^{*h} (in [%]) obtained from validating the trained ANNs on the basis of 1331 validation data sets

properties of GA*		$n_h = 3$		$n_h = 4$		$n_h = 5$		$n_h = 6$	
		reduced	classical	reduced	classical	reduced	classical	reduced	classical
12500	1	10.68	NC	13.08	12.76	10.58	10.53	12.30	12.75
1250	10	10.67	NC	11.81	11.72	14.01	13.81	10.97	11.62
250	50	10.65	NC	11.33	11.00	11.61	13.66	12.05	12.26
100	125	10.67	NC	12.81	12.96	12.51	12.39	11.85	11.77
10	1250	NC	NC	11.44	10.64	11.03	10.73	12.06	12.64
1	12500	10.87	NC	12.74	12.24	11.85	13.05	13.45	13.56

*... the first column refers to the number of generations; the second column refers to the iteration steps in the context of the GDM

obtained from networks with $n_h = 3$ and performing the “reduced-training” algorithm. Notably, no ANN with $n_h = 3$ that was trained classically was able to satisfy the convergence criterion for ANN training. Hence, results from Table 4.2 show the usefulness of employing ANNs with the smallest possible number of neurons in the hidden layer and performing the “reduced-training” algorithm. As regards the influence of the GA for determination of the initial network weights, however, no information could be extracted from the present study.

4.2.3 Back analysis of unknown material properties

In order to solve the PI problem, the vector \mathbf{p} is enlarged, containing now all five unknown material properties:

$$\mathbf{p} = [\varphi_i, \varphi_p, \varphi_r, \chi_{D,m}, G_f]^T . \tag{4.35}$$

The search intervals for the five unknown parameters are chosen based on plausibility as:

$$\begin{aligned} \varphi_i &\in [0.0^\circ, 20.0^\circ] , \\ \varphi_p &\in [27.5^\circ, 37.5^\circ] , \\ \varphi_r &\in [17.5^\circ, 27.5^\circ] , \\ \chi_{D,m} &\in [0.010, 0.125] , \\ G_f &\in [0.01 \text{ mm}, 0.50 \text{ mm}] . \end{aligned} \tag{4.36}$$

Six FE analyses of the shear tests are performed in advance. They are based on parameter sets containing different combinations of the limit values of the defined parameter intervals

(4.36). These parameter sets yield the following values of the error function \mathcal{R}^h :

$$\begin{aligned}
 \mathbf{p}_1 &= [00.0, 37.5, 17.5, 0.010, 0.50]^T \Rightarrow \mathcal{R}^h(\mathbf{p}_1) = 27.77\% , \\
 \mathbf{p}_2 &= [20.0, 37.5, 17.5, 0.010, 0.50]^T \Rightarrow \mathcal{R}^h(\mathbf{p}_2) = 27.41\% , \\
 \mathbf{p}_3 &= [00.0, 27.5, 17.5, 0.010, 0.50]^T \Rightarrow \mathcal{R}^h(\mathbf{p}_3) = 16.61\% , \\
 \mathbf{p}_4 &= [00.0, 37.5, 27.5, 0.010, 0.50]^T \Rightarrow \mathcal{R}^h(\mathbf{p}_4) = 38.54\% , \\
 \mathbf{p}_5 &= [00.0, 37.5, 17.5, 0.125, 0.50]^T \Rightarrow \mathcal{R}^h(\mathbf{p}_5) = 34.75\% , \\
 \mathbf{p}_6 &= [00.0, 37.5, 17.5, 0.010, 0.01]^T \Rightarrow \mathcal{R}^h(\mathbf{p}_6) = 41.65\% .
 \end{aligned}
 \tag{4.37}$$

Based on the six pairs of parameters and respective FE results, training of the ANN is performed. Following the findings of the previous study, a rather small value of the initial number of neurons in the hidden layer, n_h , is chosen, namely 3, satisfying condition (4.19):

$$n_h = 3 < 4.4 = \frac{42 \cdot (6 - 1)}{1 + 5 + 42} = \frac{n_o \cdot (n_d - 1)}{1 + n_i + n_o} .
 \tag{4.38}$$

It is the aim of this study to assess the influence of the GA used for the determination of the initial network weights on ANN training. For this purpose, five different PI procedures resting on different types of GAs are employed (see Table 4.3). Since only one generation is

Table 4.3: Properties of GA used for determination of the initial network weights

	number of generations	number of iteration steps in the context of GDM
PI ①	10000	1
PI ②	1000	10
PI ③	100	100
PI ④	10	1000
PI ⑤	1	10000

considered for PI ⑤, the GA reduces to a multi starting-point GDM. No genetic operations are performed during this GA. It is noteworthy that the total number of GDM iteration steps is equal for all five PIs.

The “reduced-training” algorithm characterized by $\alpha = 0.001$ is employed. The required mapping accuracy for each output value, $\bar{\mathcal{E}}^{*h}$, is set equal to 1.0%. The PI procedures

will be considered as converged, if $|\mathcal{R}^h - \mathcal{R}^*| < 0.5\%$. The following results were obtained:

$$\begin{aligned}
 \text{PI ①: } \mathbf{p}_{33} &= [5.90, 32.03, 21.63, 0.0458, 0.138]^T \Rightarrow \mathcal{R}^h(\mathbf{p}_{33}) = 10.844\% , \\
 \text{PI ②: } \mathbf{p}_{30} &= [5.85, 32.36, 22.71, 0.0468, 0.111]^T \Rightarrow \mathcal{R}^h(\mathbf{p}_{30}) = 10.843\% , \\
 \text{PI ③: } \mathbf{p}_{24} &= [5.54, 32.31, 21.93, 0.0457, 0.129]^T \Rightarrow \mathcal{R}^h(\mathbf{p}_{24}) = 10.844\% , \\
 \text{PI ④: } \mathbf{p}_{24} &= [5.05, 32.11, 21.30, 0.0445, 0.148]^T \Rightarrow \mathcal{R}^h(\mathbf{p}_{24}) = 10.842\% , \\
 \text{PI ⑤: } \mathbf{p}_{20} &= [4.46, 32.43, 22.26, 0.0439, 0.126]^T \Rightarrow \mathcal{R}^h(\mathbf{p}_{20}) = 10.844\% .
 \end{aligned}
 \tag{4.39}$$

PI ① required 27 iteration steps. Considering the six FE analyses performed in advance, the total number of FE simulations required to solve the PI problem is equal to $6 + 27 = 33$. The 33-rd FE analysis, resting on the parameter set \mathbf{p}_{33} , yields values of the error functions \mathcal{R}^* and \mathcal{R}^h satisfying $|\mathcal{R}^h - \mathcal{R}^*| \leq 0.5\%$.

Notably, with a decreasing number of generations and an increasing number of GDM iteration steps performed for determination of initial weights, the number of FE analyses required to solve the PI problem is decreasing. PI ⑤, employing a multi-starting point GDM, yields the best results. It requires only 14 PI iteration steps and, hence, $6 + 14 = 20$ FE analyses.

The evolutions of the estimates for the unknown parameters and the error functions \mathcal{R}^h and \mathcal{R}^* obtained by PI ⑤ are shown in Figure 4.7. The vertical arrows refer to the results

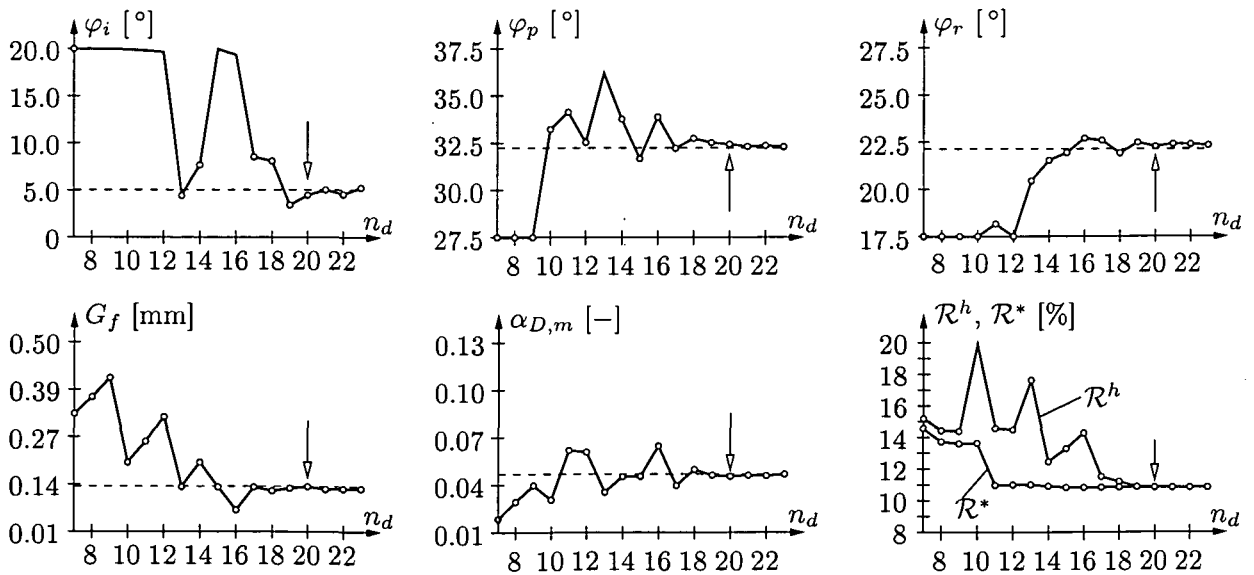


Figure 4.7: Estimates of unknown parameters and values of the error functions \mathcal{R}^h and \mathcal{R}^* obtained from PI ⑤

for $n_d = 20$, i.e., to the first set satisfying $|\mathcal{R}^h - \mathcal{R}^*| < 0.5\%$. The number of neurons in the hidden layer of the respective ANN had to be increased step by step from 3 to 12 in order to meet the criterion for termination of ANN training.

The optimal parameter set, \mathbf{p}_{opt} , corresponding to the absolute minimum of \mathcal{R}^h is computed by means of the GDM starting from the parameter set \mathbf{p}_{20} obtained by PI ⑤, reading

$$\mathbf{p}_{opt} = [5.20, 32.21, 22.08, 0.0449, 0.128]^T \Rightarrow \mathcal{R}^h(\mathbf{p}_{opt}) = 10.837\% . \quad (4.40)$$

The values of this parameter set are indicated by dashed lines in Figure 4.7.

The sensitivity of a parameter contained in the parameter set \mathbf{p}_{20} of PI ⑤ can be estimated by the error function \mathcal{R}^* provided by the ANN. Figure 4.8(a) illustrates five sections through the error function \mathcal{R}^* . These sections contain the estimated minimum

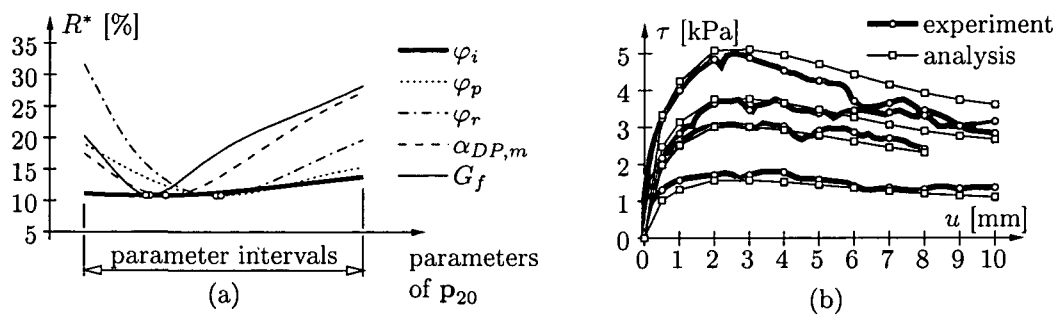


Figure 4.8: (a) ANN-estimated sensitivities of parameters (the minima of the respective functions are indicated by circles) and (b) τ - u curves obtained from \mathbf{p}_{20}

of the error function, which is marked by circles in Figure 4.8(a). For each section, four parameters were kept constant and set equal to the values of parameter set \mathbf{p}_{20} of PI ⑤, whereas the remaining parameter is varied over its entire interval (see (4.36)). The thick curve, e.g., indicates that the influence of a change of φ_i on the error function \mathcal{R}^* is small. Consequently, the chosen measurement values do not contain enough information to identify φ_i reliably.

The numerical results from FE analyses of the direct shear tests, based on the optimal parameter set \mathbf{p}_{opt} (see (4.40)), are shown in Figure 4.8(b). The good agreement between numerical and experimental results indicates the adequacy of the employed material model for the simulation of the mechanical behavior of a granular material.

4.2.4 Concluding remarks

Based on the numerical results obtained from the performed studies, the two following conclusions can be drawn:

- As regards training of the ANN,

- choosing the smallest number of neurons in the hidden layer which allows the training procedure to converge in the sense of the criterion (4.12) and
- employing the “reduced-training” algorithm

yields a trained ANN which provides optimal interpolations between the given data sets.

- Regarding determination of the initial network weights for training of the ANN, the multi starting-point GDM performs better than GAs. This is a consequence of both (i) the large number of unknown network weights and (ii) the nonlinearity of the error function \mathcal{R}^{*h} characterized by numerous local minima.

In the following applications of the proposed PI method to two problems taken from geotechnical engineering, these conclusions will be considered. Accordingly, the employed ANNs will be trained by means of the “reduced-training” algorithm, with $\alpha = 0.001$ such as used in Sections 4.2.2 and 4.2.3. The initial network weights will be computed by means of the multi starting-point GDM.

4.3 Application to ground improvement by means of jet grouting

Jet grouting is a ground-improving technique used to create *in situ* bodies consisting of cemented soil. A hollow drilling rod is used to produce a bore hole at the location where the ground should be improved (see Figure 4.9 (a)). Through nozzles located at the end of

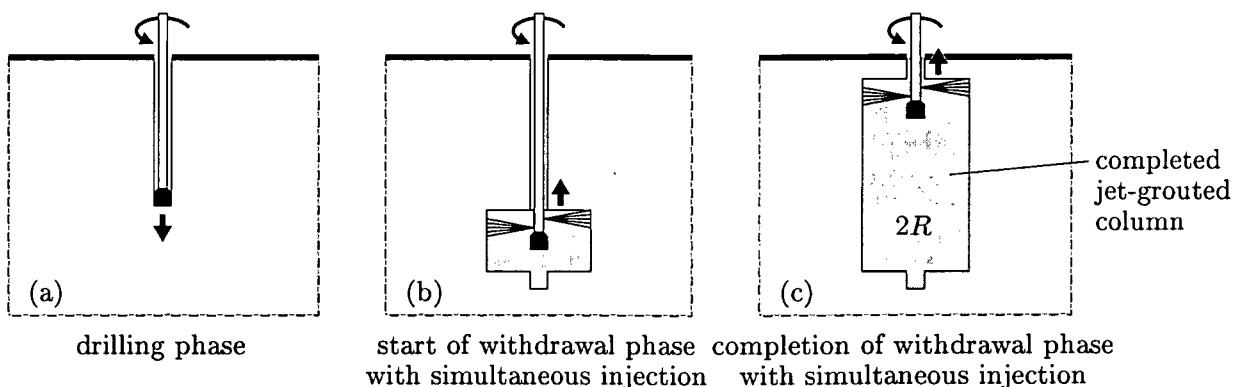


Figure 4.9: Construction sequence of jet grouting (Henn, 1996) (R : radius of jet-grouted column)

the drilling rod, thin high-pressure jets of cement grout are discharged laterally into the

borehole wall (see Figure 4.9 (b)). These jets erode the surrounding soil. Consequently, the cement grout is mixing with the *in situ* soil. After hydration, a jet-grouted soil, characterized by low permeability and increased strength, is obtained. Withdrawing and rotating the drilling rod during jet grouting, results in a column-like body of improved soil (see Figure 4.9 (c)).

4.3.1 Statement of problem and proposed solution

The properties of jet-grouted columns depend on both the mechanical properties of the *in situ* soil and grouting characteristics, such as (Henn, 1996)

- the jet grouting system (single-, double-, or triple-rod jet grouting; for details, see (Chambosse and Kirsch, 1995; Furth and Wendland, 1998)),
- the work pressure,
- the injection time which corresponds to the rate at which the drilling rods are rotated and withdrawn (see Figure 4.9).

These factors have an influence on the dimensions of the jet-grouted column (radius R) and the material properties of the jet-grouted soil. The latter mainly depend on the cement content z , i.e., the percental amount of cement mass per unit mass of the obtained jet-grouted soil. Up to now, no mathematical or mechanical models were employed for determination of the radius R . Still, test columns are produced in order to find out the column radius for a specific type of soil and a specific set of grouting parameters: These columns need to be excavated after the hydration of the injected cement. This procedure is time-consuming and expensive. Moreover, in case of variable ground conditions, the obtained column properties might be valid only for an area close to the test column. As regards the cement content, no information can be extracted from the test columns.

Recently, a new approach exploiting the exothermal character of the hydration process, i.e., the chemical reaction between cement and water, was described (Lackner et al., 2001; Brandstätter et al., 2002). Based on *in situ* temperature measurements at the center of the jet-grouted column, both the cement content z of jet-grouted soil and the column radius R can be determined via back analysis. In the context of the proposed PI method, both unknown parameters are collected in the vector $\mathbf{p} = [R, z]^T$. Selected values of the measured temperature history are collected in the vector \mathbf{u} .

Continuous application of back analysis during the construction process allows to assess the performance of jet grouting at the construction site. It provides insight into the

geometrical dimensions of the zones of improved soil. Based on these data, grouting parameters can be continuously adapted in order to obtain the desired width of jet-grouted soil bodies. The number of test columns can be reduced to a minimum.

4.3.2 Numerical analysis of temperature history in jet-grouted columns

The vector \mathbf{p} , containing the unknown model parameters, is related to the temperature history at the center of the jet-grouted column by means of thermochemical analysis. Thermochemical analyses of cementitious materials account for both the thermally activated nature of the hydration process and the release of latent heat. As regards thermochemical analyses of jet-grouted columns, because of $L/R \gg 1$, where L denotes the length of the column, the three-dimensional analysis model can be reduced to a plane model. Hereby, only the cross section of the column needs to be considered. The temperature flow in the longitudinal direction of the column is not taken into account. Moreover, the axisymmetry of the model with respect to the drilling axis allows to consider only one segment of the jet-grouted column and the respective soil. The remaining axisymmetric problem is solved by means of the FEM. The respective FE formulation can be found in (Hellmich et al., 1999a). Figure 4.10 shows the employed discretization of the jet-grouted column and the surrounding soil.

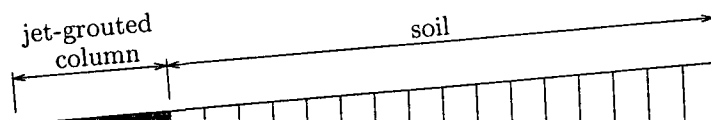


Figure 4.10: FE mesh considering only a segment of the jet-grouted column and the respective soil

For the description of the hydration process in jet-grouted soil, a thermochemical material model is employed. The underlying field equation is derived from the first law of thermodynamics. In the absence of volume heat sources and of negligible terms such as, e.g., the heat release in consequence of deformations, this law is given as (Ulm and Coussy, 1995)

$$\rho c \dot{T} - \ell_{\xi} \dot{\xi} = -\operatorname{div} \mathbf{q} , \quad (4.41)$$

with ρ [kg/m³] as the density, c [kJ/(kg K)] as the specific heat capacity, and ℓ_{ξ} [kJ/m³] as the latent heat of hydration per unit volume of jet-grouted soil. \mathbf{q} is the heat flow vector. It is related to the temperature T via Fourier's linear (isotropic) heat conduction law,

$$\mathbf{q} = -k \operatorname{grad} T , \quad (4.42)$$

with k [kJ/(m h K)] as the thermal conductivity.

In Eq. (4.41), ξ represents the degree of hydration. It is defined as the mass of hydrates formed in a unit volume of jet-grouted soil divided by the mass of hydrates at the end of the hydration process. The evolution of ξ is assumed to depend only on the mass of hydrates formed and on the current temperature (weak couplings). The employed Arrhenius-type evolution law reflects the thermally activated nature of the chemical reaction (Ulm and Coussy, 1995):

$$\dot{\xi} = \tilde{A}(\xi) \exp\left(-\frac{E_a}{RT}\right), \quad (4.43)$$

where T is the temperature in Kelvin, E_a is the activation energy, and R is the universal constant for ideal gases, with $E_a/R \approx 4000$ K (Freiesleben Hansen and Pedersen, 1977). The chemical affinity \tilde{A} is the driving force of the hydration reaction. It is different for each type of cement and was determined for PZ 275, which is the type of cement usually employed for jet grouting, as (Brandstätter et al., 2002)

$$\tilde{A}(\xi) = a \frac{1 - \exp(-b\xi)}{1 + c\xi^d} \quad [\text{s}^{-1}], \quad (4.44)$$

with $a = 8.24 \text{ s}^{-1}$, $b = 13.3$, $c = 117.2$, and $d = 6.63$.

4.3.3 Parameter identification

The proposed mode of PI is applied to a test column at a construction site in Vienna. The column was produced by means of double-rod jet grouting. Hereby, the erosion capability of the cement-grout jet was increased by an additional ring-shaped jet of air. The cement grout used consisted of Portland cement PZ 275 and water. The water/cement-ratio was 1.0. Jet grouting started approximately 3.5 m below ground level. The rod was withdrawn and rotated until the column has reached a length of 3 m (see Figure 4.11 (a)). Right after jet grouting, a temperature sensor was installed at the center of the column. The measured temperature history is plotted in Figure 4.11 (b). For back analysis of R and z , 21 discrete values at different instants of time were selected (see Table 4.4). Hence, $n_o = 21$.

Table 4.4: Selected temperature values used for back analysis

t [h]	T [°C]	t [h]	T [°C]	t [h]	T [°C]	t [h]	T [°C]	t [h]	T [°C]	t [h]	T [°C]	t [h]	T [°C]
5	25.4	20	34.1	50	38.9	80	37.8	110	35.8	140	33.7	170	31.7
10	29.7	30	36.7	60	38.9	90	37.2	120	34.9	150	32.9	180	31.3
15	32.5	40	38.4	70	38.4	100	36.5	130	34.3	160	32.5	190	30.8

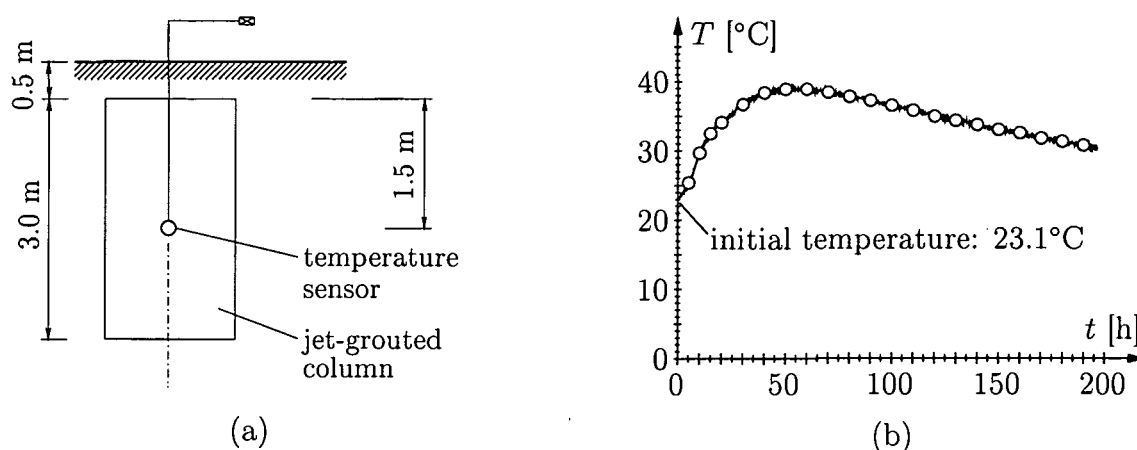


Figure 4.11: Test column at a construction site in Vienna: (a) known dimensions of jet-grouted column and location of temperature sensor, and (b) measured temperature history (temperature values used for back analysis are indicated by circles)

Properties of the surrounding soil such as density, heat capacity, and thermal conductivity are taken from standard text books as 2000 kg/m^3 , $1.0 \text{ kJ}/(\text{kg K})$, and $3.0 \text{ kJ}/(\text{m h K})$, respectively (see, e.g., (Baehr and Stephan, 1998; Özişik, 1985; Kakaç and Yener, 1985; Pitts and Sissom, 1977)). The injection of cement grout into the *in situ* soil during jet grouting results in an increase of the density of the soil from 2000 to 2300 kg/m^3 . In order to account for the rather large heat capacity of water ($c = 4.18 \text{ kJ}/(\text{kg K})$), the heat capacity is increased from 1.0 to $1.3 \text{ kJ}/(\text{kg K})$. The thermal conductivity of jet-grouted soil is set equal to $4.0 \text{ kJ}/(\text{m h K})$.

The search intervals for the values of the unknown parameters R and z are chosen as

$$\begin{aligned} R &\in [0.2 \text{ m}, 2.0 \text{ m}] , \\ z &\in [2\%, 16.7\%] . \end{aligned} \quad (4.45)$$

The radii of the columns attained in jet-grouting applications, reported in the open literature, are in the chosen interval. Regarding the interval selected for the cement content z , the upper bound of 16.7% refers to the limit case of application of the thermochemical material model outlined in Subsection 4.3.2. This limit case is characterized by an increase of the temperature up to 100°C . For the present problem, this temperature increase is equal to $100 - 23.1 = 76.9^\circ\text{C}$, where 23.1°C is the initial temperature of the improved soil (see Figure 4.11 (b)). The latent heat resulting in an increase of the temperature to 100°C under adiabatic conditions can be determined from Eq. (4.41), considering $\text{div } \mathbf{q} = 0$:

$$\ell_\xi = 76.9 \rho c = 76.9 \cdot 2300 \cdot 1.3 = 229931 \text{ kJ}/(\text{m}^3 \text{ jet-grouted soil}). \quad (4.46)$$

On the other hand, the latent heat is related to the cement content z , reading

$$\ell_{\xi} = 600 \rho z \text{ [kJ/(m}^3 \text{ jet-grouted soil)]}, \quad (4.47)$$

where the coefficient 600 refers to the latent heat in [kJ] of one kilogram cement (Byfors, 1980). Combining Eqs. (4.46) and (4.47) yields the aforementioned value of the upper bound of the cement content:

$$z \leq \frac{\ell_{\xi}}{600 \rho} = \frac{229931}{600 \cdot 2300} = 0.167 = 16.7\%. \quad (4.48)$$

On the basis of the chosen parameter intervals, four FE simulations are performed prior to back analysis. Hence, $n_d = 4$. The respective parameter sets are obtained from combining the limit values given in (4.45). Hereby, the combination $\mathbf{p} = [2.0, 0.167]^T$ is disregarded. Because of the large dimensions of the column, this parameter set would result in almost adiabatic conditions in the jet-grouted column. Because of the cement content of 16.7%, an increase of the temperature of up to 100°C would be obtained. Such an increase is not confirmed by the available temperature data, given in Figure 4.11 (b). Therefore, an alternative parameter set containing the mean values of the interval limits given in (4.45) is chosen:

$$\begin{aligned} \mathbf{p}_1 &= [0.20, 0.020]^T \Rightarrow \mathcal{R}^h(\mathbf{p}_1) = 55.2\%, \\ \mathbf{p}_2 &= [0.20, 0.167]^T \Rightarrow \mathcal{R}^h(\mathbf{p}_2) = 40.3\%, \\ \mathbf{p}_3 &= [2.00, 0.020]^T \Rightarrow \mathcal{R}^h(\mathbf{p}_3) = 14.5\%, \\ \mathbf{p}_4 &= [1.10, 0.094]^T \Rightarrow \mathcal{R}^h(\mathbf{p}_4) = 64.2\%. \end{aligned} \quad (4.49)$$

FE analyses based on the parameter sets \mathbf{p}_1 to \mathbf{p}_4 do not yield results of satisfactory accuracy (see values of the error \mathcal{R}^h in (4.49)). These four parameter sets and the respective FE results are the basis for the first estimate of optimal parameters in the context of the proposed PI method. Based on $n_i = 2$, referring to the two unknown model parameters, $n_o = 21$, and $n_d = 4$, the initial number of neurons in the hidden layer of the ANN is chosen as $n_h = 2$, satisfying condition (4.19):

$$n_h = 2 < 2.625 = \frac{21 \cdot (4 - 1)}{1 + 2 + 21} = \frac{n_o \cdot (n_d - 1)}{1 + n_i + n_o}. \quad (4.50)$$

Regarding training of the ANN, the required mapping accuracy for each output value, $\bar{\mathcal{E}}^{*h}$, is set equal to 1.0%. Training procedures, still violating criterion (4.12) after 250 000 iteration steps within the framework of the GDM are viewed as having failed to converge, followed by an increase of the number of neurons in the hidden layer by one. The PI is assumed to have converged, if the indicator $|\mathcal{R}^h - \mathcal{R}^*|$ is smaller than or equal to 0.5%. The

estimates of the unknown parameters and the evolution of the values of the error functions \mathcal{R}^h and \mathcal{R}^* , obtained in the course of PI, are given as (see also Figure 4.12):

$$\begin{aligned}
 \mathbf{p}_5 &= [0.28, 0.037]^T \Rightarrow \mathcal{R}^*(\mathbf{p}_5) = 3.2\%, \quad \mathcal{R}^h(\mathbf{p}_5) = 45.5\%, \\
 \mathbf{p}_6 &= [0.67, 0.040]^T \Rightarrow \mathcal{R}^*(\mathbf{p}_6) = 2.3\%, \quad \mathcal{R}^h(\mathbf{p}_6) = 14.4\%, \\
 \mathbf{p}_7 &= [0.77, 0.037]^T \Rightarrow \mathcal{R}^*(\mathbf{p}_7) = 1.5\%, \quad \mathcal{R}^h(\mathbf{p}_7) = 10.9\%, \\
 \mathbf{p}_8 &= [1.14, 0.035]^T \Rightarrow \mathcal{R}^*(\mathbf{p}_8) = 1.8\%, \quad \mathcal{R}^h(\mathbf{p}_8) = 5.3\%, \\
 \mathbf{p}_9 &= [0.90, 0.040]^T \Rightarrow \mathcal{R}^*(\mathbf{p}_9) = 1.9\%, \quad \mathcal{R}^h(\mathbf{p}_9) = 2.8\%, \\
 \mathbf{p}_{10} &= [0.89, 0.042]^T \Rightarrow \mathcal{R}^*(\mathbf{p}_{10}) = 1.9\%, \quad \mathcal{R}^h(\mathbf{p}_{10}) = 2.0\%,
 \end{aligned} \tag{4.51}$$

The parameter set \mathbf{p}_{10} yields values of the error functions \mathcal{R}^* and \mathcal{R}^h signalling convergence of the PI by $|\mathcal{R}^h - \mathcal{R}^*| = 0.1\% < 0,5\%$.

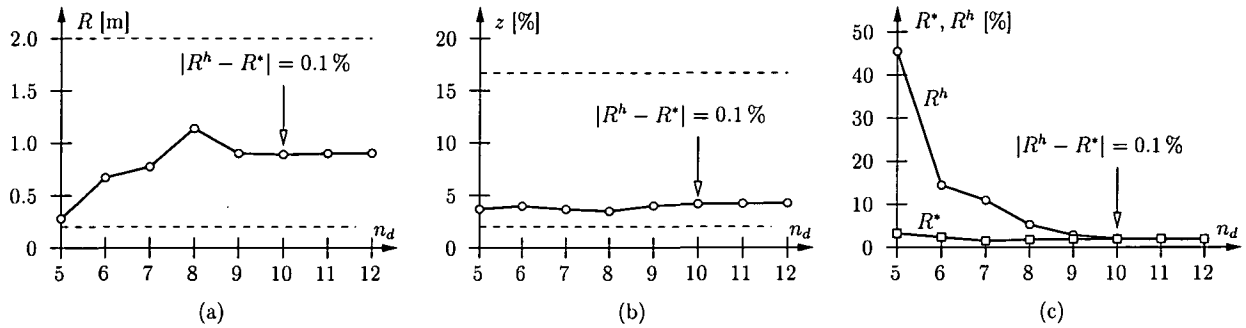


Figure 4.12: Results from back analysis: evolution of (a) R , (b) z , and (c) \mathcal{R}^* and \mathcal{R}^h obtained in the course of PI

The estimated optimal parameter sets obtained in four subsequent PI iteration-steps do not significantly outperform the result obtained from \mathbf{p}_{10} :

$$\begin{aligned}
 \mathbf{p}_{11} &= [0.90, 0.042]^T \Rightarrow \mathcal{R}^*(\mathbf{p}_{11}) = 2.0\%, \quad \mathcal{R}^h(\mathbf{p}_{11}) = 1.8\%, \\
 \mathbf{p}_{12} &= [0.90, 0.043]^T \Rightarrow \mathcal{R}^*(\mathbf{p}_{12}) = 1.9\%, \quad \mathcal{R}^h(\mathbf{p}_{12}) = 1.9\%, \\
 \mathbf{p}_{13} &= [0.90, 0.042]^T \Rightarrow \mathcal{R}^*(\mathbf{p}_{13}) = 1.9\%, \quad \mathcal{R}^h(\mathbf{p}_{13}) = 1.9\%, \\
 \mathbf{p}_{14} &= [0.89, 0.043]^T \Rightarrow \mathcal{R}^*(\mathbf{p}_{14}) = 1.9\%, \quad \mathcal{R}^h(\mathbf{p}_{14}) = 1.8\%.
 \end{aligned} \tag{4.52}$$

Hence, the indicator based on the difference between \mathcal{R}^* and \mathcal{R}^h (criterion (4.23)) provided a good estimate of the quality of the obtained parameters. The small value of $\mathcal{R}^h(\mathbf{p}_{10})$ indicates good agreement between the respective numerical results and the measurement data (see Figure 4.13(a)). The value of \mathcal{R}^h corresponding to the identified parameter set is a measure for the adequacy of the employed numerical model to simulate the hydration process in jet-grouted soil. The radius of the jet-grouted column obtained by means of PI agrees well with the radius observed at the excavated test column, see Figure 4.13(b).

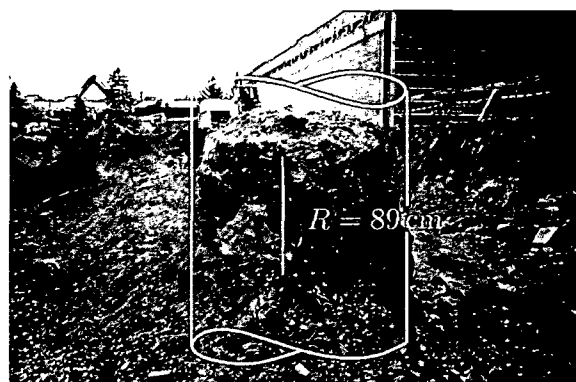
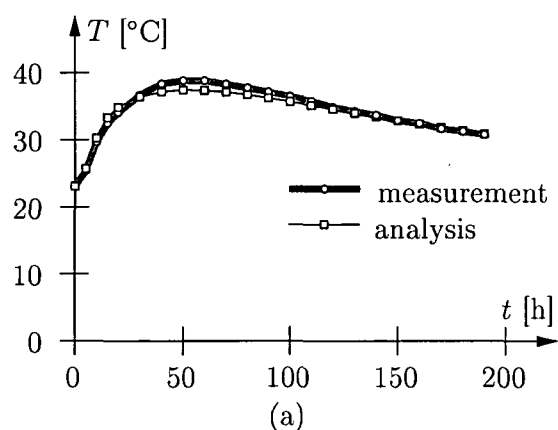


Figure 4.13: Results from back analysis: (a) temperature history corresponding to the identified parameter set \mathbf{p}_{10} and (b) excavated test column

4.4 Application to NATM tunneling

The New Austrian Tunneling Method (NATM) has proved to be a flexible and economic mode of construction. Basic characteristics of this method are the application of shotcrete onto the tunnel walls immediately after the excavation of a section of the tunnel and monitoring of the displacements at measurement cross-sections. The shotcrete shell is comparably thin and flexible. Recently developed hybrid methods (Rokahr and Zachow, 1997; Hellmich et al., 2001; Lackner and Mang, 2001) allow for quantification of the stress state and, hence, of the so-called level of loading of the shotcrete lining (Hellmich et al., 2001). They combine *in situ* displacement measurements of the shotcrete lining and a material model for shotcrete. The aforementioned 3D displacement measurements are performed at so-called measurement points (MPs) in the measurement cross-sections (MCS), see Figure 4.14. At the MPs small reflectors are installed at the tunnel lining right after application of shotcrete. The displacement data obtained at the MPs are interpolated both in space and time, yielding a time-dependent displacement field of the tunnel shell. This displacement field represents the boundary values of the structural model. This model represents a specific MCS of the tunnel, referred to as *considered MCS* (see Figure 4.14). Hereby, longitudinal deformations may be accounted for by consideration of displacement measurements at the adjacent MCSs (see Figure 4.14).

4.4.1 Statement of problem and proposed solution concept

Hybrid methods allow for determination of the so-called level of loading for already constructed and, hence, monitored parts of the shotcrete lining (Hellmich et al., 2001). However, genuine predictions of (i) future stress states in the already constructed shotcrete

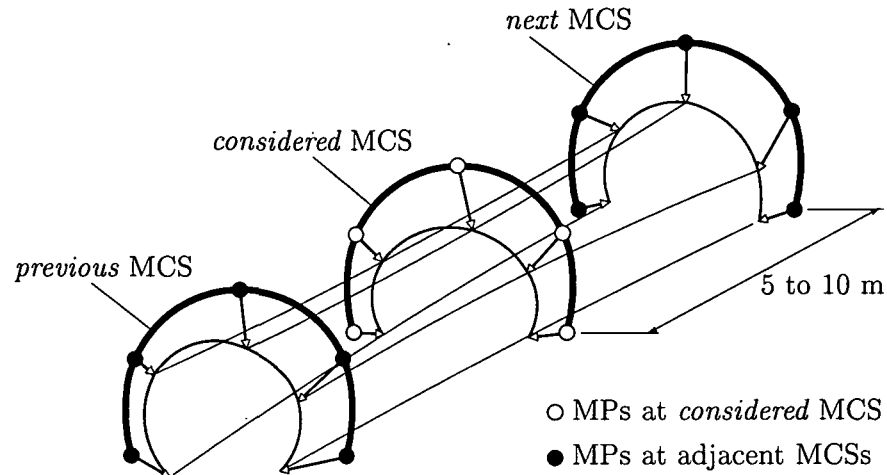


Figure 4.14: Spatial interpolation of displacements between MPs in the context of hybrid methods in tunneling

shell, and of (ii) stress states in not yet constructed parts of the tunnel are very difficult. They require consideration of the interaction between the shotcrete shell and the surrounding soil/rock formations. Whereas material properties of shotcrete are well known from laboratory tests, little is known about the material properties of the surrounding soil/rock.

In order to specify unknown soil/rock parameters, use of the presented PI method is proposed. The numerical model employed for PI considers both the shotcrete lining and the surrounding soil/rock formation. Hence, material parameters of soil/rock layers can be related to different types of measurements such as displacements at MPs, surface settlements, and extensometer measurements. Unknown material parameters will be determined at specific cross sections of the tunnel, favorably at MCSs. During PI, the time span considered in the numerical analyses ranges from the time instant associated with the start of the excavation at the *considered* MCS to the day at which the analysis is performed. Based on the identified material parameters, displacements and, hence, future stress states of the tunnel shell can be predicted. There are two different types of predictions (see Figure 4.15):

1. The first type of predictions is characterized by continuation of the numerical simulation for the *considered* MCS based on the identified parameters. This type of predictions provides information about future displacements and stress states at the *considered* (already installed) MCS.
2. In case of moderately changing geological conditions, the soil/rock parameters determined at already installed MCSs may still be valid a stretch ahead of the tunnel face. Hence, based on identified parameters, numerical analyses of the tunnel excavation

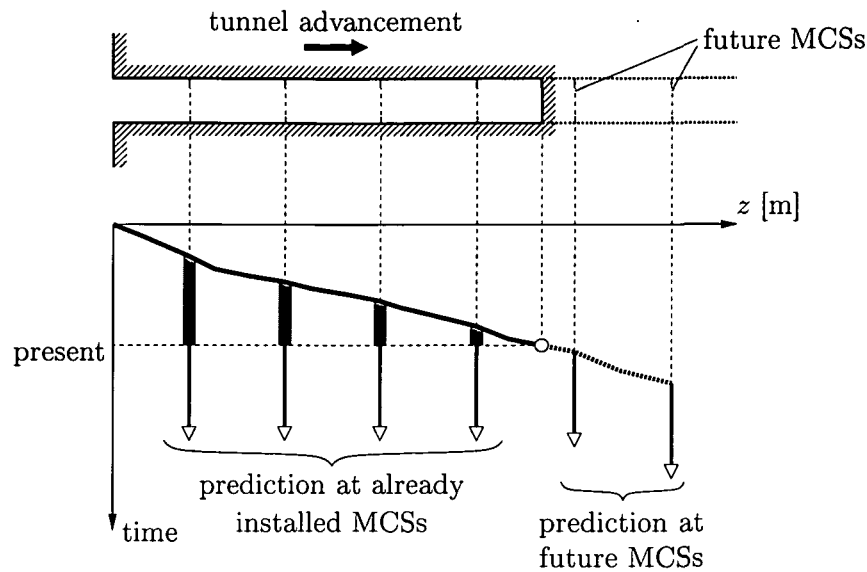


Figure 4.15: Illustration of two types of predictions on the basis of soil/rock parameters obtained from PI, i.e., prediction either at already installed or at yet not installed MCSs

at future (not yet installed) MCSs are possible.

Both types of predictions would represent a significant progress in tunnel engineering. Beside the possibility of adaptation and optimization of tunnel-driving parameters, they would allow to assess the safety of the tunnel and, hence, reduce the risks for the construction crew.

In the following sections, the first steps towards this goal are described. By means of an example problem, unknown material parameters of two different soil layers are identified via back analysis.

4.4.2 Numerical analysis of the excavation process

The example presented in this paper refers to the planned excavation of the station tube "Taborstraße" of the Vienna underground line U2. The soil in this area of Vienna consists mainly of cohesionless material such as gravels and sands. The geological conditions and the location of the station tube are illustrated in Figure 4.16(a). The tunnel is excavated sequentially. The three excavation steps are as follows: top heading, bench, and invert. After each excavation step, shotcrete is applied onto the newly excavated tunnel surface. The numerical analyses are performed by means of the FEM. The employed FE discretization is shown in Figure 4.16(b).

For the simulation of the mechanical behavior of the soil, the material model used in Subchapter 4.2 is extended to viscoplasticity. As a first approximation, the evolution laws

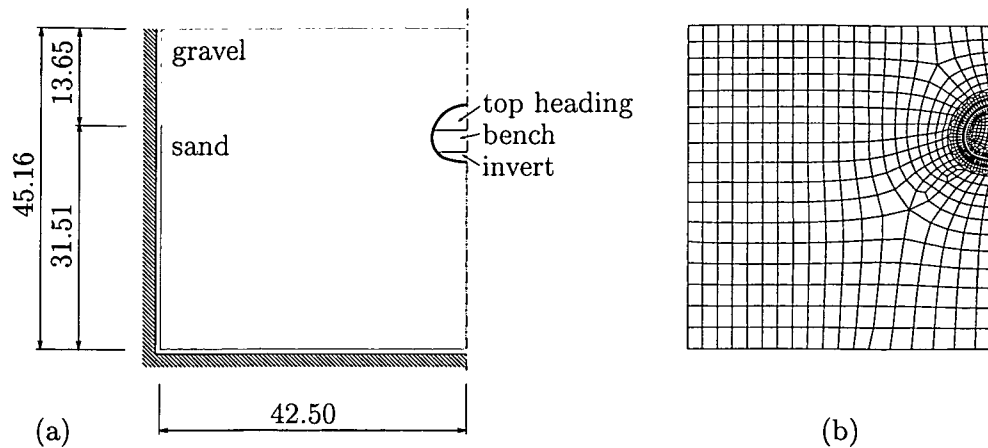


Figure 4.16: Underground station “Taborstraße”: (a) geometrical dimensions (in [m]) of the numerical model and (b) FE mesh consisting of 991 finite elements

for the viscoplastic strains and the hardening parameter κ_D are chosen according to the law by Duvaut and Lions (Duvaut and Lions, 1972),

$$\dot{\epsilon}^{vp} = \frac{1}{\tau} \mathbf{C}^{-1}(\boldsymbol{\sigma} - \boldsymbol{\sigma}^\infty) \quad \text{and} \quad \dot{\kappa}_D = -\frac{1}{\tau}(\kappa_D - \kappa_D^\infty). \quad (4.53)$$

τ is the relaxation time describing the time-dependent behavior of soil. $\boldsymbol{\sigma}^\infty$ and κ_D^∞ correspond to the solution for rate-independent plasticity, i. e., to the solution for infinitely slow loading.

Shotcrete is modeled as a reactive porous medium. For a detailed description, see (Hellmich et al., 1999b) and references therein. Dissipative phenomena at the microlevel of the material are accounted for by means of (internal) state variables and energetically conjugated thermodynamic forces, related to the state variables via state equations. The rates of the internal state variables are related to the corresponding thermodynamic forces by means of evolution equations.

Four dissipative phenomena govern the material behavior of shotcrete:

1. The *hydration* causes chemical shrinkage strains, aging elasticity, and strength growth. The extent of the hydration process is defined by the degree of hydration ξ .
2. *Microcracking* of hydrates yields plastic strains. The state of microstructural changes resulting from microcracking (i. e., hardening/softening) is described by hardening variables χ .
3. Stress-induced *dislocation-like processes* within the hydrates result in flow (or long-term) creep strains. The state of respective microstructural changes is described by the viscous flow.

4. Stress-induced *microdiffusion of water* in the capillary pores between the hydrates result in viscous (or short-term) creep strains.

Microcracking is described by means of a multi-surface chemoplasticity model (see Figure 4.17). It consists of the Drucker-Prager surface for description of shotcrete subjected

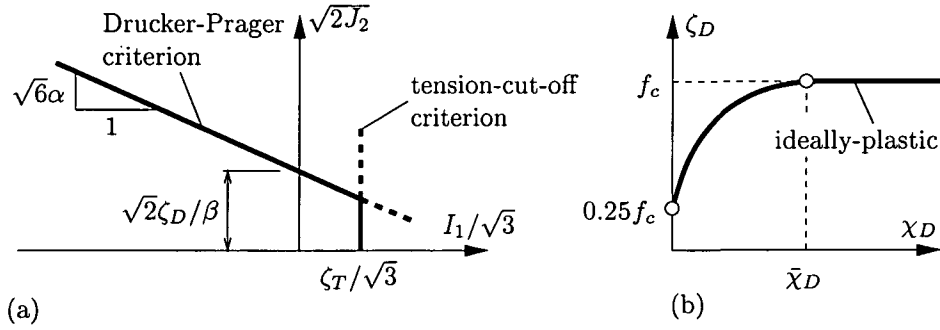


Figure 4.17: Multi-surface plasticity model for shotcrete: (a) yield surfaces in the $(I_1/\sqrt{3})$ - $(\sqrt{2}J_2)$ -space and (b) strain-hardening within the framework of the Drucker-Prager criterion (f_c : uniaxial compressive strength)

to compressive loading and the tension-cut-off criterion for simulation of tensile failure, reading

$$f_D(\sigma, \zeta_D) = \sqrt{J_2} + \alpha I_1 - \zeta_D(\chi_D, \xi)/\beta \quad \text{and} \quad f_T(\sigma, \zeta_T) = I_1 - \zeta_T(\xi). \quad (4.54)$$

The material parameters α and β are determined by means of the uniaxial compressive strength f_c and the biaxial compressive strength f_b of shotcrete, (Lackner et al., 2000)

$$\alpha = \frac{f_b/f_c - 1}{\sqrt{3}(2f_b/f_c - 1)} \quad \text{and} \quad \beta = \frac{\sqrt{3}(2f_b/f_c - 1)}{f_b/f_c}. \quad (4.55)$$

Increase of the compressive strength ζ_D from $0.25f_c$ to f_c in the context of strain hardening is considered, see Figure 4.17(b). For the tensile strength ζ_T , only chemical hardening is considered, giving $\zeta_T = \zeta_T(\xi)$.

4.4.3 “Measurement data” of underground station “Taborstraße”

The construction of the station tube “Taborstraße” is scheduled for spring 2004. Hence, measurement data are not available. Therefore, “measurement data” are generated by numerical analysis prior to parameter identification. The material parameters employed for the two soil layers in this analysis are given in Table 4.5. Similar to the material parameters used in Subchapter 4.2, a very small value was assigned to the cohesion of

Table 4.5: Material parameters of both soil layers (chosen based on plausibility) employed for the generation of “measurement data” by means of a numerical analysis

	sand	gravel
Young’s modulus E [N/mm ²]	65	80
Poisson’s ratio ν [-]	0.350	0.316
angle of internal friction $\varphi = \varphi_i = \varphi_p = \varphi_r$	36.5°	42.0°
relaxation time τ [h]	1.0	1.0

the sand and the gravel. The material properties of shotcrete are taken from (Lackner et al., 2000). From the obtained numerical results, histories of surface settlements and displacements of three MPs of the shotcrete lining are recorded (see Figures 4.18 and 4.19). Such measurements are nowadays routinely performed at every NATM construction site.

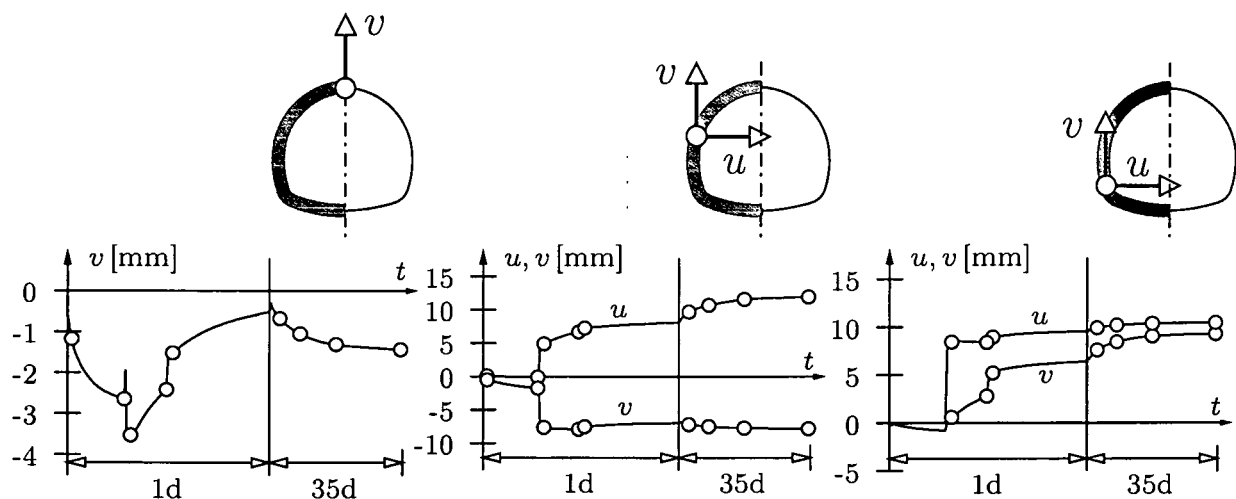


Figure 4.18: “Measurement data” generated by numerical analysis: histories of horizontal and vertical displacement component, u and v , at selected points of shotcrete lining

Hence, they are available in the course of the construction process.

4.4.4 Parameter identification

During back analysis, five material parameters listed in Table 4.5 are assumed to be unknown. They are collected in the vector \mathbf{p} , reading

$$\mathbf{p} = [E_{sand}, \varphi_{sand}, \tau, \varphi_{gravel}, E_{gravel}]^T, \tag{4.56}$$

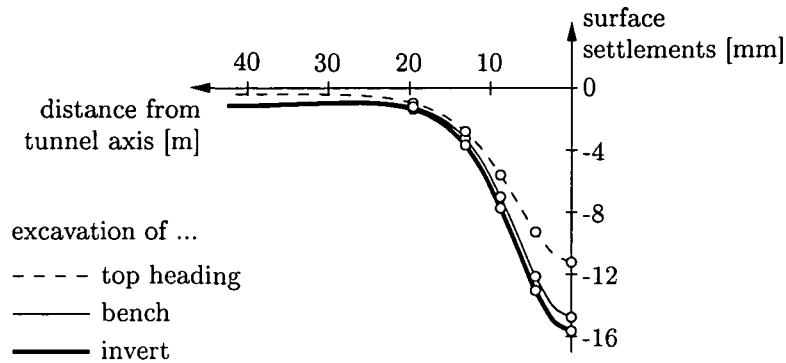


Figure 4.19: "Measurement data" generated by numerical analysis: surface settlements

where $\tau_{sand} = \tau_{gravel} = \tau$. Accordingly, $n_i = 5$. The intervals for the unknown parameters are chosen based on plausibility as

$$\begin{aligned}
 E_{sand} &\in [60.0 \text{ N/mm}^2, 80.0 \text{ N/mm}^2] , \\
 \varphi_{sand} &\in [33.0^\circ, 41.0^\circ] , \\
 \tau &\in [0.15 \text{ h}, 1.50 \text{ h}] , \\
 \varphi_{gravel} &\in [35.0^\circ, 45.0^\circ] , \\
 E_{gravel} &\in [70.0 \text{ N/mm}^2, 100.0 \text{ N/mm}^2] .
 \end{aligned}
 \tag{4.57}$$

For back analysis, the displacement histories illustrated in Figures 4.18 and 4.19 are treated as measurement data provided by the construction site. 56 discrete values referring to different measurement curves are selected for PI (see circles in Figures 4.18 and 4.19). They are collected in the vector \mathbf{u} , yielding $n_o = 56$.

Contrary to the previous examples, the values of some of the measurement data u_r , i.e., of displacements of the tunnel shell are close to zero. Accordingly, the definitions of the error functions \mathcal{R}^h and \mathcal{R}^* (see Equations (2.1) and (4.1)), characterized by relating the error of the r -th output value to the r -th measurement data, must be adapted. An alternative definition of the error functions is obtained by relating the error of the r -th output value of the c -th measurement curve to the mean value \bar{u}_c of all selected measurements referred to the respective measurement curve:

$$\bar{u}_c = \frac{1}{n_{o,c}} \sum_{r=1}^{n_{o,c}} |u_{c,r}| .
 \tag{4.58}$$

In Equation (4.58), $n_{o,c}$ represents the number of selected measurements associated with curve c . The adapted error functions are introduced as

$$\mathcal{R}^h \rightarrow \sqrt{\frac{1}{n_o} \sum_{c=1}^{n_m} \sum_{r=1}^{n_{o,c}} \left(\frac{u_{c,r}^h(\mathbf{P}) - u_{c,r}}{\bar{u}_c} \right)^2} ,
 \tag{4.59}$$

$$\mathcal{R}^* \rightarrow \sqrt{\frac{1}{n_o} \sum_{c=1}^{n_m} \sum_{r=1}^{n_{o,c}} \left(\frac{u_{c,r}^*(\mathbf{p}) - u_{c,r}}{\bar{u}_c} \right)^2}, \quad (4.60)$$

where n_m is the number of measurement curves. In the present example, $n_m = 8$.

Moreover, some numerical results for the displacements of the tunnel shell might be very close to zero. Accordingly, the definitions of the error function \mathcal{R}^{*h} (see Equation (4.6)) and the error value used in the accuracy criterion for ANN training (4.12), characterized by relating the error of the r -th output value to the r -th value of numerical results, must be adapted too. By analogy, these definitions are:

$$\mathcal{R}_d^{*h} \rightarrow \frac{1}{n_o} \sum_{c=1}^{n_m} \sum_{r=1}^{n_{o,c}} \left(\frac{u_{c,r}^*(\mathbf{p}_d) - u_{c,r}^h(\mathbf{p}_d)}{\bar{u}_c} \right)^2, \quad (4.61)$$

$$\mathcal{E}_{r,d}^{*h} \rightarrow \mathcal{E}_{r,c,d}^{*h} = \left| \frac{u_{c,r}^*(\mathbf{p}_d) - u_{c,r}^h(\mathbf{p}_d)}{\bar{u}_c} \right| \quad \forall \quad \begin{cases} r = 1, 2, \dots, n_{o,c} \\ c = 1, 2, \dots, n_m \\ d = 1, 2, \dots, n_d. \end{cases} \quad (4.62)$$

Twelve FE analyses are performed in advance in order to provide twelve different data sets. They are based on different parameter sets containing different combinations of the limit values of the defined parameter intervals (4.57), reading

$$\begin{aligned} \mathbf{p}_1 &= [60, 33, 0.15, 35, 70]^T \Rightarrow \mathcal{R}^h(\mathbf{p}_1) = 148.8\% , \\ \mathbf{p}_2 &= [80, 33, 0.15, 35, 70]^T \Rightarrow \mathcal{R}^h(\mathbf{p}_2) = 125.9\% , \\ \mathbf{p}_3 &= [60, 41, 0.15, 35, 70]^T \Rightarrow \mathcal{R}^h(\mathbf{p}_3) = 116.9\% , \\ \mathbf{p}_4 &= [60, 33, 1.50, 35, 70]^T \Rightarrow \mathcal{R}^h(\mathbf{p}_4) = 24.3\% , \\ \mathbf{p}_5 &= [60, 33, 0.15, 45, 70]^T \Rightarrow \mathcal{R}^h(\mathbf{p}_5) = 86.2\% , \\ \mathbf{p}_6 &= [60, 33, 0.15, 35, 100]^T \Rightarrow \mathcal{R}^h(\mathbf{p}_6) = 124.1\% , \\ \mathbf{p}_7 &= [80, 41, 1.50, 45, 100]^T \Rightarrow \mathcal{R}^h(\mathbf{p}_7) = 29.9\% , \\ \mathbf{p}_8 &= [60, 41, 1.50, 45, 100]^T \Rightarrow \mathcal{R}^h(\mathbf{p}_8) = 20.1\% , \\ \mathbf{p}_9 &= [80, 33, 1.50, 45, 100]^T \Rightarrow \mathcal{R}^h(\mathbf{p}_9) = 23.2\% , \\ \mathbf{p}_{10} &= [80, 41, 0.15, 45, 100]^T \Rightarrow \mathcal{R}^h(\mathbf{p}_{10}) = 28.0\% , \\ \mathbf{p}_{11} &= [80, 41, 1.50, 35, 100]^T \Rightarrow \mathcal{R}^h(\mathbf{p}_{11}) = 25.2\% , \\ \mathbf{p}_{12} &= [80, 41, 1.50, 45, 70]^T \Rightarrow \mathcal{R}^h(\mathbf{p}_{12}) = 23.3\% . \end{aligned} \quad (4.63)$$

The PI is assumed to have converged if the indicator $|\mathcal{R}^h - \mathcal{R}^*|$ is smaller than or equal to 0.5%. The required mapping accuracy for each output value, $\bar{\mathcal{E}}^{*h}$, is set equal to 2.5%, which is significantly smaller than the smallest value of \mathcal{R}^h obtained from the FE analyses performed in advance. Training procedures which still violate criterion (4.12) after 250 000 iteration steps in the context of the GDM are viewed as having failed to converge. In this case the number of neurons in the hidden layer is increased by one. Based on these

settings, three prognoses for the optimal parameter set were computed, giving \mathbf{p}_{13} to \mathbf{p}_{15} :

$$\begin{aligned} \mathbf{p}_{13} &= [65.7, 38.6, 1.122, 42.6, 79.8]^T \Rightarrow \mathcal{R}^*(\mathbf{p}_{13}) = 2.0\%, \mathcal{R}^h(\mathbf{p}_{13}) = 7.1\%, \\ \mathbf{p}_{14} &= [65.0, 35.0, 1.173, 40.2, 77.6]^T \Rightarrow \mathcal{R}^*(\mathbf{p}_{14}) = 1.0\%, \mathcal{R}^h(\mathbf{p}_{14}) = 4.0\%, \\ \mathbf{p}_{15} &= [64.9, 36.5, 1.100, 42.0, 79.1]^T \Rightarrow \mathcal{R}^*(\mathbf{p}_{15}) = 1.1\%, \mathcal{R}^h(\mathbf{p}_{15}) = 2.2\%, \end{aligned} \quad (4.64)$$

Parameter set \mathbf{p}_{15} yields a value of the indicator $|\mathcal{R}^h - \mathcal{R}^*|$ that is equal to 1.1 %, which is still larger than 0.5 %. $\mathcal{R}^h(\mathbf{p}_{15})$ is equal to 2.2 % indicating already good agreement between numerical results and “measurement data”. Moreover, $\mathcal{R}^h(\mathbf{p}_{15})$ is smaller than the mapping accuracy $\bar{\mathcal{E}}^{*h} = 2.5\%$ used for training of the ANN. In order to guarantee an adequate approximation of FE results by the ANN, the mapping accuracy $\bar{\mathcal{E}}^{*h}$ must be adapted to the smallest value of the error \mathcal{R}^h obtained so far. Accordingly, for the subsequent PI iteration steps, $\bar{\mathcal{E}}^{*h}$ is set equal to 1.5 % $< \mathcal{R}^h(\mathbf{p}_{15}) = 2.2\%$, 1.0 % $< \mathcal{R}^h(\mathbf{p}_{16}) = 1.5\%$, and 0.5 % $< \mathcal{R}^h(\mathbf{p}_{17}) = 0.7\%$ for determination of \mathbf{p}_{16} , \mathbf{p}_{17} , and \mathbf{p}_{18} , respectively. The results obtained from these three PI iteration steps can be summarized as follows

$$\begin{aligned} \mathbf{p}_{16} &= [65.3, 36.3, 1.075, 42.0, 79.1]^T \Rightarrow \mathcal{R}^*(\mathbf{p}_{16}) = 0.7\%, \mathcal{R}^h(\mathbf{p}_{16}) = 1.5\%, \\ \mathbf{p}_{17} &= [65.4, 36.3, 1.048, 41.8, 79.6]^T \Rightarrow \mathcal{R}^*(\mathbf{p}_{17}) = 0.4\%, \mathcal{R}^h(\mathbf{p}_{17}) = 0.7\%, \\ \mathbf{p}_{18} &= [65.1, 36.4, 1.007, 42.0, 80.0]^T \Rightarrow \mathcal{R}^*(\mathbf{p}_{18}) = 0.4\%, \mathcal{R}^h(\mathbf{p}_{18}) = 0.2\%. \end{aligned} \quad (4.65)$$

Parameter set \mathbf{p}_{17} yields values of the error functions \mathcal{R}^* and \mathcal{R}^h , signalling convergence of the PI by $|\mathcal{R}^h - \mathcal{R}^*| = 0.3\% < 0.5\%$ (see Figure 4.20(a)). Since the “measurement data”

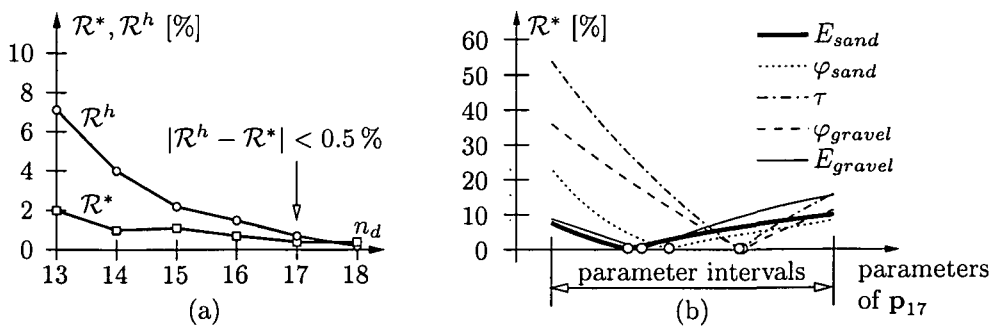


Figure 4.20: Results from back analysis: (a) evolutions of \mathcal{R}^* and \mathcal{R}^h obtained in the course of PI and (b) ANN-estimated sensitivities of parameters (the minima of the respective functions are indicated by circles)

were generated by means of a numerical analysis, PI should finally give the parameters employed in this analysis listed in Table 4.5. In fact, parameter set \mathbf{p}_{17} represents a satisfactory solution of the PI problem. Hence, the indicator based on the difference between \mathcal{R}^* and \mathcal{R}^h (criterion (4.23)) provided a good estimate of the quality of the obtained parameters.

Figure 4.20(b) illustrates the estimated sensitivity of the parameters contained in parameter set \mathbf{p}_{17} . The plotted curves represent sections through the error function \mathcal{R}^* . These sections contain the estimated minimum of the error function, which is marked by circles. For each section four parameters were kept constant and set equal to the values of parameter set \mathbf{p}_{17} , whereas the remaining parameter was varied over its entire interval (see (4.57)). The dash-dotted curve indicates that τ has the largest influence on \mathcal{R}^* . The remaining parameters of the bottom layer, i.e., E_{sand} and φ_{sand} , on the other hand, show the smallest influence on the error function \mathcal{R}^* .

4.4.5 Parameter identification based on inaccurate measurement data

In general, measurement data provided by the construction site are afflicted with inaccuracies. In order to assess the influence of these inaccuracies on the performance of the proposed PI method, the measurement data illustrated in Figures 4.18 and 4.19 are modified:

$$u_{c,r} \rightarrow u_{c,r} \cdot (1 + \delta), \quad c = 1, 2, \dots, n_m, \quad r = 1, 2, \dots, n_{o,c}, \quad (4.66)$$

where the value of δ is related to the inaccuracy of the measurement data. A negative value of δ , e. g., indicates that the surface settlements and displacements of the shotcrete tunnel shell reported by the construction site are too small.

Six different values of δ are chosen (see Table 4.6) to obtain six sets of inaccurate measurement data. For each of them, PI is performed independently as described in Section 4.4.4. These back analyses aim at determining parameter sets that yield numerical results which fit to the respective measurement data as well as possible. Consequently, $u_{c,r}$ needs to be replaced in Equ. (2.1) by $u_{c,r} \cdot (1 + \delta)$, resulting in the following condition for an optimal parameter set:

$$\mathcal{R}^h(\mathbf{p}, \delta) = \sqrt{\frac{1}{n_m} \sum_{c=1}^{n_m} \frac{1}{n_{o,c}} \sum_{r=1}^{n_{o,c}} \left(\frac{u_{c,r}^h(\mathbf{p}) - u_{c,r} \cdot (1 + \delta)}{\bar{u}_c \cdot (1 + \delta)} \right)^2} \rightarrow \min. \quad (4.67)$$

Table 4.6 contains the percentage difference between the optimal parameters obtained from these six PIs and the parameters listed in Table 4.5. In general, back analysis on the basis of inaccurate settlements and displacements of the tunnel shell, which are too small (triggered by $\delta < 0$), result in an increase of the values for the optimal parameter set. A positive value of δ , on the other hand, yields a decrease of the parameters. Notably, the percentage error of Young's modulus of both soil layers and of the relaxation time τ are closely related to the value of δ . The influence of δ on the angles of internal friction is significantly smaller.

Table 4.6: Influence of the value of δ on the parameter values obtained from PI

	δ	E_{sand}	φ_{sand}	τ	φ_{gravel}	E_{gravel}
PI1	-10.0 %	+10.3 %	+0.6 %	+9.2%	+0.4 %	+11.3%
PI2	-5.0 %	+4.7 %	+0.3 %	+5.4%	+0.1 %	+6.0%
PI3	-2.5 %	+2.2 %	-0.2 %	+2.8%	+0.2 %	+2.2%
PI4	+2.5 %	-2.1 %	-0.1 %	-2.2%	± 0.0 %	-2.4%
PI5	+5.0 %	-4.7 %	-0.4 %	-2.0%	-0.4 %	-5.0%
PI6	+10.0 %	-8.6 %	-0.9 %	-4.8%	-0.7 %	-9.3%

4.4.6 Predictions of displacements and of the level of loading of the shotcrete tunnel shell

Based on the parameters obtained from six PIs of the previous section, PI1 to PI6 (see Table 4.6), the structural behavior of the tunnel at a future MCS, i.e., of one that has not yet been installed, will be investigated in the following. The (changed) geological conditions and the (changed) location of the station tube at the future MCS are illustrated in Figure 4.21. Characteristic results obtained from the FE analyses performed on the

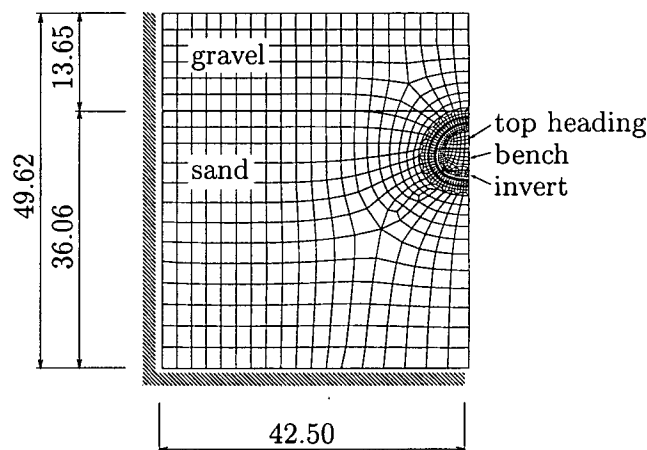


Figure 4.21: Future MCS of underground station "Taborstraße": geometrical dimensions (in [m]) of the numerical model and FE mesh consisting of 1071 finite elements

basis of the six parameter sets computed in Section 4.4.5 are listed in Table 4.7. These results are genuine predictions of the structural behavior at a future MCS.

In order to assess these predictions, an additional FE analysis on the basis of the material parameters given in Table 4.5 is performed. The respective characteristic results

Table 4.7: Prognoses of characteristic values describing the structural behavior at a future MCS (for the definition of \bar{L}_2 see (Beer, 2003))

material parameters obtained from ...	maximum values of ...		
	surface settlements	vertical displacement at top of the shotcrete shell	level of loading \bar{L}_2
PI1 ($\delta=-10\%$)	1.72 cm	1.67 cm	32.2%
PI2 ($\delta=-5\%$)	1.81 cm	1.68 cm	32.8%
PI3 ($\delta=-2.5\%$)	1.86 cm	1.70 cm	33.5%
PI4 ($\delta=+2.5\%$)	1.95 cm	1.72 cm	34.1%
PI5 ($\delta=+5\%$)	2.01 cm	1.73 cm	34.5%
PI6 ($\delta=+10\%$)	2.10 cm	1.75 cm	35.5%

are listed in Table 4.8.

Table 4.8: Characteristic values describing the structural behavior at a future MCS obtained from an FE analysis based on the material parameters listed in Table 4.5 (for the definition of \bar{L}_2 see (Beer, 2003))

maximum values of ...		
surface settlements	vertical displacement at top of the shotcrete shell	level of loading \bar{L}_2
1.91 cm	1.70 cm	33.7%

A comparison of the values listed in Tables 4.7 and 4.8 allows an assessment of the prognoses of the structural behavior at a future MCS. Deviations of surface settlements from the respective value given in Table 4.8 are closely related to the value of δ , whereas the influence of δ on the maximum displacement at the top of the tunnel shell is significantly smaller. The maximum level of loading of the shotcrete tunnel shell changes only slightly with δ . To summarize, the characteristic values of the structural behavior at a future MCS were well predicted, taking into account the considered range of measurement inaccuracies of $\pm 10\%$. This result indicates that the presented mode of PI can be expected to be useful for real-life applications even in case of inaccurate measurement data, such as frequently provided by the construction site.

4.5 Extension to first-order approximation neural networks

ANNs employed for the already presented mode of PI provided a map of FE input parameters onto respective FE results. However, the sensitivities of the FE results, i. e., the partial derivatives of the FE results with respect to the FE input parameters were not considered during training of the ANNs. Therefore, such ANNs can be referred to as *zero-order approximation artificial neural networks*, $\mathcal{O}_{(0)}$ -ANNs. In this subchapter an extension towards ANNs providing an approximation of both FE results and their sensitivities is presented. Respective ANNs are referred to as *first-order approximation artificial neural networks*, $\mathcal{O}_{(1)}$ -ANNs.

4.5.1 Outline of the extended parameter identification method

$\mathcal{O}_{(1)}$ -ANNs are trained in order to minimize both, the zero-order approximation error and of the first-order approximation error defined as

$$\mathcal{R}_{(0)}^{*-h} = \sqrt{\frac{1}{n_d} \sum_{d=1}^{n_d} \mathcal{R}_{(0),d}^{*-h}}, \quad \text{and} \quad \mathcal{R}_{(1)}^{*-h} = \sqrt{\frac{1}{n_d} \sum_{d=1}^{n_d} \mathcal{R}_{(1),d}^{*-h}}, \quad (4.68)$$

respectively. $\mathcal{R}_{(0),d}^{*-h}$ and $\mathcal{R}_{(1),d}^{*-h}$ denote the the squared zero-order approximation error and the squared first-order approximation error referring to the d -th data set. These two error functions are defined as

$$\mathcal{R}_{(0),d}^{*-h} = \frac{1}{n_o} \sum_{r=1}^{n_o} \left(\frac{u_r^*(\mathbf{p}_d) - u_r^h(\mathbf{p}_d)}{\bar{u}} \right)^2, \quad \bar{u} = \frac{1}{n_o} \sum_{r=1}^{n_o} |u_r|, \quad (4.69)$$

and

$$\mathcal{R}_{(1),d}^{*-h} = \frac{1}{n_i} \sum_{j=1}^{n_i} \left(\frac{\frac{\partial \mathcal{R}^*(\mathbf{p}_d)}{\partial p_j} - \frac{\partial \mathcal{R}^h(\mathbf{p}_d)}{\partial p_j}}{\text{mean}_{j,d} \left[\frac{\partial \mathcal{R}^h(\mathbf{p}_d)}{\partial p_j} \right]} \right)^2. \quad (4.70)$$

Eq. (4.70) contains derivatives of the error functions \mathcal{R}^h and \mathcal{R}^* with respect to FE input-parameters.⁴ Accordingly, $\mathcal{R}_{(1),d}^{*-h}$ represents a measure of the differences between the sensitivities of $\mathcal{R}^*(\mathbf{p}_d)$, provided by the ANN, and the sensitivities of $\mathcal{R}^h(\mathbf{p}_d)$, determined by

⁴ \mathcal{R}^h describes the difference between *in situ* measurements u_r and corresponding quantities obtained from a numerical analysis u_r^h . \mathcal{R}^* describes the difference between *in situ* measurements u_r and the corresponding output quantities of the ANN u_r^* . \mathcal{R}^h and \mathcal{R}^* were defined in Eqs. (2.1) and (4.1) as

$$\mathcal{R}^h(\mathbf{p}) = \sqrt{\frac{1}{n_o} \sum_{r=1}^{n_o} \left(\frac{u_r^h(\mathbf{p}) - u_r}{\bar{u}} \right)^2} \quad \text{and} \quad \mathcal{R}^*(\mathbf{p}) = \sqrt{\frac{1}{n_o} \sum_{r=1}^{n_o} \left(\frac{u_r^*(\mathbf{p}) - u_r}{\bar{u}} \right)^2}. \quad (4.71)$$

numerical analyses. The denominator of the expression in the parentheses of Eq. (4.70) represents the arithmetic mean value of the already computed sensitivities of $\mathcal{R}^h(\mathbf{p}_d)$:

$$\text{mean}_{j,d} \left[\frac{\partial \mathcal{R}^h(\mathbf{p}_d)}{\partial p_j} \right] = \frac{1}{n_d} \frac{1}{n_i} \sum_{d=1}^{n_d} \sum_{j=1}^{n_i} \left| \frac{\partial \mathcal{R}^h(\mathbf{p}_d)}{\partial p_j} \right|. \quad (4.72)$$

Evaluation of $\mathcal{R}_{(1),d}^{*-h}$ requires computation of the derivatives of \mathcal{R}^h and \mathcal{R}^* with respect to the input parameters p_j , $j = 1, 2, \dots, n_i$, as

$$\begin{aligned} \frac{\partial \mathcal{R}^h(\mathbf{p}_d)}{\partial p_j} &= \frac{\partial \mathcal{R}^h(\mathbf{p}_d)}{\partial u_r^h} \frac{\partial u_r^h}{\partial p_j} = \frac{1}{\mathcal{R}^h(\mathbf{p}_d)} \frac{1}{n_o} \sum_{r=1}^{n_o} \left(\frac{u_r^h(\mathbf{p}_d) - u_r}{\bar{u}^2} \right) \frac{\partial u_r^h(\mathbf{p}_d)}{\partial p_j}, \\ \frac{\partial \mathcal{R}^*(\mathbf{p}_d)}{\partial p_j} &= \frac{\partial \mathcal{R}^*(\mathbf{p}_d)}{\partial u_r^*} \frac{\partial u_r^*}{\partial p_j} = \frac{1}{\mathcal{R}^*(\mathbf{p}_d)} \frac{1}{n_o} \sum_{r=1}^{n_o} \left(\frac{u_r^*(\mathbf{p}_d) - u_r}{\bar{u}^2} \right) \frac{\partial u_r^*(\mathbf{p}_d)}{\partial p_j}. \end{aligned} \quad (4.73)$$

$\partial u_r^h(\mathbf{p}_d)/\partial p_j$ and $\partial u_r^*(\mathbf{p}_d)/\partial p_j$ denote the partial derivatives of FE results and ANN output values with respect to the input parameters. In order to avoid major modifications of the employed FE code, $\partial u_r^h(\mathbf{p}_d)/\partial p_j$ are approximated by finite difference expressions

$$\frac{\partial u_r^h(\mathbf{p}_d)}{\partial p_j} \approx \frac{\Delta u_r^h(\mathbf{p}_d)}{\Delta p_j}, \quad j = 1, 2, \dots, n_i. \quad (4.74)$$

Accordingly, approximation of the sensitivities $\partial u_r^h(\mathbf{p}_d)/\partial p_j$ requires n_i additional FE simulations. The sensitivities of ANN outputs, $\partial u_r^*(\mathbf{p}_d)/\partial p_j$, are computed with the backpropagation algorithm

$$\frac{\partial u_r^*(\mathbf{p}_d)}{\partial p_j} = \frac{\partial u_r^*(\mathbf{p}_d)}{\partial \tilde{u}_r^*} \frac{\partial s(\sigma_r^o)}{\partial \sigma_r^o} \sum_{k=1}^{n_h} \left(w_{kr}^{ho} \frac{\partial s(\sigma_k^h)}{\partial \sigma_k^h} w_{jk}^{ih} \right) \frac{\partial \tilde{p}_j}{\partial p_j}. \quad (4.75)$$

Training of $\mathcal{O}_{(1)}$ -ANNs aims at

$$\mathcal{R}_{(0)}^{*-h} + \mathcal{R}_{(1)}^{*-h} \rightarrow 0 \quad (4.76)$$

by iterative adaption of the network weights. Analogously to the already presented mode of PI, a gradient descent method in weight space is performed. Hence, network weight corrections are defined as

$$\Delta w_{jk}^{ih} = \Delta w_{jk}^{ih} \left(\frac{\partial [\mathcal{R}_{(0)}^{*-h} + \mathcal{R}_{(1)}^{*-h}]}{\partial w_{jk}^{ih}} \right), \quad \Delta w_{kr}^{ho} = \Delta w_{kr}^{ho} \left(\frac{\partial [\mathcal{R}_{(0)}^{*-h} + \mathcal{R}_{(1)}^{*-h}]}{\partial w_{kr}^{ho}} \right). \quad (4.77)$$

The calculation scheme for computation of the derivatives appearing in Eqs. (4.77) are summarized in Appendix B. Training of the $\mathcal{O}_{(1)}$ -ANN will be terminated, if all $\mathcal{O}_{(1)}$ -ANN output values and their sensitivities meet the respective desired values with prespecified

accuracy. Hence, for termination of $\mathcal{O}_{(1)}$ -ANN training the following two conditions must be satisfied:

$$\mathcal{E}_{r,d(0)}^{*h} = \left| \frac{u_r^*(\mathbf{P}d) - u_r^h}{\bar{u}} \right| \leq \bar{\mathcal{E}}_{(0)}^{*h} \quad \forall r, d, \quad \mathcal{E}_{r,j(1)}^{*h} = \left| \frac{\frac{\partial \mathcal{R}^*}{\partial p_j} - \frac{\partial \mathcal{R}^h}{\partial p_j}}{\text{mean}_{j,d} \left(\frac{\partial \mathcal{R}^h}{\partial p_j} \right)} \right| \leq \bar{\mathcal{E}}_{(1)}^{*h} \quad \forall r, j, \quad (4.78)$$

where $\bar{\mathcal{E}}_{(0)}^{*h}$ and $\bar{\mathcal{E}}_{(1)}^{*h}$ denote two prespecified threshold values.

4.5.2 Application to ground improvement by means of jet grouting

The PI problem described in Subchapter 4.3 is revisited. In the following, the PI problem is solved again based on both $\mathcal{O}_{(0)}$ -ANNs and $\mathcal{O}_{(1)}$ -ANNs. The respective PI algorithms are referred to as $\mathcal{O}_{(0)}$ -PI and $\mathcal{O}_{(1)}$ -PI. The results of these two independently performed PIs will be assessed taking into account the approximation of \mathcal{R}^h provided by the two ANNs.

The search intervals for the values of the unknown parameters R and z are chosen as

$$\begin{aligned} R &\in [0.2 \text{ m}, 2.0 \text{ m}] , \\ z &\in [2 \% , 16.7 \%] . \end{aligned} \quad (4.79)$$

In order to obtain deep insight into the PI problem, $51 \times 51 = 2601$ thermochemical FE analyses were performed, resting on different input parameter combinations taken from the intervals (4.79). The differences between the obtained temperature histories and the selected measurements u_r ($r = 1, 2, \dots, 21$) are quantified by means of \mathcal{R}^h . In general, such a comprehensive numerical study is unfeasible. In the present case of only two unknown parameters and a rather small FE model, the computational efforts associated with 2601 FE analyses was acceptable. The obtained 2601 values of the error function \mathcal{R}^h permit to illustrate isolines of \mathcal{R}^h as a function of the radius R and the cement content z , see Figure 4.22 (a).

Both PI algorithms aim at determination of the parameter set $R = 89 \text{ cm}$, $z = 4.3 \%$ which is associated with $\mathcal{R}^h = 1.9 \%$, located at the bottom of banana-like shaped valley of the error function \mathcal{R}^h , see Figure 4.22 (a). This insight in the shape of \mathcal{R}^h as a function of R and z will be used to assess the two PI algorithms. However, this *a priori* knowledge is *not* available for the two PI algorithms.

Both algorithms are started after having performed four FE analyses in advance. These

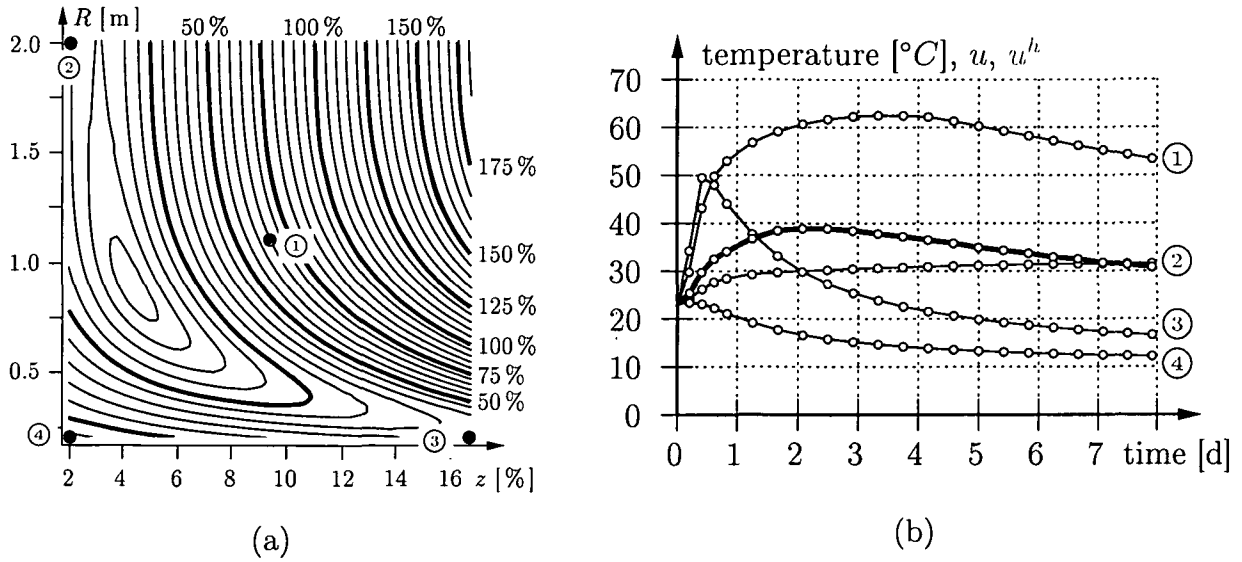


Figure 4.22: (a) Isolines of \mathcal{R}^h over the entire parameter space corresponding to the intervals given in (4.79), and (b) temperature histories obtained from the FE analyses performed in advance (blue) and in-situ measurements (red)

FE simulations are based on the input parameters

$$\begin{aligned}
 \mathbf{p}_1 &= [0.20, 0.020]^T \Rightarrow \mathcal{R}^h(\mathbf{p}_1) = 55.2\%, \\
 \mathbf{p}_2 &= [0.20, 0.167]^T \Rightarrow \mathcal{R}^h(\mathbf{p}_2) = 40.3\%, \\
 \mathbf{p}_3 &= [2.00, 0.020]^T \Rightarrow \mathcal{R}^h(\mathbf{p}_3) = 14.5\%, \\
 \mathbf{p}_4 &= [1.10, 0.094]^T \Rightarrow \mathcal{R}^h(\mathbf{p}_4) = 64.2\%.
 \end{aligned}
 \tag{4.80}$$

Since none of these parameter sets is optimal, the obtained values of the error functions \mathcal{R}^h are rather large. The obtained temperature histories do not meet the measurements, see Figure 4.22 (b). The four numerical analyses performed in advance suffice to start the $\mathcal{O}_{(0)}$ -PI. However, in order to start the $\mathcal{O}_{(1)}$ -PI, eight additional FE analyses must be performed. They are required to compute the sensitivities of \mathcal{R}^h with respect to the radius R and the cement content z of the jet-grouted soil column. These additional FE analyses are resting on the input parameters

$$\begin{aligned}
 R_{1,1} &= 0.2 \text{ m} + \Delta R, & z_{1,1} &= 0.020, \\
 R_{1,2} &= 0.2 \text{ m}, & z_{1,2} &= 0.020 + \Delta z,
 \end{aligned}
 \tag{4.81}$$

$$\begin{aligned}
 R_{2,1} &= 0.2 \text{ m} + \Delta R, & z_{2,1} &= 0.167, \\
 R_{2,2} &= 0.2 \text{ m}, & z_{2,2} &= 0.167 + \Delta z,
 \end{aligned}
 \tag{4.82}$$

$$R_{3,1} = 2.0 \text{ m} + \Delta R, \quad z_{3,1} = 0.020,$$

$$R_{3,2} = 2.0 \text{ m}, \quad z_{3,2} = 0.020 + \Delta z, \quad (4.83)$$

$$\begin{aligned} R_{4,1} &= 1.1 \text{ m} + \Delta R, & z_{4,1} &= 0.094, \\ R_{4,2} &= 1.1 \text{ m}, & z_{4,2} &= 0.094 + \Delta z, \end{aligned} \quad (4.84)$$

Thereby, $\Delta R = (2.0 - 0.2)/100 = 0.018 \text{ m}$ and $\Delta z = (0.167 - 0.020)/100 = 0.00147$, i. e., changes in the parameters were set equal to one-hundredth of the width of the parameter search intervals. Based on the results from the four FE simulations performed in advance and the additional eight FE analyses, the sensitivities of \mathcal{R}^h are evaluated, i. e., $\partial\mathcal{R}^h/\partial R$ and $\partial\mathcal{R}^h/\partial z$ are computed at $\mathbf{p} = \mathbf{p}_1$, $\mathbf{p} = \mathbf{p}_2$, $\mathbf{p} = \mathbf{p}_3$, and $\mathbf{p} = \mathbf{p}_4$. They serve as input for the $\mathcal{O}_{(1)}$ -PI.

For the $\mathcal{O}_{(0)}$ -PI, the threshold value $\bar{\mathcal{E}}^{*h}$ for the criterion controlling termination of ANN training, see (4.12), is set equal to 1%. Both respective threshold values of the $\mathcal{O}_{(1)}$ -PI, i. e., $\bar{\mathcal{E}}_{(0)}^{*h}$ and $\bar{\mathcal{E}}_{(1)}^{*h}$ which were introduced in (4.78), are set equal to 2.5%. All three threshold values are kept constant throughout both PIs.

Results from the first PI iteration steps

At the end of the first iteration step, both trained ANNs provide an error function \mathcal{R}^* . They represent approximations of \mathcal{R}^h . \mathcal{R}^* referring to the $\mathcal{O}_{(0)}$ -ANN almost coincides with \mathcal{R}^h at four points in the parameter space, see green circles in Figure 4.23 (a). These points correspond to the parameter sets listed in (4.80). In the case of the $\mathcal{O}_{(1)}$ -ANN, both the values of \mathcal{R}^* and the sensitivities $\partial\mathcal{R}^*/\partial R$ and $\partial\mathcal{R}^*/\partial z$ almost coincide with \mathcal{R}^h , $\partial\mathcal{R}^h/\partial R$, and $\partial\mathcal{R}^h/\partial z$ at these four points in the parameter space, see green circles in Figure 4.23 (b). Hence, the tangential planes of \mathcal{R}^* and \mathcal{R}^h are almost the same at these four points. After termination of ANN training, both a genetic algorithm and a GDM search in the entire parameter space $R \in [0.2 \text{ m}, 2.0 \text{ m}]$ and $z \in [2\%, 16.7\%]$ for the parameter set corresponding to the absolute minimas of both error surfaces \mathcal{R}^* . These parameter sets represent prognoses for the optimal parameter set, see the red squares in Figures 4.23 (a) and (b). In order to assess these estimates, FE analyses based on the estimated parameter sets are performed. Resting on the results of these analyses, values of \mathcal{R}^h are computed. The two first iteration steps can be summarized as:

$$\begin{aligned} \mathcal{O}_{(0)}\text{-ANN} : \mathbf{p}_5 &= [0.42, 0.034]^T \Rightarrow \mathcal{R}^*(\mathbf{p}_5) = 2.5\%, \quad \mathcal{R}^h(\mathbf{p}_5) = 35.5\%, \\ \mathcal{O}_{(1)}\text{-ANN} : \mathbf{p}_5 &= [2.00, 0.034]^T \Rightarrow \mathcal{R}^*(\mathbf{p}_5) = 5.6\%, \quad \mathcal{R}^h(\mathbf{p}_5) = 10.5\%, \end{aligned} \quad (4.85)$$

$|\mathcal{R}^h - \mathcal{R}^*|$ is equal to 33.0% in the $\mathcal{O}_{(0)}$ -PI and equal to 4.9% in the $\mathcal{O}_{(1)}$ -PI. This indicates that the approximation of \mathcal{R}^h by \mathcal{R}^* provided by both the $\mathcal{O}_{(0)}$ -ANN and the $\mathcal{O}_{(1)}$ -ANN is not satisfactory but rather poor. Accordingly, the $\mathcal{O}_{(0)}$ -PI and $\mathcal{O}_{(1)}$ -PI cannot be viewed

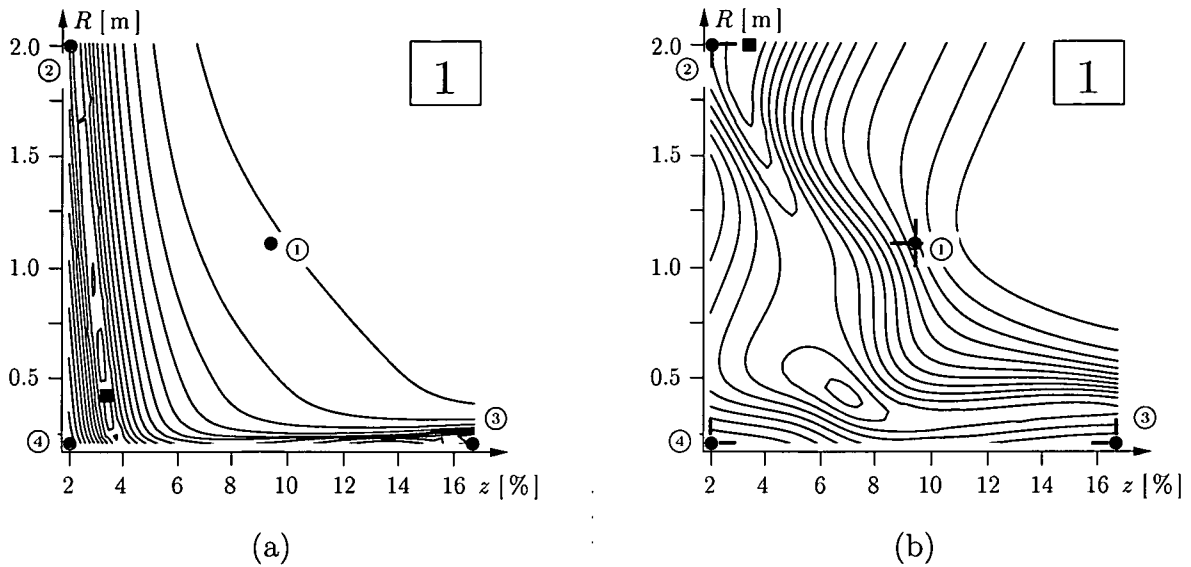


Figure 4.23: Isolines of \mathcal{R}^* representing approximations of the actual error function \mathcal{R}^h (see Figure 4.22 (a)) obtained at the end of the first PI iteration step resting on a (a) $\mathcal{O}_{(0)}$ -ANN and (b) $\mathcal{O}_{(1)}$ -ANN

as having converged. Both PI algorithms must be continued. However, $33.0\% > 4.9\%$ indicates the $\mathcal{O}_{(1)}$ -ANN provides an approximation of \mathcal{R}^h which is not as worse as it is the case for the $\mathcal{O}_{(0)}$ -ANN.

The following three conclusions were drawn without knowledge of the actual shape of the error function \mathcal{R}^h :

- both approximations of \mathcal{R}^h by \mathcal{R}^* are rather poor,
- however, the approximation of \mathcal{R}^h by \mathcal{R}^* resting on the $\mathcal{O}_{(1)}$ -ANN is not as worse as is the case for the $\mathcal{O}_{(0)}$ -ANN, and
- both PI algorithms cannot be viewed as having converged.

Now, this knowledge is used *a posteriori* to assess these conclusions. Comparing the isolines of \mathcal{R}^* illustrated in Figures 4.23 (a) and (b) with the isolines of \mathcal{R}^h , see Figure 4.22 (a), these conclusions are confirmed.

Results from the second PI iteration steps

The FE analyses performed to assess the first estimates of the optimal parameter set increased the number of known data sets by one. Hence, the next $\mathcal{O}_{(0)}$ -ANN is trained based on five given data sets. In order to train the $\mathcal{O}_{(1)}$ -ANN, two additional FE simulations must

be performed. The aim of these two additional analyses is to compute an approximation of the sensitivities of \mathcal{R}^h with respect to R and z at $\mathbf{p} = \mathbf{p}_5 = [2.00, 0.034]^T$.

After training of the $\mathcal{O}_{(0)}$ -ANN the provided error surface \mathcal{R}^* almost coincides with \mathcal{R}^h at five points, see the green dots in Figure 4.24 (a). The values of the error function \mathcal{R}^* and

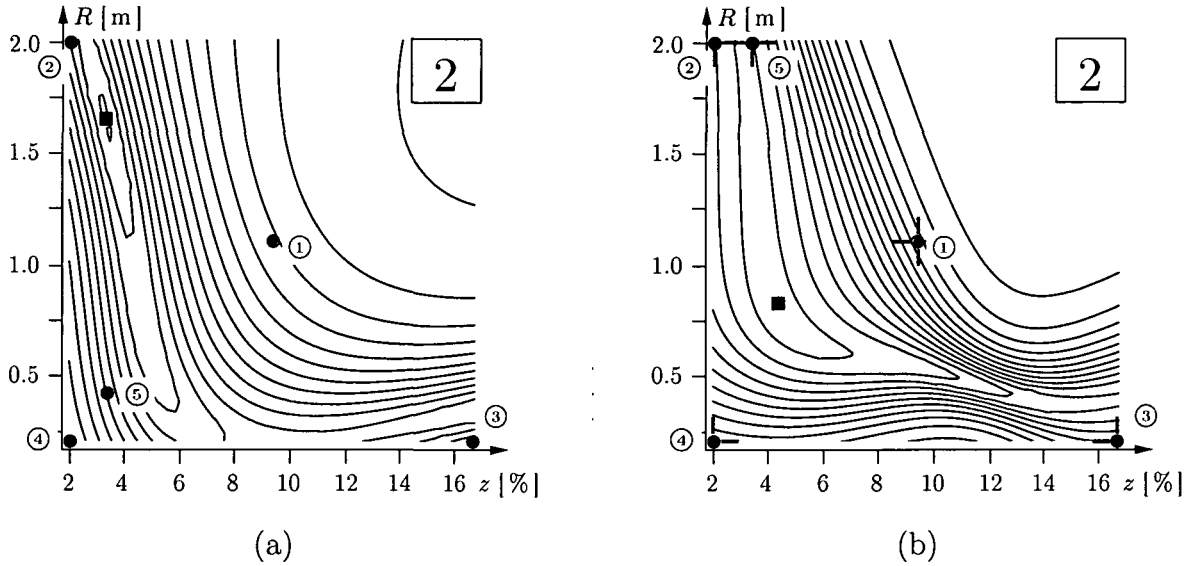


Figure 4.24: Isolines of \mathcal{R}^* representing approximations of the actual error function \mathcal{R}^h (see Figure 4.22 (a)) obtained at the end of the second PI iteration step resting on a (a) $\mathcal{O}_{(0)}$ -ANN and (b) $\mathcal{O}_{(1)}$ -ANN

its derivatives with respect to R and z provided by the trained $\mathcal{O}_{(1)}$ -ANN almost coincide with the corresponding values of \mathcal{R}^h at five points, see the green dots in Figure 4.24 (b). Again, a genetic algorithm and a GDM yield the two parameter sets associated with the global minima of the two error surfaces \mathcal{R}^* , see the red squares in Figures 4.24 (a) and (b). In order to assess these estimates, FE analyses based on the estimated parameter sets are performed. Resting on the results of these analyses, values of \mathcal{R}^h are computed. The two second iteration steps can be summarized as:

$$\begin{aligned}
 \mathcal{O}_{(0)}\text{-ANN} : \mathbf{p}_6 &= [1.66, 0.033]^T \Rightarrow \mathcal{R}^*(\mathbf{p}_6) = 4.4\%, \quad \mathcal{R}^h(\mathbf{p}_5) = 9.4\%, \\
 \mathcal{O}_{(1)}\text{-ANN} : \mathbf{p}_6 &= [0.83, 0.043]^T \Rightarrow \mathcal{R}^*(\mathbf{p}_6) = 8.0\%, \quad \mathcal{R}^h(\mathbf{p}_5) = 3.3\%,
 \end{aligned}
 \tag{4.86}$$

$|\mathcal{R}^h - \mathcal{R}^*|$ is equal to 5.0% in the $\mathcal{O}_{(0)}$ -PI and equal to 4.7% in the $\mathcal{O}_{(1)}$ -PI. This indicates that the approximation of \mathcal{R}^h by \mathcal{R}^* provided by both the $\mathcal{O}_{(0)}$ -ANN and the $\mathcal{O}_{(1)}$ -ANN are better than in the previous iteration step. However, the results are still not satisfactory. Accordingly, the $\mathcal{O}_{(0)}$ -PI and $\mathcal{O}_{(1)}$ -PI cannot be viewed as having converged. Both PI algorithms must be continued. 5.0% > 4.7% again indicates the $\mathcal{O}_{(1)}$ -ANN provides an approximation of \mathcal{R}^h which is not as worse as is the case for the $\mathcal{O}_{(0)}$ -ANN.

The following conclusions were drawn without knowledge of the actual shape of the error function \mathcal{R}^h :

- both approximations of \mathcal{R}^h by \mathcal{R}^* are better than the ones in the previous iteration step,
- the approximation of \mathcal{R}^h by \mathcal{R}^* resting on the $\mathcal{O}_{(1)}$ -ANN is again better as is the case for the $\mathcal{O}_{(0)}$ -ANN,
- however, both approximations do not represent a satisfactory result, and
- hence, both PI algorithms cannot be viewed as having converged.

Now, this knowledge is used *a posteriori* to assess these conclusions. Comparing the isolines of \mathcal{R}^* illustrated in Figures 4.24 (a) and (b) with the isolines of \mathcal{R}^h , see Figure 4.22 (a), these conclusions are again confirmed.

Results from the last PI iteration steps

The FE analyses performed to assess the second estimates of the optimal parameter set increased the number of known data sets by one. Hence, the next $\mathcal{O}_{(0)}$ -ANN is trained based on six given data sets. In order to train the $\mathcal{O}_{(1)}$ -ANN, two additional FE simulations must be performed. The aim of these two additional analyses is to compute an approximation of the sensitivities of \mathcal{R}^h with respect to R and z at $\mathbf{p} = \mathbf{p}_6 = [0.83, 0.043]^T$.

Results of the iteration steps three and four of the $\mathcal{O}_{(0)}$ -PI lead to conclusions similar to those drawn from iteration step two. Therefore, they are not discussed herein. Instead, results from iteration step five of the $\mathcal{O}_{(0)}$ -PI and iteration step three of the $\mathcal{O}_{(1)}$ -PI are presented. After training of the $\mathcal{O}_{(0)}$ -ANN, the provided error surface \mathcal{R}^* almost coincides with \mathcal{R}^h at eight points, see green dots in Figure 4.25 (a). These eight points refer to the four FE analyses performed in advance (① to ④) and four FE simulations carried out to assess the quality of estimates from the previous four PI iteration steps (⑤ to ⑧). The error surface \mathcal{R}^* and its derivatives with respect to R and z provided by the trained $\mathcal{O}_{(1)}$ -ANN almost coincide with the corresponding values of \mathcal{R}^h at six points, see the green dots in Figure 4.25 (b).

A genetic algorithm and a GDM yield the two parameter sets associated with the global minima of the two error surfaces \mathcal{R}^* , see the red squares in Figures 4.25 (a) and (b). In order to assess these estimates, FE analyses based on the estimated parameter sets are performed. Resting on the results of these analyses, values of \mathcal{R}^h are computed. The two

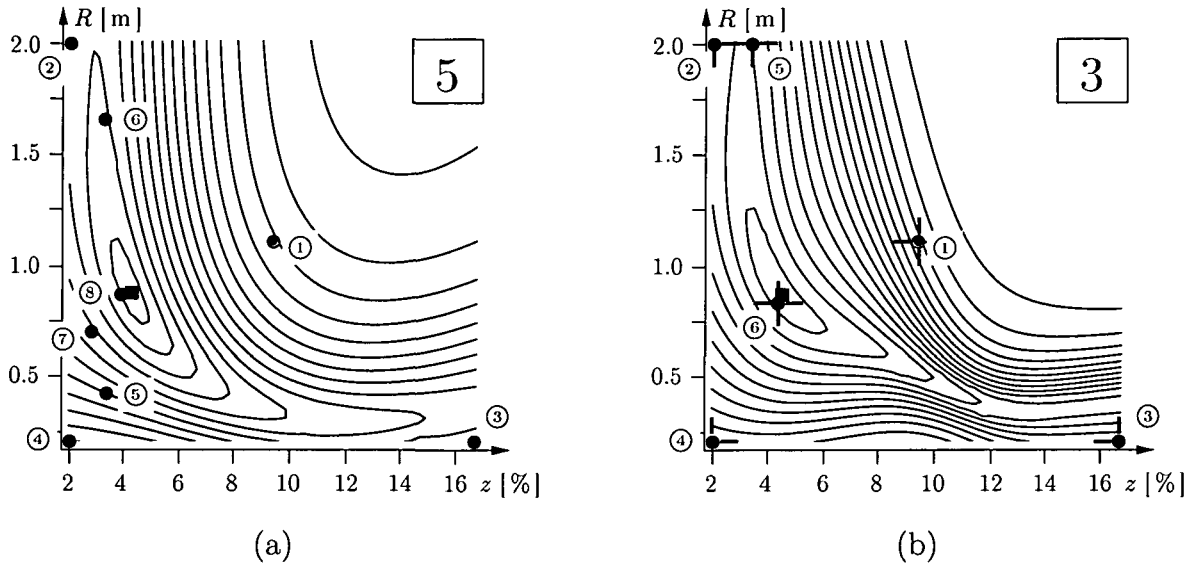


Figure 4.25: Isolines of \mathcal{R}^* representing approximations of the actual error function \mathcal{R}^h (see Figure 4.22 (a)) obtained (a) at the end of the fifth PI iteration step resting on a $\mathcal{O}_{(0)}$ -ANN and (b) at the end of the third PI iteration step resting on a $\mathcal{O}_{(1)}$ -ANN

mentioned iteration steps can be summarized as:

$$\begin{aligned}
 \mathcal{O}_{(0)}\text{-ANN} : \mathbf{p}_9 &= [0.88, 0.042]^T \Rightarrow \mathcal{R}^*(\mathbf{p}_9) = 2.2\%, \quad \mathcal{R}^h(\mathbf{p}_5) = 2.2\%, \\
 \mathcal{O}_{(1)}\text{-ANN} : \mathbf{p}_6 &= [0.87, 0.044]^T \Rightarrow \mathcal{R}^*(\mathbf{p}_6) = 1.8\%, \quad \mathcal{R}^h(\mathbf{p}_5) = 1.9\%,
 \end{aligned}
 \tag{4.87}$$

Hence, $|\mathcal{R}^h - \mathcal{R}^*| \leq 0.1\%$ holds in both cases. This results indicates that the approximations of \mathcal{R}^h by \mathcal{R}^* are of good quality at least in the domain of interest, i. e., in the vicinity of the solution of the PI. Thus, the parameter sets obtained are good estimates for the optimal parameter set. Both PI algorithms can be viewed as having converged.

Again, the following conclusions were drawn without knowledge of the actual shape of the error function \mathcal{R}^h :

- both approximations of \mathcal{R}^h by \mathcal{R}^* are rather good at least in the vicinity of the solution of the PI, and
- both PI algorithms can be viewed as having converged

Now, this knowledge is used *a posteriori* to assess these conclusions. Comparing the isolines of \mathcal{R}^* illustrated in Figures 4.25 (a) and (b) with the isolines of \mathcal{R}^h , see Figure 4.22 (a), these conclusions are again confirmed.

Comparison of the obtained results

If $\mathcal{O}_{(0)}$ -PI and $\mathcal{O}_{(1)}$ -PI were assessed on the basis of the number of required iteration steps, the algorithm involving the $\mathcal{O}_{(1)}$ -ANN would turn out to be the better one. Based on $\mathcal{O}_{(1)}$ -ANNs, it took only three PI iteration steps to obtain a parameter set in the immediate vicinity of the true solution, whereas it took five PI iteration steps to obtain a comparable results based on $\mathcal{O}_{(0)}$ -ANNs. However, from the point of view of required FE analyses, the assessment of the two PIs is different. The $\mathcal{O}_{(0)}$ -PI, on the one hand, was started after having performed four FE analyses in advance. In the course of the $\mathcal{O}_{(0)}$ -PI another five FE analyses were carried out in order to assess the estimates of optimal parameters. Hence, in total, nine FE simulations were required to solve the PI problem resting on $\mathcal{O}_{(0)}$ -ANNs. The $\mathcal{O}_{(1)}$ -PI, on the other hand, was started after having performed twelve FE analyses in advance. They include four analyses performed to determine values of the error function \mathcal{R}^h , and another eight simulations required to compute the sensitivities of \mathcal{R}^h with respect to R and z . In order to obtain the solution of the PI, another seven FE analyses were carried out. Hence, in total, 19 FE simulations were required to solve the PI problem resting on $\mathcal{O}_{(1)}$ -ANNs. The $\mathcal{O}_{(1)}$ -PI required more than twice as many FE analyses as compared to the $\mathcal{O}_{(0)}$ -PI.

It follows from these assessments that a PI algorithm involving $\mathcal{O}_{(1)}$ -ANNs can further reduce the number of iteration steps required to solve a PI problem. However, the respective number of FE analyses is significantly larger as compared to a PI algorithm involving $\mathcal{O}_{(0)}$ -ANNs. Moreover, the computation time required for training of a $\mathcal{O}_{(1)}$ -ANN is significantly larger as compared to a $\mathcal{O}_{(0)}$ -ANN. Therefore, in the investigated PI problem $\mathcal{O}_{(1)}$ -PI could not outperform $\mathcal{O}_{(0)}$ -PI.

4.6 Conclusions

An iterative parameter identification (PI) method resting on soft computing was proposed. Artificial neural networks (ANNs) were used to approximate the underlying finite element (FE) analysis of the problem under consideration. They were trained to map input parameters for FE analyses onto respective numerical results. Based on the trained ANN, a GA was used for determination of an estimate of optimal parameters. Moreover, the trained ANN provides an approximation of the sensitivity of the unknown parameters. Hence, sensitivity analyses are no longer required to check the quality of an obtained solution. The proposed algorithm combines advantages of gradient-free and gradient-based PI methods, i.e., the entire parameter space is searched for an optimal solution and only few FE analyses are required to find optimal parameters. The latter is essential for PI in

geotechnical problems which, in general, are characterized by large-scale FE models.

The proposed PI method was applied to two problems taken from geotechnical engineering. Based on the obtained results, the following conclusions can be drawn:

- Based on temperature measurements at the center of jet-grouted columns, the proposed PI method was used to determine the column radius and the cement content of the improved soil. A thermochemical FE analysis, which was used to simulate the hydration process in the jet-grouted column, was approximated by an ANN. Ten FE analyses were required in the course of PI. The identified column radius was assessed by excavating the investigated test column. Good agreement between the identified radius and the radius measured at the construction site was obtained.
- In the second application, the proposed PI method was employed for determination of unknown material parameters in tunneling. The ANN was trained to approximate the results from the FE analysis used for the simulation of the excavation of the tunnel. Based on available measurements of the displacements of the tunnel lining and of surface settlements, the unknown parameters were identified. 15 FE analyses were required to solve the PI problem. So far, only a 2D model was employed in the course of back analysis in tunneling. The tunnel excavation process, however, is a three-dimensional problem. Future work will be directed to extend the proposed 2D model to three dimensions. In fact, the presented approach for PI is essential to render PI feasible for large-scale 3D models.

The developed mode of PI, which involves so-called zero-order approximation neural networks, $\mathcal{O}_{(0)}$ -ANNs, was extended to a mode of PI involving first-order approximation neural networks, $\mathcal{O}_{(1)}$ -ANNs. They are trained (i) to map input parameters for FE analyses onto respective numerical results, and (ii) to reproduce the sensitivities of the FE results with respect to the input parameters. These sensitivities were approximated by finite difference expressions, computed on the basis of additional FE analyses. It was shown that a PI algorithm involving $\mathcal{O}_{(1)}$ -ANNs can further reduce the number of iteration steps required to solve a PI problem. However, the respective number of FE analyses is significantly larger as compared to a PI algorithm involving $\mathcal{O}_{(0)}$ -ANNs. Moreover, computation time required for training of a $\mathcal{O}_{(1)}$ -ANN is significantly larger as compared to the duration of $\mathcal{O}_{(0)}$ -ANN training. Therefore, in the investigated PI problem $\mathcal{O}_{(1)}$ -PI could not outperform $\mathcal{O}_{(0)}$ -PI.

Chapter 5

Loading of a gravel-buried steel pipe subjected to rockfall

In this chapter, parameter identification from well-designed or chosen material tests is addressed. It is emphasized that identification of material parameters and verification of structural models should be strictly separated in order to allow for reliable prognoses of non-tested situations.

As an example, the development of an analysis tool for the prediction of the loading of a gravel-buried steel pipeline subjected to rockfall is described. The reliability test is based on two physically and statistically independent sets of experiments, the first being related to material model developments (see Subchapter 5.2) and the second to structural model verification (see Subchapter 5.4). Experimental set ① follows either from the design, performance, and evaluation of a testing series of the elasticity of gravel, or from the wealth of data on (triaxial) gravel strength and steel material properties documented in the open literature. For verification of a structural Finite Element (FE) model of the buried steel pipe, an experiment on a real-scale gravel-buried steel pipe was designed, performed, and evaluated. The obtained data are collected into experimental set ②. Simulation results obtained from a structural model based on the material parameters identified from experimental set ① compare very well to the results of measurements from experimental set ②. Thus, the developed model is well suited to provide insight into the structural behavior of the gravel-buried steel pipe, also for rockfall events with different boulder masses and different heights of fall, and/or for different overburdens, or for different materials surrounding the gravel-filled trench (e. g. granite, soft soil).

Gravel is able to serve as an energy-absorbing and load-distributing protection system

for steel pipes subjected to moderate rockfall scenarios. However, for heavy rock boulders (such as investigated herein, e.g. $m = 18260$ kg) and heights of fall up to 100 m or even more, the task of gravel should be restricted to energy absorption, and additional construction elements should be buried in order to distribute and carry impact loads.

5.1 Introduction

The rapid climate change in recent years leads to thawing of former permafrost regions in Alpine regions in general and in the Austrian Alps in particular. One consequence of this evolution is an increased rockfall activity. This motivates closer study of protection systems for transalpine infrastructure such as roads, railways, and pipelines.

Herein, the last type of aforementioned infrastructure is considered. The development of an analysis tool that permits reliable predictions of the loading of a gravel-buried steel pipeline subjected to rockfall is described. The reliability test is based on two physically and statistically independent sets of experiments, the first being related to material model developments (see Subchapter 5.2) and the second to structural model verification (see Subchapter 5.4).

Experimental set ① is used for the identification of material parameters for steel and gravel, i. e., of physical quantities attached to a “representative volume element” with a characteristic length scale of one to several decimeters for gravel, and of less than one millimeter for steel. This identification is possible because the related experiments are characterized by homogeneous conditions, i. e., by the absence of spatial gradients of material parameters and loading conditions in the aforementioned length scales. Thus, the identified parameters are independent of structure-specific boundary conditions: they are valid for virtually all structures made of the investigated types of steel and gravel.

The identified material parameters are then used to simulate the structural behavior of gravel-buried steel pipes with special emphasis of the loading of such structures arising from the impact of downfalling rock boulders. For verification of these simulations, an experiment on a real-scale gravel-buried steel pipe was designed, performed, and evaluated. The obtained data are collected into experimental set ②. Simulation results obtained from a structural model based on the material parameters identified from experimental set ① are compared to the results of measurements from experimental set ②. In this way, experimental set ② allows for validation (i) whether the sophistication of the material description based on the experimental set ① is sufficient for the assessment of the loading of a gravel-buried steel pipe subjected to rockfall, and (ii) to which extent the class of structures “gravel-buried steel pipes” has to be modeled by means of 3D nonlinear Finite

Elements.

In case of a positive validation, the structural model can be used to reliably predict the influence of the impact force and the burying height on the loading of the steel pipe. This is an important contribution to the estimation of the safety of this type of infrastructure.

5.2 Theoretical and experimental material characterization

This subchapter deals with the material characterization of steel and gravel. Resting on performed experiments as well as on test data taken from the open literature, the involved material parameters are identified. They correspond to the elasto-plastic properties of steel and to the elastic properties, shear failure, and the compactional behavior of gravel. The scattering of the material parameters is especially addressed.

5.2.1 Elasto-plastic material behavior of steel

Steel is a homogeneous and isotropic recipe material. Marketable types of steel are produced under well defined conditions. Therefore, scattering of the material properties of steel is well controlled and, as compared to gravel, insignificant.

Herein, steel is characterized by small-strain von Mises elasto-plasticity, see (Lubliner, 1990; Simo and Taylor, 1985) and references therein. In this framework, the description of steel requires knowledge of three material parameters: Young's modulus E , Poisson's ratio ν , and the uniaxial yield strength σ_y . These material parameters are taken from the inspection certificate referring to the pipe-steel under investigation (EUROPIPE, 1993):

$$E = 210 \text{ GPa}, \quad \nu = 0.3, \quad \sigma_y = 514 \text{ MPa}. \quad (5.1)$$

5.2.2 Elasto-plastic material behavior of gravel

Wide-range grained gravel is commonly used to bury pipelines. Such a material shows a rather complex behavior: (i) It is not able to carry tensile loads, (ii) a linear elastic behavior can be observed only under moderate loading conditions and in the case of unloading, (iii) it shows shear failure under distinctive deviatoric loading, and (iv) it is characterized by a hardening behavior associated with compaction under predominantly volumetric loading.

The elasto-plastic cap model (DiMaggio and Sandler, 1971; Sandler and Rubin, 1979; Hofstetter et al., 1993) suitably represents the material behavior of gravel, whereby the elastic domain follows the isotropic linear generalized Hooke's law (Mang and Hofstetter,

2000):

$$\boldsymbol{\sigma} = \mathbf{C} : (\boldsymbol{\varepsilon} - \boldsymbol{\varepsilon}^P), \quad (5.2)$$

where $\boldsymbol{\sigma}$ denotes the Cauchy stress tensor, and $\boldsymbol{\varepsilon}$ and $\boldsymbol{\varepsilon}^P$ stand for the linear strain tensor and the plastic strain tensor, respectively. \mathbf{C} represents the isotropic elasticity tensor which can be expressed as a function of the bulk modulus K and the shear modulus G reading

$$\mathbf{C} = K \mathbb{I} \otimes \mathbb{I} + 2G \left(\mathbb{II} - \frac{1}{3} \mathbb{I} \otimes \mathbb{I} \right) \quad (5.3)$$

where \mathbb{I} and \mathbb{II} denote the 2nd-order unity tensor and the 4th-order unity tensor, respectively. The latter is defined as

$$\mathbb{II}_{ijkl} = \frac{1}{2} (\delta_{ik} \delta_{jl} + \delta_{il} \delta_{jk}), \quad (5.4)$$

with δ_{ik} , δ_{jl} , δ_{il} , and δ_{jk} denoting the coordinates of the Kronecker tensor in \mathbb{R}^3 , which is defined as

$$\delta_{ij} = \begin{cases} 1 & \text{for } i = j, \\ 0 & \text{for } i \neq j. \end{cases} \quad (5.5)$$

The relations between the two independent components C_{1111} and C_{1212} and the elastic constants shear modulus G , bulk modulus K , Young's modulus E , and Poisson's ratio ν read

$$\begin{aligned} G &= C_{1212}, & E &= [(3C_{1111} - 4C_{1212})C_{1212}]/(C_{1111} - C_{1212}), \\ K &= C_{1111} - \frac{4}{3}C_{1212}, & \nu &= (C_{1111} - 2C_{1212})/[2(C_{1111} - C_{1212})]. \end{aligned} \quad (5.6)$$

In the principle stress space, the elastic domain is bounded by three surfaces, see Figure 5.1 (a): (i) a tension cut-off accounts for tensile failure, (ii) a Drucker-Prager surface defines shear failure under distinctive deviatoric stress states, and (iii) an ellipsoidal cap represents the hardening of the material associated with compaction. In mathematical terms, these functions read (Kropik, 1994; Kropik and Mang, 1996)

$$\begin{aligned} f_1(\boldsymbol{\sigma}) &= I_1 - T = 0, \\ f_2(\boldsymbol{\sigma}) &= \|\mathbf{s}\| - F_e(I_1) = 0 && \text{for } T \geq I_1 \geq \zeta, \\ f_3(\boldsymbol{\sigma}, \zeta) &= F_c(\|\mathbf{s}\|, I_1, \zeta) - F_e(\zeta) = 0 && \text{for } \zeta \geq I_1 \geq X(\zeta), \end{aligned} \quad (5.7)$$

with

$$\begin{aligned} F_e(\xi) &= \alpha - \vartheta \xi, \\ F_c(\|\mathbf{s}\|, I_1, \zeta) &= \sqrt{\|\mathbf{s}\|^2 + ([I_1 - L(\zeta)]/R)^2}, \end{aligned} \quad (5.8)$$

and

$$L(\zeta) = \begin{cases} \zeta & \text{if } \zeta < 0, \\ 0 & \text{if } \zeta \geq 0. \end{cases} \quad (5.9)$$

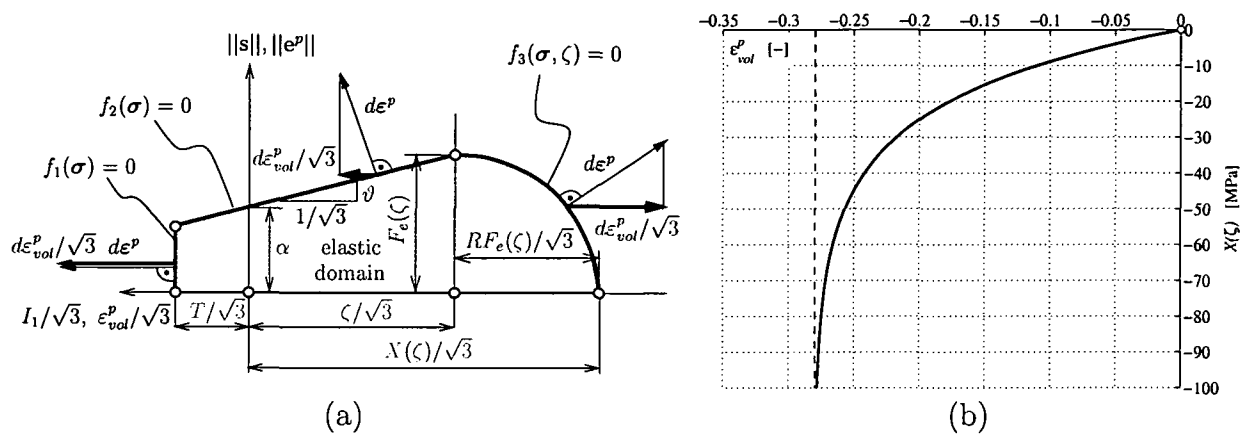


Figure 5.1: Cap model for gravel: (a) elastic domain and direction of plastic flow, respectively, in a meridional plane of the principal stress and the plastic strain space, respectively; (b) exponential hardening law for compaction based on $D = 0.05 \text{ MPa}^{-1}$ and $W = 0.28$

The direction of plastic flow is given by an associated flow rule (Kropik, 1994; Kropik and Mang, 1996)

$$d\epsilon^p = \sum_{\alpha \in J_{act}} d\lambda_{\alpha} \frac{\partial f_{\alpha}}{\partial \sigma}, \quad (5.10)$$

where consistency parameters are denoted as $d\lambda_{\alpha}$ and J_{act} stands for the set of active yield surfaces, defined as $J_{act} = \{\alpha \in [1, 2, 3] \mid f_{\alpha}(\sigma, \zeta) = 0\}$. Loading in the cap mode leads to compaction, whereas loading in the failure-surface mode or in the tension cut-off mode leads to plastic volume dilatation, see Figure 5.1(a). While the tension cut-off and the Drucker-Prager surface are fixed in the stress space, the ellipsoidal cap expands if activated, reflecting material compaction in terms of

$$\epsilon_{vol}^p = -W (1 - \exp[D X(\zeta)]) , \quad (5.11)$$

with

$$X(\zeta) = \zeta + R F_e(\zeta), \quad (5.12)$$

where ζ denotes the hardening state variable. For a graphical representation of Eq. (5.11) see Figure 5.1(b). Algorithmic issues of this model can be found in (Hofstetter et al., 1993; Kropik, 1994; Kropik and Mang, 1996).

The loading surfaces presented are defined by seven material parameters: T , α , ϑ , W , D , R , and ζ_{ini} , the initial value of the hardening state variable ζ . T refers to the failure of gravel under tensile loading. α and ϑ correspond to shear failure of gravel. They can be calculated from the Mohr-Coulomb parameters: cohesion c and angle of internal friction φ . Enforcing, e. g., the Drucker-Prager meridian to coincide with the compressional

Mohr-Coulomb meridian yields the relationships (Kropik, 1994)

$$\alpha = \sqrt{24} c \cos \varphi / (3 - \sin \varphi) \quad \text{and} \quad \vartheta = \sqrt{8/3} \sin \varphi / (3 - \sin \varphi). \quad (5.13)$$

W and D govern the hardening law (5.11). W is equal to the maximum attainable compaction of gravel; D is a shape parameter for the relationship between $X(\zeta)$ and ε_{vol}^P , see Figure 5.1 (b). R and ζ_{ini} define the shape and the initial size of the cap. R is the ratio of the major diameters of the ellipsoidal cap; ζ_{ini} refers to the initial center point of the cap.

In the following, these seven plastic parameters as well as two constants defining isotropic elasticity will be determined. Identification of the plastic parameters is based on the wealth of triaxial experiments documented in the literature. Elasticity of gravel is characterized by very large scattering, as is mentioned in standard textbooks (Studer and Ziegler, 1986), where values of Young's modulus range between 50 and 1000 MPa. This was the motivation to conduct a test series on the gravel used for the protection of the considered steel pipe, as will be described in the following.

5.2.3 Identification of gravel elasticity

Stiffness of gravel is often determined by the static load platen test (Terzaghi et al., 1996). This test, however, gives access to only one stiffness parameter, which, in addition, is not necessarily related to elasticity, but rather to a combined elasto-plastic loading. The unloading path of such a test does refer to elasticity, but still does not provide access to both constants of isotropic elasticity.

As a remedy, dynamic tests are performed, allowing for identification of gravel elasticity on the basis of the theory of wave propagation in elasto-plastic solids (Kolsky, 1953; Kolsky and Prager, 1964). In such media, elastic and plastic waves are encountered, the first ones being faster than the second ones. Therefore, the elastic waves, which are of interest herein, are easily detectable. The respective velocities of longitudinal waves, v_ℓ , and those of shear waves, v_s , give access to both constants of isotropic elasticity, via

$$v_\ell = \sqrt{\frac{C_{1111}}{\rho}}, \quad v_s = \sqrt{\frac{C_{1212}}{\rho}}. \quad (5.14)$$

where C_{1111} and C_{1212} are components of the 4-th order tensor \mathbf{C} defined in Eq. (5.3), and ρ denotes the mass density of gravel.

For determination of wave velocities in gravel, the following test set-up was realized: In a quarry a trench of 25 m length, 4 m width, and 2 – 3 m depth was filled with wide-range-grained gravel, see Figure 5.2. The volume fraction of fine-, medium-, and coarse-gravel (diameters from 2 – 63 mm) was equal to 60%. The remaining volume fraction of 40%

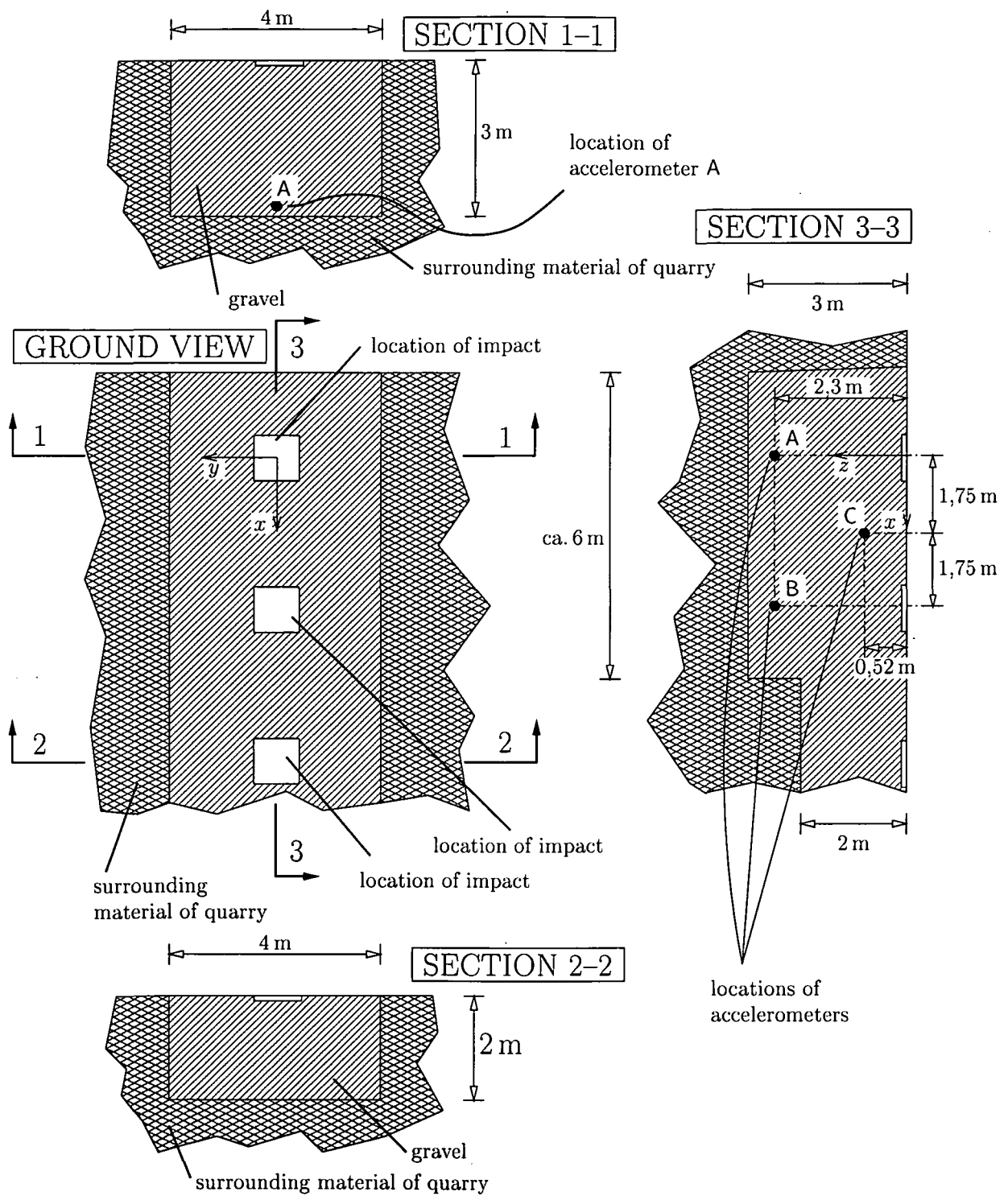


Figure 5.2: Test trench filled with gravel, positions of accelerometers A, B, C, and locations of impact of both the bucket of a dredger and rock boulders, respectively

consisted of edged stones (diameters from 63 – 200 mm). The gravel was filled into the trench in layers of 25 cm thickness. Each layer was densified by hand-guided compaction units. The mass density of the material was equal to 1800 kg/m^3 . Three accelerometers, denoted as A, B, and C, were installed at well-defined locations, see Figure 5.2, and buried during the filling process of the testing trench. Before that, the accelerometers were fixed to steel bodies of dimensions $30 \text{ cm} \times 30 \text{ cm} \times 30 \text{ cm}$, see Figure 5.3. They ensure that the accelerometers detect the acceleration history of a representative volume element of gravel rather than that of single stones.

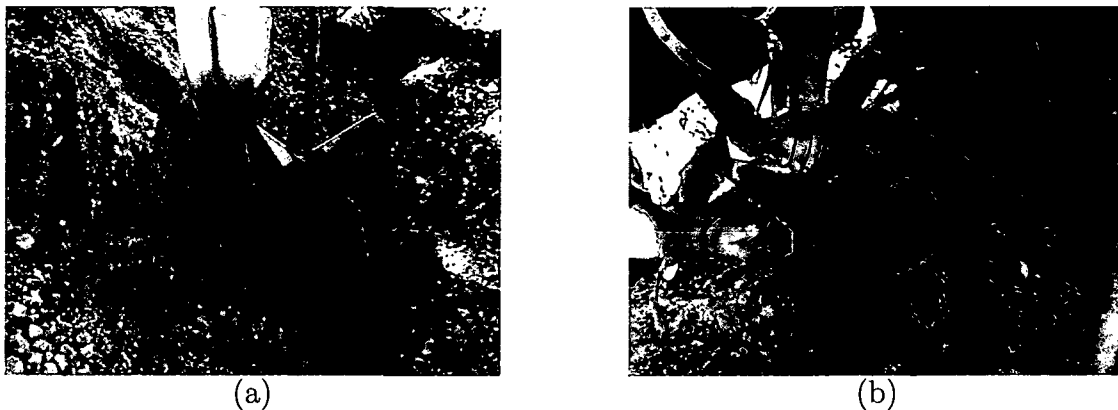


Figure 5.3: Steel body linking an accelerometer to a representative volume element of gravel: (a) position in buried condition (b) view from the bottom side showing the box containing the accelerometer

Signals are produced by hitting the bucket of a dredger vertically onto the surface of the gravel body built into the trench. They lead to propagation of both longitudinal and shear waves through the gravel. The fronts of these waves spread though the gravel hemi-spherically with direction-dependent intensity. The maximum intensity of longitudinal waves occurs in the vertical axis through the impact location. The intensity of the longitudinal waves decreases rapidly with increasing angle from this axis. In contrast, the intensity of the shear waves is zero in the vertical direction, and increases with increasing deviation from this direction.

The surface locations at which the signals are transmitted by hitting the bucket onto the gravel are indicated in Figure 5.2. The time instant of the signal transmission is recorded by a fourth accelerometer which is placed in the immediate vicinity of the respective hitting locations, see Figure 5.2.3 (a). The signal is recognized by the occurrence of accelerations which are by orders of magnitude larger than the oscillation width of measurement noise, related to gravel in a state of rest, see Figure 5.2.3 (b). The first acceleration value lying outside the interval of the measurement noise indicates the onset of dynamic excitation. In the same way, the time instants at which the waves reach the buried accelerometers are

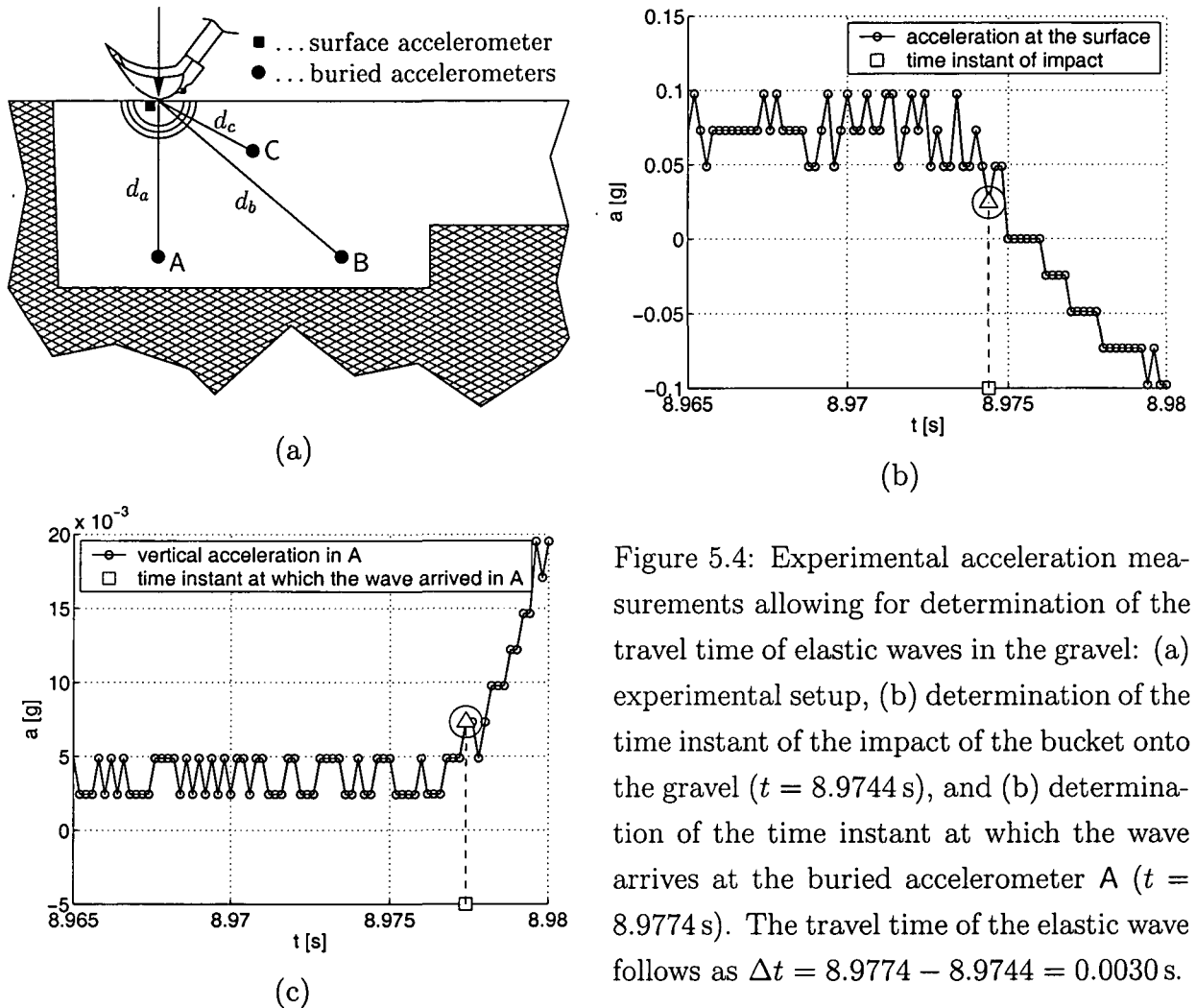


Figure 5.4: Experimental acceleration measurements allowing for determination of the travel time of elastic waves in the gravel: (a) experimental setup, (b) determination of the time instant of the impact of the bucket onto the gravel ($t = 8.9744$ s), and (c) determination of the time instant at which the wave arrives at the buried accelerometer A ($t = 8.9774$ s). The travel time of the elastic wave follows as $\Delta t = 8.9774 - 8.9744 = 0.0030$ s.

determined, see Figure 5.2.3 (c). Wave velocities are determined as the ratio of the distance d between the accelerometer at the surface and the buried accelerometers and of the time span needed for this travel, see Figure 5.2.3 (a). This time span is the difference between the time instants of bucket impact and of wave arrival at the buried accelerometers.

It follows from the aforementioned wave intensities that the buried accelerometer detects a signal related to a longitudinal wave; if it lies directly underneath the location of the bucket impact. In the same experiment, all other buried accelerometers detect signals related to shear waves. In this way, a total of 25 experiments allows for determination of 19 values for longitudinal wave velocities, and of 66 values for shear wave velocities. Insertion of these values and of $\rho = 1800 \text{ kg/m}^3$ into Eqs. (5.14) delivers the values for C_{1111} and C_{1212} , listed in Appendix C.

From a statistical perspective the elasticity values given in Appendix C are *samples* for C_{1111} and C_{1212} , respectively. In the following, they will be used to estimate characteristics

of the *populations* of C_{1111} and C_{1212} . Considering the necessary positiveness of the values for C_{1111} and C_{1212} and assuming the distributions of these stiffnesses to be results of multiplicative mechanisms of a number of influence factors (Benjamin and Cornell, 1970), implies the choice of lognormal distributions for characterization of C_{1111} and C_{1212} . The value m referring to the maximum of the probability density function of a lognormally distributed population is given as:

$$m = \exp(\mu - \sigma^2), \quad (5.15)$$

where μ and σ are the expected value and the standard deviation, respectively, of the logarithmized population, which is normally distributed. The population parameters μ and σ can be estimated by analyzing samples (Bortz, 1999; Benjamin and Cornell, 1970).

The following considerations deal with such an analysis of a *sample* Ξ_i , $i = 1, 2, \dots, n$, of a normally distributed Ξ -*population*. The mean value \bar{x} and the empirical standard-deviation s of a sample are given as

$$\bar{x} = \frac{1}{n} \sum_{i=1}^n \Xi_i, \quad s = \sqrt{\frac{1}{n-1} \sum_{i=1}^n (\Xi_i - \bar{x})^2}, \quad (5.16)$$

where n denotes the sample size. The sample parameters \bar{x} and s can be interpreted as the most probable estimates for μ and σ of the Ξ -*population*. Moreover, based on \bar{x} and s , a two-sided confidence interval of the expected value μ of the Ξ -*population*, $[\mu_{low}, \mu_{upp}]$, is determined as

$$\mu_{low} = \bar{x} - \frac{s \cdot t_{n-1, 1-\alpha/2}}{\sqrt{n}} \leq \mu \leq \bar{x} + \frac{s \cdot t_{n-1, 1-\alpha/2}}{\sqrt{n}} = \mu_{upp}, \quad (5.17)$$

where $t_{n-1, 1-\alpha/2}$ denotes the t -value that cuts an area equal to $1 - \alpha/2$ of the Student's t distribution with $n - 1$ degrees of freedom. α stands for the significance level which is equal to 5% for a 95%-confidence interval, see e. g. (Bortz, 1999; Benjamin and Cornell, 1970), such as employed herein. A two-sided confidence interval for the standard deviation σ of the Ξ -*population*, $[\sigma_{low}, \sigma_{upp}]$, is determined as:

$$\sigma_{low} = \sqrt{\frac{(n-1) \cdot s^2}{\chi_{n-1, 1-\alpha/2}^2}} \leq \sigma \leq \sqrt{\frac{(n-1) \cdot s^2}{\chi_{n-1, \alpha/2}^2}} = \sigma_{upp}, \quad (5.18)$$

where $\chi_{n-1, 1-\alpha/2}^2$ denotes the χ^2 -value that cuts an area equal to $1 - \alpha/2$ of the chi-squared distribution with $n - 1$ degrees of freedom, see e. g. (Bortz, 1999; Benjamin and Cornell, 1970). Inserting $\mu = \bar{x}$ and $\sigma = s$ in Eq. (5.15), yields the most probable estimate of the value m referring to the maximum of the probability density function of the lognormally distributed population as $\bar{m} = \exp(\bar{x} - s^2)$. Evaluation of Eq. (5.15) with (i) $\mu = \mu_{low}$

and $\sigma = \sigma_{low}$ and (ii) $\mu = \mu_{upp}$ and $\sigma = \sigma_{upp}$ yields an upper and a lower bound for m as $m_{low} = \exp(\mu_{low} - \sigma_{low}^2)$ and $m_{upp} = \exp(\mu_{upp} - \sigma_{upp}^2)$.

The corresponding statistical analyses of the logarithmized samples of C_{1111} and C_{1212} (given in Appendix C) yield

$$\begin{aligned} \bar{C}_{1111} &= 340 \text{ MPa}, & C_{1111}^{low} &= 178 \text{ MPa} \leq C_{1111} \leq 511 \text{ MPa} = C_{1111}^{upp}, \\ \bar{C}_{1212} &= 71.7 \text{ MPa}, & C_{1212}^{low} &= 46.3 \text{ MPa} \leq C_{1212} \leq 100 \text{ MPa} = C_{1212}^{upp}, \end{aligned} \quad (5.19)$$

see also Figure 5.5. According to the Eqs. (5.6), the bounds for C_{1111} and C_{1212} can also

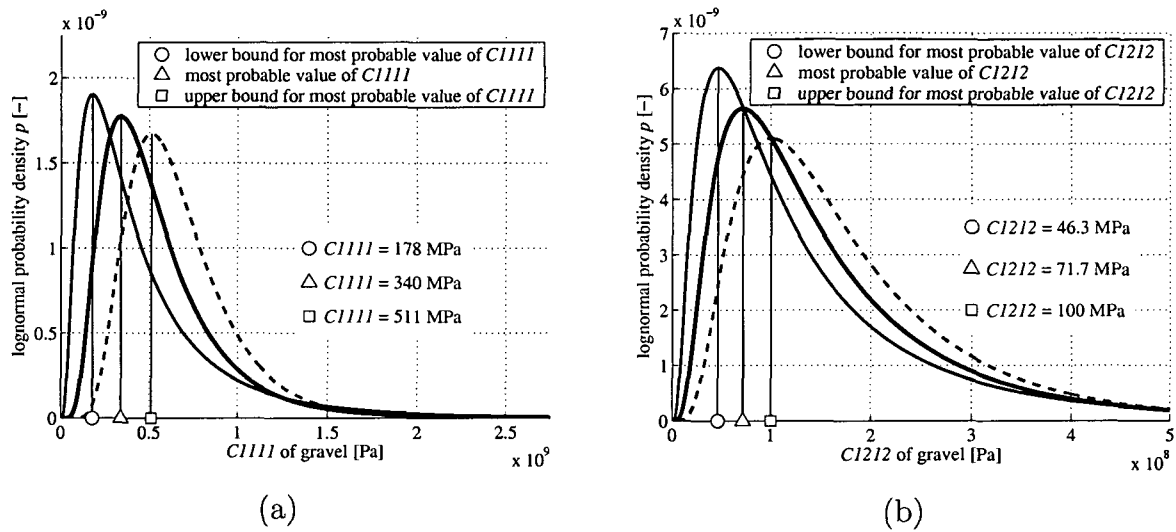


Figure 5.5: Lognormal probability distribution functions obtained from statistical analyses of the experimentally determined samples for (a) C_{1111} and (b) C_{1212}

be given in terms of the shear and the bulk modulus, G and K , or in terms of the Young's modulus and the Poisson's ratio, E and ν :

$$\begin{aligned} \bar{G} &= 72 \text{ MPa}, & G_{low} &= 46 \text{ MPa} \leq G \leq 100 \text{ MPa} = G_{upp}, \\ \bar{K} &= 244 \text{ MPa}, & K_{low} &= 116 \text{ MPa} \leq K \leq 378 \text{ MPa} = K_{upp}, \\ \bar{E} &= 196 \text{ MPa}, & E_{low} &= 123 \text{ MPa} \leq E \leq 276 \text{ MPa} = E_{upp}, \\ \bar{\nu} &= 0.366, & \nu_{low} &= 0.324 \leq \nu \leq 0.378 = \nu_{upp}. \end{aligned} \quad (5.20)$$

5.2.4 Identification of inelastic behavior of gravel

Identification of the parameters governing shear failure of gravel

Over the last decades a wealth of experimental data referring to the shear strength of gravel has been published in the literature, see, e. g., (Penumadu and Zhao, 1999) and references therein. Commonly, triaxial compression tests were carried out on cylindrical specimens:

First, hydrostatic compression is applied up to a specific confinement pressure p . Whereas p is subsequently kept constant, the specimens are subjected to additional uniaxial loading in the direction of the cylinder axis, up to shear failure. Penumadu and Zhao (Penumadu and Zhao, 1999) give detailed information on ten triaxial tests published originally in (Marachi et al., 1969; Al-Hussaini, 1971; Leslie, 1975; Alva-Hurtado and Selig, 1981); the tested gravels differed in grain shape, grain size, grain distribution, mineral hardness, and void ratio. The applied confinement pressures p ranged from 103 kPa to 4481 kPa. Penumadu and Zhao document each experiment by two diagrams referring to the *second phase* of the triaxial test: A $(\sigma_1 - \sigma_3) - \varepsilon_{axi}$ diagram shows the relation between the additionally applied uniaxial stress¹ over the axial strain of the cylindrical specimen. An $\varepsilon_{axi} - \varepsilon_{vol}$ diagram shows the evolution of volumetric strain as a function of the axial strain.

The experimental results are illustrated herein in an $I_1 - \|s\|$ diagram, i. e., in a meridional plane of the principal stress space, see Figure 5.6. There, all stress paths of hydrostatic precompression follow the I_1 axis starting from the origin of the coordinate system. The additional uniaxial compression results in an ascending path with slope 2/3. The maximum

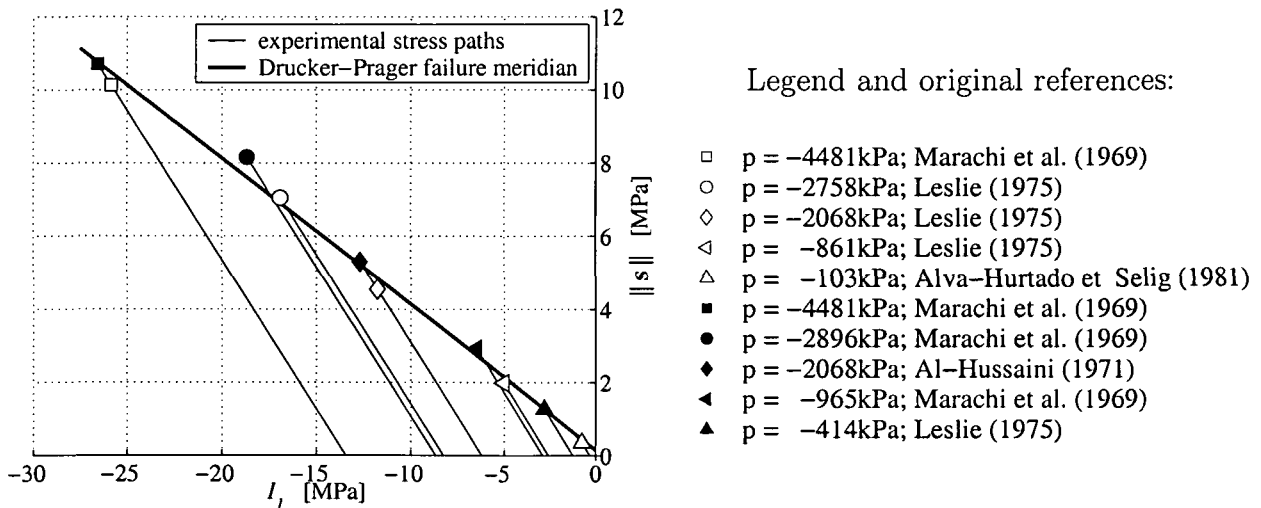


Figure 5.6: Experimental data referring to shear failure of gravel taken from (Penumadu and Zhao, 1999) and corresponding failure meridian in a meridional plane of the principal stress space

values $\max(\sigma_1 - \sigma_3)$ in the $(\sigma_1 - \sigma_3) - \varepsilon_{axi}$ diagrams of Penumadu and Zhao correspond to the points of shear failure indicated in Figure 5.6. The corresponding coordinates as functions

¹At the beginning of the second phase of the experiment, $\sigma_1 = \sigma_3 = p$. The 1-direction coincides with the direction of uniaxial loading. Therefore, $|\sigma_1|$ increases during the second phase of the experiment, whereas σ_3 stays equal to the confinement pressure p .

of $\max(\sigma_1 - \sigma_3)$ and p are

$$\begin{aligned} (I_1)_{sf} &= \max(\sigma_1 - \sigma_3) + 3p, \\ \|s\|_{sf} &= \sqrt{[\max(\sigma_1 - \sigma_3) + p - (I_1)_{sf}/3]^2 + 2[p - (I_1)_{sf}/3]^2}, \end{aligned} \quad (5.21)$$

where the indices sf stand for “shear failure”. The ten tests taken from (Penumadu and Zhao, 1999) are evaluated according to Eqs. (5.21), see the I_1 - $\|s\|$ diagram illustrated in Figure 5.6. The experimental points referring to shear failure can be approximated ($r^2 = 0.995$) by a linear failure meridian

$$\|s\| - 149087 + 0.3997 I_1 = 0 \quad \text{for} \quad \|s\| \text{ and } I_1 \text{ in [Pa]}. \quad (5.22)$$

Eq. (5.22) can be interpreted as a Drucker-Prager failure meridian. From a comparison of Eq. (5.22) with Eq. (5.7)₂ the Drucker-Prager parameters follow as $\alpha = 149$ kPa and $\vartheta = 0.40$. Alternatively, Eq. (5.22) can be interpreted as a compressive Mohr-Coulomb failure meridian, described mathematically by insertion of the Eqs. (5.13) into Eq. (5.7)₂. Comparing the result with Eq. (5.22), yields $c = 90.8$ kPa and $\varphi = 36.1^\circ$. Remarkably, one set of c and φ satisfactorily characterizes shear failure of gravels which differ in grain shape, grain size, grain distribution, mineral hardness, and void ratio. Thereby, c is very small compared to the characteristic deviator stresses $\|s\|$ encountered in the triaxial tests; this is expressed by referring to gravel as a “cohesionless” material.

Identification of the parameters governing compaction of gravel

Identification of the material parameters, W and D , characterizing the behavior of gravel in compaction is based on $(\sigma_1 - \sigma_3)$ - ε_{axi} and ε_{axi} - ε_{vol} diagrams of (Penumadu and Zhao, 1999), evaluated in the form of σ_m - ε_{vol} diagrams, see Figure 5.7. Thereby, $\sigma_m = I_1/3$ is the mean normal-stress. Apparently, grain shape, grain size, grain distribution, mineral hardness, void ratio, and hydrostatic precompression have a non-negligible influence on the behavior of gravel in compaction.

Herein, rather small mean stresses are of interest, see also Subsection 5.4, which implies identification of $W = 0.28$ and $D = 0.05 \text{ MPa}^{-1}$, respectively, see Figure 5.7. Obviously, high confinement pressures are not predicted well by the cap model as far as the volumetric strains are concerned: the model answer is too compliant. However, they have no relevance herein.

Initial size and shape of the cap and tensile failure of gravel

The initial size and the shape of the cap is determined from constant volume tests, $R = 4.4$ and $\zeta_{ini} = 0$ kPa, see (Kropik, 1994). For numerical reasons, the material parameter

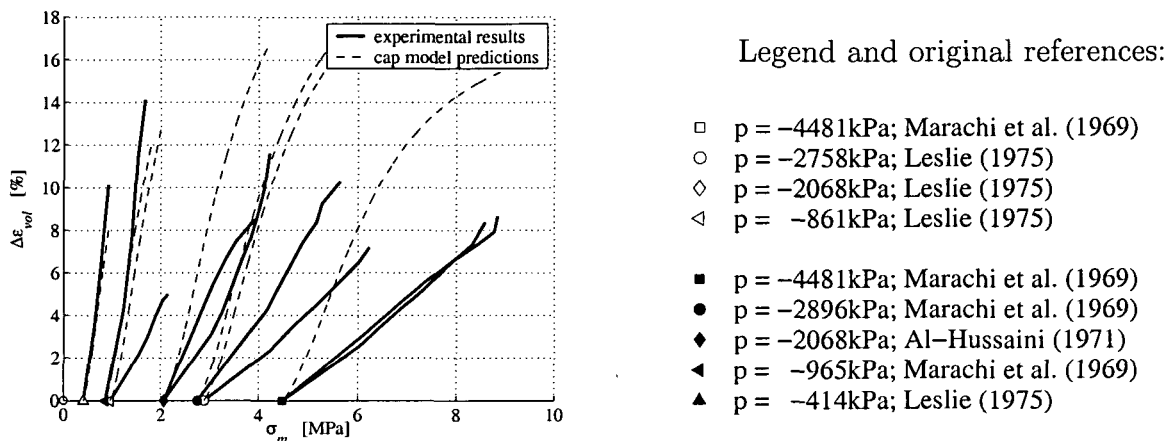


Figure 5.7: Experimental data referring to the behavior of gravel in compaction, taken from (Penumadu and Zhao, 1999) and respective cap-model output for $D = 0.05 \text{ MPa}^{-1}$ and $W = 0.28$

referring to tensile failure of gravel, T , is not set equal to zero. Instead, a negligibly small positive value (100 Pa) is assigned to T .

5.2.5 Discussion and final remarks regarding the identified material parameters of gravel

In Sections 5.2.3 and 5.2.4 the material parameters of wide-range-grained gravel were identified. Elastic properties of gravel were determined from the theory of wave propagation in isotropic bodies. A statistical analysis yielded most probable values for the bulk modulus, the shear modulus, Young's modulus, and Poisson's ratio. Taking into account the scattering of these parameters, a lower and an upper bound of these elastic parameters were calculated based on 95%-confidence intervals of the governing statistical parameters. The results indicated that the elastic properties of gravel scatter significantly. Analyzing the inelastic properties of gravel, it was found that the Mohr-Coulomb failure criterion based on *one* specific choice of the cohesion and the angle of internal friction is well suited to describe shear failure of *various* types of gravel. However, a non-negligible influence of grain shape, grain size, grain distribution, mineral hardness, void ratio, and confinement pressure on the behavior of gravel in compaction was encountered. Nevertheless, the hardening law proposed by DiMaggio, Sandler, and Rubin in the 1970s, (DiMaggio and Sandler, 1971; Sandler and Rubin, 1979), is a reasonable approach to describe compaction of a specific type of gravel. The nine material parameters of gravel are listed in Table 5.1.

Table 5.1: Material parameters of gravel

elastic behavior [Hooke's law]:	$K = 244 \text{ MPa}, G = 72 \text{ MPa},$
shear failure [Drucker-Prager criterion]:	$\alpha = 149 \text{ kPa}, \vartheta = 0.40,$
behavior in compaction [DiMaggio-Sandler model]:	$W = 0.28, D = 0.05 \text{ MPa}^{-1},$
(initial) shape of the cap [approach by Kropik]:	$R = 4.4, \zeta_{ini} = 0 \text{ kPa},$
tensile-loading behavior [tension cut-off]:	$T = 0.1 \text{ kPa} \approx 0.$

5.3 Estimation of penetration depth and impact force arising from rockfall onto gravel

Numerical modeling of rockfall events requires knowledge about the penetration depths of rock boulders into gravel and about the dynamic forces resulting from the impact. Lack of a standard procedure for estimation of these quantities has motivated penetration experiments for rocks impacting onto gravel. A dimensional analysis of the underlying physical problem will be described in Section 5.3.1. Together with pertinent contributions to the impact of projectiles onto concrete and soil in the literature (Forrestal et al., 1994; Forrestal et al., 1996; Li and Chen, 2003; Forrestal et al., 2003) this analysis is the basis for the design of experiments described in Section 5.3.2. Experimental results will be evaluated and discussed in Section 5.3.3 which contains the desired estimation of the penetration depth and the impact force as a function of the height of fall, the boulder mass, and the indentation resistance of the gravel.

5.3.1 Impact of rocks onto gravel – Dimensional analysis

For engineering design of rockfall protection systems, impact of rocks is commonly characterized by three relevant physical quantities (Labieuse et al., 1996): the penetration depth X , the impact duration Δt_i , and the impact force F . In the following, the rock boulders are treated as rigid impactors which do not break into pieces during impact. Therefore, X , Δt_i , and F do not depend on the deformational behavior of the rock. Based on well-accepted physical assumptions concerning the impact of projectiles onto soil and concrete targets (Forrestal et al., 1994; Forrestal et al., 1996; Li and Chen, 2003) X , Δt_i , and F are assumed to be governed by the boulder mass m , the impact velocity of the boulder, v_0 , the characteristic length of the boulder nose, d , and the dimensionless sharpness of the boulder nose, N^* ; moreover, X , Δt_i , and F are assumed to depend on the mass density of the gravel, ρ_g , and the strength-like indentation resistance of the gravel, R . Formally,

these dependencies can be written as

$$\begin{aligned} X &= f_1(m, v_0, d, N^*; \rho_g, R), \\ \Delta t_i &= f_2(m, v_0, d, N^*; \rho_g, R), \\ F &= f_3(m, v_0, d, N^*; \rho_g, R). \end{aligned} \quad (5.23)$$

The present work is restricted to geometrically similar rock boulders impacting onto gravel in an identical manner. Hence, N^* is a constant. Similarly, a specific type of gravel is considered, which is commonly used for energy-absorbing layers. This renders also ρ_g as a constant. The indentation resistance R for one and the same value of ρ_g is characterized by significant scattering. Therefore, R is not treated as a constant, but as a probabilistic variable which will be analyzed statistically. Writing the Eqs. (5.23) for $\rho_g = \text{const.}$ and $N^* = \text{const.}$ yields

$$\begin{aligned} X &= f_1(m, v_0, d, R), \\ \Delta t_i &= f_2(m, v_0, d, R), \\ F &= f_3(m, v_0, d, R). \end{aligned} \quad (5.24)$$

The basis of dimensional analysis is (Barenblatt, 1996; Jones, 1989; Buckingham, 1914) that physical laws do not depend on arbitrarily chosen units of measurements. This implies that functions describing physical laws such as, e. g., f_1 , f_2 , and f_3 in the Eqs. (5.24), must possess a fundamental property, called generalized homogeneity, which allows for the reduction of the number of arguments in these functions. For this purpose, the dimension functions of the involved physical quantities are introduced. In the present case they read

$$\begin{aligned} [X] &= L^1 M^0 T^0, & [\Delta t_i] &= L^0 M^0 T^1, & [F] &= L^1 M^1 T^{-2}, \\ [d] &= L^1 M^0 T^0, & [m] &= L^0 M^1 T^0, & [v_0] &= L^1 M^0 T^{-1}, & [R] &= L^{-1} M^1 T^{-2}, \end{aligned} \quad (5.25)$$

where L, M, and T are abstract positive numbers related to arbitrary changes of the chosen units of measurements (Barenblatt, 1996). They are called base dimensions of length, mass, and time, respectively. The next step in dimensional analysis is to divide the N governing parameters, here d , m , v_0 , and R , ($N = 4$), into k dimensionally independent and $(N - k)$ dimensionally dependent quantities. Dimensionally independent quantities have a dimension function which cannot be expressed in terms of a product of powers of the dimensions of the remaining quantities. The number of dimensionally independent quantities is equal to the rank of the so-called exponent matrix of dimension. For problems described by the Eqs. (5.24) this matrix reads as

$$\begin{array}{c|ccc|ccc} & [d] & [m] & [v_0] & [R] & [X] & [\Delta t_i] & [F] \\ \hline \left| \begin{array}{c} L \\ M \\ T \end{array} \right| & \left[\begin{array}{cccc|ccc} 1 & 0 & 1 & -1 & 1 & 0 & 1 \\ 0 & 1 & 0 & 1 & 0 & 0 & 1 \\ 0 & 0 & -1 & -2 & 0 & 1 & -2 \end{array} \right] & & & & & & \end{array} \quad (5.26)$$

with a rank of three, indicating that $k = 3$. Accordingly, three of the four governing parameters in the Eqs. (5.24) are dimensionally independent (e.g. d , m , and v_0), whereas one of the four governing parameters ($N - k = 4 - 3 = 1$) is dimensionally dependent (e.g. R). The Pi-Theorem (Buckingham, 1914) states that each one of the relationships in the Eqs. (5.24) can be written as a relationship between a dimensionless parameter and $(N - k)$ dimensionless products, yielding

$$\pi_X = \frac{X}{d} = \mathcal{F}_1 \left(\pi_R = \frac{m v_0^2}{R d^3} \right), \quad (5.27)$$

$$\pi_{\Delta t_i} = \frac{\Delta t_i v_0}{d} = \mathcal{F}_2 \left(\pi_R = \frac{m v_0^2}{R d^3} \right), \quad (5.28)$$

$$\pi_F = \frac{F d}{m v_0^2} = \mathcal{F}_3 \left(\pi_R = \frac{m v_0^2}{R d^3} \right), \quad (5.29)$$

where \mathcal{F}_1 , \mathcal{F}_2 , and \mathcal{F}_3 are dimensionless functions which do not depend on units of measurements. Hence, they are invariant with regard to changes of the chosen unit system. Remarkably, dimensional analysis has allowed for the reduction of the number of arguments in the functions f_1 , f_2 , and f_3 from four to one, see the Eqs. (5.24) and (5.27) – (5.29), reducing the efforts required to analyze these physical laws by three orders of magnitude. The functions \mathcal{F}_1 , \mathcal{F}_2 , and \mathcal{F}_3 will be determined subsequently in a hybrid (analytical-experimental) approach.

5.3.2 Design of experiments

The experimental investigation consisted of impact tests performed to determine the indentation characteristics of different rock boulders impacting onto gravel. The tests were performed with the help of a truck-mounted crane. The available crane restricted the rock-boulder mass to 20000 kg and the height of fall to 20 m. According to geologists, representative heights of fall in real-life situations are by far larger than 20 m. Hence, the test design had to be defined such that the obtained results allow for an extrapolation to rockfall scenarios that could not be investigated experimentally. In order to provide such an extrapolation, existing formulae for the estimation of the penetration depth of non-deformable impactors were applied to the present problem of rockfall onto gravel. In particular, Forrestal's formulae (Forrestal et al., 1994; Forrestal et al., 1996) describing penetration depth of non-deformable projectiles onto concrete and soil targets turned out to be well suited for interpolations between experimental data. They were presented in

dimensionless form by Li and Chen (Li and Chen, 2003), reading as

$$\frac{X}{d} = \sqrt{\frac{1 + k \pi/4 N}{1 + I/N} \frac{4k}{\pi} I} \quad \text{for } \frac{X}{d} \leq k, \quad (5.30)$$

$$\frac{X}{d} = \frac{2}{\pi} N \ln \left[\frac{1 + I/N}{1 + k \pi/4 N} \right] + k \quad \text{for } \frac{X}{d} > k. \quad (5.31)$$

X denotes the penetration depth, d is the diameter of the projectile, see Fig. 5.8 (b), N is a geometry function characterizing the sharpness of the impactor nose, I is the impact function describing the intensity of the impact, and k is the dimensionless depth of a surface crater. The geometry function N is defined as

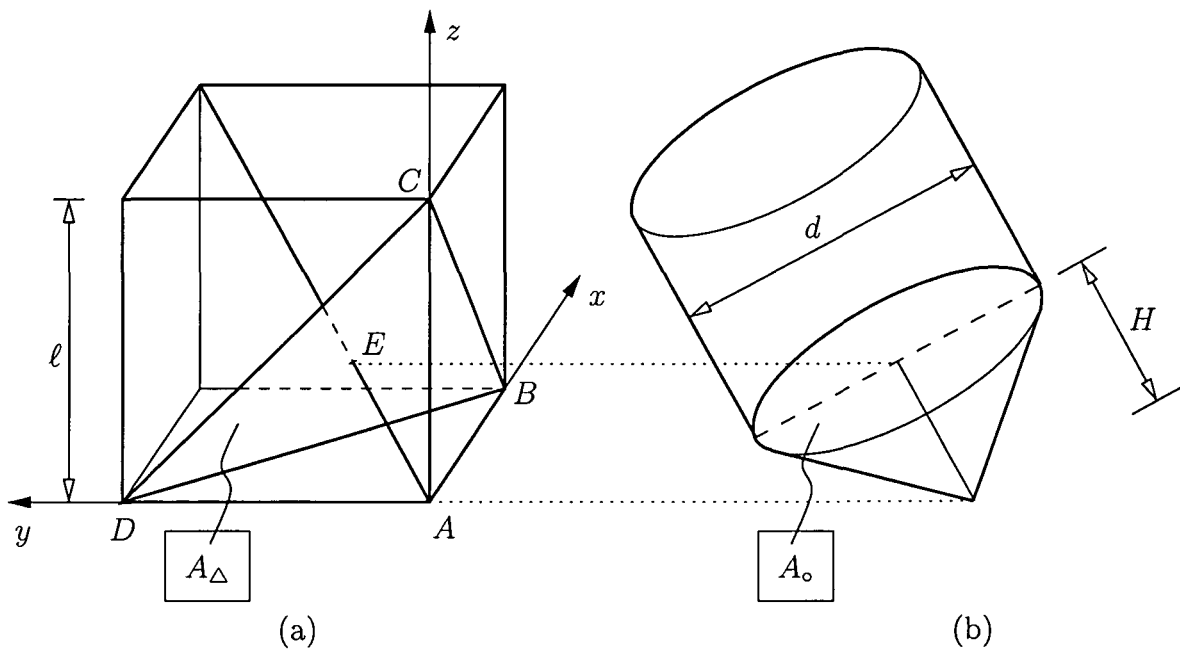


Figure 5.8: (a) cubic impactor with pyramidal nose and (b) equivalent impactor with conical nose

$$N = \frac{m}{\rho_s d^3 B N^*}, \quad (5.32)$$

where m denotes the mass of the impactor, ρ_s is the mass density of the target material, B is a dimensionless compressibility parameter of the impacted material, and N^* is the nose shape factor. B is equal to 1.2 for soil targets (Forrestal et al., 1994). The impact function I is defined as

$$I = \frac{m v_0^2}{R d^3}, \quad (5.33)$$

where v_0 denotes the impact velocity and R is a strength-like parameter, which can be interpreted as the indentation resistance of the target material (Forrestal et al., 2003).

The impact function I is equal to the argument π_R of the dimensionless functions \mathcal{F}_1 , \mathcal{F}_2 , and \mathcal{F}_3 , see Eq. (5.27), $I \equiv \pi_R$. Finally, k is defined as (Li and Chen, 2003)

$$k = 0.707 + \frac{H}{d}, \quad (5.34)$$

where H stands for height of the impactor nose, see Fig. 5.8 (b).

Li and Chen (Li and Chen, 2003) investigated the validity of the Eqs. (5.30) and (5.31) on the basis of the results of 82 different impact tests (Li and Chen, 2003). For all experiments (i) the dimensionless penetration depth $(X/d)_{test}$ was calculated from the measured values X_{test} and d_{test} , and (ii) the functions N and I were evaluated according to Eq. (5.32) and Eq. (5.33), respectively. Thereby, large intervals for $(X/d)_{test}$, N , and I were covered, see Table 5.2. The evaluation of the Eqs. (5.30) and (5.31) with the experimental values for N and I yielded 82 values of estimated dimensionless penetration depths X/d . They agreed well with the corresponding 82 values of $(X/d)_{test}$. Hence, the validity of the Eqs. (5.30) and (5.31) was proved in (Li and Chen, 2003) for the intervals of $(X/d)_{test}$, N , and I given in Table 5.2.

Table 5.2: Intervals of $(X/d)_{test}$, N , and I for which the validity of Eqs. (5.30) was proved in (Li and Chen, 2003)

validity interval of $(X/d)_{test}$	validity interval of N	validity interval of I
[0.04 ; 5.80]	[0.53 ; 96.63]	[0.03 ; 10.97]

In the present research, rock boulders of approximately cubic shape are considered to be relevant for rockfall scenarios. Cubes can be dropped such that they hit the ground with a face, an edge, or a tip. Thereby, the largest penetration depth, considered to be relevant for design purposes, will be obtained, if a cubic boulder impacts onto the ground with a tip. For this case, the dimensionless model of the Eqs. (5.30) – (5.34) will be specialized in the following.

The pyramidal nose of a cubic rock boulder is approximated by an equivalent conical nose such that the same amount of target volume is displaced at equal penetration depths. Hence, the area A_o of the circular base of a conical nose is set equal to the area A_Δ of the triangular base BCD of the pyramid $ABCD$, see Fig. 5.8:

$$A_o = \frac{d^2 \pi}{4} = A_\Delta = \frac{\ell^2 \sqrt{3}}{2} \Rightarrow d = \sqrt{\frac{2\sqrt{3}}{\pi}} \ell = 1.050 \sqrt[3]{V}, \quad (5.35)$$

where V denotes the volume of the cube, with $\ell = \sqrt[3]{V}$ as its side length. Furthermore, the height H of the conical nose is set equal to the height of the pyramid $ABCD$, i. e., the

distance of points A and E , see Fig. 5.8, yielding

$$H = \frac{\ell \sqrt{3}}{3} = 0.5774 \sqrt[3]{V}. \quad (5.36)$$

The nose shape factor N^* for conical impactors is defined as (Li and Chen, 2003)

$$N^* = \frac{1}{1 + 4\psi^2} \quad \text{with} \quad \psi = \frac{H}{d}. \quad (5.37)$$

Inserting the Eqs. (5.35) and (5.36) into the Eqs. (5.34) and (5.37), yields $k = 1.257$, $\psi = 0.5498$, and $N^* = 0.4527$. Inserting the latter result, Eq. (5.35), and $m = V \rho_r$ (where ρ_r denotes the mass density of granite) into Eq. (5.32) yields the expression for N for the special case of cubic impactors of granite,

$$N = \frac{(V \rho_r)}{\rho_s (1.050^3 V) B N^*} = 2.385. \quad (5.38)$$

In Eq. (5.38) ρ_r and $\rho_g = \rho_s$ were set equal to 2700 kg/m^3 and 1800 kg/m^3 , respectively. $N = 2.385$ lies within the interval $[0.53; 96.63]$ for which the validity of the Eqs. (5.30) and (5.31) was proved by Li and Chen (Li and Chen, 2003), see Table 5.2. Inserting $N = 2.385$ and $k = 1.257$ into the Eqs. (5.30) and (5.31) yields an expression of Forrestal's formulae for the special case of granite boulders of approximately cubic shape impacting with a tip onto a material with the mass density $\rho_s = 1800 \text{ kg/m}^3$:

$$\frac{X}{d} = \sqrt{\frac{2.263 I}{(1 + I/2.385)}} \quad \text{for} \quad \frac{X}{d} \leq 1.257, \quad (5.39)$$

$$\frac{X}{d} = 1.518 \ln \left[\frac{1 + I/2.385}{1.414} \right] + 1.257 \quad \text{for} \quad \frac{X}{d} > 1.257. \quad (5.40)$$

The Eqs. (5.39) and (5.40) represent the dimensionless function $\mathcal{F}_1(\pi_R \equiv I)$ appearing in Eq. (5.27) (for a graphical representation see Fig. 5.9).

In order to specify rock boulder masses and heights of fall for the experimental setup, I is specialized for cubic impactors of granite: Therefore, Eq. (5.35), $m = V \rho_r$ ($\rho_r = 2700 \text{ kg/m}^3$), and $v_0 = \sqrt{2g h_f}$ (where $g = 9.81 \text{ m/s}^2$ stands for the gravitational acceleration and h_f for the height of fall) are inserted into Eq. (5.33), yielding

$$I = \frac{(V \rho_r) (2g h_f)}{(1.050^3 V) R} = \frac{45\,750 \cdot h_f}{R} \quad \dots \quad h_f \text{ in [m]} \quad \text{and} \quad R \text{ in [Pa]}. \quad (5.41)$$

Remarkably, the factor $m/d^3 = \rho_r/1.050^3$ turns out to be constant for cubic granite boulders falling onto a tip, rendering I to be a function of h_f and R only. Inserting Eq. (5.41) into Eq. (5.39), yields

$$\frac{X}{d} = \sqrt{\frac{103500 h_f}{R + 19180 h_f}} \quad \text{for} \quad \frac{X}{d} \leq 1.257 \quad \dots \quad h_f \text{ in [m]} \quad \text{and} \quad R \text{ in [Pa]}, \quad (5.42)$$

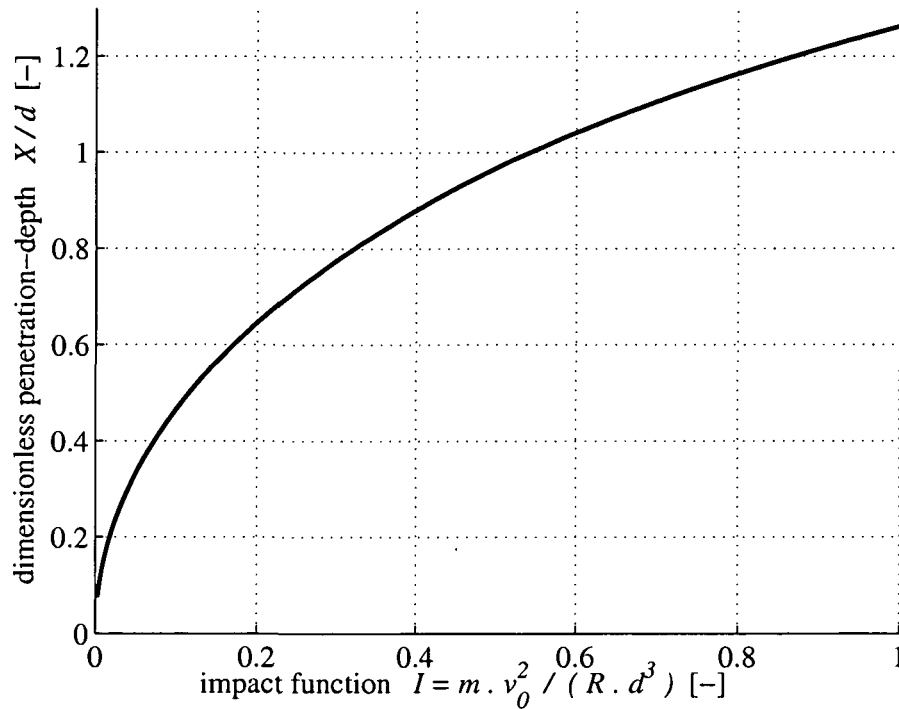


Figure 5.9: Dimensionless penetration depth X/d as a function of I for approximately cubic granite-boulders with mass m and characteristic length d , impacting at velocity v_0 with a tip onto a material with indentation resistance R and mass density $\rho_g = 1800 \text{ kg/m}^3$

According to Eq. (5.42), the estimation of the penetration depth X for the impact of a granite boulder with a characteristic length d falling from the height h_f onto gravel, requires knowledge about the indentation resistance R of gravel, which can be obtained by means of back analysis from experimental results. Based on Eq. (5.42), three different rock boulder masses and three different heights of fall were defined for the impact experiments. Thereby, $m \leq 20000 \text{ kg}$ and $h_f \leq 20 \text{ m}$ had to be taken into account. The sign of equality refers to the limiting values depending on the available type of crane. Rock-boulder masses and heights of fall were chosen such that equally-spaced penetration depths could be expected according to Eq. (5.42): For constant R and h_f , this relation yields $X \propto d$. Together with Eq. (5.35) and $m = V \rho_r$, this results in $X \propto \sqrt[3]{m}$. Therefore, masses of three granite boulders were chosen such that $\sqrt[3]{m}$ is approximately equally-spaced resulting in $m \in \{4380 \text{ kg}; 10160 \text{ kg}; 18260 \text{ kg}\}$. For specification of three different heights of fall, it was assumed that $19180 h_f$, with $h_f \in [0 \text{ m}; 20 \text{ m}]$, can be neglected in comparison with R in Eq. (5.42) which yields $X \propto \sqrt{h_f}$ for constant R and d . This assumption was justified *a posteriori*, since back-analyzed values for R are of the order of magnitude 10^7 Pa , see Table 5.3 and Section 5.3.3. Based on $X \propto \sqrt{h_f}$, three heights of fall were chosen such

that $\sqrt{h_f}$ is equally-spaced. Mathematical results were rounded to the nearest integer resulting in $h_f \in \{2 \text{ m}; 9 \text{ m}; 20 \text{ m}\}$.

In a quarry a trench of 25 m length, 4 m width, and 2 m depth was filled with wide-range-grained gravel: the volume fraction of fine-, medium-, and coarse-gravel (diameters from 2 – 63 mm) was equal to 60 %. The remaining volume fraction of 40 % consisted of edged stones (diameters from 63 – 200 mm). The gravel was filled into the trench in layers of 25 cm thickness. Each layer was densified by hand-guided compaction units. The mass density of the gravel was equal to 1800 kg/m^3 .

Each rock boulder was equipped with an accelerometer PCB-353B03 (PCB PIEZOTRONICS Inc., 2002), allowing to measure the acceleration of the rock in the vertical direction.

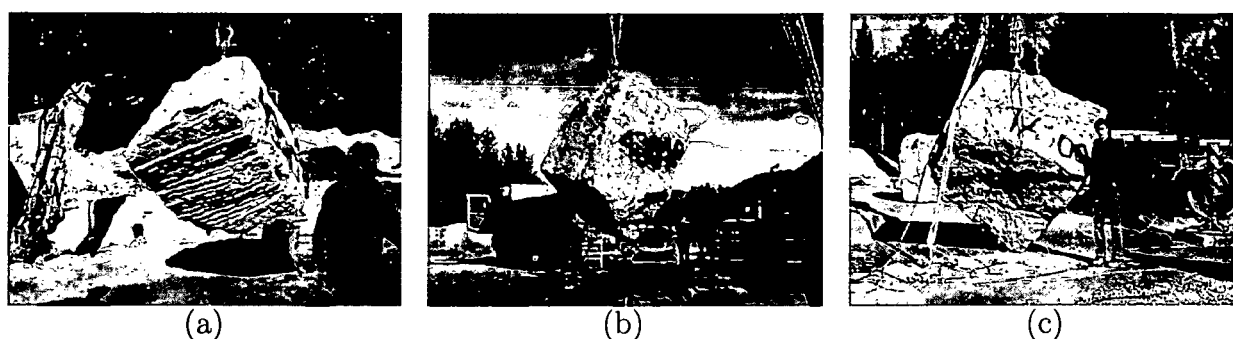


Figure 5.10: (a) 4380 kg granite boulder, (b) 10160 kg granite boulder, (c) 18260 kg granite boulder

5.3.3 Evaluation of experimental results

Penetration depths X were measured as a function of the mass m of the rock boulders and the height of fall h_f . This was done by means of a stadia rod after the rocks had been lifted out of the crater, see Table 5.3. In some cases, the granite boulders tipped over immediately after the impact. Thereby, the tip of the rock dug the flank of the crater, rendering measurement of the penetration depth with the stadia rod useless. Consequently, penetration depths were calculated by integrating the accelerometer measurements twice. Since these measurements were afflicted with inaccuracies, this analysis did not yield realistic values for the penetration depths. Hence, for further evaluation of test results for penetration depths, only five experimental results are available. The dimensionless penetration depths X/d obtained from these five tests lie within the interval $[0.16; 0.43]$. Remarkably, this interval is part of the interval $[0.04; 5.80]$, for which the validity of the Eqs. (5.30) and (5.31) was proved by Li and Chen (Li and Chen, 2003), see Table 5.2.

Table 5.3: Penetration depths measured by means of a stadia rod after lifting the rocks out of their crater, characteristic length d of the rock boulders, and results from back analysis of the indentation resistance R according to the Eq. (5.42)

mass (m)	height of fall (h_f)	penetration depth (X)	remark	characteristic length (d)	indentation resistance (R)
4380 kg	2.03 m	0.14 m	tipped over		
4380 kg	8.94 m	0.21 m	tipped over		
4380 kg	19.30 m	0.37 m	tipped over		
10160 kg	2.00 m	0.26 m		1.63 m	$8.13 \cdot 10^6$ Pa
10160 kg	8.55 m	0.51 m		1.63 m	$8.91 \cdot 10^6$ Pa
10160 kg	18.75 m	0.53 m	tipped over		
18260 kg	2.05 m	0.34 m	tipped over		
18260 kg	8.62 m	0.65 m		1.99 m	$8.16 \cdot 10^6$ Pa
18260 kg	18.67 m	0.82 m		1.99 m	$10.98 \cdot 10^6$ Pa
18260 kg	18.85 m	0.85 m		1.99 m	$10.29 \cdot 10^6$ Pa

Estimation of penetration depth

Material parameters of soil, in general, and of gravel, in particular, are characterized by a large scattering (Terzaghi et al., 1996). Hence, the scatter of the indentation resistance R is expected to be by far larger than possible measurement inaccuracies concerning m , h_f , and X . This allows for back analysis of R for each of the five considered tests. For this purpose, considering $m = V \rho_g$, $\rho_g = 1800 \text{ kg/m}^3$, and Eq. (5.35), the characteristic length d of the respective rock boulders is calculated first (see Table 5.3). Secondly, Eq. (5.42) allows for calculation of the indentation resistance of gravel, R , from the values for X , d , and h_f given in Table 5.3. The back-analyzed values for R are ranging between 8.13 MPa and 10.98 MPa. They constitute a sample of the statistical population of the strength-like indentation resistance, with sample size $n = 5$.

According to commonly used standards such as, e. g., the EUROCODE (CEN-EVN-1991-1, 1994), the design of structures should be based on 5%-quantiles of strengths. A respective small value for the indentation resistance will yield large penetration depths but small impact forces. Since both penetration depths and impact forces are relevant for the design of rockfall protection systems, not only the 5%-quantile of R , but also its 95%-quantile is calculated. The respective high value of indentation resistance will yield

relatively small penetration depths but large impact forces.

The strength-like indentation resistance can only take positive values. Taking this into account and assuming that the distribution of the indentation resistance represents the result of a multiplicative mechanism of a number of influence factors, (Benjamin and Cornell, 1970), the lognormal distribution is suitable to describe the statistical characteristics of the R -population. Consequently, the sample of the logarithms of the back-analyzed values, $\log[(R)_i/R^*]$, $i = 1, 2, \dots, 5$, can be considered as normally distributed. The constant R^* is introduced in order to provide a dimensionless argument for the natural logarithm. Since R^* does not influence the final results, it is set equal to an arbitrary value; herein $R^* = 1 \text{ Pa}$.

The expected value and the variance of a normally distributed population, denoted as μ and σ , respectively, permit evaluation of the 5 %- and 95 %-quantiles of the population. These values are estimated analogously to the procedure described by König et al. (König et al., 1998) for compressive strengths of concrete. I. e., first the mean value \bar{x} and the empirical standard-deviation s of the logarithmic sample with the size $n = 5$ are determined. This gives

$$\bar{x} = \frac{1}{n} \sum_{i=1}^n \log \left(\frac{R_i}{R^*} \right) = 16.04 \quad \text{for} \quad R^* = 1 \text{ Pa}, \quad (5.43)$$

and

$$s^2 = \frac{1}{n-1} \sum_{i=1}^n \left[\log \left(\frac{R_i}{R^*} \right) - \bar{x} \right]^2 \Rightarrow s = 0.1362, \quad (5.44)$$

respectively. Based on these quantities, a *two*-sided confidence interval for the expected value μ of the $\log[R/R^*]$ -population, $[\mu_{low}, \mu_{upp}]$, is determined as follows:

$$\mu_{low} = \bar{x} - \frac{s \cdot t_{n-1, 1-\alpha/2}}{\sqrt{n}} \leq \mu \leq \bar{x} + \frac{s \cdot t_{n-1, 1-\alpha/2}}{\sqrt{n}} = \mu_{upp}, \quad (5.45)$$

where $t_{n-1, 1-\alpha/2}$ denotes the t -value that cuts an area equal to $1 - \alpha/2$ of the Student's t distribution with $n - 1$ degrees of freedom. α stands for the significance level which is equal to 5 % for a 95 % confidence interval, see e. g. (Bortz, 1999). Inserting Eqs. (5.43) and (5.44), $n = 5$, $\alpha = 5 \%$, and $t_{4, 0.975} = 2.776$ into (5.45), yields

$$\mu_{low} = 15.87 \leq \mu \leq 16.21 = \mu_{upp} \quad \text{for} \quad R^* = 1 \text{ Pa}. \quad (5.46)$$

In order to obtain an upper bound of the standard deviation σ of the $\log[R/R^*]$ -population, a *one*-sided confidence interval is determined,

$$\sigma \leq \sqrt{\frac{(n-1) \cdot s^2}{\chi_{n-1, \alpha}^2}} = \sigma_{upp}, \quad (5.47)$$

where $\chi_{n-1, \alpha}^2$ denotes the χ^2 -value that cuts an area equal to α of the chi-squared distribution with $n - 1$ degrees of freedom, see e. g. (Bortz, 1999). Inserting Eq. (5.44), $n = 5$, $\alpha = 5\%$, and $\chi_{4, 0.05}^2 = 0.7107$ into (5.47) yields

$$\sigma \leq 0.3230 = \sigma_{upp}. \quad (5.48)$$

Probability distribution functions of the indentation resistance resting on \bar{x} , μ_{low} , μ_{upp} , and σ_{upp} according to Eqs. (5.43), (5.46), and (5.48) are illustrated in Fig. 5.11. The 5%- and

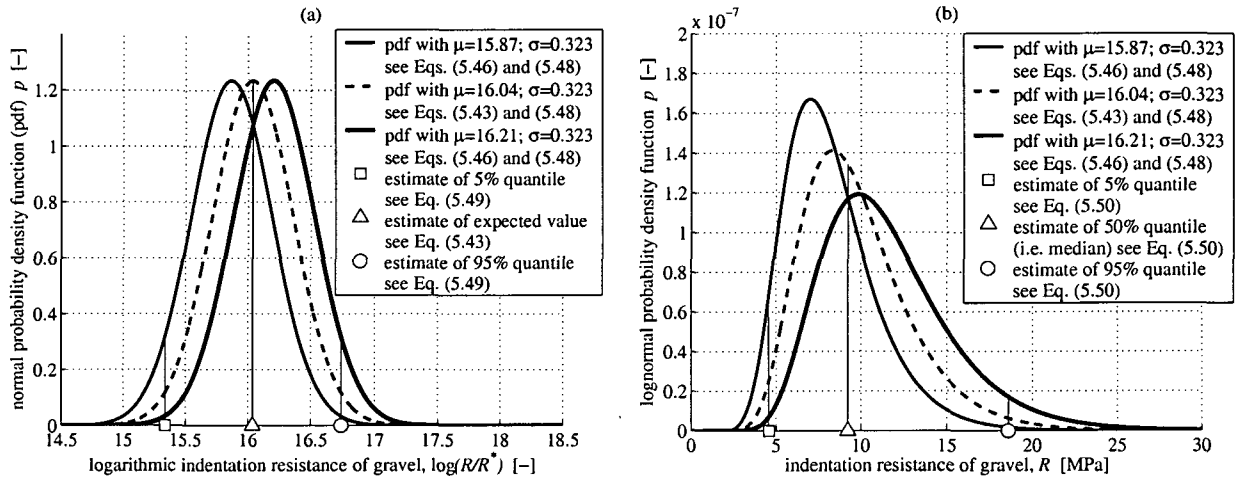


Figure 5.11: Probability distribution functions (pdfs) of the indentation resistance providing estimates of the 5%-quantile and the 95%-quantile of the indentation resistance (shaded areas are equal to 5%): (a) pdfs of normally distributed $\log(R/R^*)$ -population (b) pdfs of lognormally distributed R -population; (both diagrams are equivalent representations)

95%-quantiles of the $\log[R/R^*]$ -population are calculated on the basis of 95% confidence intervals for the expected value μ and the standard deviation σ of the $\log[R/R^*]$ population as

$$\begin{aligned} \log\left(\frac{R}{R^*}\right)_{5\%} &= \mu_{low} - z_{0.025} \cdot \sigma_{upp} = 15.34, & \text{for } R^* = 1 \text{ Pa}, \\ \log\left(\frac{R}{R^*}\right)_{95\%} &= \mu_{upp} + z_{0.025} \cdot \sigma_{upp} = 16.74, & \text{for } R^* = 1 \text{ Pa}, \end{aligned} \quad (5.49)$$

with the numerical values of μ_{low} , μ_{upp} and σ_{upp} from the Eqs. (5.46) and (5.48). $z_{0.025} = 1.6449$ denotes the z -value that cuts an area equal to 95% of the standardized normal distribution. Application of the exponential function to \bar{x} , $\log(R/R^*)_{5\%}$ and $\log(R/R^*)_{95\%}$, see Eqs. (5.43) and (5.49), and multiplication of the obtained results with $R^* = 1 \text{ Pa}$ finally yields

$$R_{50\%} = 9.22 \cdot 10^6 \text{ Pa}, \quad R_{5\%} = 4.58 \cdot 10^6 \text{ Pa}, \quad \text{and} \quad R_{95\%} = 18.58 \cdot 10^6 \text{ Pa}, \quad (5.50)$$

where $R_{50\%} = R^* \cdot \exp(\bar{x})$, $R_{5\%}$, and $R_{95\%}$ denote the median (i. e., the 50%-quantile), the 5%-quantile and the 95%-quantile of the R -population, respectively. Penetration depth - height of fall diagrams based on $R_{5\%}$ and $R_{95\%}$ (Fig. 5.12) show wide bounds for the probability-based estimates of penetration depths. These bounds follow from the

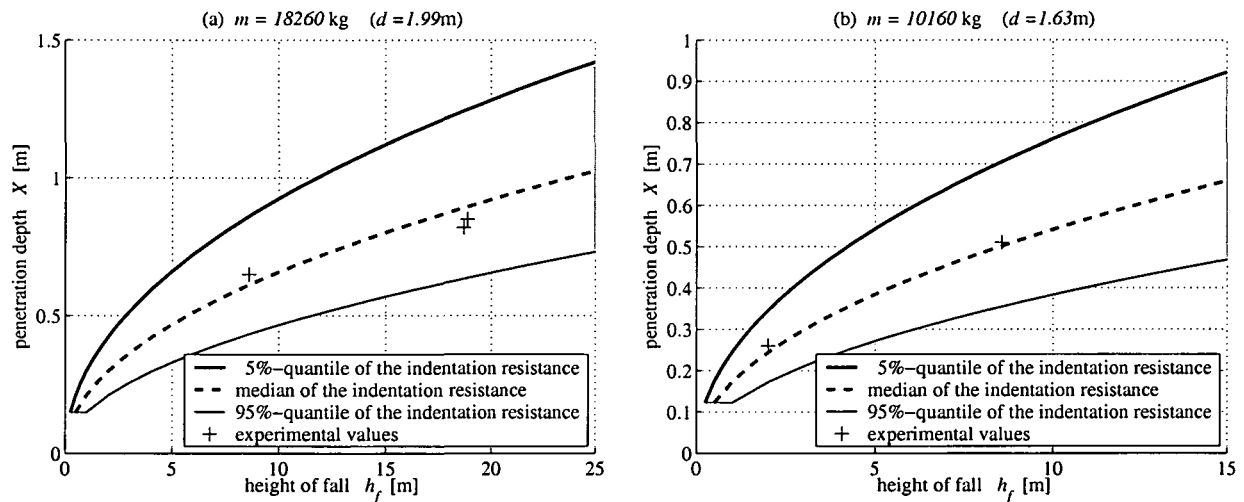


Figure 5.12: Comparison of model results (Eq. (5.42) with $R = R_{5\%}$, $R = R_{50\%}$, $R = R_{95\%}$) and experimental results (see Table 5.3) for (a) the 18260 kg rock boulder and (b) the 10160 kg rock boulder

scatter of the material properties of gravel but also from the statistically small number of performed tests. Nevertheless, the model results based on the estimate of the median of the indentation resistance, $R_{50\%}$, show very good agreement ($r^2 = 0.982$) with the experimentally obtained penetration depths (see also Fig. 5.12 and Table 5.3). This fact underlines the usefulness of the presented approach.

Estimation of impact duration and impact force

The design of protection systems for rockfall requires estimates of both the penetration depths and the dynamic forces acting onto the system during the impact. Newton's second law for a rock boulder reads: $F_r(t) = m \cdot a(t)$, where $F_r(t)$ denotes the resultant of the forces acting on a rock boulder with mass m at time t , moving with the total acceleration $a(t)$. Consideration of Newton's third law – "*Actioni contrariam semper et aequalem esse reactionem*" – permits calculation of the force F_g acting onto the hit material (gravel) as:

$$F_g(t) = m \cdot [g - a(t)], \quad (5.51)$$

where g stands for the gravitational acceleration. Consequently, the estimation of impact forces requires a model for the description of the deceleration of the rock boulder during

impact. The following kinematic conditions at the beginning ($t = 0$) and at the end ($t = \Delta t_i$) of the impact are considered:

$$\begin{aligned}
 t = 0 & : a = g \dots (5.52.a), & v = v_0 = \sqrt{2gh_f} \dots (5.52.b), & w = 0 \dots (5.52.c), \\
 t = \Delta t_i & : a = 0 \dots (5.52.d), & v = 0 \dots (5.52.e), & w = X \dots (5.52.f),
 \end{aligned}
 \tag{5.52}$$

where v and w denote the indentation velocity and the indentation depth, respectively. X stands for the penetration depth according to the Eqs. (5.42), which is determined for a specific rockfall event characterized by specific values m , h_f , and R .

Information on the deceleration history of rock boulders is obtained from measurements of the aforementioned PCB-353B03 accelerometer. Although these measurements suffer from quantitative inaccuracies, they provide qualitative insight into the impact kinematics, see, e.g. Fig. 5.13. The measured acceleration histories can be approximated by a bell-

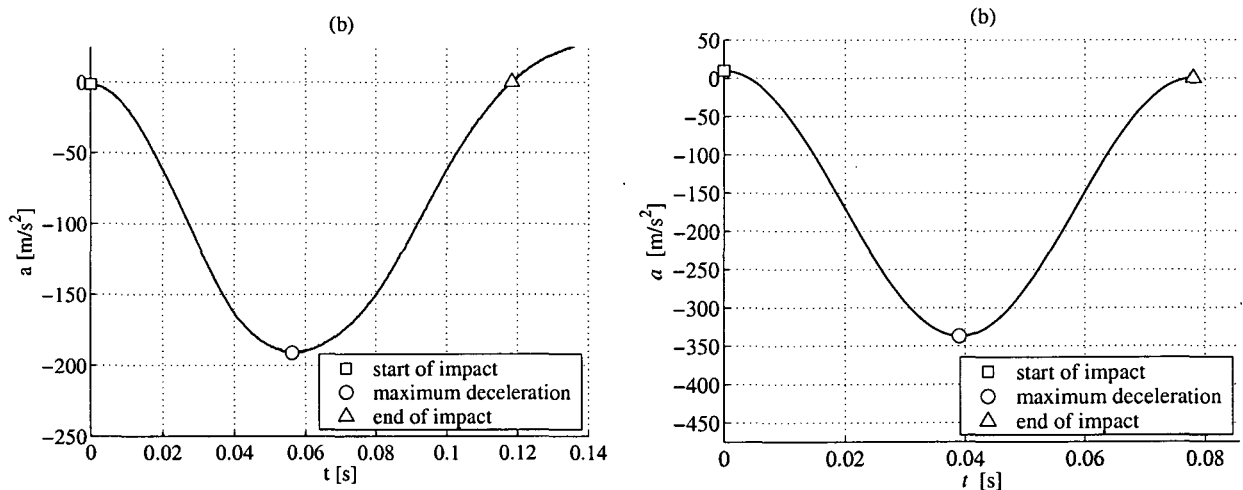


Figure 5.13: (a) Typical acceleration history (suffering from quantitative inaccuracies) recorded by the PCB-353B03 accelerometer (PCB PIEZOTRONICS Inc., 2002) for a rock boulder with mass $m = 10160$ kg falling from a height $h_f = 8.55$ m and (b) qualitatively equivalent acceleration history for this rockfall experiment ($X = 0.51$ m), according to the Eqs. (5.52), (5.53), and (5.56)

shaped curve. As a first approximation, the acceleration histories will be described as a cosine-like function

$$a(t) := g \left(1 - \frac{t}{\Delta t_i} \right) - \left(\frac{v_0}{\Delta t_i} + \frac{g}{2} \right) \left[1 - \cos \left(\frac{2\pi t}{\Delta t_i} \right) \right]. \tag{5.53}$$

Definition (5.53) satisfies the conditions $a(0) = g$ and $a(\Delta t_i) = 0$. The function $v(t)$ is

obtained by integrating the Eq. (5.53):

$$v(t) = v_0 + g \left(t - \frac{t^2}{2 \Delta t_i} \right) - \left(\frac{v_0}{\Delta t_i} + \frac{g}{2} \right) \left[t - \frac{\Delta t_i}{2\pi} \sin \left(\frac{2\pi t}{\Delta t_i} \right) \right]. \quad (5.54)$$

The function $w(t)$ is obtained by integrating the Eq. (5.54):

$$w(t) = v_0 t + g \left(\frac{t^2}{2} - \frac{t^3}{6 \Delta t_i} \right) - \left(\frac{v_0}{\Delta t_i} + \frac{g}{2} \right) \left\{ \frac{t^2}{2} + \frac{\Delta t_i^2}{4\pi^2} \left[\cos \left(\frac{2\pi t}{\Delta t_i} \right) - 1 \right] \right\}. \quad (5.55)$$

The integration constants are specified such that the Eqs. (5.54) and (5.55) satisfy the conditions $v(0) = v_0$ and $w(0) = 0$. Moreover, Eq. (5.54) satisfies the condition $v(\Delta t_i) = 0$. Consideration of the boundary condition $w(\Delta t_i) = X$, see Eq. (5.52.f), finally yields:

$$X = \frac{\Delta t_i v_0}{2} + \frac{\Delta t_i^2 g}{12}. \quad (5.56)$$

$g = 9.81 \text{ m/s}^2$ is generally smaller by at least one order of magnitude than the maximum deceleration during impact, e. g. $\max |a| = 340 \text{ m/s}^2$, see Fig. 5.13(b). Therefore, to keep the following developments as simple as possible, the condition $a(0) = g$, see Eq. (5.52.a), may be approximated by setting $a(0)$ equal to 0. This results in the omission of the second term on the right-hand side of Eq. (5.56), yielding

$$X = \frac{\Delta t_i v_0}{2} \Rightarrow \frac{\Delta t_i v_0}{d} = 2 \frac{X}{d}. \quad (5.57)$$

Insertion of Eq. (5.57) into the Eqs. (5.27) and (5.28) allows to identify the relation $\mathcal{F}_2 = 2 \mathcal{F}_1$. Hence, a diagram for the dimensionless impact duration $\Delta t_i v_0/d$ can be obtained by rescaling the ordinate of the (X/d) - I diagram of Fig. 5.9 representing $\pi_X = \mathcal{F}_1(\pi_R = I)$, by the factor 2, see Fig. 5.14.

In order to assess the validity of Eq. (5.57), the impact duration of the experimentally investigated rock boulder with a mass of 18260 kg, falling down from a height of 18.85 m, is analyzed. For the respective values of Table 5.3, Eq. (5.57) yields

$$\Delta t_i = \frac{2 X}{v_0} = \frac{2 X}{\sqrt{2 g h_f}} = \frac{2 \cdot 0.85}{\sqrt{2 \cdot 9.81 \cdot 18.85}} = 0.088 \text{ s}. \quad (5.58)$$

This value of Δt_i is compared with experimentally obtained data. For this purpose, images of the impact, recorded by a SONY DCR-PC120 video camera, are analyzed (Fig. 5.15). The recording frequency of the camera was equal to 25 Hz. Therefore, the time span between two following images was equal to 0.04 s. The time instant of the first contact of the rock boulder and the gravel lay between the time instants at which Img. 2 and Img. 3 were recorded. The end of the impact lay between the time instants at which Img. 4 and Img. 5 were recorded. Therefore, the actual impact duration must lie between 0.04 s

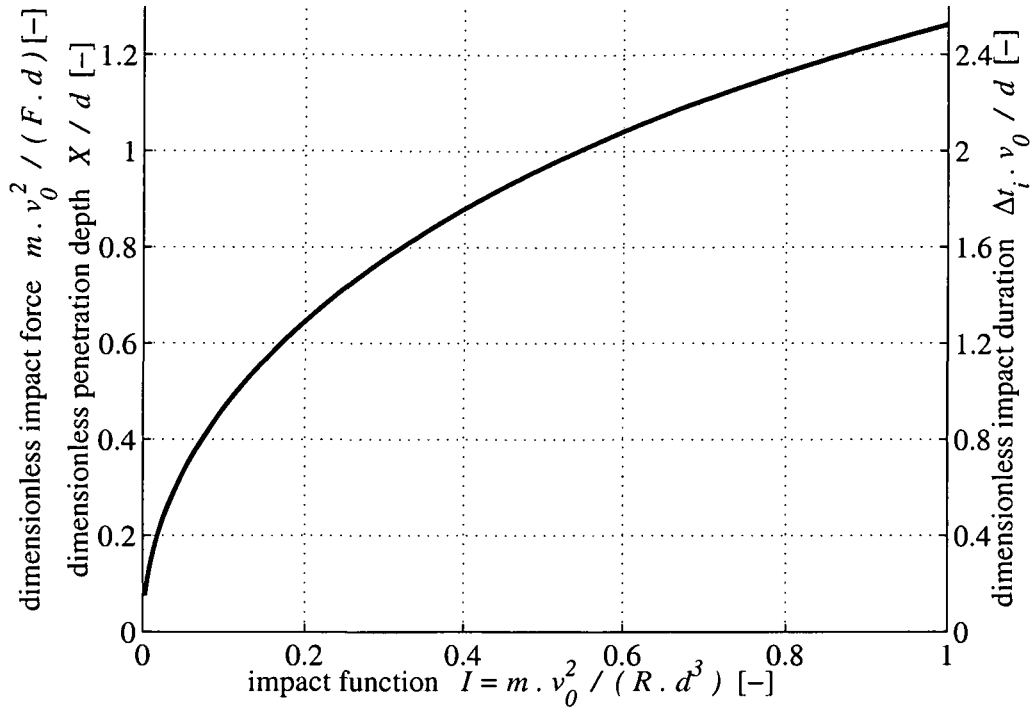


Figure 5.14: Dimensionless penetration depth X/d , impact duration $\Delta t_i v_0/d$, and impact force $m v_0^2/(F d)$ as functions of I for granite boulders of approximately cubic shape (mass density $\rho_r = 2700 \text{ kg/m}^3$) with mass m and characteristic length d , impacting at the velocity v_0 with a tip onto gravel with indentation resistance R and mass density $\rho_g = 1800 \text{ kg/m}^3$

and 0.12 s. Hence, the value for the impact duration according to the approximation of Eq. (5.57), $\Delta t_i = 0.088 \text{ s}$, does not contradict experimental results.

Specialization of Eq. (5.53) for $g \ll \max |a|$ and satisfaction of the condition $da/dt = 0$ renders the time instant $t_{\max |a|}$ at which the deceleration of the rock boulder takes on a maximum:

$$t_{\max |a|} = \frac{\Delta t_i}{2}. \quad (5.59)$$

Substituting this result into Eq. (5.53) with $g \ll \max |a|$ yields the maximum deceleration of the rock boulder $\max |a|$ as

$$\max |a| = \frac{2 v_0}{\Delta t_i}. \quad (5.60)$$

The maximum impact force F acting onto the gravel is obtained by insertion of Eq. (5.60) into Eq. (5.51). Neglecting again g in comparison to $\max |a|$, yields

$$F = \frac{2 v_0 m}{\Delta t_i}. \quad (5.61)$$

Multiplication of the reciprocal representation of Eq. (5.61) by $m v_0^2/d$ and consideration

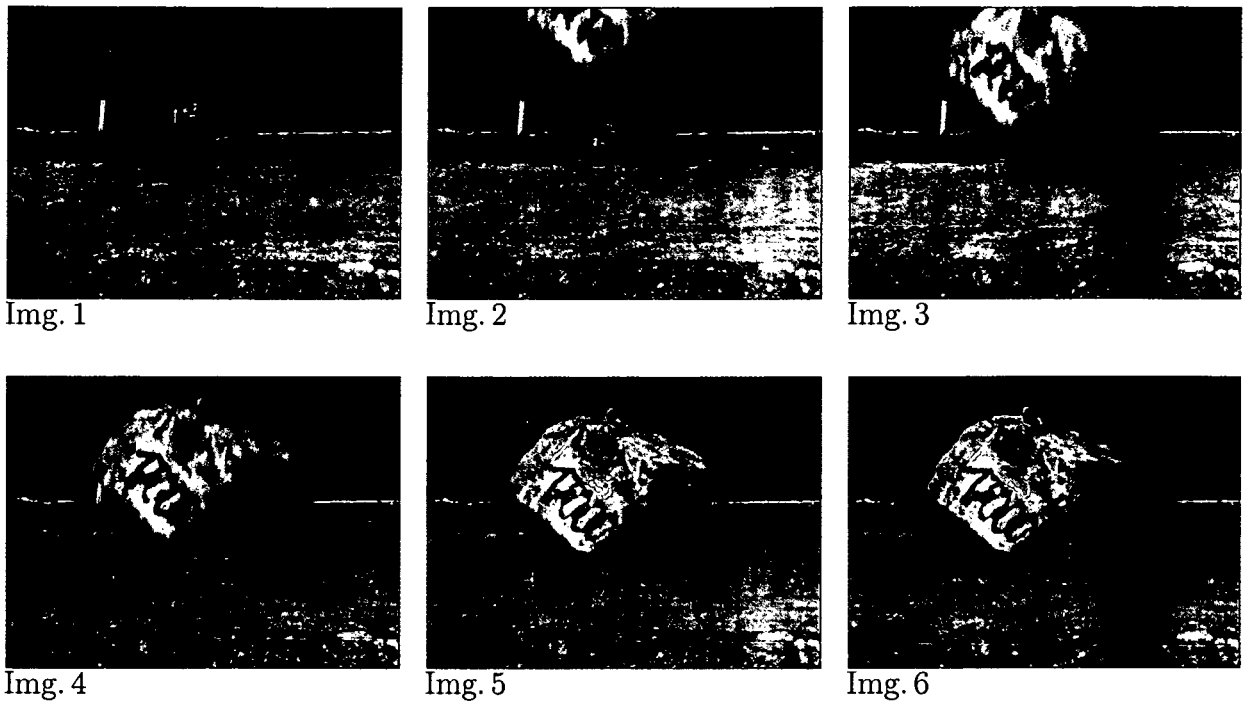


Figure 5.15: Images recorded by a SONY DCR-PC120 video camera of the impact of the 18260 kg rock boulder falling down from 18.85 m; the time span between two following images is equal to 0.04 s

of Eq. (5.57) leads to the dimensionless relation

$$\frac{m v_0^2}{F d} = \frac{\Delta t_i v_0}{2 d} = \frac{X}{d} \quad (5.62)$$

Insertion of Eq. (5.62) into the Eqs. (5.27) and (5.29) allows to identify the relation $\mathcal{F}_3 = 1/\mathcal{F}_1$. Hence, a diagram for the dimensionless impact force $m v_0^2/(F d)$ can be obtained by adding an additional label to the ordinate of the (X/d) - I diagram of Fig. 5.9 representing $\pi_X = \mathcal{F}_1(\pi_R = I)$, see Fig. 5.14.

From the dimensionless three-in-one diagram illustrated in Fig. 5.14, several dimensional diagrams can be derived, such as the ones shown in Fig. 5.16. For design purposes, where the penetration depth is relevant, diagrams obtained with the 5%-quantile of the indentation resistance should be considered, see Figs. 5.16(a) and (b). For cases where impact forces are of interest, diagrams obtained with the 95%-quantile of the indentation resistance are relevant, see Figs. 5.16(c) and (d). The dimensional diagrams show that the penetration depth is a strongly nonlinear function of the height of fall and the mass of the rock boulder, see Figs. 5.16(a) and (b). The maximum impact force depends also strongly on h_f and m . However, the nonlinearities are not so pronounced as for X , see Figs. 5.16(c) and (d). Remarkably, the impact duration does not vary significantly with the height of fall, whereas the rock boulder mass is a governing factor for Δt_i , see Figs. 5.16(e) and (f).

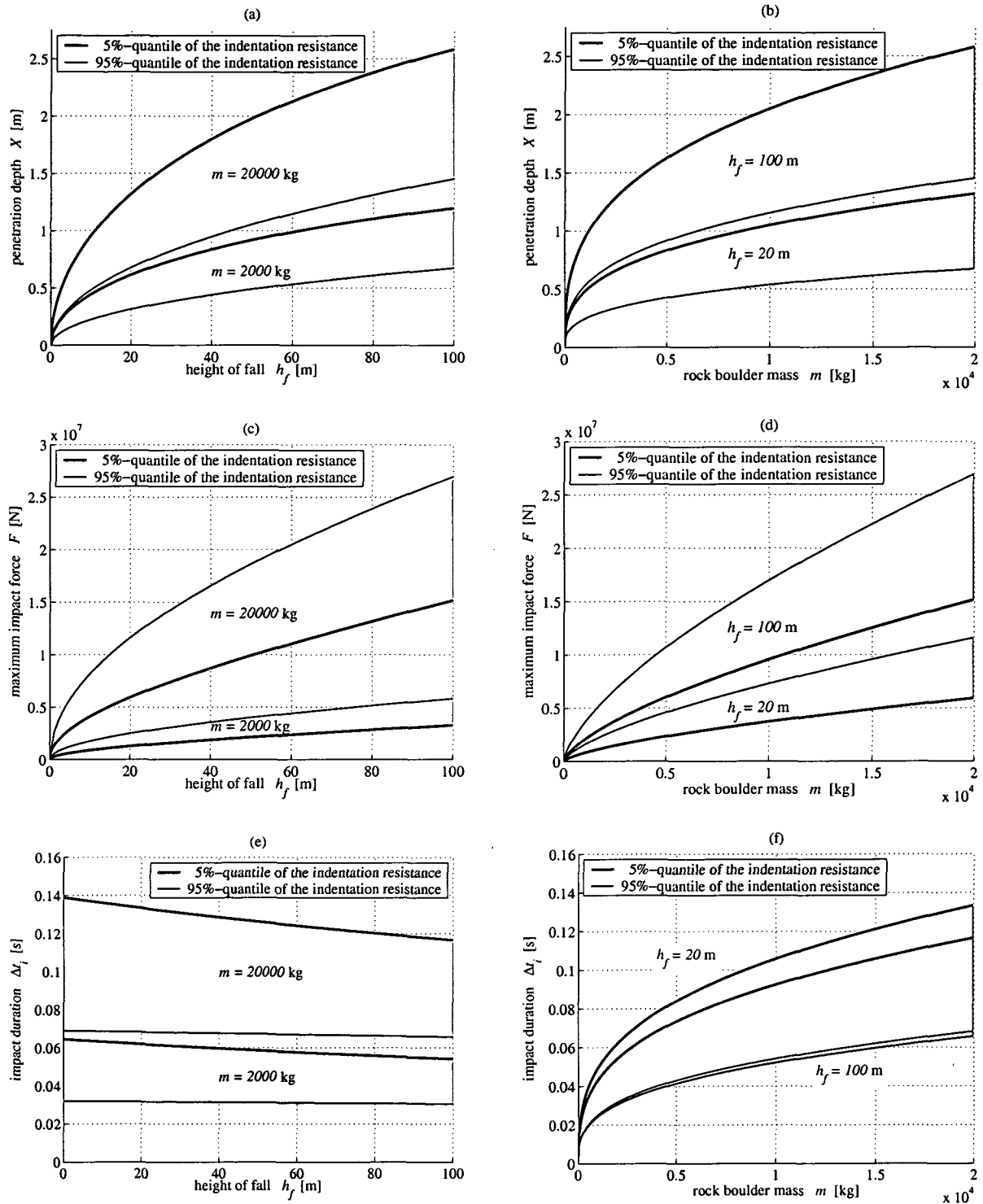


Figure 5.16: Dimensional diagrams derived from the dimensionless diagram in Fig. 5.14 concerning the penetration depth X , see (a) and (b), the maximum impact force F , see (c) and (d), and the impact duration Δt_i , see (e) and (f), as a function of the height of fall h_f , the rock boulder mass m , and the indentation resistance of gravel, R

5.3.4 Summary and Conclusions

In this subchapter rockfall events characterized by rock boulders of approximately cubic shape impacting with a tip onto gravel, were analyzed. Based on dimensional analysis, it was found that three dimensionless parameters, representing the penetration depth, the impact duration, and the impact force, are functions of only one single dimensionless parameter which includes the strength-like indentation resistance of gravel and the height of fall. These findings may be considered as an extension of formulae for dimensionless penetration depth, reported by Li and Chen (Li and Chen, 2003). These formulae, which are based on Forrestal's relationships (Forrestal et al., 1994; Forrestal et al., 1996) describing the penetration depth of non-deformable projectiles onto concrete and soil targets, were adopted for rockfall scenarios. This adaption was the basis for the design of rockfall experiments comprising different heights of fall (< 20 m) and different rock boulder masses (< 20000 kg). Results from these experiments allow for identification of the indentation resistance of gravel, which is characterized by a significant scatter as is typical for material parameters in geotechnical engineering. In order to quantify this scatter, back-analyzed values for the indentation resistance were evaluated statistically, allowing for the estimation of the 5%- and 95%-quantiles of the indentation resistance of gravel. Insertion of these values into the aforementioned dimensionless functions leads to bounds for the penetration depth, the impact duration, and the impact force, as functions of the height of fall and the mass of the rock boulders. These bounds are consistent with the probability-based philosophy of commonly used standards such as, e. g. the EUROCODE (CEN-EVN-1991-1, 1994). Given the wide range of dimensionless parameters for which Li and Chen have validated their dimensionless formulae, the aforementioned bounds even comprise rockfall events that could not be investigated experimentally.

5.4 Development and assessment of a structural model

This subchapter deals with the experimental and numerical realization and verification of a structural model that provides reliable estimates of the loading of a gravel-buried steel pipe subjected to rockfall. In more detail, a pipeline with an outer diameter $d_a = 1016$ mm and a wall thickness $s = 11.13$ mm is considered. It is buried in the middle of a trench of 3 m width, resting on a 50 cm thick layer of sand. The tube is laterally buried up to a height of 40 cm by sand, and the rest of the trench is filled by wide-range-grained gravel, see Figure 5.17 (a). The volume fraction of fine-, medium-, and coarse-gravel (diameters

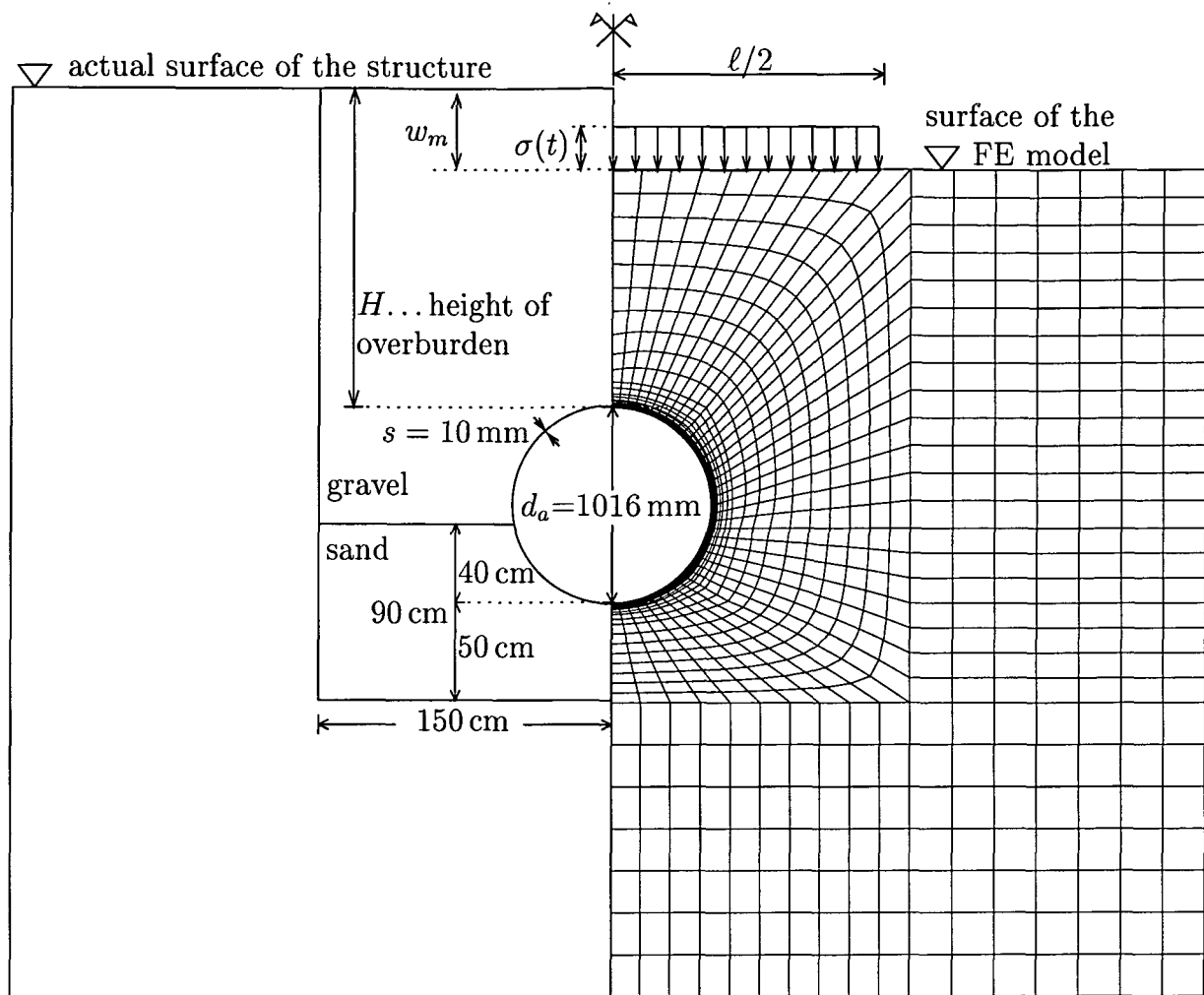


Figure 5.17: Geometric dimensions of the problem under consideration, and simplified structural model of the buried pipeline used for the preliminary Finite Element analysis

from 2 – 63 mm) is equal to 60%. The remaining volume fraction of 40% consists of edged stones (diameters from 63 – 200 mm). The gravel is filled into the trench in layers of 25 cm thickness, which are densified by hand-guided compaction units. The mass density of the material is equal to 1800 kg/m^3 .

If a downfalling rock boulder impacts onto the overburden of the pipe, the kinetic energy of the rock boulder is transformed into other types of energy. The gravel acts as an energy-absorbing and load-distributing system. Most of the impact energy is dissipated such that inelastic deformations in the overburden are produced, i. e., an impact crater is caused. Other parts of the impact energy are transmitted by elasto-plastic waves through the gravel to the buried pipeline. The latter represents a rather stiff component of the statically overdetermined load-carrying system.

5.4.1 Preliminary investigation of structural behavior – design of experimental setup

In order to obtain *reliable* insight into the structural behavior of a gravel-buried pipeline subjected to rockfall, real-scale experiments are very beneficial. Obviously, such tests cannot be performed along the track of an existing pipeline which is in full service. Real-scale rockfall tests require the production of an experimental pipeline track. For definition of (i) the minimum length of such a track required for representative experimental results and of (ii) an adequate measurement system recording the loading of the pipe during the impact, a preliminary Finite Element analysis (PFEA) was performed.

For this analysis, a simplified, but nevertheless reasonable representation of the loads arising from rockfall was chosen. Instead of modeling the almost completely inelastic indentation process of the rock boulder, the overburden of the FE model was reduced by the mean indentation depth w_m (see Figure 5.17 and Appendix D). Spatially constant normal stresses with a time-dependent amplitude were applied to the surface of the FE model. Assuming that an approximately cubic rock boulder impacts with a face onto the overburden, a quadratic area of the impact was considered; with side length $\ell = \sqrt[3]{V}$, where V denotes the volume of the rock boulder. Consequently, the prescribed normal stresses σ follow from the impact force history $F(t)$ as $\sigma(t) = F(t)/\ell^2$. For the PFEA, $F(t)$ was approximated by a polynomial, see Appendix D. As a first approximation, all phenomena except for the indentation of the rock boulder were assumed to be of isotropic and linear elastic nature. Accordingly, transient-dynamic linear-elastic analyses were performed, and a comprehensive parameter study was carried out. As far as the properties of the impact are concerned, the penetration depth was set equal to 60 cm. This assumption corresponds to a rockfall event that took place in September 2001 in the Austrian Alps, where a down-falling rock boulder caused a 60 cm deep crater into the overburden of a mountain-crossing pipeline. Corresponding to this choice of the penetration depth, the mean indentation depth w_m (see Figure 5.17 (b)) was set equal to 40 cm. Rock boulder masses were chosen out of the interval [21200 kg; 53000 kg] (these data correspond to rock boulder volumes out of [8 m³; 20 m³]), and heights of fall were chosen out of the interval [5 m; 30 m]. The height of overburden of the pipeline, H (see Figure 5.17 (b)), was set equal to 1.2 m, 1.6 m, and 2.4 m, respectively. Values chosen for Young's modulus, Poisson's ratio, and mass density of steel, gravel, sand, and the soil surrounding the trench containing the pipeline are summarized in Table 5.4. The PFEA comprised two types of two-dimensional structural simulations: The first model was developed to study the behavior of the pipe beneath the impact location. For this purpose plane strain FE simulations referring to the cross-sectional plane of the pipe were performed. The second model was developed to study the

Table 5.4: Young's modulus, Poisson's ratio, and mass density of steel, gravel, sand, and soil chosen for the PFEA

material	Young's modulus E	Poisson's ratio ν	mass density ρ
steel	210 GPa	0.3	7850 kg/m ³
gravel, sand	[0.05 GPa; 1.00 GPa]	0.3	2000 kg/m ³
soil*	[0.5 GPa; 50 GPa]	[0.17 ; 0.3]	[2000 kg/m ³ ; 2650 kg/m ³]

* $E = 50$ GPa, $\nu = 0.17$, and $\rho = 2650$ kg/m³ refer to granite

load-carrying mode of the pipe idealized as an elastically-supported truss.

The following results of the PFEA, providing insight into the structural behavior of a gravel-buried steel pipe subjected to rockfall, are remarkable: (i) dead load results in stresses in the pipe, which are by two orders of magnitude smaller than the stresses caused by the investigated types of impact, see, e. g., Figure 5.18 (a). Hence, dead load does not have to be taken into account in the case of a numerical analysis considering rockfall. (ii) the load-carrying behavior of the (almost) infinitely long pipe is governed by both a local and a global loading effect. The local effect is observed in the vicinity of the impact location only. It arises from the concentrated impact load and is referred to as ovalization of the pipe. The global effect corresponds to the load distribution in the direction of the axis of the cylindrical tube. In this context, the structural behavior of the pipe refers to an (almost) infinitely long elastically-supported truss subjected to a single, rather concentrated load. (iii) Results of dynamic FE simulations were compared with results obtained by quasi-static analyses. In the latter simulations, the maximum dynamic impact-force was applied to the numerical model in a quasi-static manner. Both types of analyses yielded similar results, i. e., the obtained maximum von Mises stresses differ by less than 5%, see e. g. Figure 5.18 (a). This is an acceptably small deviation for technical design purposes. Accordingly, the propagation of elastic waves resulting from the impact are not important for the loading of the pipe. This follows from two circumstances: (a) elastic waves resulting from the impact propagate through the entire structure during a time span much shorter than the duration of the impact. (b) Reflected waves do not contribute significantly to the loading of the pipe, because they produce a loading which is much more diffuse than the concentrated loading resulting from the impact. Therefore, quasi-static analyses can be performed instead of dynamical analyses. This reduces the required numerical efforts by orders of magnitude. Moreover, the discretized domain for the analysis of rockfall does not need to be larger than the domain to be considered in static analyses. This is different for vibration problems in soil-dynamics, see, e. g., (Studer and Ziegler, 1986). Vibration

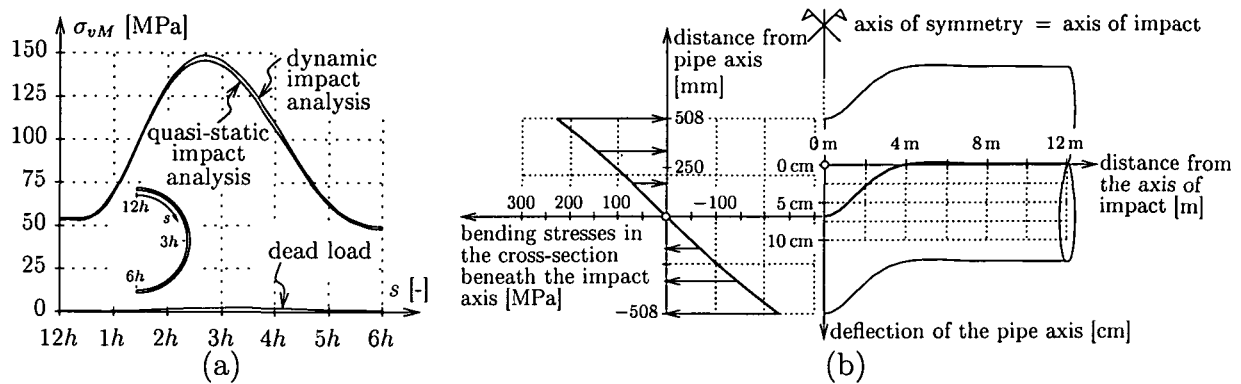


Figure 5.18: Results from the PFEA: (a) ovalization of the cross-section of the pipe: distribution of von Mises stress along the inner surface of the pipe resulting from dead load and from rock boulder impact, obtained from a dynamic and a quasi-static analysis, respectively, and (b) load-carrying mode of the pipe idealized as an elastically-supported truss: deflection of the pipe axis as a function of the distance from the axis of the impact and bending stresses of the pipe obtained beneath the impact axis (analysis parameters: height of overburden: $H = 1.2$ m; investigated rockfall event: $h_f = 10$ m, $V = 15$ m³, $X = 0.6$ m [see Appendix D]; material properties [see also Table 5.4]: (i) gravel and sand: $E = 0.5$ GPa, (ii) surrounding soil [limiting case]: rigid)

problems are characterized by oscillation periods which are comparable to or even smaller than the characteristic time span required for waves to pass through the structures.

The following two results of the PFEA allow for definition of the experimental setup for a real-scale test: (i) Both load-carrying modes of the pipe, i. e., ovalization of the tube and loading of the pipe as an elastically-supported truss, cause stresses of the same order of magnitude, Figures 5.18 (a) and (b). As far as ovalization of the cross-section of the pipe is concerned, the maximum loading of the tube in terms of the von Mises stress appears at the inner surface of the pipe slightly above $3h$ and $9h$ respectively.² Moreover, a local loading-maximum is encountered at $12h$ on the outer surface of the pipe. The maximum von Mises stresses obtained in the simulation as an elastically-supported truss appears at $12h$ and $6h$, respectively. They correspond to bending of the tube. Based on these results, strain gauges (SG) were applied at positions of maximum stress: in two measurement cross-sections (MCS), one directly beneath the impact location, and one at a distance of

²Positions in a cross-section of a pipe are addressed similar to a clock face: $12h$ refers to the top of the cross-section, $6h$ corresponds to the bottom of the pipe, and $3h$ and $9h$ refer to lateral points of the cross-section on the same height as the axis of the tube, see Figure 5.19.

6 m from this location (see Figure 5.19), SG were fixed at $12h$ on the outer surface of the pipe and on $3h$, $6h$, and $9h$ at the inner surface of the pipe, see Figure 5.19. (ii) Bending

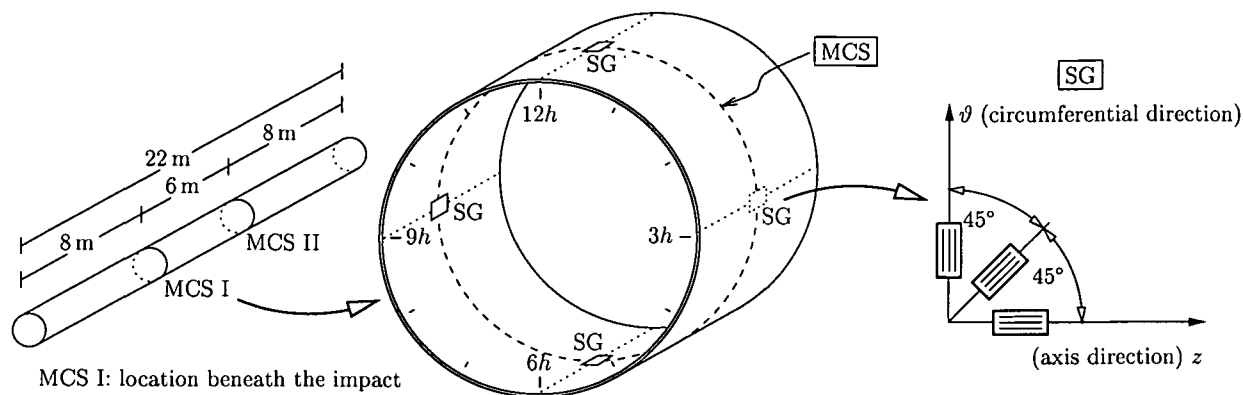


Figure 5.19: Locations of measurement cross-sections (MCS) along the axis of the pipe, application positions of strain gauges (SG) at a MCS, and orientation of strain gauges at each application point

of the pipe acting as an elastically-supported truss is significant only within a distance up to 8 m from the impact location. Therefore, the experimental pipeline track must have at least a length of 16 m. The investigated type of steel pipe is commonly produced piecewise (length of pieces 11 m). Two pieces were welded together, resulting in tube of 22 m length for the experimental setup.

5.4.2 Real-scale rockfall test: performance and results

In a quarry, in an area used as a disposal for excavation material, the steel pipe was buried with wide-range-grained gravel as illustrated in Figure 5.17(a). Thereby, the height of overburden H was equal to 2 m. At a distance of 8 m from each end of the tube MCSs were installed, referred to as MCS I and MCS II, respectively. They were equipped with four SG as illustrated in Figure 5.19. A granite boulder of approximately cubic shape with a mass $m = 18260$ kg (see Figure 5.10(c)) was dropped vertically from height $h_f = 18.85$ m onto the buried pipeline such that it impacted with a tip. The intersection of the axis of impact with the axis of the pipe coincided with MCS I. The impact of the rock boulder caused a crater of 85 cm depth. The impact energy was equal to 3.53 MJ. During the impact, the loading of the pipe was measured by means of the SG, with a frequency of 4800 Hz.

These strain histories were converted into stress histories by means of ideal elasto-plasticity of von Mises type (see e. g. (Lubliner, 1990) and Figures 5.4.2) assuming plane stress conditions. The corresponding material parameters for the steel pipe are given in Eq. (5.1). The plane stress assumption is obviously reasonable for the SG at $3h$, $6h$, and $9h$,

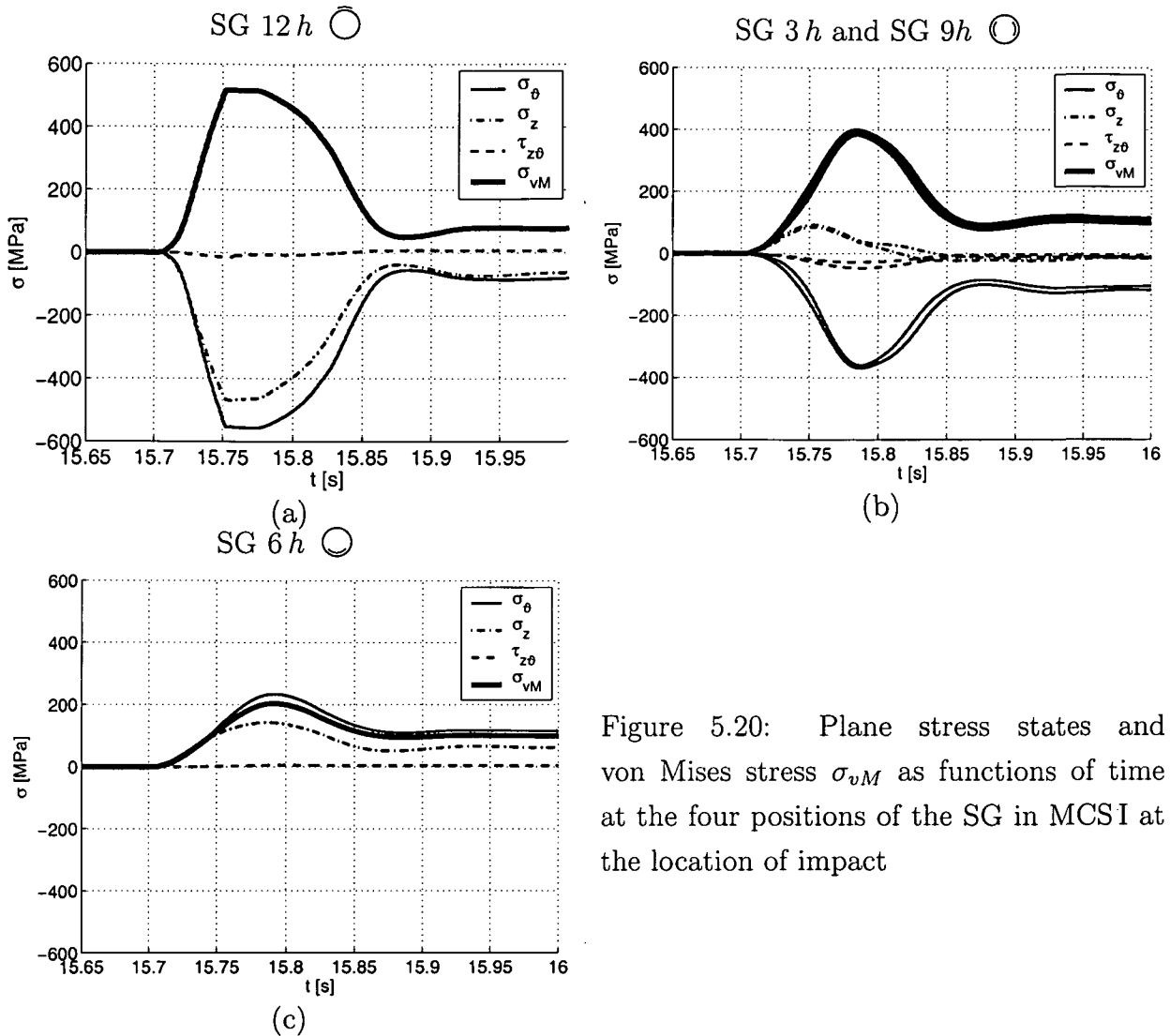


Figure 5.20: Plane stress states and von Mises stress σ_{vM} as functions of time at the four positions of the SG in MCSI at the location of impact

since these three SG were located at the inner *free* surface of the pipe. SG 12*h*, however, was located on the outer surface of the pipe. There, the stress state is characterized by a non-vanishing radial stress component σ_r , violating the assumption of a plane stress condition. Nevertheless, since the pipe is thin walled, i. e., $s/d_a = 0.011 \ll 1$, the assumption of a plane stress state is reasonable even for SG 12*h*, (Timoshenko, 1959). Accordingly, σ_r was neglected with respect to the stress components in the circumferential direction, σ_ϑ , and in the axial direction, σ_z .

At SG 12*h* in MCSI, the pipe steel yielded, (see Eq. (5.1)₃ and Figure 5.4.2 (a)). There, σ_ϑ and σ_z were compressive stress components of the same order of magnitude, whereas the shear stress $\tau_{z\vartheta}$ was negligibly small. At SG 3*h* and SG 9*h*, virtually the same stress histories were obtained (Figure 5.4.2 (b)). This result, together with $\tau_{z\vartheta} \approx 0$ at all SG, indicates that the tip of the rock boulder impacted indeed directly above the axis of the tube in MCSI. The maximum von Mises stress at SG 3*h* and SG 9*h* reached 75% and

77% of the yield stress, respectively. σ_{θ} was responsible for this situation. The histories of σ_{θ} at SG 12h, 3h, and 9h correspond to ovalization of the pipe. At SG 6h, the maximum von Mises stress reached only 40% of the yield stress (Figure 5.4.2 (b)). Hence, the loading at the bottom of the pipe was significantly smaller than the one at the top.

The stresses at MCS II, located at a distance of 6 m from the axis of impact, were mainly caused by bending. The only stress components that exceeded ± 20 MPa were the axial stress components σ_z at 12h and at 6h. At the top of the pipe, $\max \sigma_z(t) = 100$ MPa, and at the bottom, $\min \sigma_z(t) = -60$ MPa. This indicates that, at MCS II, the pipe was subjected to bending and a tensile normal force.

5.4.3 3D Finite Element structural model

The 3D load-carrying behavior, revealed by the PFEA, requires a 3D FE model for the prediction of the loading of gravel-buried steel pipes subjected to rockfall. Making use of symmetry conditions, it suffices to discretize one fourth of the entire structure, see Figure 5.21. The axis of symmetry coincides with the impact axis. In a quasi-static analysis, which, following from the PFEA, is adequate (see Section 5.4.1), the maximum impact force, $\max[F(t)]$, is applied to the surface of the FE model, the overburden of which is reduced by the mean penetration depth w_m with respect to the real overburden in the real-scale experiment, see Figure 5.21. For the magnitude and the location of the maximum impact force, $\max[F(t)]$ and w_m , respectively, the kinematic model for the penetration of rock boulders described in Subchapter 5.3 is used. For this purpose, the gravitational acceleration is again neglected in comparison to the maximum deceleration of the rock boulder during impact, i. e., g is set equal to zero in Eq. (5.51) and Eqs. (5.53) to (5.55). It follows from the Eqs. (5.51) and (5.53) that the maximum impact force occurs at $t = \Delta t_i/2$. Specializing Eq. (5.55) for $t = \Delta t_i/2$ yields

$$w_m = w(\Delta t_i/2) = v_o \Delta t_i \left(\frac{3}{8} + \frac{1}{2\pi^2} \right) = 0.72 \text{ m}, \quad (5.63)$$

considering $v_o = \sqrt{2gh_f} = 19.2$ m/s and Eq. (5.58). Accordingly, the height of overburden of the pipe considered in the FE model is reduced by 0.72 m, yielding an FE-modeled height of overburden of 1.28 m, see Figure 5.21. The corresponding maximum impact force follows from Eq. (5.61) as

$$\max[F(t)] = \frac{2v_o m}{\Delta t_i} = 7.94 \text{ MN}, \quad (5.64)$$

considering Eq. (5.58), $v_o = 19.2$ m/s, and $m = 18260$ kg. This force is applied at the surface of the FE model. The stress distribution resulting from the penetration of the tip

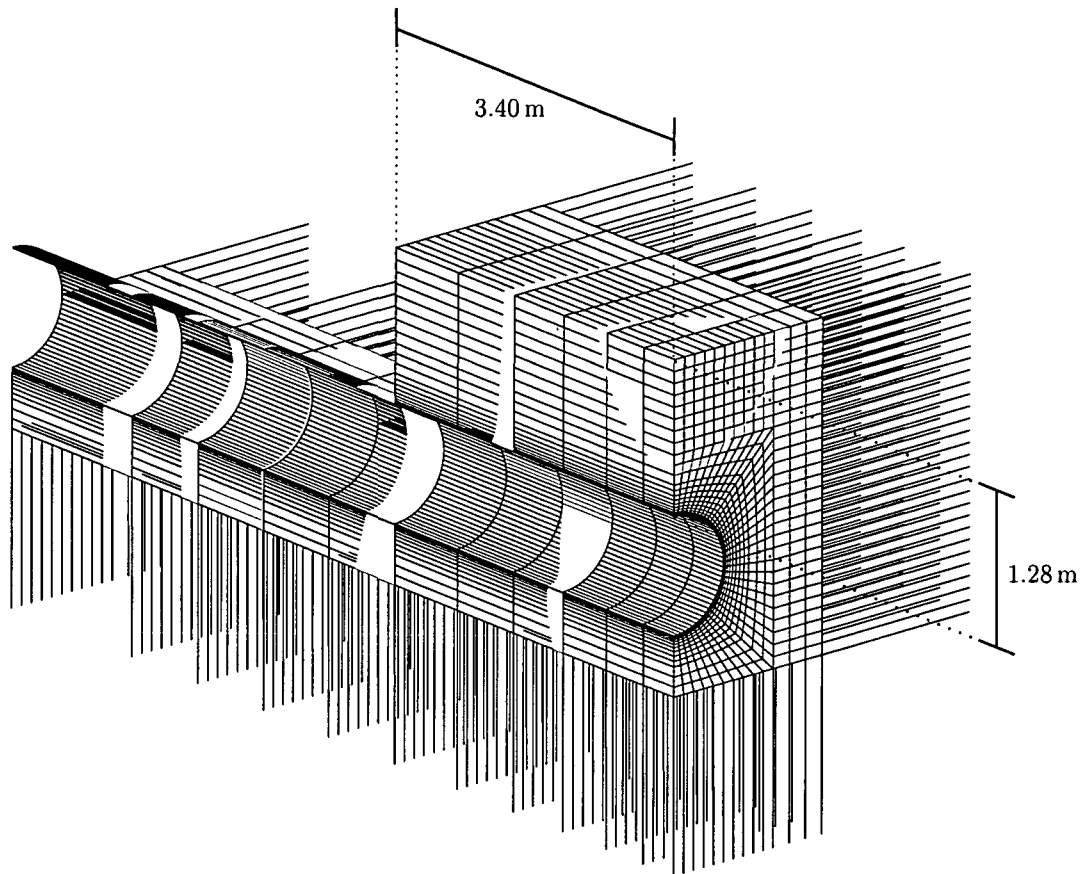


Figure 5.21: FE discretization used for the simulation of the performed experiment: the mesh consists of 8634 three-dimensional brick elements and 426 bar elements simulating linear springs

of the rock boulder is computed by means of an axisymmetric linear-elastic FE model, comprising the gravel and the tip of the granite boulder – approximated as a conical indenter at a penetration depth $w_m = 72$ cm, see Figure 5.22. The FE mesh consists of 16200 axisymmetric elements with triangular cross-sections. The maximum impact force $\max[F(t)]$ is applied to the conical indenter as spatially constant surface stresses σ , see Figure 5.22 (a). The material parameters for gravel are taken from Table 5.1, and those for granite from Table 5.4. The vertical stresses obtained for the axisymmetric FE model in a horizontal section through the model at the tip of the rock boulder (Figure 5.22 (b)) serve as surface loads for the 3D FE model of Figure 5.21.

Since dead load is not considered in the 3D FE analysis, the overburden of the pipe is only discretized to simulate the load distribution. In this context, it is noteworthy that the stresses arising from the impact are rather concentrated, i.e., they are restricted to the vicinity of the impact axis. Therefore, discretization of the overburden at a distance of

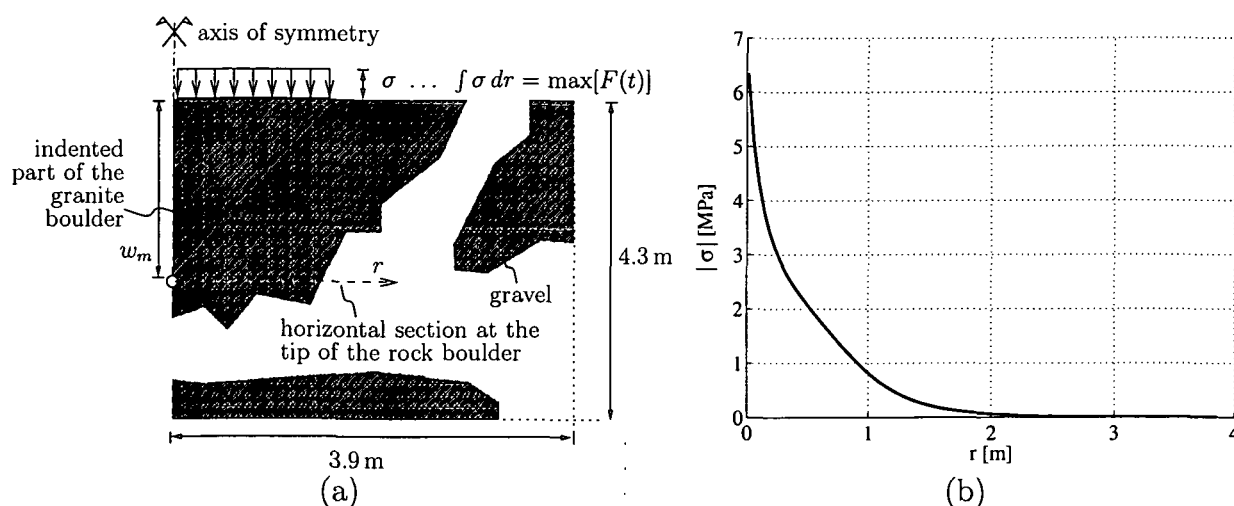


Figure 5.22: (a) Axisymmetric analysis performed to obtain the distribution of surface loads applied to the 3D FE model, depicted in (b).

more than 3.4 m from the impact axis is not necessary. In this part of the structure, only the material beside and beneath the tube is discretized, see Figure 5.21. This reduction of the FE model allows for a speed-up of the computation time by approximately 50%. The material beside and beneath the trench, i. e., wet and, hence, rather soft clay, is represented by a Winkler foundation, modeled by bar elements representing linear springs. The coefficient for the sub-grade reaction k_s , characterizing the elastic foundation of the trench is set equal to 18 MN/m^3 , which is the mean value of the interval $[12 \text{ MN/m}^3; 24 \text{ MN/m}^3]$ recommended for soft clay in (Joint Departments of the Army and the Air Force, 1983). The material parameters for steel and gravel were taken from the Eqs. (5.1) and from Table 5.1, respectively. Finite elements with bilinear shape functions for the displacements are used. The non-linear elasto-plastic FE simulation is performed in an incremental iterative way based on consistent tangent moduli (Hofstetter et al., 1993; Simo and Hughes, 1998).

The computed stresses in the pipe at MCSI are compared to the corresponding experimental results, see Table 5.5 (for a graphical representation of the obtained von Mises stresses along the inner surface of the pipe in MCSI see the thick solid line in Figure 5.23 (a)). In general, the simulated behavior of the steel pipe reflects the experimentally observed behavior of the tube in a satisfactory manner both qualitatively and quantitatively. In MCSI, at $12h$ and $3h$, very good agreement between the numerical predictions and the experiments is observed, The largest relative error between the numerical simulation and the experiment is obtained in MCSI at $6h$. There, the numerically predicted loading of the pipe is by 49.5% too large as compared to the experimentally obtained value. This deviation arises from the fact that gravel and sand (see Figure 5.17) were assumed to have the same material parameters. In fact, sand is characterized by a lower compressible

Table 5.5: von Mises stresses referring to the maximum loading of the pipe subjected to rockfall: experimental results, numerically obtained values, and relative errors

position	experimental result (σ_{vM}^{exp})	FE result (σ_{vM}^{FE})	relative error*
MCSI 12h ○	514 MPa	514 MPa	0.0 %
MCSI 3h ○	386 MPa	357 MPa	7.5 %
MCSI 6h ○	204 MPa	305 MPa	49.5 %

*The relative error is evaluated as $|\sigma_{vM}^{exp} - \sigma_{vM}^{FE}|/\sigma_{vM}^{exp}$.

strength as gravel. Therefore, the material beneath the pipe considered numerically is too stiff as compared to the sand which was part of the real-scale experiment. This causes an increase of the predicted maximum von Mises stress at the bottom of the pipe. Since this effect is rather local, the influence on the results at 12h and 3h is insignificant.

In regions where the highest loading of the steel pipe occurs, the developed structural model yields satisfactory results. Consequently, the developed FE model possesses predictive capabilities, i. e., model verification is accomplished successfully. In this context, it is noteworthy, that the material parameters serving as input for axisymmetric and 3D FE models were independent of the real-scale rockfall test. Hence, these parameters were not adjusted such that the FE model output agrees with the experimental results of the real-scale rockfall test as well as possible. In contrast, such a fitting of material parameters would not allow for a prediction of the behavior of the same type of structure with different boundary conditions or structural dimensions. To provide such prognoses, however, is the aim of this research.

5.5 Prognoses of the structural behavior

It was shown in the previous section that the developed FE model possesses predictive capabilities. Hence, it is well suited to provide estimates of the loading of a gravel-buried steel pipe for different loading conditions, boundary conditions, and structural dimensions. Such prognoses are addressed in the following: (i) The influence of different coefficients of sub-grade reaction on the loading of the pipe is studied (change of boundary conditions). First, k_s is set equal to 100 MN/m³ as recommended for dense sand in (Joint Departments of the Army and the Air Force, 1983). Secondly, k_s is set equal to 500 MN/m³ in order to investigate the limiting case of an almost rigid bedding. In both cases, the height of the overburden and the intensity of the impact remain those of the FE simulation performed

for the verification of the model, see Section 5.4.3. (ii) The influence of different heights of overburden ($H = 2.5$ m and $H = 3.0$ m) on the loading of the pipe is studied (change of structural dimensions). In these two simulations, the coefficient of sub-grade reaction and the intensity of the impact remain those of the FE simulation performed for the verification of the model, see Section 5.4.3. Results in terms of the von Mises stress distribution along the inner surface of the pipe in the cross-section beneath the impact are illustrated in Figures 5.23 (a) and (b).

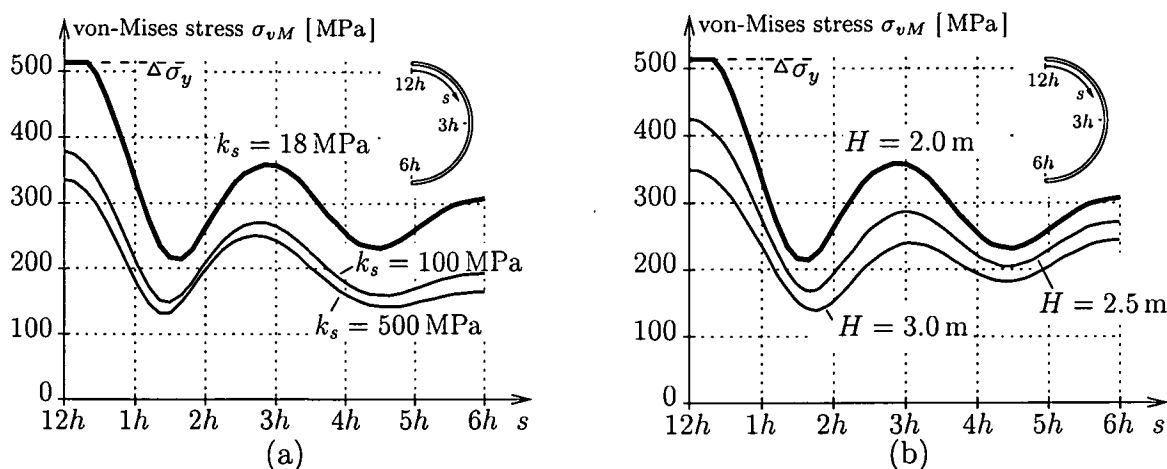


Figure 5.23: Prognoses of the distribution of the von Mises stress along the inner surface of the pipe in the cross-section beneath the impact as a function of (a) the coefficient of sub-grade reaction, and of (b) the height of overburden

For increased values of the coefficient of sub-grade reaction, the FE-predicted maximum von Mises stress of the pipe does not reach the yield stress. An increase of k_s from 18 MN/m^3 to 100 MN/m^3 and 500 MN/m^3 results in a loading of the pipe reduced by approximately 25% and 30%, respectively. It is noteworthy that the von Mises stress decreases more or less uniformly throughout the entire cross-section beneath the impact location. This is the consequence of two effects: on the one hand, a stiffer elastic foundation of the pipe trench results in smaller bending moments of the tube, which causes smaller von Mises stresses at the $12h$ and at the $6h$ position. On the other hand, the decreased stiffness ratio between the pipe steel and the bedding material results in a unloading of the pipe and in a smaller ovalization of the cross-section of the pipe beneath the impact location. This effect implies smaller von Mises stresses at the $3h$ position.

Also for increased heights of overburden, the maximum von Mises stress of the pipe, predicted by the FE simulation, does not reach the yield stress. An increase of H from 2.0 m to 2.5 m and 3.5 m results in a reduction of the loading by approximately 20% and 30%, respectively. The reduction of the von Mises stress at the $12h$ and at the $3h$ position

is larger than the one at the $6h$ position. This indicates that the increased height of overburden results in a more distributed loading of the pipe, caused by the combination of (i) significantly smaller contact stresses between the pipe and the gravel at the top of the pipe, resulting in significantly less ovalization, and of (ii) an only slightly reduced overall loading of the pipe resulting in only slightly smaller bending moments. It is noteworthy that the loading of the pipe decreased less than linearly with increasing height of overburden H . Therefore, an increase of the burying height is not a very efficient means for increasing the safety of a pipeline subjected to rockfall, see Figure 5.24. On the other hand, a decrease of

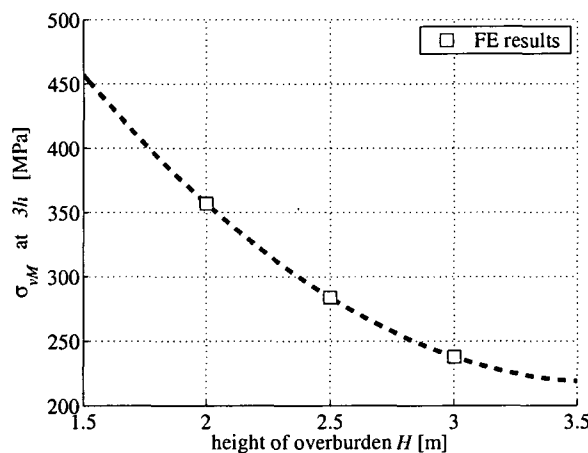


Figure 5.24: Effectiveness of an increase of the overburden on the protection of the steel pipe (reduction of characteristic steel stresses): FE-predicted von Mises stress at the $3h$ position on the inner surface of the pipe beneath the impact axis as a function of the height of overburden

H leads to a dramatic increase of the loading of the pipe. Hence, one would expect that a reduction of the height of overburden to 1.5 m or even to 1.0 m yields large zones of yielding of the steel in case of a rockfall event characterized by $m = 18260$ kg and $h_f = 18.85$ m.

5.6 Summary and conclusions

In this subchapter, the loading of a steel pipe located in a gravel-buried trench and subjected to rockfall was analyzed by means of axisymmetric and 3D FE structural models. Based on a preliminary Finite Element analysis, a real-scale experiment was designed, and requirements concerning the numerical model were defined. It was found that propagation of waves resulting from the impact are not important for the loading of the pipe. This renders a quasi-static FE simulation with application of the maximum impact force onto a FE model with an overburden reduced by the mean indentation depth adequate for numerical analyses of pipe loading caused by rockfall. This simplified representation of the

impact loads does not allow for the analysis of displacements in the immediate vicinity of the indenting rock boulder. However, remarkably, the loading of the buried steel pipe as a function of the height of overburden H and the supporting boundary conditions (Winkler foundations) can be predicted with satisfactory precision, both qualitatively and quantitatively. The developed model is well suited to provide insight into the structural behavior of the pipe subjected to different rockfall events, covered by overburdens of different thickness, and/or located in a trench surrounded by adjacent materials of different stiffness that were not investigated experimentally. The concentrated surface loads, representing the maximum impact force, cause ovalization of the cross-section of the pipe under the impact location. This local structural effect is mainly governed by the material behavior of the gravel. On the other hand, the loading of the pipe in the axial direction, which is a global structural effect, is governed by the coefficient of sub-grade reaction, characterizing the material surrounding the trench. Since there exists a non-negligible coupling of the two effects, "ovalization of the tube" and "loading of the pipe as an elastically-supported truss", a three-dimensional mode of analysis is indispensable.

It was shown that gravel may efficiently serve as an energy-absorbing and load-distributing protection system for steel pipes subjected to moderate rockfall scenarios. However, gravel is not an efficient protection system in case of rockfall events characterized by heavy rock boulders (such as investigated herein, e. g. $m = 18260$ kg) and heights of fall up to 100 m or even more. In this context, an efficient protection system for a steel pipe subjected to rockfall must satisfy two requirements:

1. Damping of the impact in order to keep the forces arising from rockfall at a reasonably small level.
2. Load distribution and load carriage in order to reduce the loading of the steel pipe.

In case of the investigated type of protection system, both tasks must be performed by gravel. However, the flexibility of gravel required for the damping of the impact is contradictory to the stiffness of gravel required for the task of load distribution and the carrying of the load. Consequently, such a protection system is not very effective.

In order to provide a highly effective protection system for a steel pipe subjected to rockfall, the aforementioned two tasks must be performed by two separate structural elements. Such a system could consist, e. g., of (i) gravel acting as an energy-absorbing and, hence, impact-damping system, and (ii) additionally buried construction elements, made, e. g., of reinforced concrete acting as a structural component allowing for the distribution and for carrying of the load.

Chapter 6

Summary and conclusions

In this thesis efforts were made to treat parameter identification in geotechnical engineering in an integrated manner. Methodical aspects were considered by developing a new, iterative parameter identification method resting on soft computing. Artificial neural networks (ANNs) were used to approximate the underlying finite element (FE) analysis of the problem under consideration. They were trained to map input parameters for FE analyses onto respective numerical results. Based on the trained ANN, a genetic algorithm was used for determination of an estimate of optimal parameters. Moreover, the trained ANN provides an approximation of the sensitivity of the unknown parameters. Hence, sensitivity analyses are no longer required to check the quality of an obtained solution. The proposed algorithm combines advantages of gradient-free and gradient-based PI methods, i.e., the entire parameter space is searched for an optimal solution and only few FE analyses are required to find optimal parameters. The latter is essential for PI in geotechnical problems which, in general, are characterized by large-scale FE models.

Conceptual aspects of parameter identification were presented considering numerical modeling of the loading of a gravel-buried steel pipe subjected to rockfall. Identification of the material parameters of gravel was based on results from designed and performed experiments as well as on testing data taken from the open literature. This data set permitted identification of physical quantities of gravel attached to a “representative volume element” which has a characteristic length of one to several decimeters. Since the experiments were free of spatial gradients of material parameters and loading conditions in that length scale, the identified parameters are independent of any structure-specific boundary conditions. Hence, they are valid for virtually all structures made of gravel, including the overburden of a steel pipeline. The identified material parameters were the basis for

the simulation of the loading of a gravel-buried steel pipe subjected to rockfall by means of a three-dimensional elasto-plastic Finite Element analysis. For verification purposes, a real-scale rockfall experiment was designed and performed. It is noteworthy that the results from this structural experiment had no influence on the identification of the material parameters of gravel. Therefore, a comparison of the numerically obtained structural behavior with results from the real-scale rockfall event allowed for an assessment of the usefulness of the chosen mode of structural modeling. In this way, model verification could be accomplished successfully. It was demonstrated, that the developed FE model is able to provide reliable prognoses of the loading of a gravel-buried steel pipe subjected to rockfall events that were not investigated experimentally.

The obtained results have shown that numerical simulations in geotechnical engineering are useful. In order to develop a numerical tool capable to provide prognoses of the structural behavior, identification of material parameters and verification of a structural model must be based on two independent sets of experiments. This is the only way to further increase the acceptance of numerical simulations in geotechnical engineering.

Chapter 7

Bibliography

- Al-Hussaini, M. (1971). Investigation of plane strain shear testing. Report 2. Drained plane strain and triaxial compression tests on crushed NAPA basalt. Techn. Reports S-71-2, Army. Engr. Waterways Exp. Sta., Vicksburg, MI.
- Alva-Hurtado, J. and Selig, E. (1981). Permanent strain behavior of railroad ballast. In Balkema, A., editor, *Proceedings of the 10th International Conference on Soil Mechanics and Foundation Engineering in Stockholm, Sweden*, volume 1, pages 543–546, Rotterdam, the Netherlands.
- Anderson, J. and Rosenfeld, E. (1988). *Neurocomputing: Foundations of Research*. MIT Press, Cambridge, MA.
- Baehr, H. and Stephan, K. (1998). *Heat and Mass Transfer*. Springer, Berlin.
- Barenblatt, G. (1996). *Scaling, Self-Similarity, and Intermediate Asymptotics*. Cambridge University Press, Cambridge, England, 1st edition.
- Beer, G. (2003). *Numerical Simulation in Tunneling*, volume 6, Chapter 10: Macht, J., Lackner, R., Hellmich, Ch., and Mang, H.A.: Quantification of stress states in shotcrete tunnel shells. Springer, Wien, New York.
- Benjamin, J. and Cornell, A. (1970). *Probability, Statistics, and Decision for Civil Engineers*. McGraw Hill Book Company.
- Bortz, J. (1999). *Statistik für Sozialwissenschaftler [Statistics for Social Scientists]*. Springer, Berlin. In German.

- Brandstätter, C., Lackner, R., and Mang, H. (2002). Bestimmung von Materialeigenschaften zementgebundener Werkstoffe mittels Temperaturmessungen: Anwendung im Rahmen des Düsenstrahlverfahrens [Evaluation of properties of cementitious materials by means of temperature measurements: Application to jet grouting]. *Bauingenieur*, 77(2):51–57. In German.
- Buckingham, E. (1914). On physically similar systems: Illustrations of the use of dimensional equations. *The Physical Review*, 4:345–376.
- Byfors, J. (1980). Plain concrete at early ages. Technical report, Swedish Cement and Concrete Research Institute, Stockholm, Sweden.
- CEN-EVN-1991-1 (1994). Eurocode 1 – Basis of design and actions on structures. European Prestandard, European Committee for Standardization, Brussels, Belgium.
- Chambosse, G. and Kirsch, K. (1995). State of the art of the jet grouting method in Germany. In *Proceedings of the 4th Pacific Rim International Conference on Water Jet Technology*, Shimizu, Japan.
- Darwin, C. (1995). *Origin of Species*. Modern Library, Random House.
- DiMaggio, F. and Sandler, I. (1971). Material models for granular soils. *Journal of Engineering Mechanics (ASCE)*, 97(3):935–950.
- Duvaut, G. and Lions, J. (1972). *Les Inequations en Mécanique et en Physique [The Inequalities in Mechanics and Physics]*. Dunod, Paris. In French.
- EUROPIPE (1993). Abnahmeprüfzeugnis nach ÖNORM EN 10204 [Inspection certificate according to ÖNORM EN 10204]. Zertifikat des Technischen Überwachungs-Vereins Österreich, Europipe Deutschland GmbH. In German.
- Fausett, L. (1994). *Fundamentals of neural networks: architectures, algorithms, and applications*. Prentice Hall, Upper Saddle River, NJ.
- Feng, X.-T., Zhang, Z., and Sheng, Q. (2000). Estimating mechanical rock mass parameters relating to the three gorges project permanent shiplock using an intelligent displacement back analysis method. *International Journal of Rock Mechanics and Mining Sciences*, 37:1039–1054.
- Forrestal, M., Altman, B., Cargile, S., and Hanchak, S. (1994). An empirical equation for penetration depth of ogive-nose projectiles into concrete targets. *International Journal of Impact Engineering*, 15(4):395–405.

- Forrestal, M., Frew, D., Hanchak, S., and Brar, N. (1996). Penetration of grout and concrete targets with ogive-nose steel projectiles. *International Journal of Impact Engineering*, 18(5):465–476.
- Forrestal, M., Frew, D., Hickerson, J., and Rohwer, T. (2003). Penetration of concrete targets with deceleration-time measurements. *International Journal of Impact Engineering*, 28(5):479–497.
- Freiesleben Hansen, P. and Pedersen, E. (1977). Måleinstrument til kontrol af betons hardening [Measurement device for controlling hardening of concrete]. *Nordisk Betong*, 1:21–25.
- Furth, A. and Wendland, S. (1998). Jet-grouted cantilever wall for slope stability. In Johnsen, L. and Berry, D., editors, *Grouts and Grouting: A potpourri of projects*, volume 80 of *Geotechnical Special Publications*. ASCE, 31–42.
- Goldberg, D. (1989). *Genetic Algorithms in Search, Optimization, and Machine Learning*. Addison Wesley.
- Gupta, J. and Sexton, R. (1999). Comparing backpropagation with a genetic algorithm for neural network training. *Omega, The International Journal of Management Science*, 27:679–684.
- Haykin, S. (1999). *Neural networks: a comprehensive foundation*. Prentice Hall, Upper Saddle River, NJ, 2nd edition.
- Hellmich, C., Mang, H., and Ulm, F.-J. (2001). Hybrid method for quantification of stress states in shotcrete tunnel shells: combination of 3D *in-situ* displacement measurements and thermochemoplastic material law. *Computers and Structures*, 79(22–25):2103–2116.
- Hellmich, C., Ulm, F.-J., and Mang, H. A. (1999a). Consistent linearization in finite element analysis of coupled chemo-thermal problems with exo- or endothermal reactions. *Computational Mechanics*, 24(4):238–244.
- Hellmich, C., Ulm, F.-J., and Mang, H. A. (1999b). Multisurface chemoplasticity I: Material model for shotcrete. *Journal of Engineering Mechanics (ASCE)*, 125(6):692–701.
- Henn, R. (1996). *Practical Guide to Grouting of Underground Structures*. ASCE Press, New York, USA.

- Hofstetter, G., Simo, J., and Taylor, R. (1993). A modified cap model: closest point solution algorithms. *Computers & Structures*, 46(2):203–214.
- Huber, N. (2000). Anwendung Neuronaler Netze bei nichtlinearen Problemen der Mechanik [Application of neural networks to nonlinear problems of mechanics]. Habilitation Thesis. Scientific Report FZKA 6504, Institute for Material Research, Karlsruhe, Germany. In German.
- Joint Departments of the Army and the Air Force (1983). *Soils and Geology Procedures for Foundation Design of Buildings and Other Structures (Except Hydraulic Structures): Technical Manual 5-818-1, Air Force Manual 88-3*. Washington, DC, USA.
- Jones, N. (1989). *Structural Impact*. Cambridge University Press, Cambridge.
- Kakaç, S. and Yener, Y. (1985). *Heat Conduction*. Hemisphere Publishing Corporation, New York, USA, 2nd edition.
- Kolsky, H. (1953). *Stress Waves in Solids*. Clarendon Press, Oxford.
- Kolsky, H. and Prager, W., editors (1964). *Stress Waves in Anelastic Solids - Proceedings of IUTAM Symposium*, Providence, R.I. IUTAM, Springer, Heidelberg.
- König, G., Soukhov, D., and Jungwirth, F. (1998). Betondruckfestigkeit nach prEN 206 und EC 1 / EC 2 – Sichere Betonproduktion [Compressive strength of concrete according to prEN 206 and EC 1 / EC 2 – Safe production of concrete]. *Beton*, 1998(11):680–688. In German.
- Kropik, C. (1994). *Three-dimensional elasto-viscoplastic finite element analysis of deformations and stresses resulting from the excavation of shallow tunnels*. Doctoral thesis, Vienna University of Technology, Vienna, Austria.
- Kropik, C. and Mang, H. (1996). Computational mechanics of the excavation of tunnels. *Engineering Computations*, 13(7):49–69.
- Labieuse, V., Descoedres, F., and Montani, S. (1996). Experimental study of rock sheds impacted by rock blocks. *Structural Engineering International*, 6(3):171–176.
- Lackner, R., Brandstätter, C., and Mang, H. (2001). Evaluation of properties of soilcrete by means of back analysis: combination of *in-situ* temperature measurements and a thermochemical material law. In Bathe, K.-J., editor, *Proceedings of the 1st MIT Conference on Computational Fluid and Solid Mechanics*, pages 1281–1284. Elsevier Science Ltd., Oxford.

- Lackner, R., Hellmich, C., and Mang, H. (2000). Synthesis of constitutive modelling and on-line measurements for the analysis of NATM tunnels. In Marovic, P., editor, *Proceedings of the 3rd Congress of the Croation Society of Mechanics*, pages 53–66, Cavtat-Dubrovnik, Croatia.
- Lackner, R. and Mang, H. (2001). Cracking in shotcrete tunnel shells. In de Borst, R., Mazars, J., Pijaudier-Cabot, G., and van Mier, J., editors, *Fracture Mechanics of Concrete Structures, Proceedings of the 4th International Conference*, pages 857–870, Cachan, France. Also published in *Engineering Fracture Mechanics*, 70:7-8, 1047–1068, 2003.
- Leslie, D. (1975). Shear strength of rock fill. Physical Properties Engrg. Study No. 526, U.S. Army Corps of Engineers, Sausalito, CA.
- Li, Q. and Chen, X. (2003). Dimensionless formulae for penetration depth of concrete target impacted by a non-deformable projectile. *International Journal of Impact Engineering*, 28(1):93–116.
- Lubliner, J. (1990). *Plasticity Theory*. Macmillan Publishing Company, New York.
- Mahnken, R. and Stein, E. (1996a). Parameter identification of viscoplastic models based on analytical derivatives of a least-squares functional and stability investigations. *International Journal of Plasticity*, 12(4):451–479.
- Mahnken, R. and Stein, E. (1996b). A unified approach for parameter identification of inelastic material models in the frame of the finite element method. *Computer Methods in Applied Mechanics and Engineering*, 136:225–258.
- Mang, H. and Hofstetter, G. (2000). *Festigkeitslehre [Strength of Materials]*. Springer, Wien, New York. In German.
- Marachi, N., Chan, C., Seed, H., and Duncan, J. (1969). Strength and deformation characteristics of rockfill materials. Report TE-69-5 for the State of California Dept. of Water Resources, University of California, Berkeley, CA.
- Marcher, T. and Vermeer, P. (2001). Macromodelling of softening in non-cohesive soils. In Vermeer, P., Diebels, S., Ehlers, W., Herrmann, H., Luding, S., and Ramm, E., editors, *Continuous and discontinuous modelling of cohesive-frictional materials, Lecture notes in Physics*, volume 568, pages 89–108. Springer, Berlin.
- McCulloch, W. and Pitts, W. (1943). A logical calculus of ideas immanent in nervous activity. *Bulletin of Mathematical Biophysics*, 5:115–133.

- Minsky, L. (1967). *Computation: Finite and Infinite Machines*. Prentice-Hall, Englewood Cliffs, NJ.
- Özişik, M. (1985). *Heat Transfer: A Basic Approach*. McGraw-Hill, London, England.
- PCB PIEZOTRONICS Inc. (2002). *Model 353B03 ICP[®] Accelerometer – Installation and Operating Manual*.
- Penumadu, D. and Zhao, R. (1999). Triaxial compression behavior of sand and gravel using artificial neural networks (ANN). *Computers & Geotechnics*, 24:207–230.
- Pitts, D. and Sissom, L. (1977). *Heat Transfer*. McGraw-Hill, London.
- Regueiro, R. and Borja, R. (1999). A finite element model of localized deformation in frictional materials taking a strong discontinuity approach. *Finite Elements in Analysis and Design*, 33:283–315.
- Rojas, R. (1996). *Theorie der Neuronalen Netze: Eine Systematische Einführung [Theory of neural networks: a systematic introduction]*. Springer, Berlin. In German.
- Rokahr, R. and Zachow, R. (1997). Ein neues Verfahren zur täglichen Kontrolle der Auslastung einer Spritzbetonschale [A new method for the daily monitoring of the stress intensity of a sprayed concrete lining]. *Felsbau – Rock and Soil Engineering*, 15(6):430–434. In German.
- Rosenblatt, F. (1958). The perceptron: a probabilistic model for information storage and organization of the brain. *Psychological Review*, 65:386–408. Reprinted in (Anderson and Rosenfeld, 1988).
- Sandler, I. and Rubin, D. (1979). An algorithm and a modular subroutine for the cap model. *International Journal for Numerical and Analytical Methods in Geomechanics*, 3:173–186.
- Simo, J. and Hughes, T. (1998). *Computational Inelasticity*. Springer, New York, Berlin, Germany.
- Simo, J. and Taylor, R. (1985). Consistent tangent operators for rate independent elastoplasticity. *Computer Methods in Applied Mechanics and Engineering*, 48:101–118.
- Spira, Y., Lackner, R., and Mang, H. (2001). Modeling of shear failure of soil: Application to the excavation of tunnels. In Waszczyszyn, Z., editor, *CD-ROM Proceedings of the 2nd European Conference on Computational Mechanics*, Cracow, Poland.

- Sterpi, D. (1999). An analysis of geotechnical problems involving strain softening effects. *International Journal for Numerical and Analytical Methods in Geomechanics*, 23:1427–1454.
- Studer, J. and Ziegler, A. (1986). *Bodendynamik [Soil Dynamics]*. Springer, Berlin. In German.
- Terzaghi, K., Peck, R., and Mesri, G. (1996). *Soil Mechanics in Engineering Practice*. John Wiley & Sons, New York, 3rd edition.
- Timoshenko, S. (1959). *Theory of Plates and Shells*. McGraw Hill Book Company, 2nd edition.
- Ulm, F.-J. and Coussy, O. (1995). Modeling of thermochemomechanical couplings of concrete at early ages. *Journal of Engineering Mechanics (ASCE)*, 121(7):785–794.
- Vanderplaats, G. (1984). *Numerical Optimization Techniques for Engineering Design*. McGraw-Hill.
- Vermeer, P. and de Borst, R. (1984). Non-associated plasticity for soils, concrete and rock. *HERON*, 29(3):3–64.
- Waszczyszyn, Z. and Ziemiański, L. (2001). Neural networks in mechanics of structures and materials – new results and prospects of applications. *Computers and Structures*, 79(22-25):2261–2276.

Appendix **A**

Genetic algorithm (GA)

A GA imitates the evolution of a population of biologic individuals (Goldberg, 1989) following DARWIN's principle of the *survival of the fittest* (Darwin, 1995). In the context of the proposed PI method, an individual represents a set of parameters.¹ The quality, i.e., the fitness of each individual of a certain generation is described by the respective value of the *fitness function* \mathcal{F} . Based on the fitness of the individuals of a generation, a new generation is computed by means of the following genetic operators:

Reproduction: Individuals are selected probabilistically and put in a so-called mating pool. Hereby, the probability to be selected is higher for individuals characterized by an above-average fitness. Hence, such individuals may be represented twice or even more times in the mating pool. Individuals characterized by a below-average fitness, on the other hand, might not be included in the mating pool. Hence, they will die out. Reproduction is terminated when the number of individuals in the mating pool is equal to the number of individuals in a generation.

Crossover: Individuals in the mating pool are arranged randomly in couples, so-called parents. Each couple is designated to yield two offsprings from exchanging some of the parental parameters. In case of two-point crossover, two crossing sites are determined randomly for each couple. These crossing sites subdivide the parental sets of parameters and represent borderlines. In between these borderlines the parameters

¹Usually, individuals of GAs are represented as binary strings. According to (Gupta and Sexton, 1999), the basic sequence of a GA is the same for binary-coded individuals and for individuals represented as a set of real numbers. Hence, the use of binary-coded individuals is not necessary in the context of the proposed PI method.

of the two parents get exchanged, yielding two new individuals, i. e., two *offsprings* (see Table A.1).

Mutation: The mutation operator is used in artificial genetic systems in order to protect the generations of losing some potentially useful genetic material (Goldberg, 1989). With small probability, parameters of offsprings get changed. E.g., one out of thousand parameters is modified. The size of this modification is determined randomly.

$$\begin{array}{rcc}
 \text{parent } \textcircled{i}: & p_1^i & | & p_2^i & p_3^i & | & p_4^i & p_5^i & \Rightarrow & \text{offspring } \textcircled{1}: & p_1^i & p_2^k & p_3^k & p_4^i & p_5^i \\
 \text{parent } \textcircled{k}: & p_1^k & | & p_2^k & p_3^k & | & p_4^k & p_5^k & & \text{offspring } \textcircled{2}: & p_1^k & p_2^i & p_3^i & p_4^k & p_5^k \\
 & & & \uparrow & & & \uparrow & & & & & & & & & \\
 & & & \text{randomly determined} & & & \text{crossing sites} & & & & & & & & &
 \end{array}$$

Table A.1: Two-point crossover for a couple of parameter sets consisting of five parameters p_j , $j = 1, 2, \dots, 5$

After reproduction, crossover, and mutation, the individuals of the new generation are obtained. Finally, a randomly selected individual is replaced by the fittest individual of the old generation. Hence, the largest fitness value obtained in the new generation is at least equal to the largest fitness value of the old generation. In general, new generations are characterized by an increased average fitness of the population.

For the proposed PI method, GAs are employed twice: for determination of the initial network weights and of the estimates of optimal model parameters. Hence, the parameter set, which was represented by an individual throughout this Appendix, is either a set of network weights or a set of model parameters. The properties of these two GAs differ in the number of individuals per generation, the fitness function \mathcal{F} , and the number of generations. The respective variables are specified in Subchapter 4.1.

Appendix **B**

Backpropagation algorithm for first-order approximation ANNs

Training of first-order approximation ANNs, $\mathcal{O}_{(1)}$ -ANNs, aims at

$$\mathcal{R}_{(0)}^{*-h} + \mathcal{R}_{(1)}^{*-h} \rightarrow 0 \quad (\text{B.1})$$

by iterative adaption of the network weights. The zero-order approximation error $\mathcal{R}_{(0)}^{*-h}$ and the first-order approximation error $\mathcal{R}_{(1)}^{*-h}$ are defined in Eqs. (4.68). A gradient descent method in the weight space is performed. Thereby, the incremental changes of the network weights are calculated according to

$$\Delta w_{jk}^{ih} = \Delta w_{jk}^{ih} \left(\frac{\partial[\mathcal{R}_{(0)}^{*-h} + \mathcal{R}_{(1)}^{*-h}]}{\partial w_{jk}^{ih}} \right), \quad \Delta w_{kr}^{ho} = \Delta w_{kr}^{ho} \left(\frac{\partial[\mathcal{R}_{(0)}^{*-h} + \mathcal{R}_{(1)}^{*-h}]}{\partial w_{kr}^{ho}} \right). \quad (\text{B.2})$$

In this Appendix, the derivatives required for computation of the network-weight corrections according to Eqs. (B.2) are presented.

Computation of the partial derivatives of $\mathcal{R}_{(0)}^{*-h}$ with respect to the network weights is performed as described in Sections 4.1.1 and 4.1.2. The derivatives of $\mathcal{R}_{(1)}^{*-h}$ with respect to the network weights read:

$$\frac{\partial \mathcal{R}_{(1)}^{*-h}}{\partial w_{jk}^{ih}} = \sum_{d=1}^{n_d} \frac{\partial \mathcal{R}_{(1)}^{*-h}}{\partial \mathcal{R}_{(1),d}^{*-h}} \frac{\partial \mathcal{R}_{(1),d}^{*-h}}{\partial w_{jk}^{ih}} \quad \text{and} \quad \frac{\partial \mathcal{R}_{(1)}^{*-h}}{\partial w_{kr}^{ho}} = \sum_{d=1}^{n_d} \frac{\partial \mathcal{R}_{(1)}^{*-h}}{\partial \mathcal{R}_{(1),d}^{*-h}} \frac{\partial \mathcal{R}_{(1),d}^{*-h}}{\partial w_{kr}^{ho}} \quad (\text{B.3})$$

with

$$\frac{\partial \mathcal{R}_{(1),d}^{*-h}}{\partial w_{jk}^{ih}} = \frac{1}{\mathcal{R}_{(1),d}^{*-h}} \frac{1}{n_d} \frac{1}{n_i} \sum_{d=1}^{n_d} \sum_{j=1}^{n_i} \frac{\frac{\partial \mathcal{R}^*(\mathbf{p}_d)}{\partial p_j} - \frac{\partial \mathcal{R}^h(\mathbf{p}_d)}{\partial p_j}}{\left[\text{mean}_{j,d} \left(\frac{\partial \mathcal{R}^h}{\partial p_j} \right) \right]^2} \frac{\partial^2 \mathcal{R}^*(\mathbf{p}_d)}{\partial p_j \partial w_{jk}^{ih}}, \quad (\text{B.4})$$

$$\frac{\partial \mathcal{R}_{(1),d}^{*-h}}{\partial w_{kr}^{ho}} = \frac{1}{\mathcal{R}_{(1),d}^{*-h}} \frac{1}{n_d} \frac{1}{n_i} \sum_{d=1}^{n_d} \sum_{j=1}^{n_i} \frac{\frac{\partial \mathcal{R}^*(\mathbf{p}_d)}{\partial p_j} - \frac{\partial \mathcal{R}^h(\mathbf{p}_d)}{\partial p_j}}{\left[\text{mean}_{j,d} \left(\frac{\partial \mathcal{R}^h}{\partial p_j} \right) \right]^2} \frac{\partial^2 \mathcal{R}^*(\mathbf{p}_d)}{\partial p_j \partial w_{kr}^{ho}}. \quad (\text{B.5})$$

Accordingly, computation of $\partial \mathcal{R}_{(1),d}^{*-h} / \partial w_{jk}^{ih}$ and $\partial \mathcal{R}_{(1),d}^{*-h} / \partial w_{kr}^{ho}$ require the second, mixed derivatives of \mathcal{R}^* with respect to the input parameters and the network weights. Considering the second one of the two Eqs. (4.73), these derivatives read:

$$\begin{aligned} \frac{\partial^2 \mathcal{R}^*(\mathbf{p}_d)}{\partial p_j \partial w_{jk}^{ih}} &= \frac{\partial}{\partial w_{jk}^{ih}} \left(\frac{1}{\mathcal{R}^*(\mathbf{p}_d)} \right) \frac{1}{n_o} \sum_{r=1}^{n_o} \frac{u_r^* - u_r}{\bar{u}^2} \frac{\partial u_r^*}{\partial p_j} + \frac{1}{\mathcal{R}^*(\mathbf{p}_d)} \frac{1}{n_o} \sum_{r=1}^{n_o} \frac{1}{\bar{u}^2} \frac{\partial u_r^*}{\partial w_{jk}^{ih}} \frac{\partial u_r^*}{\partial p_j} + \\ &+ \frac{1}{\mathcal{R}^*(\mathbf{p}_d)} \frac{1}{n_o} \sum_{r=1}^{n_o} \frac{u_r^* - u_r}{\bar{u}^2} \frac{\partial^2 u_r^*}{\partial p_j \partial w_{jk}^{ih}}, \end{aligned} \quad (\text{B.6})$$

$$\begin{aligned} \frac{\partial^2 \mathcal{R}^*(\mathbf{p}_d)}{\partial p_j \partial w_{kr}^{ho}} &= \frac{\partial}{\partial w_{kr}^{ho}} \left(\frac{1}{\mathcal{R}^*(\mathbf{p}_d)} \right) \frac{1}{n_o} \sum_{r=1}^{n_o} \frac{u_r^* - u_r}{\bar{u}^2} \frac{\partial u_r^*}{\partial p_j} + \frac{1}{\mathcal{R}^*(\mathbf{p}_d)} \frac{1}{n_o} \sum_{r=1}^{n_o} \frac{1}{\bar{u}^2} \frac{\partial u_r^*}{\partial w_{kr}^{ho}} \frac{\partial u_r^*}{\partial p_j} + \\ &+ \frac{1}{\mathcal{R}^*(\mathbf{p}_d)} \frac{1}{n_o} \sum_{r=1}^{n_o} \frac{u_r^* - u_r}{\bar{u}^2} \frac{\partial^2 u_r^*}{\partial p_j \partial w_{kr}^{ho}}. \end{aligned} \quad (\text{B.7})$$

Eqs. (B.6) and (B.7) contain the following partial derivatives with respect to network weights:

$$\frac{\partial}{\partial w_{jk}^{ih}} \left(\frac{1}{\mathcal{R}^*(\mathbf{p}_d)} \right), \quad \frac{\partial}{\partial w_{kr}^{ho}} \left(\frac{1}{\mathcal{R}^*(\mathbf{p}_d)} \right), \quad \frac{\partial u_r^*}{\partial w_{jk}^{ih}}, \quad \frac{\partial u_r^*}{\partial w_{kr}^{ho}}, \quad \frac{\partial^2 u_r^*}{\partial p_j \partial w_{jk}^{ih}}, \quad \frac{\partial^2 u_r^*}{\partial p_j \partial w_{kr}^{ho}}. \quad (\text{B.8})$$

The first two derivatives (B.8) can be calculated considering Eq. (4.1) as

$$\frac{\partial}{\partial w_{jk}^{ih}} \left(\frac{1}{\mathcal{R}^*(\mathbf{p}_d)} \right) = - \left[\frac{1}{n_o} \sum_{r=1}^{n_o} \left(\frac{u_r^*(\mathbf{p}_d) - u_r}{u_r} \right) \right]^{-\frac{3}{2}} \frac{1}{n_o} \sum_{r=1}^{n_o} \left(\frac{u_r^* - u_r}{\bar{u}^2} \right) \frac{\partial u_r^*}{\partial w_{jk}^{ih}}, \quad (\text{B.9})$$

$$\frac{\partial}{\partial w_{kr}^{ho}} \left(\frac{1}{\mathcal{R}^*(\mathbf{p}_d)} \right) = - \left[\frac{1}{n_o} \sum_{r=1}^{n_o} \left(\frac{u_r^*(\mathbf{p}_d) - u_r}{u_r} \right) \right]^{-\frac{3}{2}} \frac{1}{n_o} \sum_{r=1}^{n_o} \left(\frac{u_r^* - u_r}{\bar{u}^2} \right) \frac{\partial u_r^*}{\partial w_{kr}^{ho}}. \quad (\text{B.10})$$

The second two derivatives (B.8) which also appear in Eqs. (B.9) and (B.10) can be calculated as

$$\frac{\partial u_r^*}{\partial w_{jk}^{ih}} = \sum_{r=1}^{n_o} \left[\frac{\partial u_r^*}{\partial \tilde{u}_r^*} \frac{\partial \tilde{u}_r^*}{\partial \sigma_r^o} \frac{\partial \sigma_r^o}{\partial s(\sigma_k^h)} \right] \frac{\partial s(\sigma_k^h)}{\partial \sigma_k^h} \frac{\partial \sigma_k^h}{\partial w_{jk}^{ih}} = \sum_{r=1}^{n_o} \left[\frac{\partial u_r^*}{\partial \tilde{u}_r^*} \frac{\partial s(\sigma_r^o)}{\partial \sigma_r^o} w_{kr}^{ho} \right] \frac{\partial s(\sigma_k^h)}{\partial \sigma_k^h} \tilde{p}_{j,d}, \quad (\text{B.11})$$

$$\frac{\partial u_r^*}{\partial w_{kr}^{ho}} = \frac{\partial u_r^*}{\partial \tilde{u}_r^*} \frac{\partial \tilde{u}_r^*}{\partial \sigma_r^o} \frac{\partial \sigma_r^o}{\partial w_{kr}^{ho}} = \frac{\partial u_r^*}{\partial \tilde{u}_r^*} \frac{\partial s(\sigma_r^o)}{\partial \sigma_r^o} s(\sigma_k^h). \quad (\text{B.12})$$

The fifth term in (B.8) is a second mixed derivative of u_r^* with respect to the input parameters and the network weights linking the input layer and the hidden layer. It can be evaluated as follows:

$$\frac{\partial}{\partial w_{j\ell}^{ih}} \left(\frac{\partial u_r^*}{\partial p_j^i} \right) = \frac{\partial u_r^*}{\partial \tilde{u}_r^*} \frac{\partial}{\partial w_{j\ell}^{ih}} \left(\frac{\partial s(\sigma_r^o)}{\partial \sigma_r^o} \right) \sum_{k=1}^{n_v} \left[w_{kr}^{ho} \frac{\partial s(\sigma_k^h)}{\partial \sigma_k^h} w_{jk}^{ih} \right] \frac{\partial \tilde{p}_j^i}{\partial p_j^i} +$$

$$\begin{aligned}
& + \frac{\partial u_r^*}{\partial \tilde{u}_r^*} \frac{\partial s(\sigma_r^o)}{\partial \sigma_r^o} \sum_{k=1}^{n_v} \left[w_{kr}^{ho} \frac{\partial}{\partial w_{j\ell}^{ih}} \left(\frac{\partial s(\sigma_k^h)}{\partial \sigma_k^h} \right) w_{jk}^{ih} \right] \frac{\partial \tilde{p}_j^i}{\partial p_j^i} + \\
& + \frac{\partial u_r^*}{\partial \tilde{u}_r^*} \frac{\partial s(\sigma_r^o)}{\partial \sigma_r^o} \sum_{k=1}^{n_v} \left[w_{kr}^{ho} \frac{\partial s(\sigma_k^h)}{\partial \sigma_k^h} \frac{\partial w_{jk}^{ih}}{\partial w_{j\ell}^{ih}} \right] \frac{\partial \tilde{p}_j^i}{\partial p_j^i}.
\end{aligned} \tag{B.13}$$

The underlined terms in Eq. (B.13) can be written as:

$$\frac{\partial}{\partial w_{j\ell}^{ih}} \left(\frac{\partial s(\sigma_r^o)}{\partial \sigma_r^o} \right) = \frac{\partial^2 s(\sigma_r^o)}{\partial (\sigma_r^o)^2} \frac{\partial \sigma_r^o}{\partial s(\sigma_\ell^h)} \frac{\partial s(\sigma_\ell^h)}{\partial \sigma_\ell^h} \frac{\partial \sigma_\ell^h}{\partial w_{j\ell}^{ih}} = \frac{\partial^2 s(\sigma_r^o)}{\partial (\sigma_r^o)^2} w_{\ell r}^{ho} \frac{\partial s(\sigma_\ell^h)}{\partial \sigma_\ell^h} \tilde{p}_j^i, \tag{B.14}$$

$$\frac{\partial}{\partial w_{j\ell}^{ih}} \left(\frac{\partial s(\sigma_k^h)}{\partial \sigma_k^h} \right) = \frac{\partial^2 s(\sigma_k^h)}{\partial (\sigma_k^h)^2} \frac{\partial^2 \sigma_k^h}{\partial (w_{j\ell}^{ih})^2} = \frac{\partial^2 s(\sigma_k^h)}{\partial (\sigma_k^h)^2} \tilde{p}_j^i \delta_{kl}, \tag{B.15}$$

$$\frac{\partial w_{jk}^{ih}}{\partial w_{j\ell}^{ih}} = \delta_{kl}, \tag{B.16}$$

where δ_{kl} denotes the Kronecker symbol defined as

$$\delta_{kl} = \begin{cases} 1 & \forall k = l, \\ 0 & \forall k \neq l. \end{cases} \tag{B.17}$$

Considering Eqs. (B.14) – (B.16), Eq. (B.13) can be written as

$$\begin{aligned}
\frac{\partial^2 u_r^*}{\partial p_j^i \partial w_{j\ell}^{ih}} & = \frac{\partial u_r^*}{\partial \tilde{u}_r^*} \frac{\partial^2 s(\sigma_r^o)}{\partial (\sigma_r^o)^2} w_{\ell r}^{ho} \frac{\partial s(\sigma_\ell^h)}{\partial \sigma_\ell^h} \tilde{p}_j^i \sum_{k=1}^{n_v} \left[w_{kr}^{ho} \frac{\partial s(\sigma_k^h)}{\partial \sigma_k^h} w_{jk}^{ih} \right] \frac{\partial \tilde{p}_j^i}{\partial p_j^i} + \\
& + \frac{\partial u_r^*}{\partial \tilde{u}_r^*} \frac{\partial s(\sigma_r^o)}{\partial \sigma_r^o} \sum_{k=1}^{n_v} \left[w_{kr}^{ho} \frac{\partial^2 s(\sigma_k^h)}{\partial (\sigma_k^h)^2} \tilde{p}_j^i \delta_{kl} w_{jk}^{ih} \right] \frac{\partial \tilde{p}_j^i}{\partial p_j^i} + \\
& + \frac{\partial u_r^*}{\partial \tilde{u}_r^*} \frac{\partial s(\sigma_r^o)}{\partial \sigma_r^o} \sum_{k=1}^{n_v} \left[w_{kr}^{ho} \frac{\partial s(\sigma_k^h)}{\partial \sigma_k^h} \delta_{kl} \right] \frac{\partial \tilde{p}_j^i}{\partial p_j^i} =
\end{aligned} \tag{B.18}$$

Considering the definition of the Kronecker symbols (see Eq. (B.17)), finally yields

$$\begin{aligned}
\frac{\partial^2 u_r^*}{\partial p_j^i \partial w_{j\ell}^{ih}} & = \frac{\partial u_r^*}{\partial \tilde{u}_r^*} \frac{\partial^2 s(\sigma_r^o)}{\partial (\sigma_r^o)^2} w_{\ell r}^{ho} \frac{\partial s(\sigma_\ell^h)}{\partial \sigma_\ell^h} \tilde{p}_j^i \sum_{k=1}^{n_v} \left[w_{kr}^{ho} \frac{\partial s(\sigma_k^h)}{\partial \sigma_k^h} w_{jk}^{ih} \right] \frac{\partial \tilde{p}_j^i}{\partial p_j^i} + \\
& + \frac{\partial u_r^*}{\partial \tilde{u}_r^*} \frac{\partial s(\sigma_r^o)}{\partial \sigma_r^o} w_{\ell r}^{ho} \frac{\partial^2 s(\sigma_\ell^h)}{\partial (\sigma_\ell^h)^2} \tilde{p}_j^i w_{j\ell}^{ih} \frac{\partial \tilde{p}_j^i}{\partial p_j^i} + \\
& + \frac{\partial u_r^*}{\partial \tilde{u}_r^*} \frac{\partial s(\sigma_r^o)}{\partial \sigma_r^o} w_{\ell r}^{ho} \frac{\partial s(\sigma_k^h)}{\partial \sigma_k^h} \frac{\partial \tilde{p}_j^i}{\partial p_j^i}.
\end{aligned} \tag{B.19}$$

The last term in (B.8) is a second mixed derivative of u_r^* with respect to the input parameters and the network weights linking the hidden layer and the output layer. It can be

evaluated as

$$\begin{aligned} \frac{\partial}{\partial w_{\ell r}^{ho}} \left(\frac{\partial u_r^*}{\partial p_j^i} \right) &= \frac{\partial u_r^*}{\partial \tilde{u}_r^*} \frac{\partial}{\partial w_{\ell r}^{ho}} \left(\frac{\partial s(\sigma_r^o)}{\partial \sigma_r^o} \right) \sum_{k=1}^{n_v} \left[w_{kr}^{ho} \frac{\partial s(\sigma_k^h)}{\partial \sigma_k^h} w_{jk}^{ih} \right] \frac{\partial \tilde{p}_j^i}{\partial p_j^i} + \\ &+ \frac{\partial u_r^*}{\partial \tilde{u}_r^*} \frac{\partial s(\sigma_r^o)}{\partial \sigma_r^o} \sum_{k=1}^{n_v} \left[\frac{\partial w_{kr}^{ho}}{\partial w_{\ell r}^{ho}} \frac{\partial s(\sigma_k^h)}{\partial \sigma_k^h} w_{jk}^{ih} \right] \frac{\partial \tilde{p}_j^i}{\partial p_j^i}. \end{aligned} \quad (\text{B.20})$$

The underlined terms in Eq. (B.16) can be written as:

$$\frac{\partial}{\partial w_{\ell r}^{ho}} \left(\frac{\partial s(\sigma_r^o)}{\partial \sigma_r^o} \right) = \frac{\partial^2 s(\sigma_r^o)}{\partial (\sigma_r^o)^2} \frac{\partial \sigma_r^o}{\partial w_{\ell r}^{ho}} = \frac{\partial^2 s(\sigma_r^o)}{\partial (\sigma_r^o)^2} s(\sigma_\ell^h), \quad (\text{B.21})$$

$$\frac{\partial w_{kr}^{ho}}{\partial w_{\ell r}^{ho}} = \delta_{kl}. \quad (\text{B.22})$$

Considering Eqs. (B.21) and (B.22), Eq. (B.20) can be written as

$$\begin{aligned} \frac{\partial^2 u_r^*}{\partial p_j^i \partial w_{\ell r}^{ho}} &= \frac{\partial u_r^*}{\partial \tilde{u}_r^*} \frac{\partial^2 s(\sigma_r^o)}{\partial (\sigma_r^o)^2} s(\sigma_\ell^h) \sum_{k=1}^{n_v} \left[w_{kr}^{ho} \frac{\partial s(\sigma_k^h)}{\partial \sigma_k^h} w_{jk}^{ih} \right] \frac{\partial \tilde{p}_j^i}{\partial p_j^i} + \\ &+ \frac{\partial u_r^*}{\partial \tilde{u}_r^*} \frac{\partial s(\sigma_r^o)}{\partial \sigma_r^o} \sum_{k=1}^{n_v} \left[\delta_{kl} \frac{\partial s(\sigma_k^h)}{\partial \sigma_k^h} w_{jk}^{ih} \right] \frac{\partial \tilde{p}_j^i}{\partial p_j^i}. \end{aligned} \quad (\text{B.23})$$

Considering the definition of the Kronecker symbols according to Eq. (B.17), finally yields

$$\begin{aligned} \frac{\partial^2 u_r^*}{\partial p_j^i \partial w_{\ell r}^{ho}} &= \frac{\partial u_r^*}{\partial \tilde{u}_r^*} \frac{\partial^2 s(\sigma_r^o)}{\partial (\sigma_r^o)^2} s(\sigma_\ell^h) \sum_{k=1}^{n_v} \left[w_{kr}^{ho} \frac{\partial s(\sigma_k^h)}{\partial \sigma_k^h} w_{jk}^{ih} \right] \frac{\partial \tilde{p}_j^i}{\partial p_j^i} + \\ &+ \frac{\partial u_r^*}{\partial \tilde{u}_r^*} \frac{\partial s(\sigma_r^o)}{\partial \sigma_r^o} \frac{\partial s(\sigma_\ell^h)}{\partial \sigma_\ell^h} w_{j\ell}^{ih} \frac{\partial \tilde{p}_j^i}{\partial p_j^i}. \end{aligned} \quad (\text{B.24})$$

Appendix **C**

Experimentally obtained values of C_{1111} and C_{1212} of gravel

Table C.1: 19 values of C_{1111} in [MPa] back analyzed based on longitudinal-wave velocities evaluated from accelerometer measurements

153.81	162.47	256.09	292.63	365.55	368.21	390.88	393.76	504.75	508.47
508.47	514.28	514.28	558.05	689.51	861.29	972.32	1106.3	1106.3	

Table C.2: 66 values of C_{1212} in [MPa] back analyzed based on shear-wave velocities evaluated from accelerometer measurements

21.120	26.912	30.867	40.327	46.021	50.190	52.213	52.213	55.858	59.267
59.908	61.233	63.996	65.975	69.221	69.369	71.908	72.957	80.233	81.370
82.343	83.575	86.311	87.262	88.022	88.022	93.412	106.14	108.55	109.44
110.17	113.00	118.32	131.71	132.33	134.97	142.03	145.78	149.62	150.03
169.17	178.55	178.55	178.90	181.04	190.08	200.01	202.33	228.65	229.06
237.02	252.46	252.49	254.26	254.26	261.20	264.33	266.63	270.52	272.16
345.29	376.51	380.63	416.77	676.68	730.53				

Appendix **D**

Kinematic model of the impact used for the PFEA

Estimates of the impact-force history $F(t)$ requires information on the kinematics of the rock boulder during impact. This kinematic behavior is characterized by six boundary conditions. Three of them refer to the time instant when the boulder gets in contact with the hit surface at time instant $t = t_0 = 0$: (i) The indentation depth $w(t_0) = 0$, (ii) the impact velocity $v(t_0) = \sqrt{2gh_f}$, where $g = 9,81 \text{ m/s}^2$ represents the gravitational acceleration and h_f stands for the height of fall, which is assumed to be known, (iii) the acceleration of the boulder $a(t_0) = g$. During the impact, the indentation depth continuously increases. The force acting from the hit soil onto the impactor decelerates the boulder. At the end of the impact, characterized by the unknown time instant Δt_i , the rock boulder rests in the produced crater. This state of the boulder, at $t = \Delta t_i$, is characterized by: (iv) the indentation depth $w(\Delta t_i)$ is equal to the final penetration depth X , which is assumed to be known, (v) the impact velocity $v(\Delta t_i) = 0$; (vi) zero acceleration of the boulder, $a(\Delta t_i) = 0$.

A fifth-order polynomial is chosen for the description of the indentation depth w as a function of time t . This polynomial, denoted as $w(t)$, together with its derivatives up to the third-order, comprising the impact velocity $v(t)$ and the impact acceleration $a(t)$,

reads as

$$\begin{aligned}
 w(t) &= c_5 t^5 + c_4 t^4 + c_3 t^3 + c_2 t^2 + c_1 t + c_0, \\
 \frac{dw(t)}{dt} &= v(t) = 5 c_5 t^4 + 4 c_4 t^3 + 3 c_3 t^2 + 2 c_2 t + c_1, \\
 \frac{d^2 w(t)}{dt^2} &= a(t) = 20 c_5 t^3 + 12 c_4 t^2 + 6 c_3 t + 2 c_2, \\
 \frac{d^3 w(t)}{dt^3} &= \frac{da(t)}{dt} = 60 c_5 t^2 + 24 c_4 t + 6 c_3.
 \end{aligned} \tag{D.1}$$

The coefficients c_0 , c_1 , c_2 , c_3 , c_4 , and c_5 are set such that the conditions (i) – (vi) are met:

$$\begin{aligned}
 c_0 &= 0, & c_3 &= (-14,715 \Delta t_i^2 - 26,5756 \sqrt{h_f} \Delta t_i + 10 X) / \Delta t_i^3, \\
 c_1 &= \sqrt{2 g h_f} = \sqrt{19.62 h_f}, & c_4 &= (+14,715 \Delta t_i^2 + 35,4356 \sqrt{h_f} \Delta t_i - 15 X) / \Delta t_i^4, \\
 c_2 &= g/2 = 4.905 \text{ m/s}^2, & c_5 &= (-4,905 \Delta t_i^2 - 13,2883 \sqrt{h_f} \Delta t_i + 6 X) / \Delta t_i^5.
 \end{aligned} \tag{D.2}$$

The Eqs. (D.1) together with the Eqs. (D.2) provide estimates of the impact kinematics of a rock boulder for an arbitrarily chosen duration of the impact Δt_i . Physical plausibility allows for determination of a lower bound of Δt_i . For too small values chosen for Δt_i , the acceleration of the rock boulder will *increase* at the beginning of the impact. This contradicts the actual behavior of the rock boulder, where the force of the soil acting onto the rock boulder decelerates the motion of the impactor. Therefore, a lower bound for the impact duration is obtained by setting

$$\left. \frac{d^3 w(t)}{dt^3} \right|_{t=0} = \left. \frac{da(t)}{dt} \right|_{t=0} = 0. \tag{D.3}$$

Eq. (D.3) and Eqs. (D.1)₄ imply that $c_3 = 0$. Insertion of this result into the expression for c_3 taken from Eqs. (D.2) yields a quadratic equation for Δt_i . The physically sound solution reads

$$\min(\Delta t_i) = -0,90305 \sqrt{h_f} + \sqrt{0,81549 h_f + 0,67958 X}. \tag{D.4}$$

In the PFEA, $\min(\Delta t_i)$ was chosen such as to be an estimate of the actual impact duration, because a comparatively short impact duration yields a comparably large impact force and, hence, provides a conservative loading assumption. The force acting onto the soil during the impact of a mass m as a function of time, $F(t)$, reads

$$F(t) = m [g - a(t)]. \tag{D.5}$$

The mean indentation depth w_m by which the overburden of the FE model was reduced, is defined as

$$w_m = \frac{1}{\min(\Delta t_i)} \int_0^{\min(\Delta t_i)} w(t) dt. \tag{D.6}$$

Curriculum Vitae

Personal Details

Name	Dipl.-Ing. Bernhard Pichler
Date and Place of Birth	September 4, 1974; Vienna, Austria
Nationality	Austrian
Marital Status	Engaged
Private Address	Leibnifrostgasse 4/5, A-1040 Vienna
Professional Address	Institute for Strength of Materials Vienna University of Technology Karlsplatz 13/202, A-1040 Vienna
Phone	(+43 1) - 58801 / 202 13
Fax	(+43 1) - 58801 / 202 99
E-mail	Bernhard.Pichler@tuwien.ac.at
Homepage	http://www.fest.tuwien.ac.at/members/bp

Education and Qualifications

September 1980 – June 1984	Primary school, Vienna
September 1984 – June 1992	High school (humanistic branch), Vienna Final exam: June 4, 1992
July 1992 – February 1993	Military service
March 1993 – April 1999	Diploma studies: Civil Engineering, Vienna University of Technology Graduation with distinction: April 23, 1999
May 1999 – present	Doctoral studies, Institute for Strength of Materials, Vienna University of Technology